VENEZUELA-MEM/USA-DOE FOSSIL ENERGY REPORT IV-7

DOE/BC—92/1/SP
(DE91002259)

SUPPORTING TECHNOLOGY FOR ENHANCED OIL RECOVERY

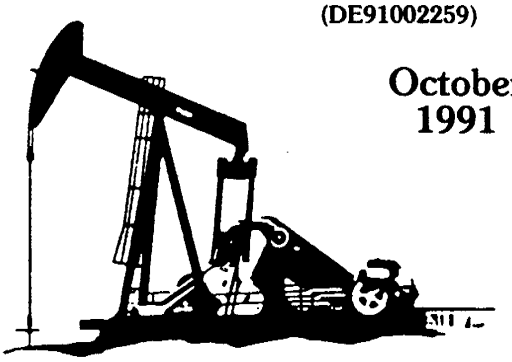

October
1991

EOR THERMAL PROCESSES

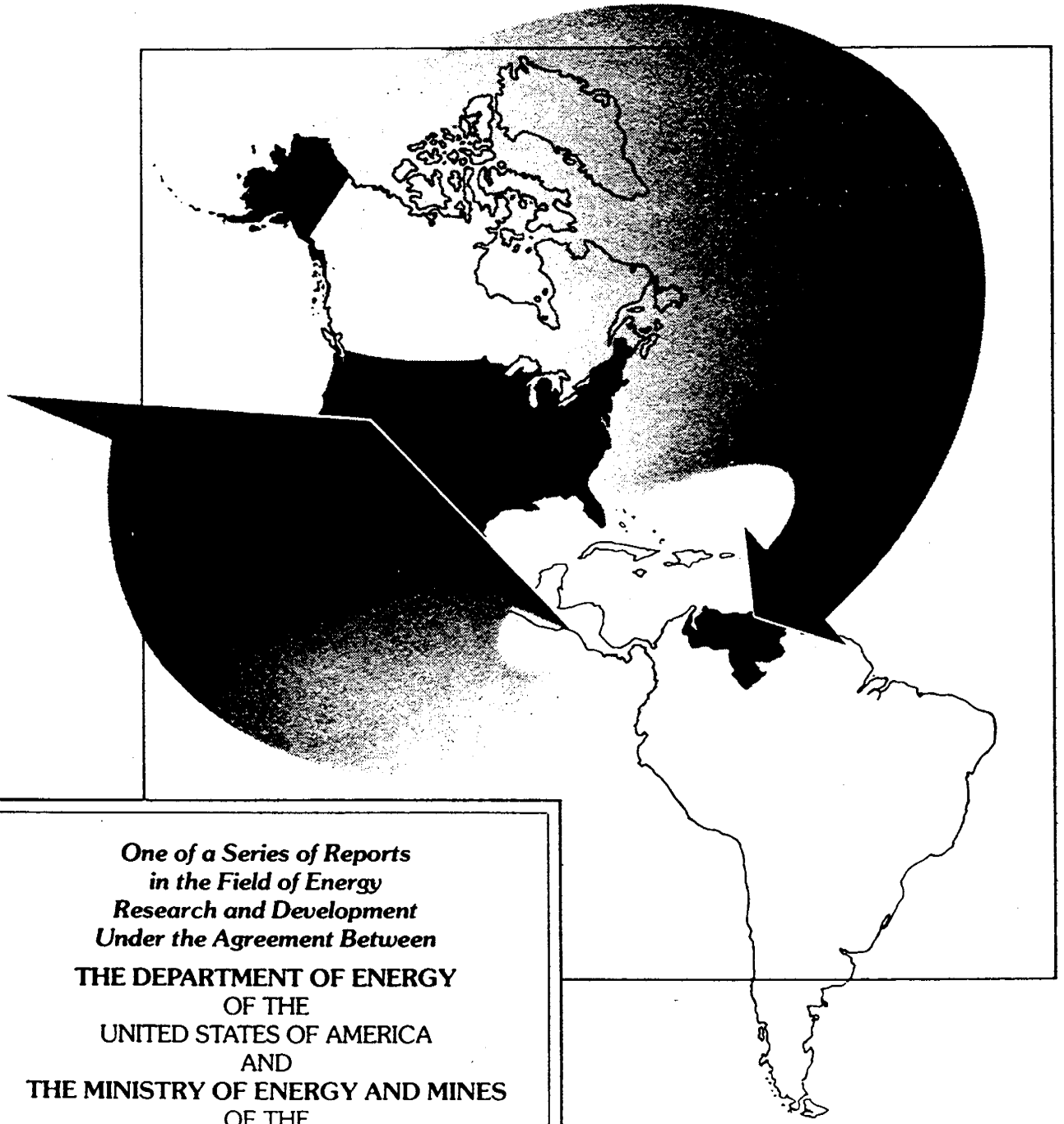

One of a Series of Reports
in the Field of Energy
Research and Development
Under the Agreement Between

THE DEPARTMENT OF ENERGY
OF THE
UNITED STATES OF AMERICA
AND
THE MINISTRY OF ENERGY AND MINES
OF THE
REPUBLIC OF VENEZUELA

DOE/BC—92/1/SP
(DE91002259)
Distribution Category UC-122

SIXTH AMENDMENT AND EXTENSION TO ANNEX IV ENHANCED OIL RECOVERY THERMAL PROCESSES

Implementing Agreement Between

THE DEPARTMENT OF ENERGY OF THE UNITED STATES OF AMERICA

And

THE MINISTRY OF ENERGY AND MINES OF THE REPUBLIC OF VENEZUELA

Submitted by:

Thomas B. Reid, Project Manager
Thermal Recovery
Bartlesville Project Office
U.S. Department of Energy

Orlando Rivas, Manager
Heavy Oil
INTEVEP, S.A.
Filial de Petroleos de Venezuela, S.A.

Approved by:

Thomas C. Wesson, Director
Bartlesville Project Office
P.O. Box 1398
Bartlesville, OK 74005

Gunter Spasic, Technology Coordinator
Petroleos de Venezeula, S.A.
Apartado Postal 169
Caracas 1010A, Venezuela

United States Department of Energy

PREFACE

An Agreement between the Department of Energy of the United States of America and the Ministry of Energy and Mines of the Republic of Venezuela to cooperate in Energy Research and Development was signed March 6, 1980. The object of cooperation under this DOE/MEMV Agreement was to promote a balanced exchange of energy technologies and to conduct joint projects in the areas of Petroleum, Solar Energy, Geothermal Energy, Hydroelectric Energy and Coal.

This Agreement supported the Agreement for Scientific and Technological Cooperation between the two countries which was signed by the Secretary of State of the U.S.A. and the Minister of Foreign Relations of Venezuela on January 11, 1980.

The original DOE/MEMV Agreement was supplemented by six annexes to describe specifically the work to be done. Over the past eight years additional annexes have been signed, resulting in a total of fourteen annexes as of August 9, 1991. The Agreement has been extended to March 6, 1993. The annexes are:

I. Characterization of Heavy Crude Oils.

II. Supporting Research in the Area of Enhanced Oil Recovery

III. Evaluation of Past and Ongoing Enhanced Oil Recovery Projects in the U.S. and Venezuela

IV. Enhanced Oil Recovery Thermal Processes

V. Drilling, Coring and Telemetry

VI. Residual Oil Saturation

VII. Petroleum Products, Use and Evaluation

VIII. Coal Preparation, Combustion and Related Technology

IX. Subsidence Due to Fluid Withdrawal

X. On-Site Training of Petroleum Engineers

XI. Energy Conservation

XII. Geochemistry (Oil Generation, Migration and Accumulation)

XIII. Microbial EOR

XIV. Exchange of Energy Related Personnel

CONTENTS

ABSTRACT

This report contains the results of efforts under the six tasks of the Sixth Amendment and Extension of Annex IV, Enhanced Oil Recovery Thermal Processes of the Venezuela/USA Agreement. The report is presented in sections (for each of the 6 tasks) and each section contains one or more reports prepared by various individuals or groups describing the results of efforts under each of the tasks.

A statement of each task, taken from the agreement, is presented on the first page of each section. The tasks are numbered 44 through 49. The first, second, thrid, fourth, fifth, and sixth reports on Annex IV, [Venezuela MEM/USA-DOE Fossil Energy Report IV-1, IV-2, IV-3, IV-4, IV-5, and IV-6 (DOE/BETC.SP-83/15, DOE/BC-84/6/SP, DOE/BC-86/2/SP, DOE/BC-87/2/SP, DOE/BC-89/1/SP, and DOE/BC-90/1/SP)] contain the results from the first 43 tasks. Those reports are dated April 1983, August 1984, March 1986, July 1987, November 1988, and December 1989 respectively.

Task 44 - DOE shall provide INTEVEP with information from the work performed by SUPRI on the transient flow behavior of steam and steam/foam flow and low pressure foam flow including data and analysis from CAT-SCAN measurements of these processes. In addition DOE/SUPRI will provide on in-situ combustion and combustion kinetics experiments with various crudes with and without catalysts used to affect the nature and amount of fuel formed.

CONTENTS

A STUDY OF END EFFECTS IN DISPLACEMENTS EXPERIMENTS

by

S. Qadeer

Stanford University
Petroleum Research Institute
Stanford, California

1.1 A STUDY OF END EFFECTS IN DISPLACEMENT EXPERIMENTS
(S. Qadeer)

The capillary discontinuities at the inlet and outlet ends of cores in displacement experiments results in the development of sharp saturation gradients. These saturation gradients are generally called capillary end effects. The outlet end effect has received a lot of attention from researchers, but the inlet effect is little understood. The purpose of this study is to fully understand these effects. To achieve this goal, flow experiments will be performed using consolidated sandstone cores. The saturations will be measured using a CT scanner.

Preliminary runs indicate a strong gravity segregation of oil and water near the inlet end during imbibition runs. This causes the oil to be trapped near the inlet face. As a result water can enter only through half of the core face. More runs are planned to study the effect of different parameters on saturation distribution near the inlet and outlet ends.

1.1.1 EXPERIMENTAL SETUP

The experiments are being performed using a core holder built from PVC. The details of this setup are given in the previous report (Brigham, et al. 1990).

One of the parameters being studied is the geometry of the flow ports in inlet and outlet end plugs. Presently we are using only one 1/8th in. hole in the middle of the plugs (there are no distribution grooves). These runs will provide data for the base case. Distribution grooves will be added and their effectiveness studied. Additional ports in both end plugs have been added so that pressures can be measured right at the face of the core. Figure 1.1.1 gives the details of the modified end plugs.

1.1.2 EXPERIMENTAL PROCEDURE

The cores used in this study are Berea sandstone. The cores are two inches in diameter and about ten inches long. After cutting the cores to desired dimensions, they are baked in an oven at 600°C for six hours and then left inside the oven overnight for slow cooling. The core is then transferred to the core holder. The air is displaced with carbon dioxide. The core is then evacuated. The sequence of injecting carbon dioxide and evacuation is repeated twice to ensure that no air is left trapped inside the core. At this point, the core is scanned at twelve locations. The scan locations are shown in Fig. 1.1.2.

Sodium iodide brine (2%) is then allowed to flow into the core under vacuum. The core is left overnight in contact with brine. After that, brine is flowed through the core at low flow rate for a day, under a back pressure of 45 psi. This is done to avoid any entrapment of gas phase in the core. The flow is then stopped and the core is again scanned to get the CT numbers for 100% brine saturated core.

At this point the oil phase is injected into the core for primary drainage. The cores are scanned at the preselected locations right at the start of the primary drainage and then after each fifteen minutes, until breakthrough. The scanning interval is then changed as required. This allows us to generate the saturation history of the process. After the primary drainage run is over, sodium iodide brine is injected into the core to get imbibition data. The scans are repeated at the same locations. We hope to get good saturation history data by this technique.

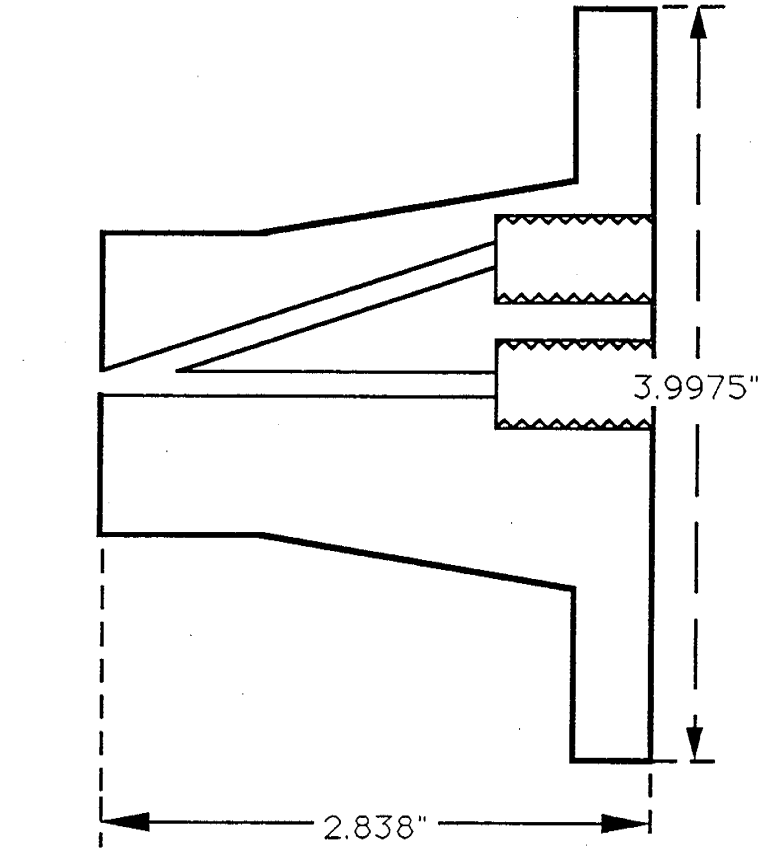

(a)

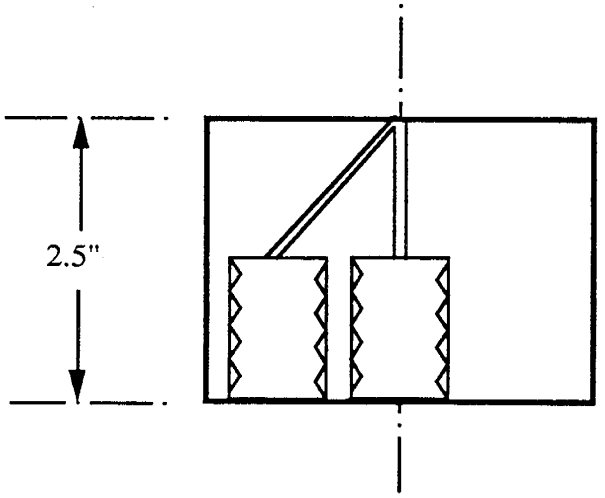

(b)

Figure 1.1.1 Modified end plugs: (a) Inlet end plug. (b) outlet end plug.

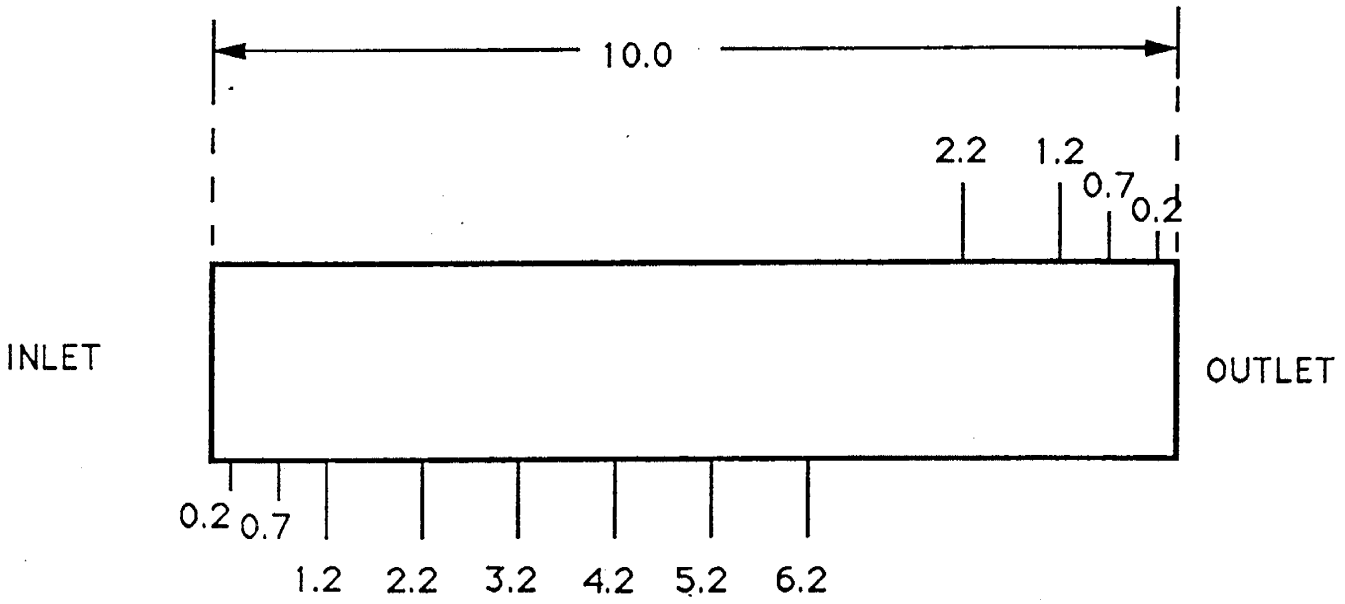

Figure 1.1.2 CT Scan Locations

1.1.3 PROBLEMS DURING PRELIMINARY RUNS

The preliminary runs were made using cyclo-hexane as the oil phase. It was observed that the rubber sleeve in the core holder and the stoppers used in the separator absorbs cyclo-hexane, and thus they expand. The increase in the volume of core sleeve in the core holder causes the overburden pressure to increase continuously. The swelling of the stoppers in the separator causes errors in data. This absorption also introduces a large material balance error, thus the recovery data are unreliable.

The rest of the system operated as designed. No problems were found in re-circulating the injected fluids. The separation system was effective in separating the oil and brine.

1.1.4 RESULTS

The objectives of the preliminary runs were two-fold: one was to check the operation of the experimental setup, and the other was to confirm that the scanner can be used to determine saturations with required accuracy.

The experimental setup worked adequately except for the sleeve and some other rubber components. The data acquisition system also worked.

The results from the scanner computer are shown in Figs. 1.1.3 through 1.1.7 and 1.1.9. These images were obtained by digitizing the image generated by the scanner computer using our Macintosh computer and enhancing the contrast and brightness by the image processing software. All the images were processed at the same settings to avoid any artifacts or false contrasts in different scans. Table 1.1.1 shows some typical CT numbers obtained from these scans.

Figure 1.1.3 shows the scans from the dry, evacuated core. The CT numbers are about 350 units. All of the CT pictures show that there is considerable beam hardening. This causes some concentric artifacts to appear in the scans. By looking at all the scans we can see that the core used is quite uniform.

Scans from the fully saturated core with 2% sodium iodide brine are shown in Fig. 1.1.4. The averaged CT numbers in each scan are about 100 units greater than those of the dry core. These scans show beam hardening. It can be noted that the beam hardening has different characteristics at different scan locations.

After measuring the absolute permeability, cyclo-hexane was injected into the core at a rate of 1.0 cc/min. The scans were taken at intervals of 15 minutes up to the breakthrough time. The scanning interval was increased to half an hour after breakthrough. The scans at the end of primary drainage are shown in Fig. 1.1.5. The CT numbers dropped by about 50 units from those of 100% brine saturated core. This gives us enough resolution to calculate saturation of brine in subsequent runs.

The measurements of CT numbers follow statistical distribution. We are in the process of analyzing the data to determine the accuracy with which we measure the saturations.

At the end of drainage, brine was injected into the core at a rate of 1 cc/min. The scans after injecting about 0.5 PV are shown in Fig. 1.1.6. The CT numbers again increased. The most interesting feature of the imbibition was observed near the inlet end. It appeared that the injected brine was strongly underriding the in-place oil at the inlet. The scans of the inlet at different times of injection are shown in Fig. 1.1.7. As can be seen, the brine enters the core through the lower half of the inlet face. Some oil is trapped in the upper half near the inlet end.

At the end of the imbibition, the inlet end of the core was scanned at the locations shown in Fig. 1.1.8. The purpose of these scans was to determine the extent of gravity underride. The results are shown in Fig. 1.1.9. As is obvious, the brine imbibes upwards in a very short

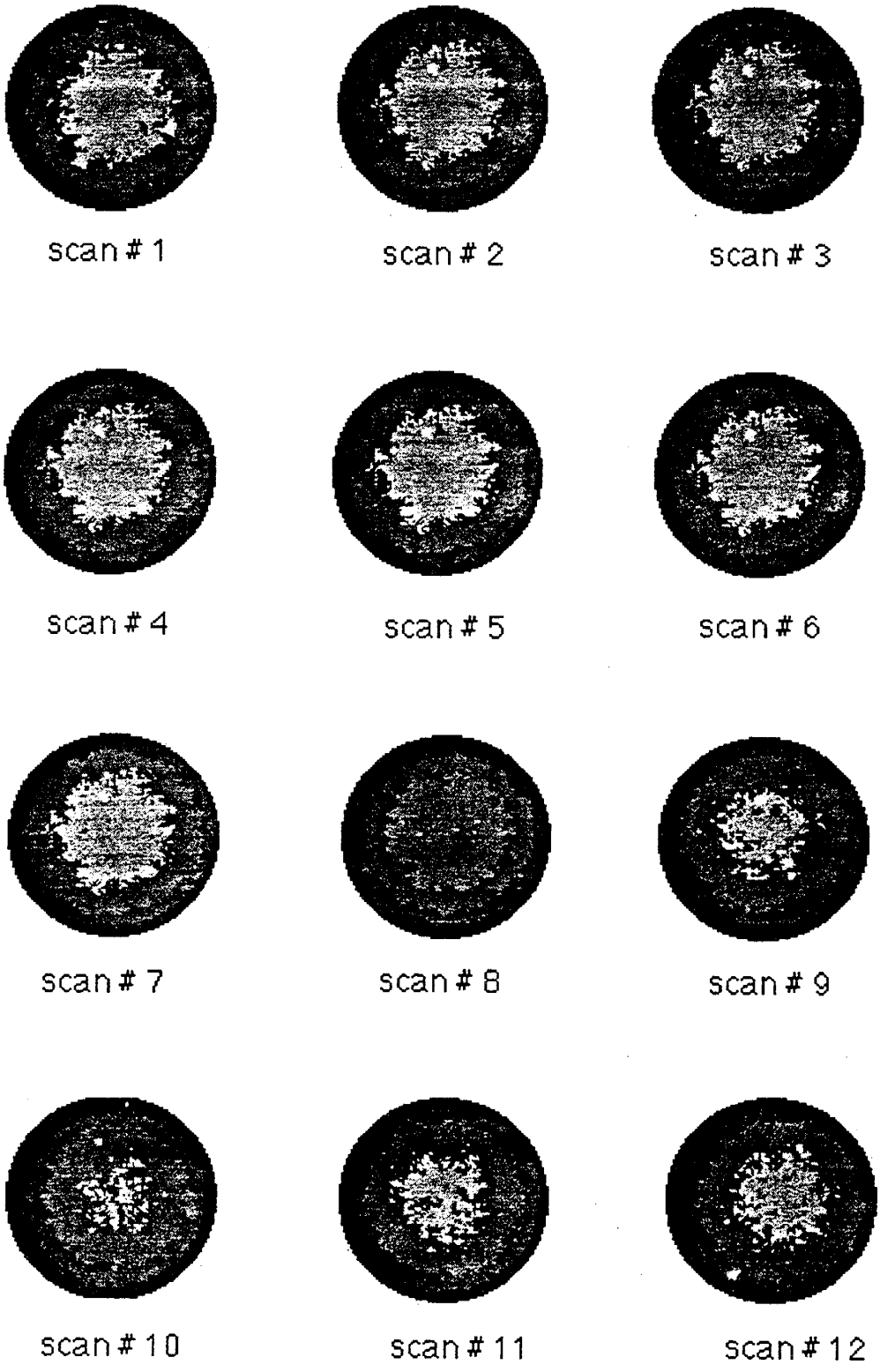

Figure 1.1.3 CT images of dry core.

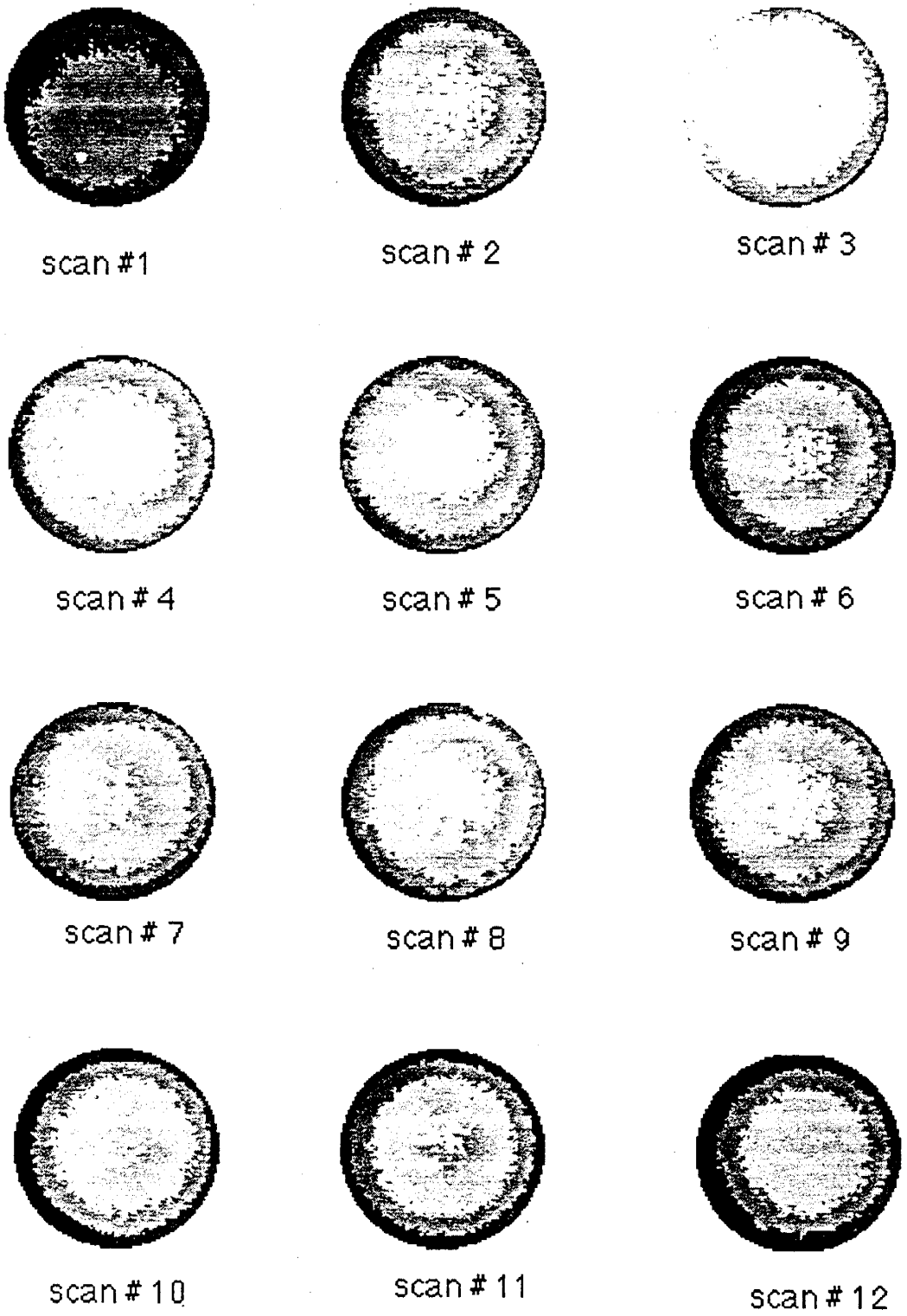

Figure 1.1.4 CT images from 100% brine saturated core.

Table 1.1.1 Typical CT Numbers

SCAN LOCATION	CT #'s			
1	363	414	311	324 / 412
6	342	471	429	460
12	356	456	448	466
	DRY	100%	D	I

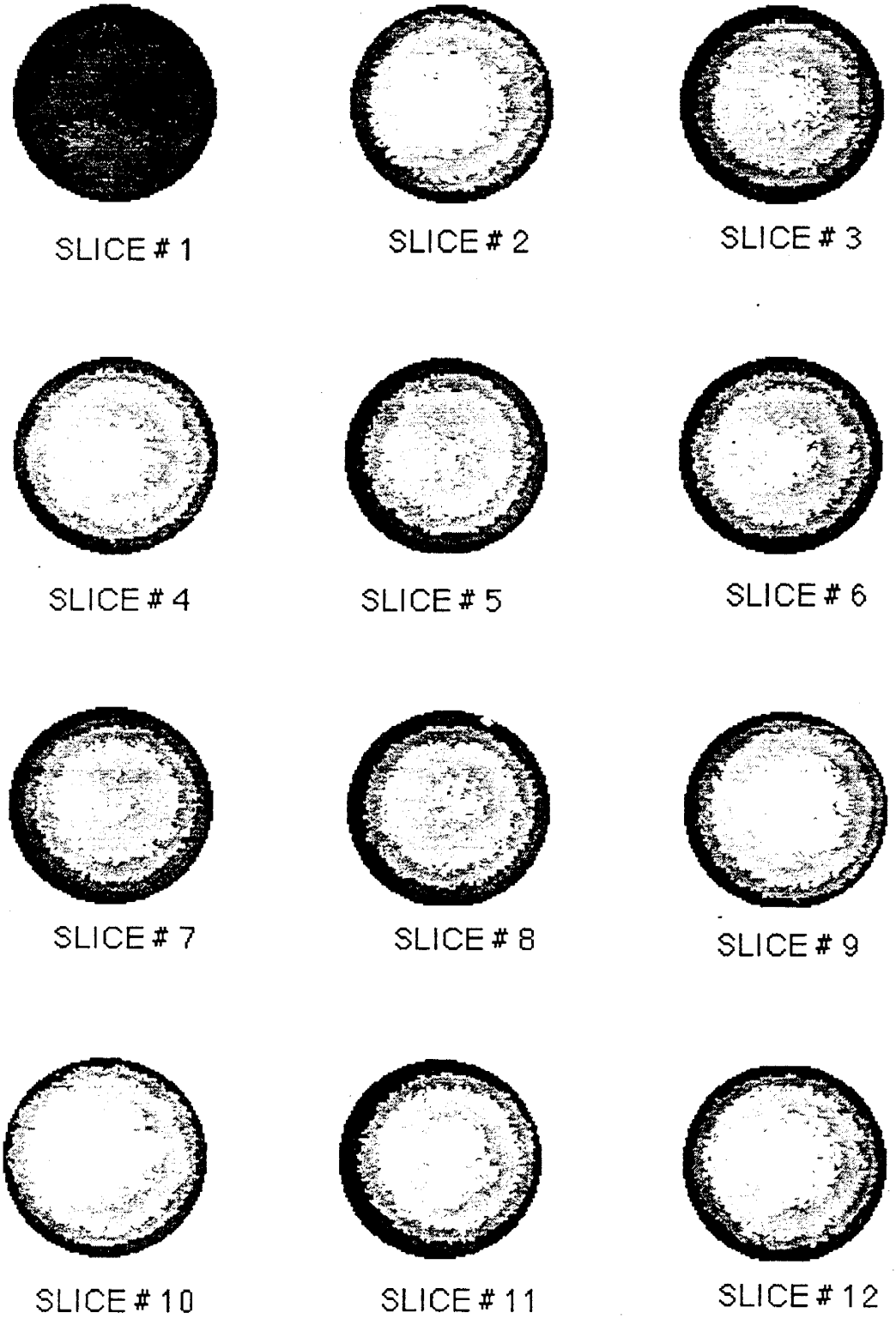

Figure 1.1.5 CT images at the end of drainage run.

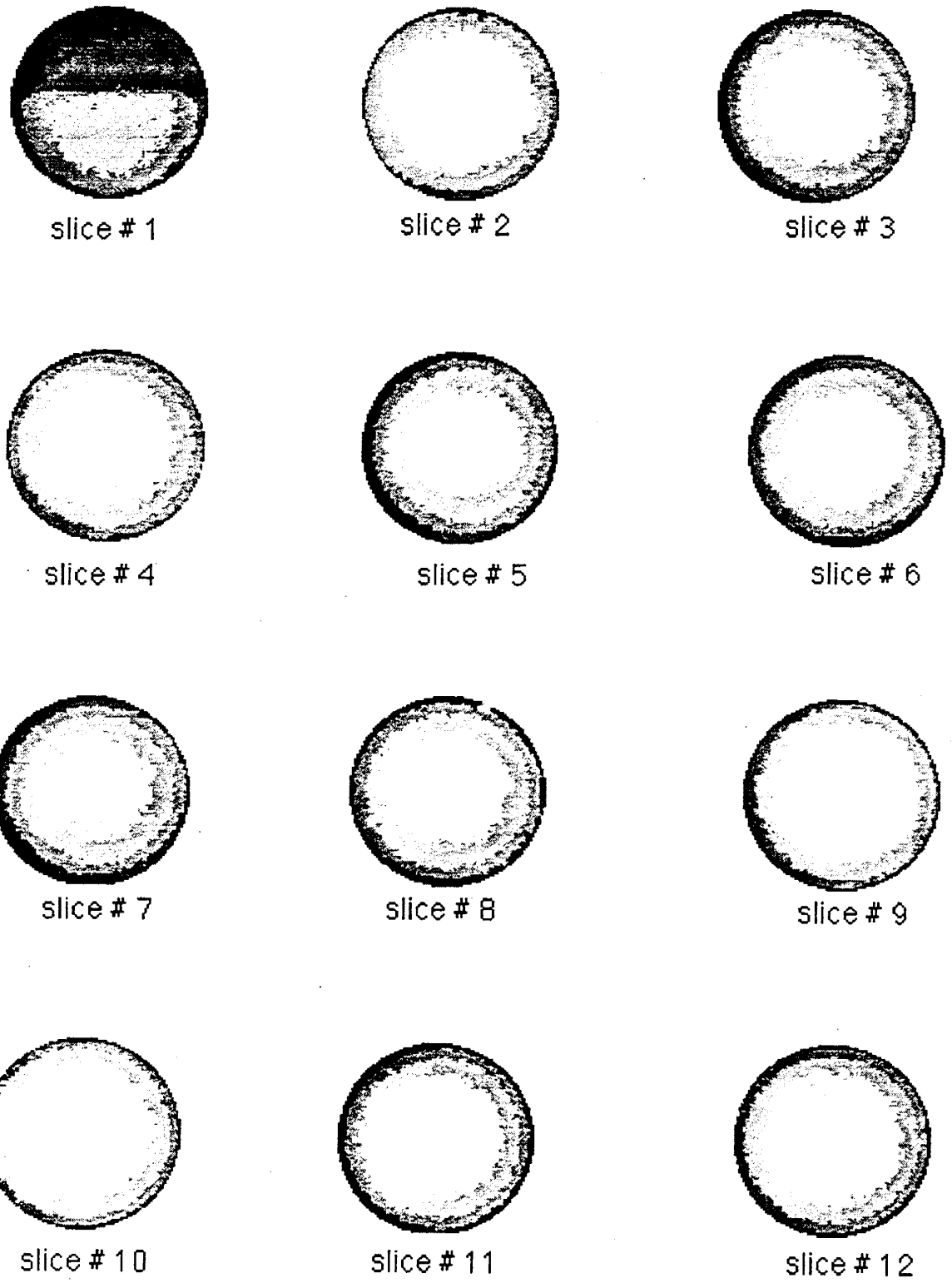

Figure 1.1.6 CT scans after imbibition run.

0.0 P.V.

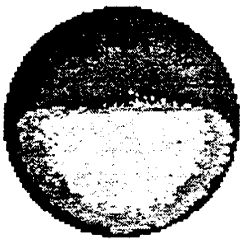

0.25 P.V.

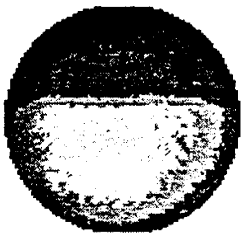

0.5 P.V.

Figure 1.1.7 Inlet end at different times.

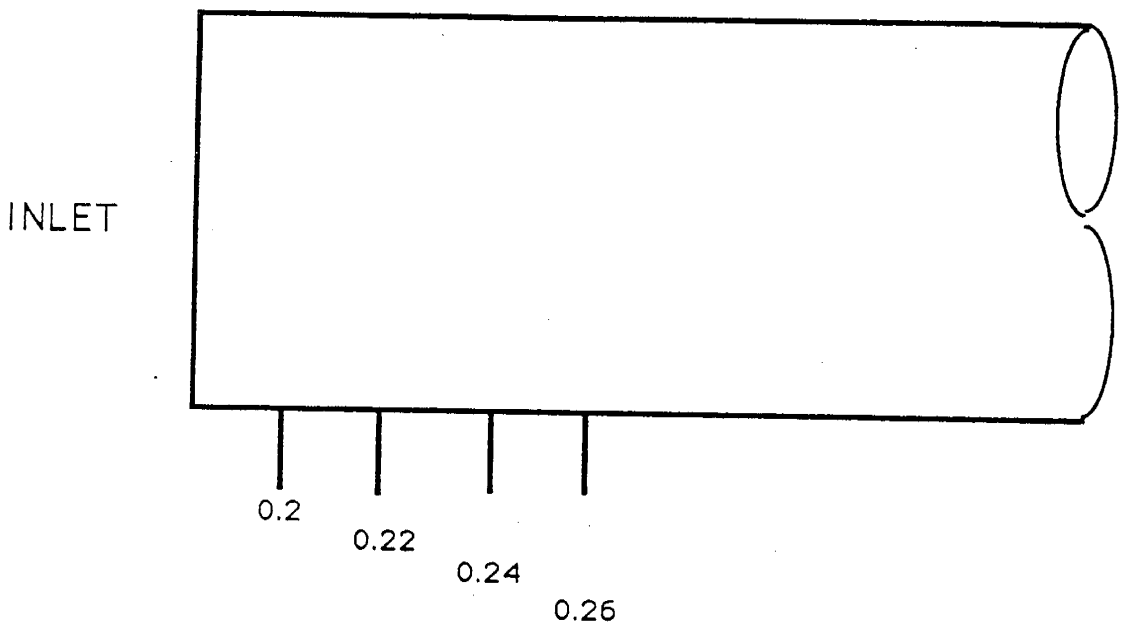

Figure 1.1.8 Scan Location for Fig. 1.1.9

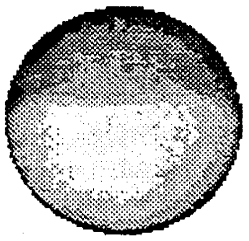

slice # 1

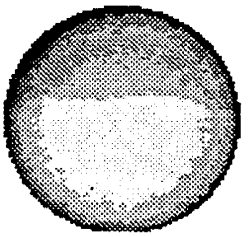

slice # 2

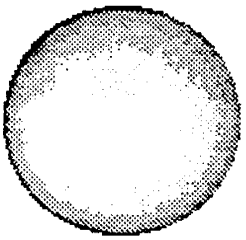

slice # 3

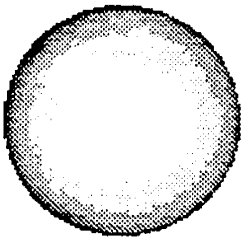

slice # 4

Figure 1.1.9 Scans to determine the extent of the inlet effect.

length. This is expected because of the strong capillary forces in the core.

Although some qualitative results were obtained in these experiments, the detailed analysis of the CT data has not been completed. This will require processing of the CT numbers and calculating the saturations at each cross-section. The results obtained so far are preliminary.

1.1.5 FUTURE PLAN

It is clear from the results obtained during preliminary runs that special software is required to process CT data in order to obtain saturations. We are in the process of acquiring a SUN work station which will allow us to use the SHELL CATPIX software for saturation determination. Additional software is required to transfer CT data from the CT computer to the SUN work station. This work is already in progress.

After acquiring the capability to calculate saturations from the CT data more runs will be made to fully understand the end effects.

To cover a broad range of operating conditions the effects of changing the viscosity ratio, the absolute permeability of the core, different end plug configurations (different geometry of the distribution grooves) will be studied. An appropriate numerical model for the inlet and outlet effects will be developed.

CAT SCAN STATUS REPORT

by

L. Castanier

Stanford University
Petroleum Research Institute
Stanford, California

1.2 CAT SCAN STATUS REPORT
(L. Castanier)

Efforts during this year have focused on two main areas: software implementation and new experiments.

1.2.1 SOFTWARE IMPLEMENTATION

A SUN SPARC workstation was purchased in order to increase our image processing capability. Transfer of the CATPIX software to the SPARC system was made without problems. Shell's CATPIX software is now installed and working on our computers. Image formating, however, remains difficult because of the nonstandard nature of our scanner. A program to transfer directly the data as CT numbers on a pixel by pixel basis from the EMI CAT scanner computer to the SPARC via RS232 interface is being written. This should allow full use of the CATPIX software specially for three-phase saturation calculations from scanner measurements. A new version of IMAGE (version 28) was obtained for use on the Macintosh. This version allows direct capture of the pictures from the video signal originating at the diagnostic console. We now have the possibility of quickly displaying and analyzing results.

1.2.2 NEW EXPERIMENTS

In addition to the transient foam flow, end effect and three-dimensional steam model experiments described elsewhere in this report, several new projects have been initiated. Although most of these are not part of the thermal recovery research program we will give a brief description of the planned research.

Fractured Media

A new epoxy core holder has been designed and built in order to study multiphase flow in fractured porous media. Two Berea sandstone cores coming from the same block will be used for oil/water flow experiments. One of the cores is compact, the other has been cut in half to simulate a fracture. The two cores will be drained and imbibed at the same rates under the scanner. Pressure gradients and saturations will be measured. Numerical simulation will be used to deduce relative permeabilities.

Drying and Wetting Fluid Distribution

In a drying or wetting porous medium fluid distribution is important. Even in the simple case of water/air systems the wetting and drying behavior of various rock samples of permeability and porosity spanning a broad range needs to be investigated. Preliminary experiments have been performed on Fontainebleau and Berea cores in order to design a proper experimental procedure.

Validation of Other Nondestructive Measurements

For the calibration of measurement methods such as resistivity or acoustic propagation it is necessary to have the saturation distribution in the sample. Measurements of saturations by CAT scan will be compared with results obtained by resistivity and sonic velocity measurements on the same cores. Design and construction of a special coreholder is in progress. This work will be performed in cooperation with the Stanford Geophysics Department.

MODIFYING IN-SITU COMBUSTION WITH METALLIC ADDITIVES

by

L. Castanier

Stanford University
Petroleum Research Institute
Stanford, California

2.1 MODIFYING IN-SITU COMBUSTION WITH METALLIC ADDITIVES
(L. Castanier)

2.1.1 ABSTRACT

In-situ combustion is the most energy efficient of thermal enhanced oil recovery methods. In light oil reservoirs, too little fuel may be deposited and in very heavy oil reservoirs too much fuel may be deposited. A research program has been initiated to try to solve these problems. We decided to test water soluble additives to attempt to modify the fuel deposition reactions. In the first stage, kinetics experiments were run on Huntington Beach (18.5° API) and Hamaca, Venezuela (10.5° API) oils in the presence of aqueous solutions of metallic salts. The results were compared with control runs with no metal present. While the presence of copper, nickel and cadmium had little or no effect; iron, tin, zinc and aluminum increased fuel laydown for Huntington Beach oil. The results were similar for the heavier Hamaca oil as no reduction in fuel was noticed with any of the metallic additives. Ketals were mixed with Hamaca oil as a way to reduce fuel. No effect was observed when the ketals were used. Eight combustion tube runs were made in the second stage of the study. Metallic additives iron, tin and zinc improved the combustion efficiency in all cases. As a result, the front velocities were increased by the metallic additives. Changes were also observed in H/C ratio of the fuel, heat of combustion, air requirements and density of the crude produced. The amount of fuel deposited varied between the two oils. For Huntington Beach oil, the amount of fuel increased in the order: zinc, control, tin and iron while for the Hamaca crude the order was: control, iron and tin. To date we have not been able to find a suitable additive to reduce fuel deposition. Iron and tin salts seem suitable agents to increase fuel when that is needed.

2.1.2 INTRODUCTION

One of the methods used to recover heavy or medium gravity crude oils is in-situ combustion. During an in-situ combustion field project, air or oxygen is injected into the reservoir to burn part of the oil in place which generates a heat front propagating through the reservoir (Fig. 2.1.1). Heat is conducted forward by conduction, convection of the combustion gasses and condensation. The oil ahead of the combustion front is displaced by gas drive from the combustion gasses, by hot water and steam drive as well as miscible drive provided by the condensed light ends. The process is controlled by the kinetics of the combustion reactions as well as the deposition of the heavy portions of the crude on the rock matrix. The "fuel" burnt is the unrecoverable carbon rich residue deposited as a result of distillation, thermal cracking and some catalytic cracking. An important parameter for the economics of the process is the amount of air needed to recover a given volume of oil (air/oil ratio). This in turn depends on the nature and amount of fuel deposited. Two limits in the amount of fuel can exist:

- For very heavy crudes, too much fuel may exist, causing excessive air requirement.
- For light crudes, not enough fuel may be deposited to sustain the combustion.

The objectives of this work are to investigate means to modify the nature and the amount of fuel burned by adding water soluble additives to the system. General screening was performed by kinetics experiments and some of the most promising products were tested in our combustion tube.

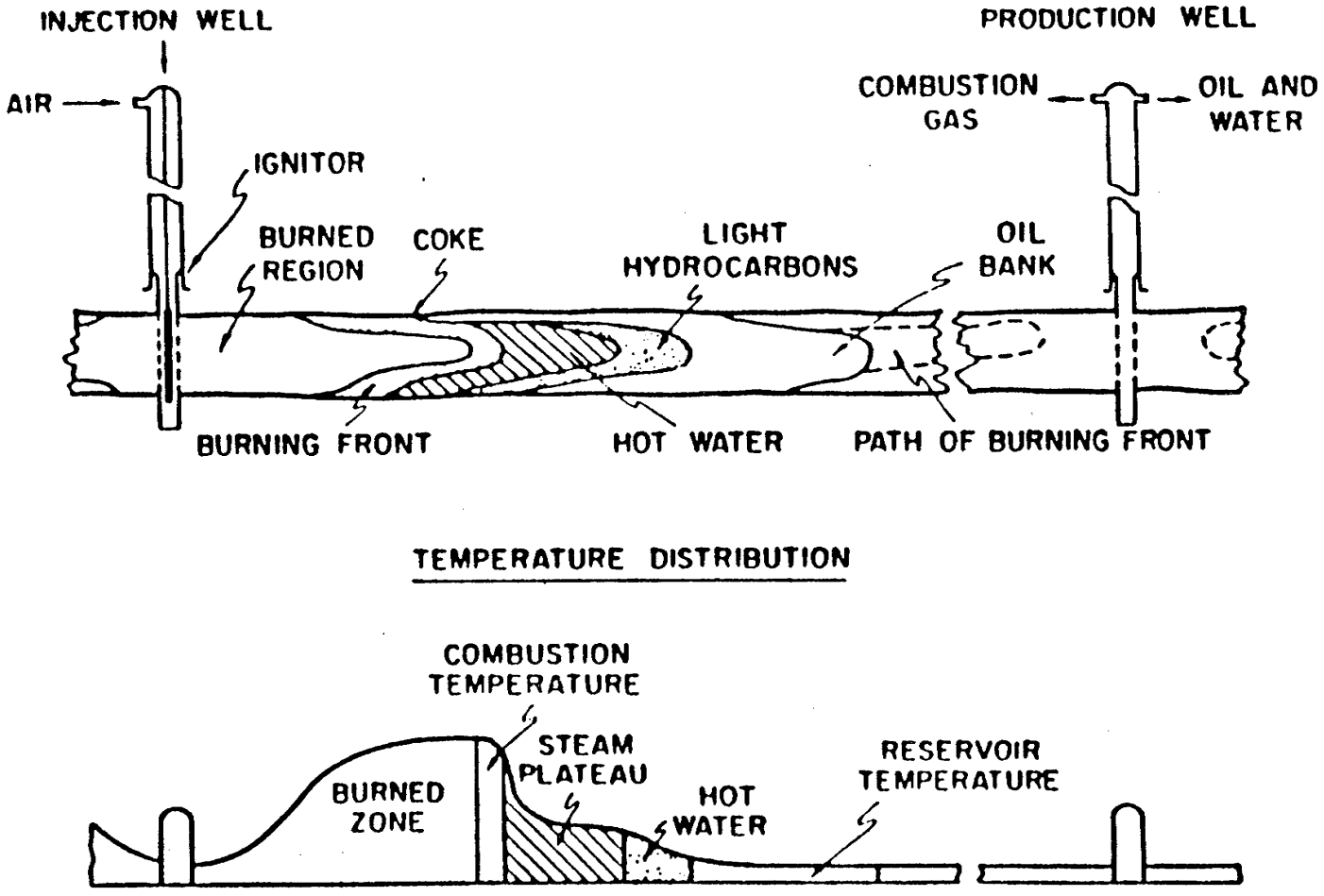

Figure 2.1.1 Cross Section of a Reservoir Subjected to In-Situ Combustion.

2.1.3 KINETICS EXPERIMENTS

The oxidation of oil during in-situ combustion involves numerous competing reactions occurring over different temperature ranges. A common procedure involves subjecting a mixture of oil, water and reservoir rock to a linear heating schedule. The effluent gasses produced when passing air through the mixture are analyzed for oxygen and carbon oxides. Numerous studies (Bousaid and Ramey, 1968, Burger and Sahuquet, 1972, Fassihi et al., 1984) established that the reactions may be grouped in three classes of competing reactions occurring over different temperature ranges. The three classes are:

- Low temperature oxidation (heterogeneous gas-liquid reactions) produced no carbon oxides.
- Medium temperature fuel formation reactions (homogeneous in the gas phase).
- Heterogeneous high temperature fuel combustion reactions.

The rates of the three classes of oxidation are considered to be functions of the oxygen partial pressure and of the fuel concentration. Metals have long been recognized for their catalytic potential in both hydrocarbon cracking and oxidation reactions. In addition, two methods to reduce fuel laydown have been suggested in the literature. The first one involves injection of a ketone acetal (ketal). The second uses surfactant to increase the oil displacement by the water bank ahead of the front. We tested only the first case because of lack of information on thermal stability of surfactants at combustion temperatures.

Experimental Apparatus and Procedure

A cell is charged with a mixture of sand, oil and water, or an aqueous solution of the additive to be tested. The cell is heated at a constant rate of temperature increase while air is passed through the sample at controlled rate and pressure. The effluent gasses are analyzed for oxygen, carbon monoxide and carbon dioxide. The experimental apparatus and procedure are similar to the ones used by Fassihi et al. (1984). They are also discussed in detail by Shallcross et al. (1989). The main components of the equipment are shown on Fig. 2.1.2. The analysis of the data was performed using the method developed by Fassihi et al. (1984) and modified by Shallcross et al. (1989). The results are expressed in terms of classic kinetics parameters in terms of Arrhenius' constants and order of reaction for the partial pressure of oxygen. Table 2.1.1 gives some properties of the crudes and describes the additives used in the experimental program.

Results and Discussion

This section is only a short summary because of space limitations. More details can be found in De los Rios (1988) and Shallcross et al. (1989). Table 2.1.2 shows the kinetic parameters obtained for Huntington Beach oil for the low temperature, medium temperature and high temperature reactions. Figures 2.1.3 - 2.1.5 show the experimental data for selected additives. The presence of stannous chloride or ferrous chloride (Fig. 2.1.3 for example) increased the level of oxygen consumed in all three reactions with these additives. The reactions occurred at lower temperatures than for the control runs. Oxygen consumption and carbon oxides production started at lower temperatures and increased in magnitude. Table 2.1.2 shows that significant changes in reaction order, activation energy and pre-Arrhenius constant were also observed for these two additives. Cupprous sulfate nickel and cadmium did not affect the results.

Table 2.1.1 Crude Oil Properties and Kinetics Program

Crude Properties		
Source	Huntington Beach	Venezuela
Gravity (°API)	18.5	10.5
%C	84.50	82.61
%H	11.53	10.47
Atomic H/C Ratio	1.64	1.52

Kinetics Program		
Additive	Molar Concentration of Additive (mole %)	Pressure (psig)
None	--	80
None	--	43
$FeCl_2 \cdot 4H_2O$	1.99	79
$FeCl_2 \cdot 4H_2O$	1.99	43
$SnCl_2 \cdot 2H_2O$	2.02	82
$SnCl_2 \cdot 2H_2O$	2.02	39
$CuSO_4 \cdot 5H_2O$	1.01	81
$CuSO_4 \cdot 5H_2O$	1.01	40
$ZnCl_2$	1.90	83
$MgCl_2 \cdot 6H_2$	1.98	83
$K_2Cr_2O_7$	2.02	80
$Al_2Cl_3 \cdot 6H_2O$	2.00	82
$MnCl_2 \cdot 4H_2O$	2.00	80
$Ni(NO_3)_2 \cdot 6H_2O$	2.00	40
$3CdSO_4 \cdot 8H_2O$	2.00	40

Table 2.1.2 Kinetic Parameters for Temperature Oxidation

Additive	Pressure (psig)	n_{II}	E_{II}/R ($°K \times 10^{-3}$)	β_{II}
High				
None	80	0.8	12.4	3.8×10^5
None	43	0.7	12.7	6.1×10^5
$FeCl_2$	79	1.2	18.4	2.5×10^8
$FeCl_2$	43	0.9	15.5	2.1×10^7
$SnCl_2$	82	1.0	14.0	1.3×10^6
$SnCl_2$	39	0.8	15.5	2.6×10^7
$CuSO_4$	81	0.7	11.9	4.9×10^5
$CuSO_4$	40	0.8	14.3	6.4×10^6
$ZnCl_2$	83	0.8	11.0	3.2×10^4
$MgCl_2$	83	0.9	12.4	2.1×10^5
$K_2Cr_2O_7$	80	0.9	11.5	6.7×10^4
Al_2Cl_3	82	0.8	12.5	3.2×10^5
$MnCl_2$	80	0.8	12.6	3.2×10^5
$Ni(NO_3)_2$	40	0.8	14.5	7.3×10^6
$CdSO_4$	40	0.8	15.4	2.1×10^7
Medium				
None	80	0.9	8.67	6.3×10^3
None	43	0.9	8.65	4.4×10^3
$FeCl_2$	79	1.0	7.62	2.0×10^2
$FeCl_2$	43	0.9	8.37	4.5×10^3
$SnCl_2$	82	1.1	9.03	3.9×10^3
$SnCl_2$	39	1.3	10.1	3.1×10^3
$CuSO_4$	81	0.8	8.22	4.5×10^3
$CuSO_4$	40	1.0	8.17	8.3×10^2
$ZnCl_2$	83	1.1	10.3	4.0×10^4
$MgCl_2$	83	1.2	10.7	2.7×10^4
$K_2Cr_2O_7$	80	1.2	10.5	2.8×10^4
Al_2Cl_3	82	1.0	8.52	2.9×10^3
$MnCl_2$	80	1.0	9.11	1.0×10^4
$Ni(NO_3)_2$	40	1.2	10.5	1.6×10^4
$CdSO_4$	40	1.3	10.3	5.9×10^3
Low				
None	80	0.9	8.15	9.6×10^3
None	43	0.9	8.17	5.6×10^3
$FeCl_2$	79	0.8	6.24	5.8×10^2
$FeCl_2$	43	0.8	5.90	2.4×10^2
$SnCl_2$	82	0.8	7.33	3.5×10^3
$SnCl_2$	39	0.7	6.11	3.8×10^2
$CuSO_4$	81	0.8	8.41	3.2×10^4
$CuSO_4$	40	0.7	8.47	2.7×10^4
$ZnCl_2$	83	0.8	7.51	5.5×10^3
$MgCl_2$	83	0.8	6.70	8.8×10^2
$K_2Cr_2O_7$	80	0.7	5.87	4.0×10^2
Al_2Cl_3	82	0.8	6.64	1.0×10^3
$MnCl_2$	80	0.7	6.48	1.1×10^3
$Ni(NO_3)_2$	40	0.7	6.98	2.1×10^3
$CdSO_4$	40	0.7	6.22	5.3×10^2

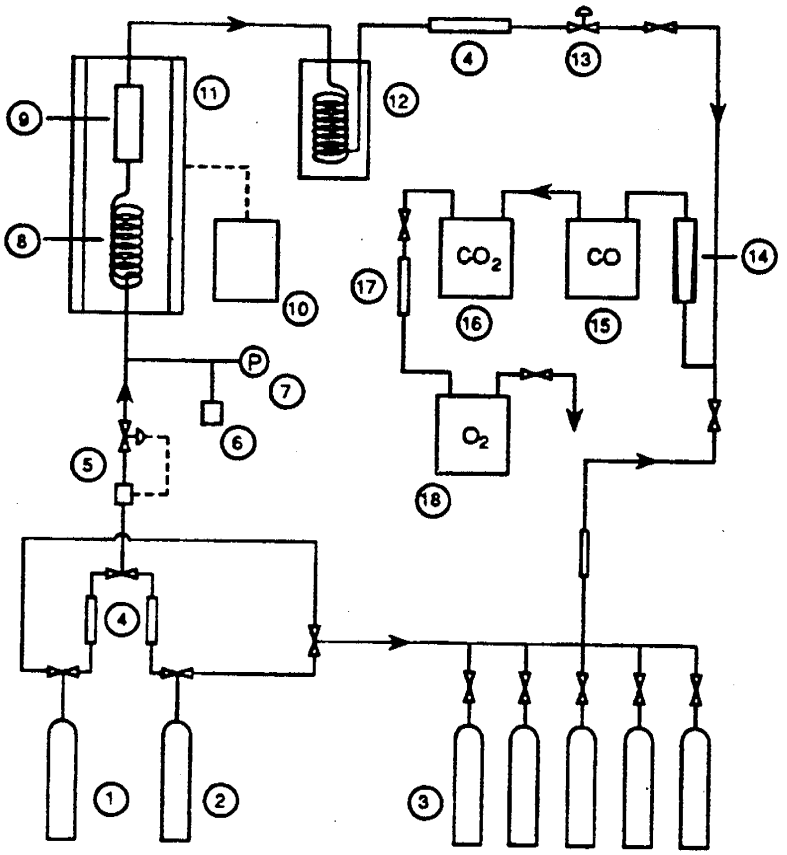

1	Air supply	10	Oven temperature controller
2	Nitrogen supply	11	Oven
3	Analyzer calibration gases	12	Production gas condenser
4	Dryer	13	Backpressure regulator
5	Mass flowrate controller	14	Rotameter
6	Pressure transducer	15	Carbon monoxide analyzer
7	Pressure gauge	16	Carbon dioxide analyzer
8	Preheating coil	17	Acid gas scrubber
9	Combustion cell	18	Oxygen analyzer

Figure 2.1.2 Schematic Representation of the Kinetics Studies Apparatus.

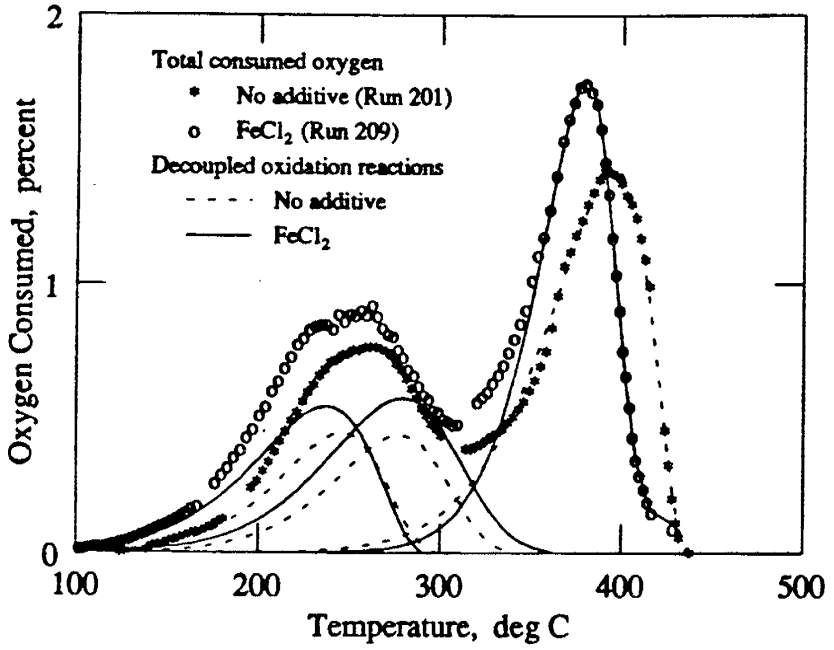

Figure 2.1.3 Effect of $FeCl_2$ Additive.

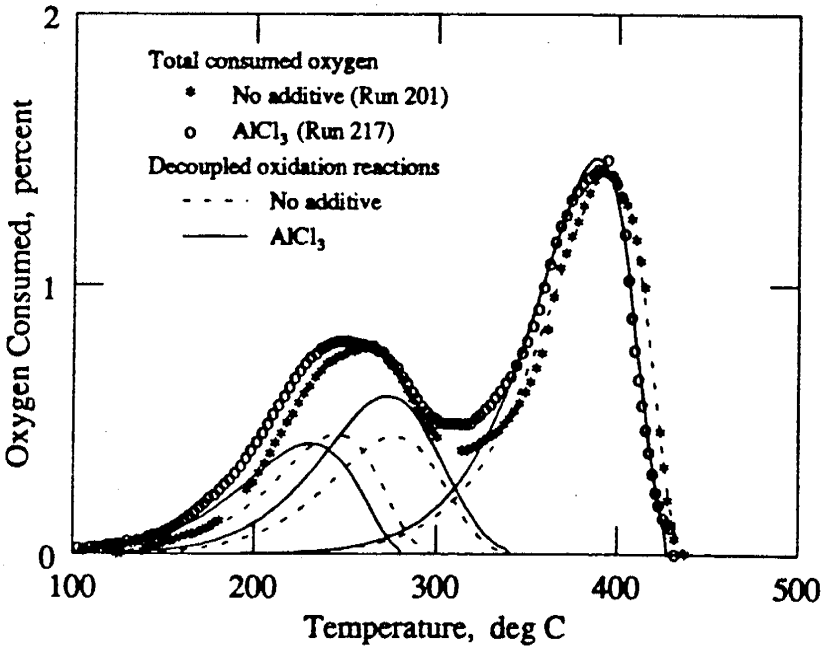

Figure 2.1.4 Effect of $AlCl_3$ Additive.

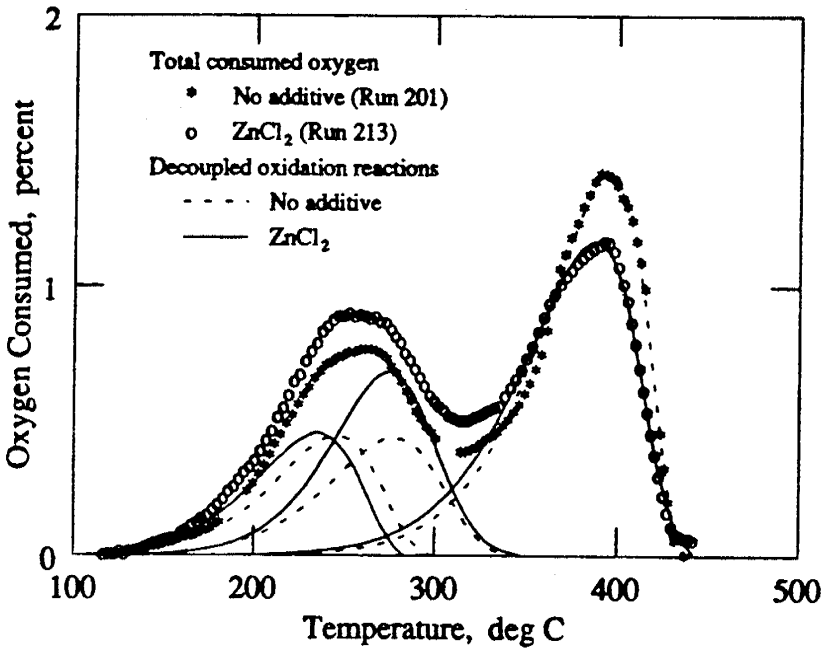

Figure 2.1.5 Effect of $ZnCl_2$ Additive.

Aluminum chloride merely shifted the temperature peak to a lower temperature (Fig. 2.1.4). Manganese has a similar effect. Zinc, chromium and magnesium increased oxygen consumption at lower temperature but decreased it over the higher temperatures (Fig. 2.1.5). The order of the low temperature reactions is relatively insensitive to the additives while a slight increase was observed in the order of the middle temperature reactions with additives. Iron and tin significantly increased the order of the high temperature reactions. For the heavier Venezuelan oil (Fig. 2.1.6), the high temperature combustion peak is more pronounced; this observation supports the conclusion that more fuel is laid down by the Hamaca oil than by the Huntington Beach oil. A ketal was added to the mixture for one run performed with Hamaca oil. If anything the fuel deposition increased slightly.

2.1.4 COMBUSTION TUBE RUNS

The kinetics experiments showed changes in the reactions of combustion caused by the presence of metallic additives. In order to obtain quantitative information on the amount and nature of the fuel formed and the air required to propagate a combustion front, it is necessary to experimentally simulate an in-situ combustion project via tube runs. Only a few combustion tube experiments have been performed to study the effect of metallic additives as catalytic agents for in-situ combustion (Racz, 1985). Based on the results of the kinetics studies a combustion tube runs program was implemented.

Experimental Apparatus and Procedure

The equipment is similar to the one used by a number of researchers at Stanford University (Satman, 1982, Fassihi et al., 1984). A schematic diagram of the system is shown on Fig. 2.1.7. The tube itself is a thin walled stainless steel cylinder of 7.6 cm diameter and 1 m length. The tube is packed with a mixture of sand, clay, oil and water or water containing the additive. Ignition is started by an electric heater at the top of the tube and combustion propagates vertically from top to bottom. Temperatures are monitored via a central thermal well. Pressures and exit gas compositions as well as flow rates are continuously measured. Fluid samples are collected and analyzed. All runs were carried on at the same flow rates, pressures and initial temperature levels. Table 2.1.3 summarizes the experimental program for Huntington Beach Oil. Hamaca oil was also tested with iron and tin additives at the same experimental conditions.

Results and Discussion

The data obtained in the tube runs were analyzed using the classic procedure of Dew and Martin (1964,1965). Some observations can be made at this stage.

Front temperatures: The temperature profiles taken during the runs exhibit distinct regions (Fig. 2.1.1). Ahead of the combustion front, there is a region at reservoir temperature. This is followed by a region where the temperature increases due to heat transfer ahead of the steam plateau. Next is the steam plateau where the temperature is constant. All of our runs having been performed at the same pressure, the steam plateau temperature ranged from 129°C to 132°C. Next the temperature rapidly increases until peak temperature is reached at the combustion front. The region behind the front shows decreasing temperatures caused by heat losses and heating of the injected air. The front temperatures for the control runs for Huntington Beach oil averaged 500°C. For stannous chloride they were around 535°C while for iron and zinc they were slightly lower than for the control runs. Temperature behavior was similar for the Hamaca oil. One must notice that the combustion front velocities increased with the presence of metallic additives.

Table 2.1.3 Summary of Combustion Tube Runs

Operating Pressure: 100-105 psig
Operating Temperature: 50-75 °C
Air Flow Rate: 3.0 standard litres per minute.

Run Designation	Control Run	Ferrous Chloride $FeCl_2.4H_2O$	Stannic Chloride $SnCl_4.5H_2O$	Zinc Chloride $ZnCl_2$
Length of Pack, cm	90.77	83.06	91.15	89.90
Porosity	35.73	35.00	39.10	39.27
Oil Saturation, %	37.47	38.67	32.43	32.21
Water Saturation, %	27.05	27.92	23.41	23.25
Concentration of Metal Salt in Water, wt. %	0.00	1.0	1.0	1.0
Vol. Oil/Vol. Rock	20.828	20.824	20.821	20.828
Vol. Water/Vol. Rock	15.035	15.031	15.030	15.034

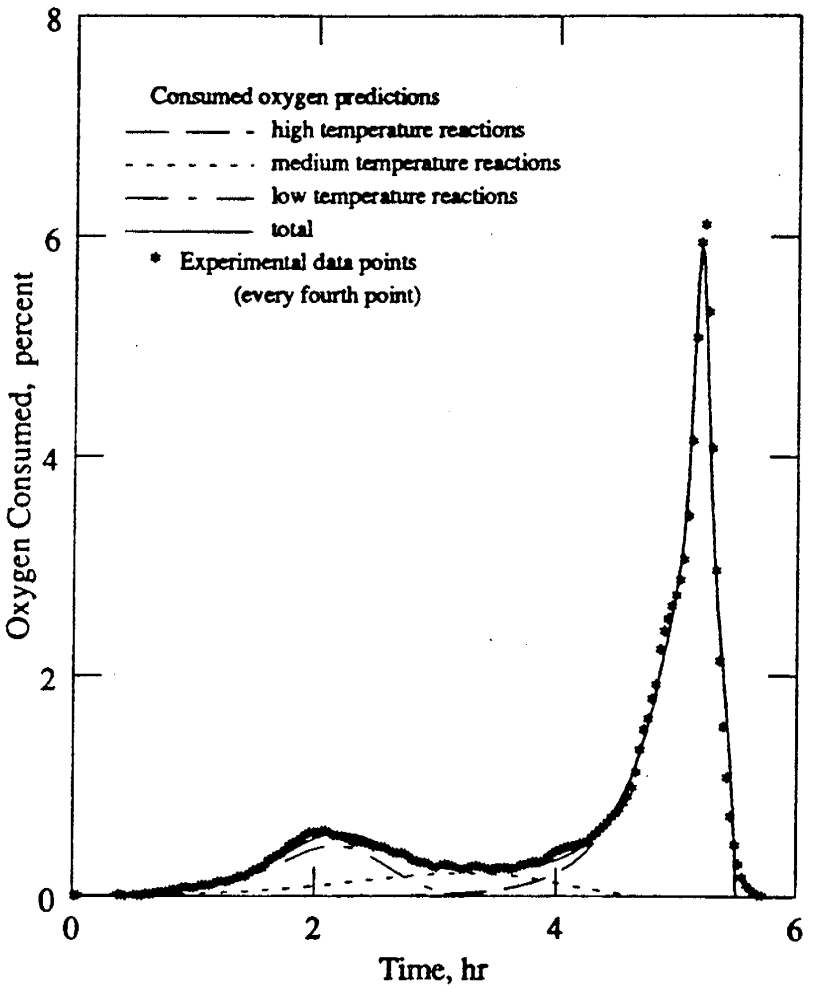

Figure 2.1.6 Oxygen Consumption for Venezuelan Oil Without Additive.

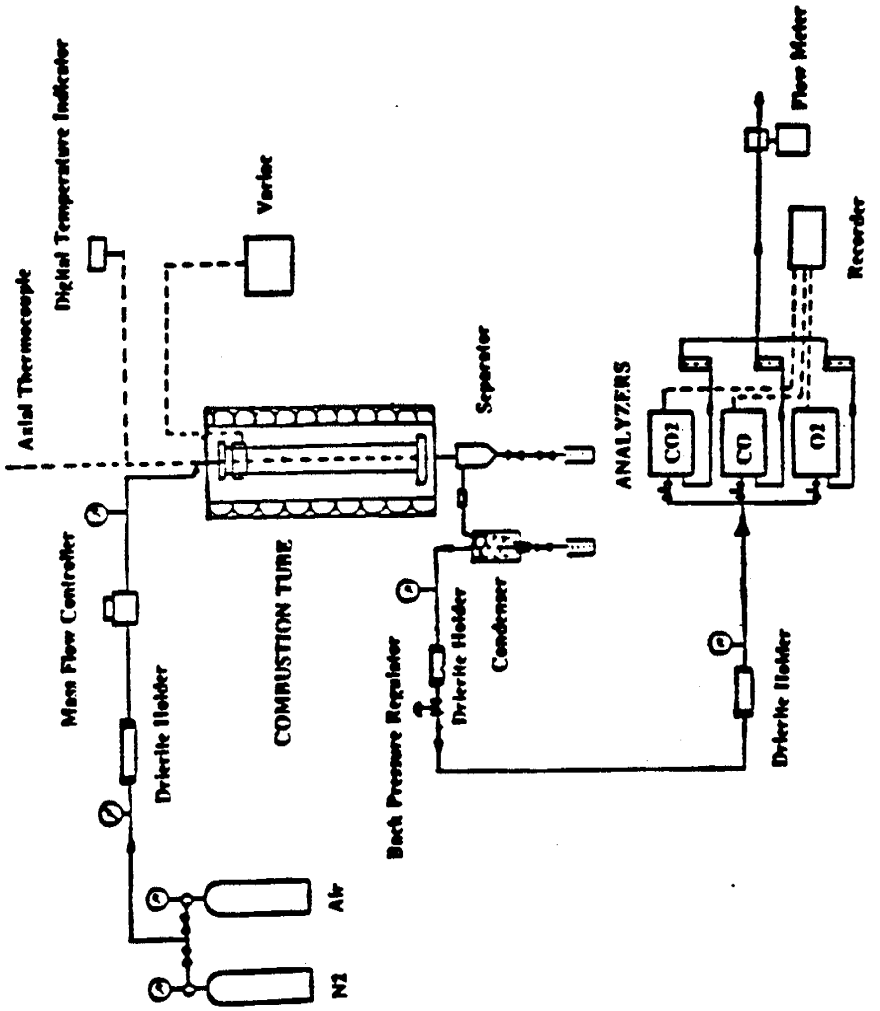

Figure 2.1.7 Schematic Diagram of the Tube Runs System.

Oxygen utilization and produced gasses: In the control runs, an average of 4 to 5 % oxygen was produced unreacted at the end of the tube. This amount was reduced to 1.3% by addition of iron in the Huntington Beach oil case and decreased to almost nothing when using tin for both oils as well as when using iron for Hamaca oil. Conversely the CO_2 produced increased in the order: control tin and iron; while the CO produced increased in the order: iron, control and tin. The CO_2/CO ratio m increased for both oils in the order: control tin and iron, ranging from 2.2 to 3.7. The H/C ratio of the fuel burnt n can be calculated from the produced gasses (Alexander et al., 1962). The two oils tested exhibited different behaviors. While for the 18.5 API Huntington Beach oil n increased in the order control, iron and tin ranging from slightly over 0 to 0.9, n for the 10.5API Hamaca oil increased in the order tin, iron and control and ranged from 1.2 to 1.8. We cannot explain this result at this stage.

Economic parameters: The economic parameters were calculated based on the gas produced with the exception of the amount of fuel burnt per unit volume of reservoir which has to be estimated from the front velocities and a material balance on the oxygen consumed. Although a detailed analysis of the results is outside the scope of this report and can be found in Baena (1990) and Tavares (1990) some comments can be made at this stage. The heat of combustion of the fuel which depends on its nature increased with the metallic additives for the lighter oil but slightly decreased for the heavy oil. The air required by unit mass of fuel burnt followed the same trends. The amount of fuel burnt per unit volume of reservoir was not changed for the lighter oil but increased in the order control, iron and tin for the heavier oil. Air/oil ratios decreased in the order control, tin and iron ranging from 14.3 to 11.5.

2.1.5 CONCLUSIONS

The metallic additives cause changes in the nature and the amount of fuel formed during an in-situ combustion process. These changes appear to depend on the type of oil used. Crude oil may be affected differently by different additives. The rock matrix in these experiments was sand and clay. It would be useful to repeat these tests with reservoir cores. The efficiency of various metals as additives does not follow the usually admitted order for cracking reactions that form coke. In general metallic additives increase the amount of fuel deposited and seem to be applicable to light oil projects where the fuel deposited without additives is not enough to sustain combustion. In heavy oil reservoirs, the presence of metals may render the process uneconomic because of increased air requirements. To date no additive has been found to decrease the fuel burnt.

KINETICS OF COMBUSTION

by

D. Mamora

Stanford University
Petroleum Research Institute
Stanford, California

2.2 KINETICS OF COMBUSTION
(D. Mamora)

Based on the frontal advance (FA) model (Tadema, 1959), the steam zone ahead of the combustion front drives a condensed hot water zone which in turn drives a cold water front and the original oil. In the steam zone, distillation of the oil would occur, leaving behind the heavier oil components as residual oil. This residual oil provides the fuel available for combustion. Logically, the denser the oil, the greater the amount of residual oil, and hence, fuel availability. This conclusion appears to be corroborated by the experimental work of Showalter (1953), which indicates an increase in the amount of fuel burned with decreasing API oil gravity. Research in SUPRI-A on the effect of steam distillation on residual oil is given in Section 2.3.

The fuel concentration at the combustion front, an important parameter for project evaluation and design, is probably the least understood parameter in in-situ combustion. This research is being carried out to obtain a better understanding of the kinetics of combustion, and is aimed at answering two basic questions:

(a) What constitutes fuel?

(b) What are the parameters that determine fuel deposition?

Two other factors affect the fuel concentration at the combustion front. Firstly, at the combustion front, the temperatures are significantly higher than the temperature in the steam zone. For high temperature oxidation (HTO) — at temperatures in excess of some 650°F — cracking occurs, resulting in the formation of lighter oil components, part or all of which can be displaced ahead of the combustion front. This would then result in a decrease in the fuel concentration. Secondly, low temperature oxidation (LTO) — ahead of the combustion front and at temperatures less than some 650°F — has been indicated to result in an increase in the fuel concentration (Alexander, et al. 1962).

From the foregoing, it is clear that the kinetics of the combustion reactions are rather complex. The main objectives of this research will be to investigate the following.

(i) The nature and amount of fuel and produced fluids.

(ii) The effect of varying oxygen concentration and pressure on the kinetics of combustion.

Kinetic cell and combustion tube experiments are planned, varying the type of crude and sand, oil saturation, air flux and, for kinetics experiments, the oxygen concentration and pressure. The oil will be analyzed for both composition and type (paraffin, aromatic and asphaltene ratios).

2.2.1 PROGRESS TO DATE

Research work commenced six months ago. Most of the time was spent in setting up the kinetics/combustion laboratory, as summarized below.

1. All previous equipment was dismantled and mounted on panels for safe and easy operation. Gas and liquid flow lines were replumbed, 1/8 inch steel tubings being used wherever possible to minimize fluid travel time from the combustion source to the measuring instruments. Electric cable routing was modified for safe operation. A 10 psi pressure relief valve and an acid scrubber were installed in the sample gas stream prior to the

Beckman CO and CO_2 analyzers to avoid accidental damage to these instruments. A new water cooled condenser was constructed to serve both the kinetic cell and the combustion tube. Instead of having a manifold at the calibration gas cylinders, a single gas line was installed between the measuring instruments and the calibration gas cylinder to be sampled to avoid contamination.

2. A gas chromatograph (HP 5710A) was installed, incorporating two 8' × 1/8 in. Carbosphere packed columns (for measuring Nitrogen) and a Vici 8 port automatic gas sampler.
3. A high performance liquid chromatograph (Waters Model 440) was repaired and installed. The packed columns for oil composition analysis are yet to be selected and purchased.
4. An IBM-AT computer was installed and a program was written which enables the computer to both store data and control the measuring instruments via the HP 3497A data logger. In addition, CO_2, CO, O_2, N_2, thermocouple temperature and gas chromatograph readings can be continuously plotted on the computer screen. Further, the program also integrates the gas chromatograph readings and computes the Nitrogen percentage in the sample gas stream.
5. Fabrication of a new kinetic cell and of a combustion tube was completed.
6. Four crude oil samples were received. Three were from Thums Oil's Wilmington field and one from Esso Canada's Cold Lake field.

A schematic of the experimental set-up is shown in Fig. 2.2.1, while a schematic of the data acquisition and control system is given in Fig. 2.2.2.

The main problem to date has been the malfunction of the Beckman CO and CO_2 analyzers. After a lengthy investigation, it was determined that the detector cell windows in both analyzers were leaking. This caused concern since the detectors were replaced only about two years ago. Communication with the manufacturer indicated that the cause of these leaks was most likely the presence of HCl gas in the sample gas stream, which attacked the epoxy used to seal the detector windows. HCl gas was certainly produced in the sample gas during previous combustion experiments using metal additives, eg. $FeCl_2$, $SnCl_2$. Both detectors were then replaced, and an isolation cap was installed (Fig. 2.2.3) between the detector and sample gas cell to avoid direct contact between the sample gas and the detector window.

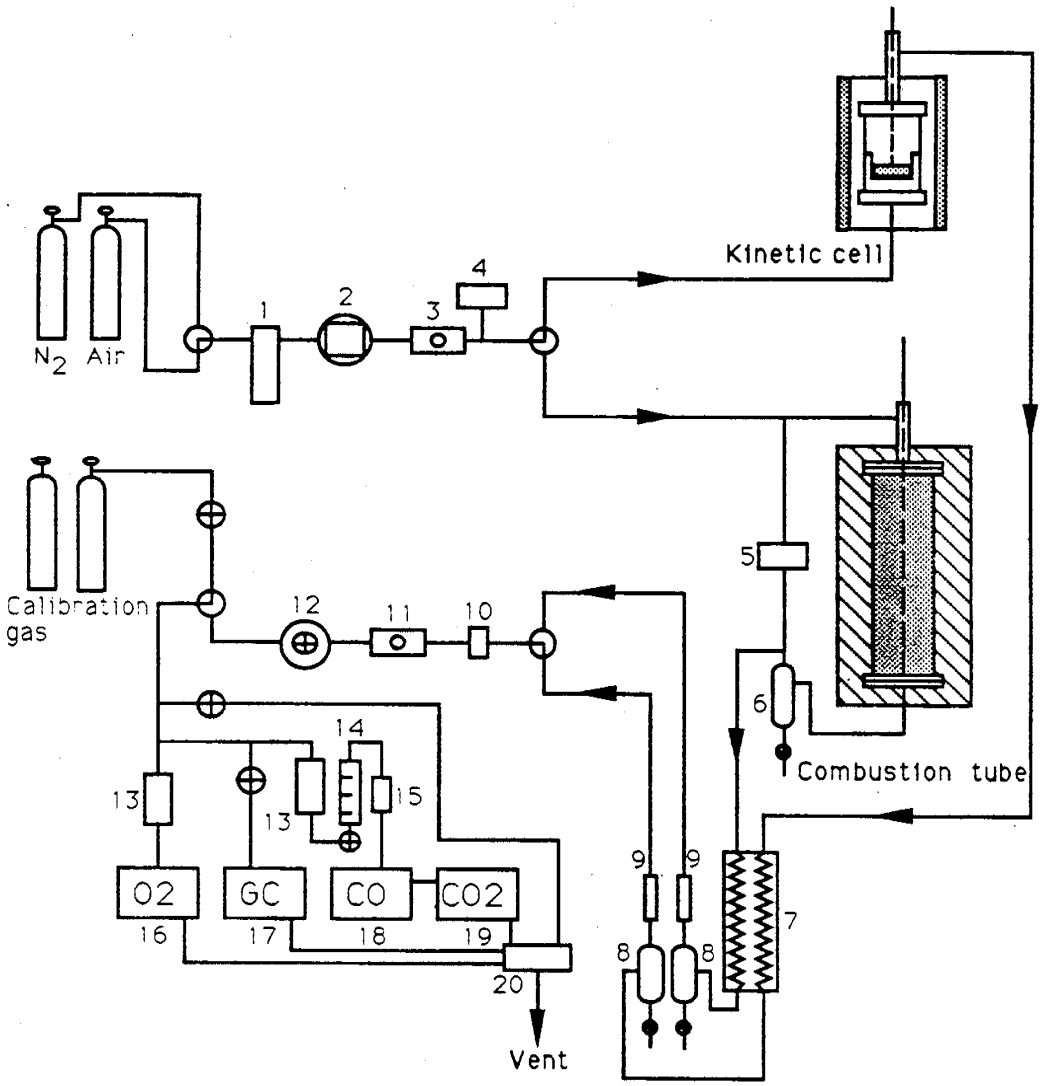

Figure 2.2.1 Schematic of Experimental Set-Up

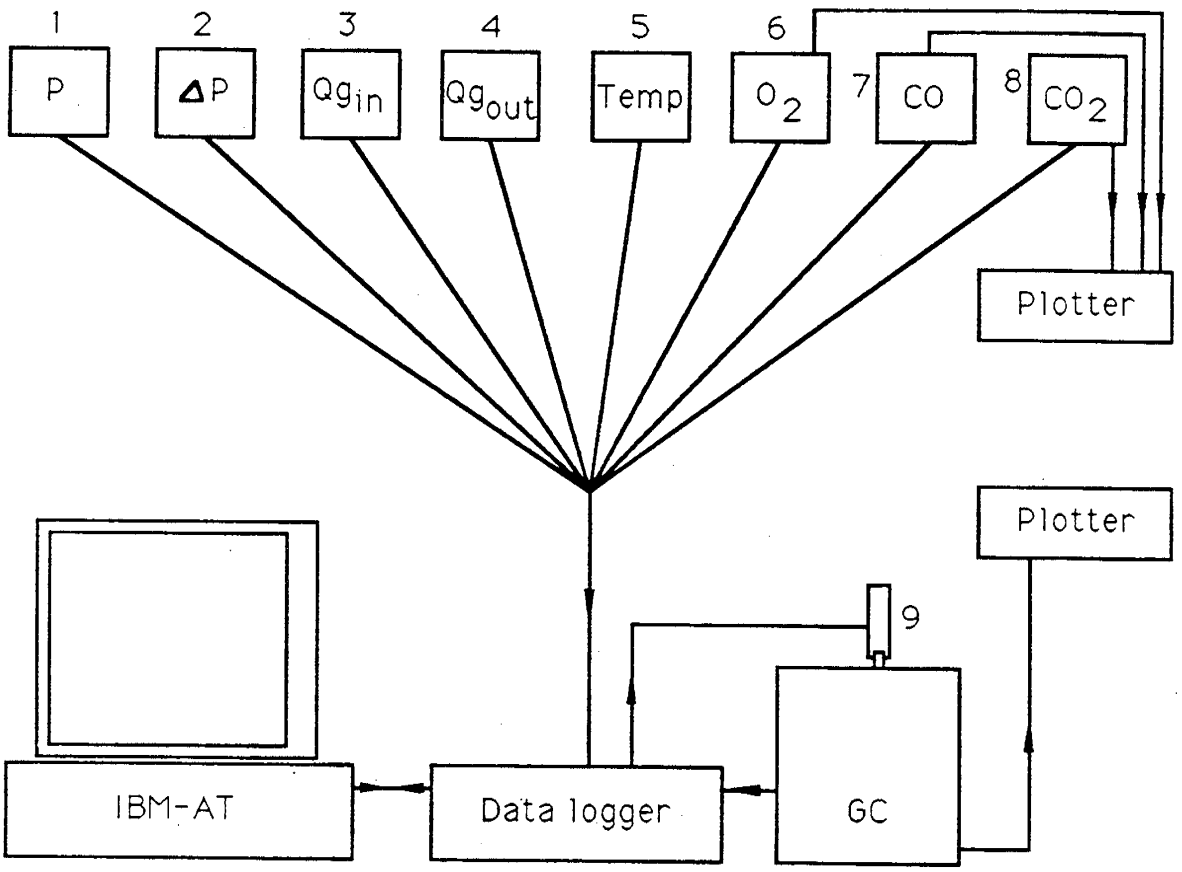

1. Pressure transducer
2. Pressure transducer
3. Mass flow controller
4. Flow transducer
5. Thermocouple temp.
6. Oxygen analyser
7. CO analyser
8. CO2 analyser
9. Auto gas sampler

Figure 2.2.2 Data Acquisition/Control Schematic

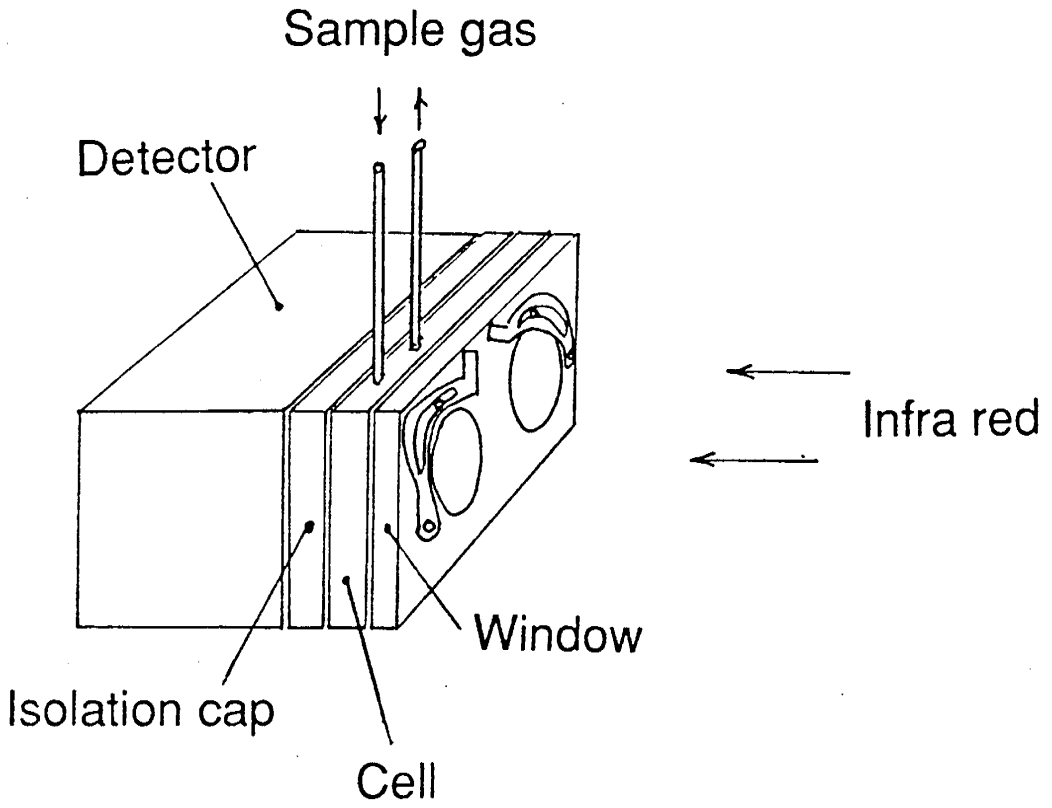

Figure 2.2.3 Schematic of Beckman Analyzer Detector

STUDY OF RESIDUAL OIL SATURATION FOR STEAM INJECTION AND FUEL CONCENTRATION FOR IN-SITU COMBUSTION

by

K.T. Lim

Stanford University
Petroleum Research Institute
Stanford, California

2.3 STUDY OF RESIDUAL OIL SATURATION FOR STEAM INJECTION AND FUEL CONCENTRATION FOR IN-SITU COMBUSTION

(K. T. Lim)

2.3.1 ABSTRACT

Steam distillation is the main mechanism which reduces residual oil during steam injection. It is the main recovery mechanism in steamflooding of light oil reservoirs. It distills lighter components from the initial oil. The residuum becomes heavier. Mixing of the distilled components with initial oil ahead of steam front results in lighter produced oil. A generalized approach to quantify these quality changes has been developed for California crude. Application of the results to the determination of fuel concentration and hydrogen-to-carbon ratio for in-situ combustion will be investigated.

2.3.2 INTRODUCTION

In a steamflood four characteristic zones advance radially outwards. The steam zone drives a condensed hot water and hydrocarbon zone, which in turn drives a cold water front and reservoir oil. In essence a cold waterflood and then hot waterflood preceeds the steam zone. When there is steam override and gravity segregation, mixing of these zones may occur.

Willman et. al. (1961) studied the contributions of various recovery mechanisms associated with steam injection. They concluded that the principal mechanisms responsible for additional oil are thermal expansion of oil, viscosity reduction and steam distillation. Studies by Duerksen and Hsueh[2] concluded that steam distillation yields can be significant, even for heavy crudes.

Steam distillation is the main mechanism which reduces the residual oil behind the hot water front during a steamflood. Willman et. al. (1961) also concluded that the steam zone residual oil saturation is independent of initial oil saturation. At a given steam injection condition, the residual oil saturation is essentially composition dependent.

In reservoirs containing light oil, steam distillation is the major mechanism contributing towards improved recovery. The emergence of steam distillation drive as an important enhanced recovery method has been discussed by Belvins et. al. (1984).

Distillation of the in-situ crude oil causes the produced oil to be lighter than the initial oil. An increase of 2° to 4° API has been observed both during laboratory experiments (Willman et. al. 1961, Wu and Fulton, 1971) and field tests (Konopnicki et. al. 1979, Valleroy et. al. 1967, Volek and Pryor, 1972). Consequently, the residual oil in the steam zone has an increasing content of heavier components. Similar observations have been made during in-situ combustion field tests (Gates and Ramey, 1958). A major objective of this study will be to determine from the information available changes in quality of produced oil (compared to the initial oil). Existing laboratory and field data will be interpreted in the light of the findings.

Information regarding the quality change in residual and produced oil is not widely available in the literature. Konopnicki (1979) estimated that the residual oil API gravity decreased from 35.2 to 25.6 for the initial oil in the case of Shiells Canyon Field. Although other authors mentioned that residual oils were analyzed, no quantitative data appears to be available.

Information on the crude quality change during steamflooding can be useful. The amount and API gravity of the residual oil can be calculated from material balance. Information on residual oil can be related to the fuel concentration for in-situ combustion. During an in-situ combustion process, the mechanism ahead of the combustion region closely resembles a steamflooding process.

2.3.3 OBJECTIVES

This project has the following main objectives:

1. To develop a general procedure to quantify residual oil saturation and crude oil quality changes as a result of steam injection,

2. To correlate steamflood residual oil saturation and gravity with fuel concentration and hydrogen-to-carbon ratio for in-situ combustion, and

3. To verify the correlations experimentally.

2.3.4 STEAM DISTILLATION YIELDS

Steam distillation has been studied by many authors. The general observation is that steam distillation can be significant, even for heavy crudes. Attempts to correlate steam distillation yields with API gravity, viscosity, simulated distillation yields and other factors have been made. Wu and Brown, (1975) Wu and Elder (1983) observed a linear relationship between steam distillation yield and API gravity. Duerksen and Hsueh (1983) pointed out the effect of wax content on steam distillation yield and stated that the steam distillation yield for California crudes with low wax content is approximately

$$\% \text{ Yield} = 2 \times (^\circ\text{API})$$

Some steam distillation data found in the literature are plotted in Fig. 2.3.1. Each set of data displays some form of linear relationship. However, they are unique to the conditions at which the experiments were carried out.

It was also observed that the studies cited either the experimental temperature or pressure, and not both. It may be assumed that the experiments were carried out at saturated steam conditions. This is generally true. At a given temperature, the partial pressure of hydrocarbon at cut-off steam-oil ratios may become very small. The total pressure in the system will, therefore, be very close to the saturated steam pressure. As will be discussed later, it is important to measure both the temperature and pressures at which an experiment is conducted.

The correlations cited in the literature may be unique to the respective experimental conditions. Without a common basis, they may not be compared directly. A common basis of comparing these data is proposed below.

2.3.5 BUREAU OF MINES (BuMines) DISTILLATION DATA

The BuMines Routine Method Distillation database contains crude assay of all major reservoirs in the United States. Atmospheric distillation yields up to 527°F, and yields at 40mmHg and temperature up to 527°F are reported. Useful information can be retrieved from this database without having to resort to more complicated laboratory experiments.

Equivalent atmospheric distillation temperatures for sub-atmospheric pressure distillation conditions were determined using vapor pressure calculations. Vapor pressure charts of (Lee and Kesler, 1980) were used. With known vapor pressure and temperature, the equivalent normal boiling point, NBP, of the hydrocarbon can be determined. This NBP represents the equivalent atmospheric distillation temperature. Assumption was made here that at the 'cut' conditions vapor pressure is contributed solely by the heaviest distilled hydrocarbon component.

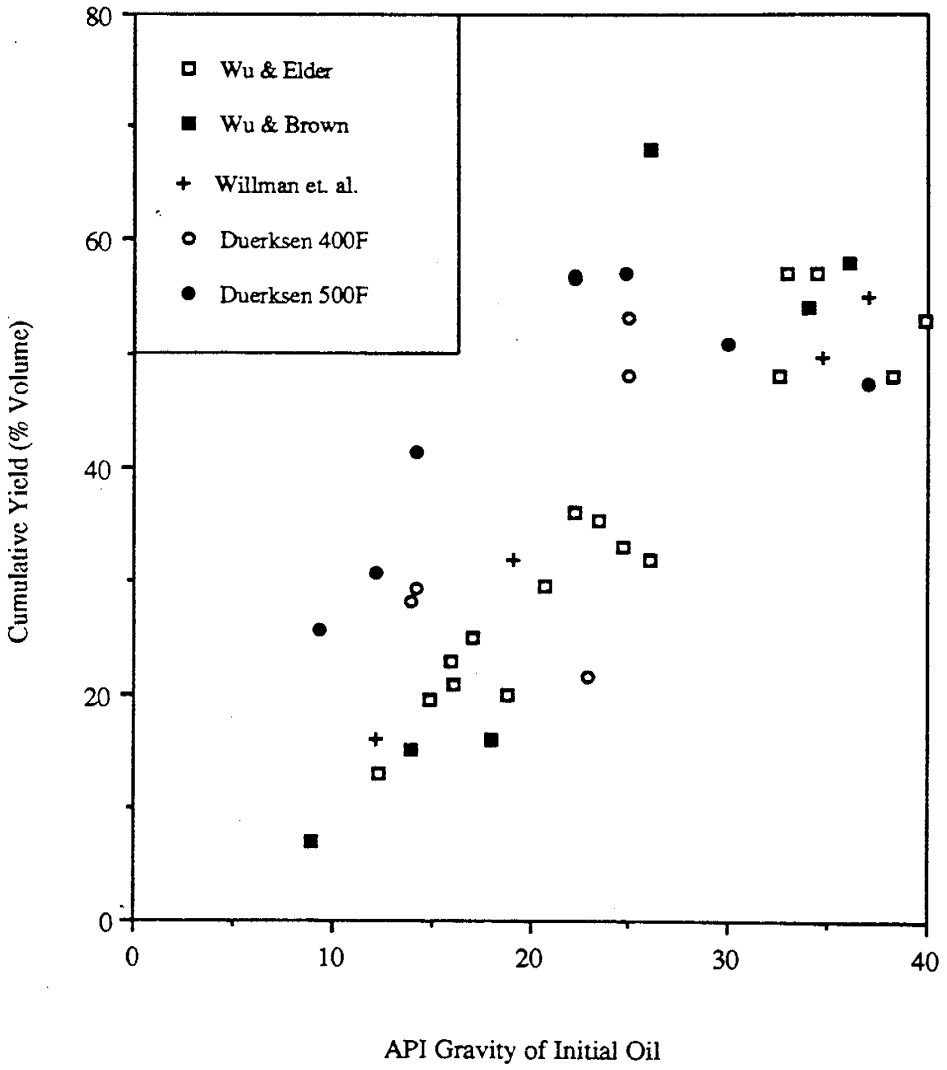

Figure 2.3.1 Steam Distillation Data From Literature

In this study data from 71 California crude samples were analyzed. These data are extracted from a DOE report by Coleman et. al. (1978). Figure 2.3.2 shows the cumulative distillation yield as a function of API gravity for cut number 12. This is the equivalent gas-oil cut at 437°F and 40 mmHg. The equivalent normal boiling point is 634°F. A linear relation in the form

$$\% \text{ Yield} = 1.75 * \text{°API of initial oil}$$

gives a satisfactory correlation. Cumulative yields for other distillation cuts are shown in Fig. 2.3.3. Where applicable, the equivalent normal boiling points are listed.

It is apparent from Fig. 2.3.3 that the cumulative yield is temperature dependent. Higher temperatures results in progressively higher yields.

2.3.6 COMPARING STEAM DISTILLATION DATA AND BuMines DATA

The equivalent atmospheric distillation temperature, or its equivalent NBP, of various steam distillation conditions can be calculated. This would enable comparison of steam distillation yields and BuMines data on a common basis.

Both the steam distillation temperature and pressure are required. Partial pressures of steam and hydrocarbon make up the total pressure. At a given temperature,

$$\text{Total vapor pressure} = \text{vapor pressure of steam} + \text{vapor of hydrocarbon}$$

Vapor pressure of saturated steam at a given temperature can be easily determined, either from well known equations or physical data handbooks. Vapor pressure of the hydrocarbon being distilled should be the difference between the total pressure and vapor pressure of saturated steam.

Knowing the vapor pressure and temperature, the equivalent NBP of the hydrocarbon can be determined. A vapor pressure equation, or chart (Lee and Kesler, 1980) can be used. The NBP is the same as the equivalent atmospheric distillation temperature. In this way distillation yields at similar at NBP, or equivalent atmospheric distillation temperatures, can be compared directly.

As noted above, steam distillation data available in the literature quoted either the experimental temperature or pressure, not both. Comparisons are not possible at this moment.

A problem of similar nature arises in field applications. Measurements of both pressure and temperature in the reservoir may be scarce, or not available. Further studies into this aspect of the problem will be necessary.

2.3.7 CHANGES IN CRUDE OIL QUALITY

Steam distillation extracts lighter components of the initial oil. The residuum, therefore, must become heavier. Blending of the distilled portion with the initial oil ahead of the steam front results in lighter produced oil. This phenomena has been observed in steam injection projects. API Gravity of produced oil is some 2 to 4 degrees higher than the initial oil. Similar observation has also been made in in-situ combustion projects.

The change in API gravities can be calculated by material balance. Consider the oil as a two component system. One component is distillable and the other not distillable at a given condition. If API gravities of both the distilled component and residuum can be predicted, then the material balance can be accomplished.

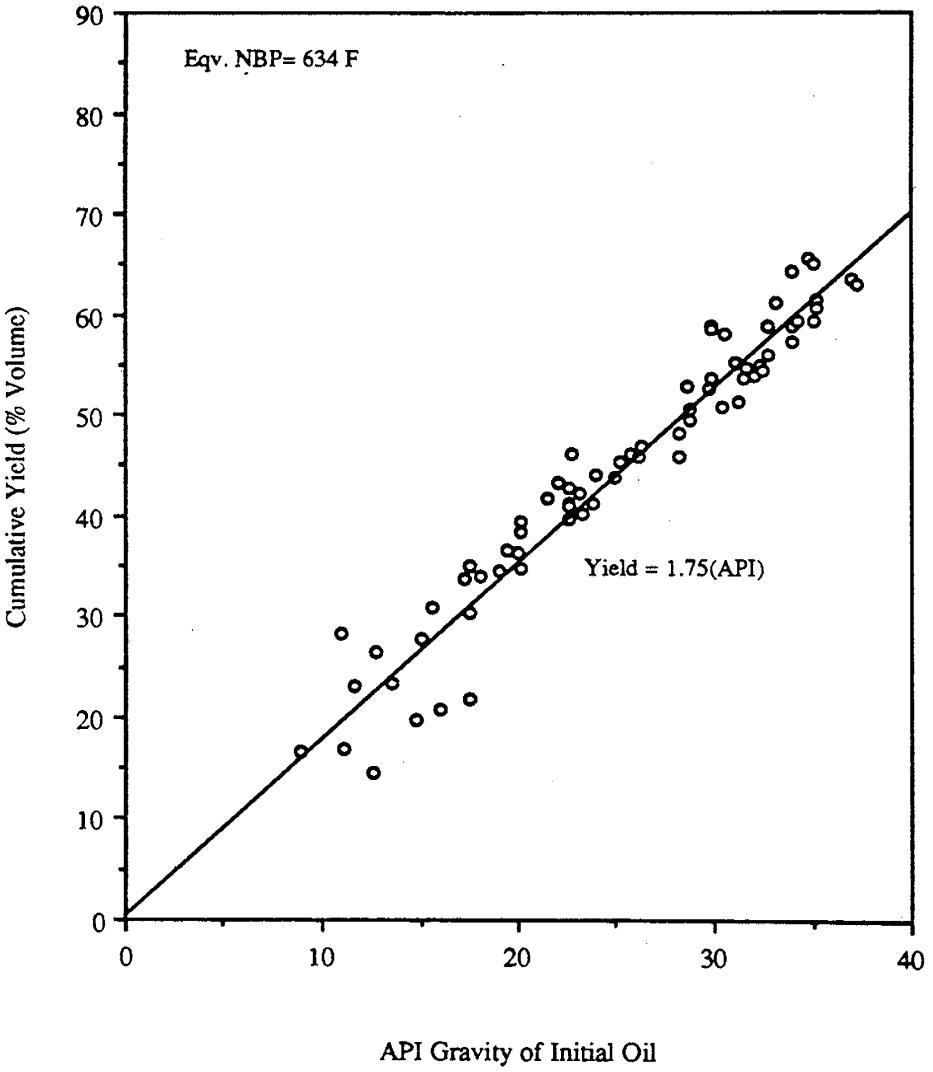

Figure 2.3.2 California Crude Distillation, BuMines Routine Method
Cumulative Yield to Cut #12 (437F, 40mmHg)

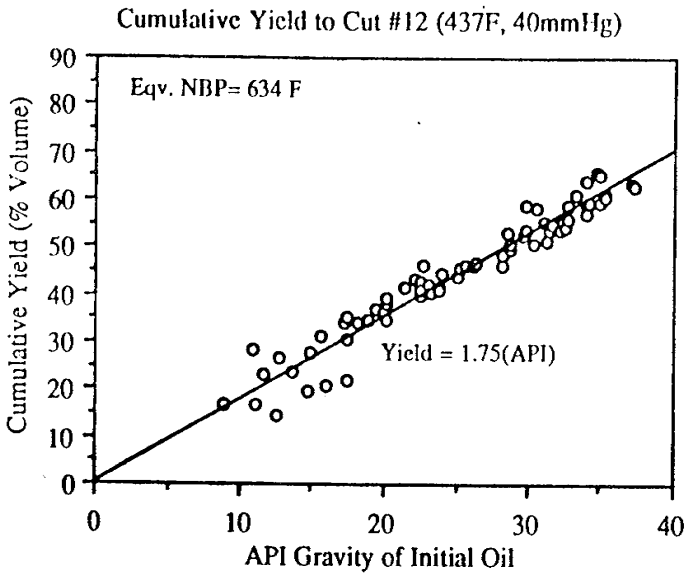

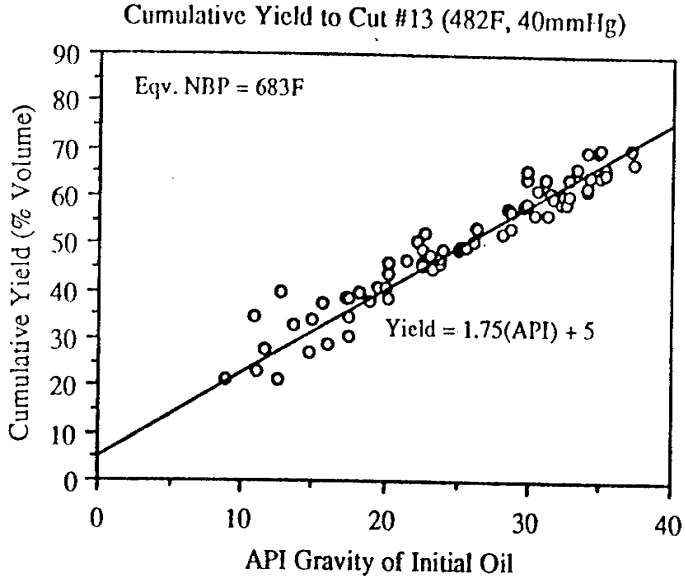

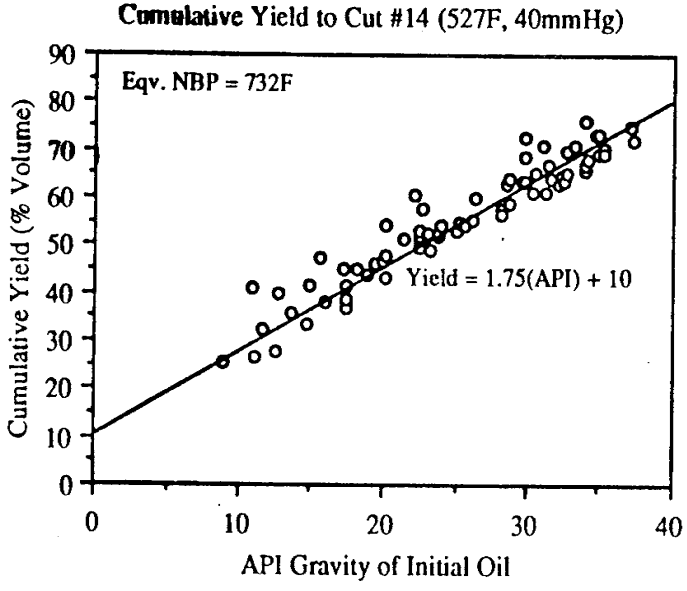

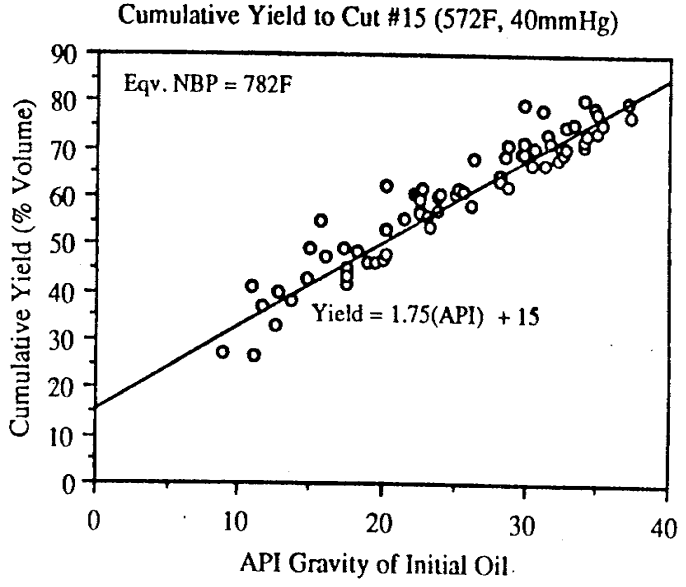

Figure 2.3.3 California Crude Distillation by BuMines Routine Method: Cumulative Yield at Various Cuts.

Figure 2.3.4 shows the distilled and residuum API gravities for California crude at a given distillation cut. The distilled portion is substantially lighter than the initial oil. For example light components distilled from a 15° API oil is about 36° API. This is more than twice the initial API. On the other hand, the reduction in API gravity of the residuum is less drastic. An oil initially of 15° API will have residuum of 11° API.

When the distilled component is mixed with the initial oil, change in the produced oil is evident. Figure 2.3.5 shows the effect of mixing one volume of distilled component with an equal volume of initial oil. The same set of data from Fig. 2.3.4 was used. A 2 to 4° API increase in the API gravity can be expected from oil initially at 10 to 20° API. This is consistent with laboratory and field observations.

The ratio of 1:1 mix is approximately what can be expected in the reservoir with steam override and gravity segregation. Plots similar to Fig. 2.3.5 for various distillation cuts, or equivalent normal boiling points do not display substantially different results.

It is apparent that a general approach to calculate the API gravity change of produced oil has been developed. The application of these correlations can be viewed in a different light. If the amounts and qualities of both the initial oil and produced oil are known, the amount and gravity of residual oil can be calculated. This information can be extended to the estimation of fuel concentration and hydrogen-to-carbon, H/C, ratio for in-situ combustion. Similar approach can also be used to predict the change in produced oil quality for in-situ combustion projects.

2.3.8 FUEL CONCENTRATION FOR IN-SITU COMBUSTION

Fuel concentration for in-situ combustion can be derived from residual oil saturation and gravity. Other factors such as rock type and surface area are also of importance and are being studied.

Another parameter of interest is the hydrogen-to-carbon ratio, H/C. It is proposed that the universal-oil-product constant, UOP K-factor, be used as a correlating parameter (Hougen et. al. 1954). Figures 2.3.6 and 2.3.7 are charts from which API gravity and H/C can be related. The UOP K-factor and boiling point can be determined from known API gravity and viscosity at 122°F (or 50°C) using Fig. 2.3.6. Figure 2.3.7 relates the UOP K-factor and boiling point to the per-cent hydrogen by weight. It can be translated to H/C ratio with ease. The possibility of integrating Figs. 2.3.6 and 2.3.7 into one relating API gravity and H/C ratio, with UOP K-factor as the variable will be investigated.

2.3.9 EXPERIMENTAL SETUP

An experiment is currently being set up. The main purpose is to verify the general correlation described above. A schematic of the experiment is shown in Fig. 2.3.8.

Sand pack in 2 inch ID, 20 inch long aluminum tubing will be steamflooded at constant temperature. Quality changes will be monitored. The construction of aluminum tubing allows for computer-aided-tomography, CAT, scanning. This will enable in-situ measurement of saturation profiles, before and after steam injection.

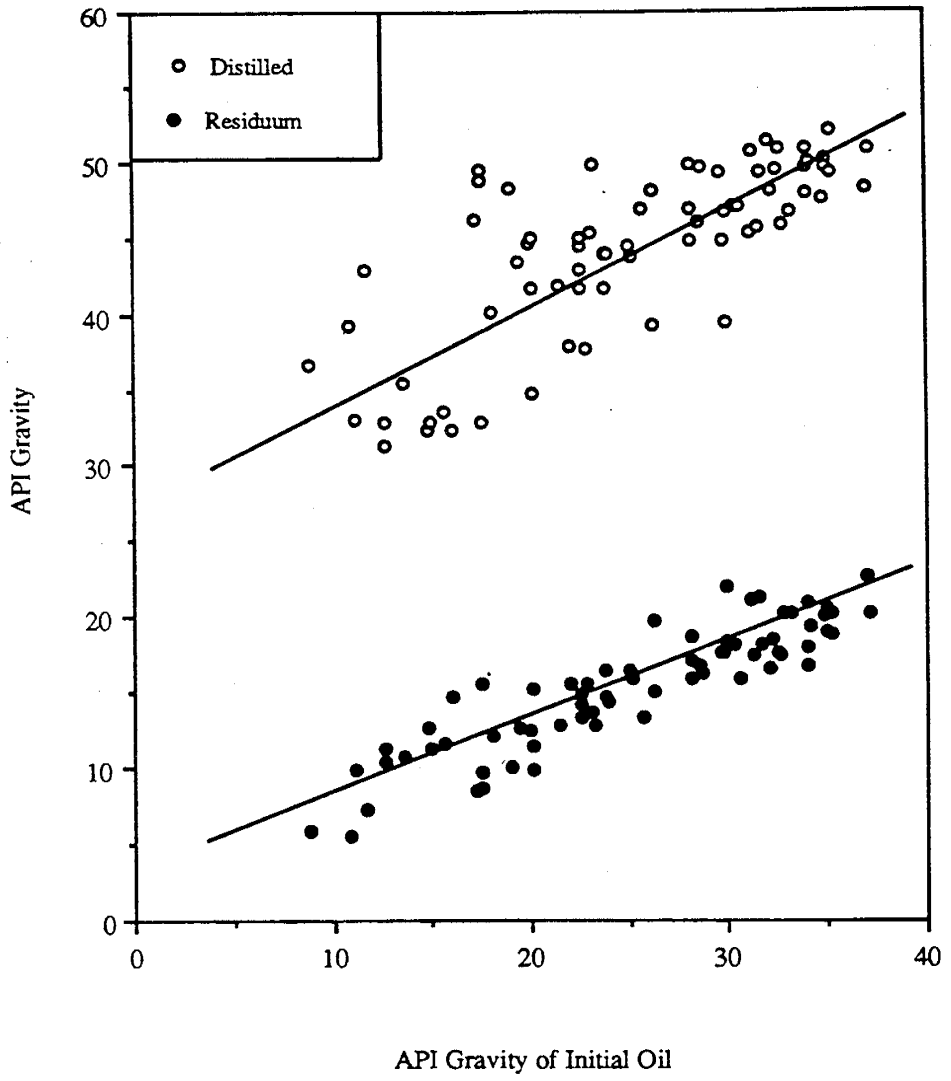

Figure 2.3.4 Californian Crude Distillation, BuMines Routine Method
Distilled & Residuum API, Cut= 527F, 760 mmHg

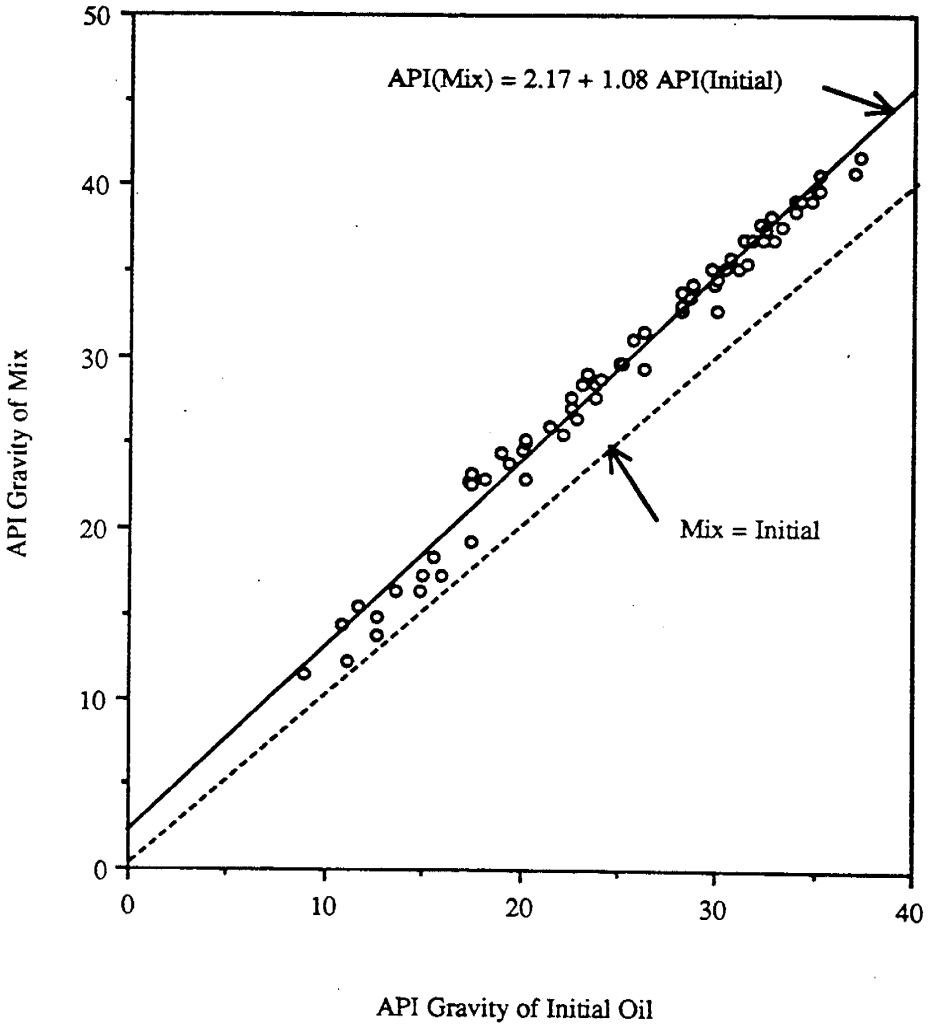

Figure 2.3.5 Gravity of Mix (Distilled + Initial Oil)
(Ratio 1:1)

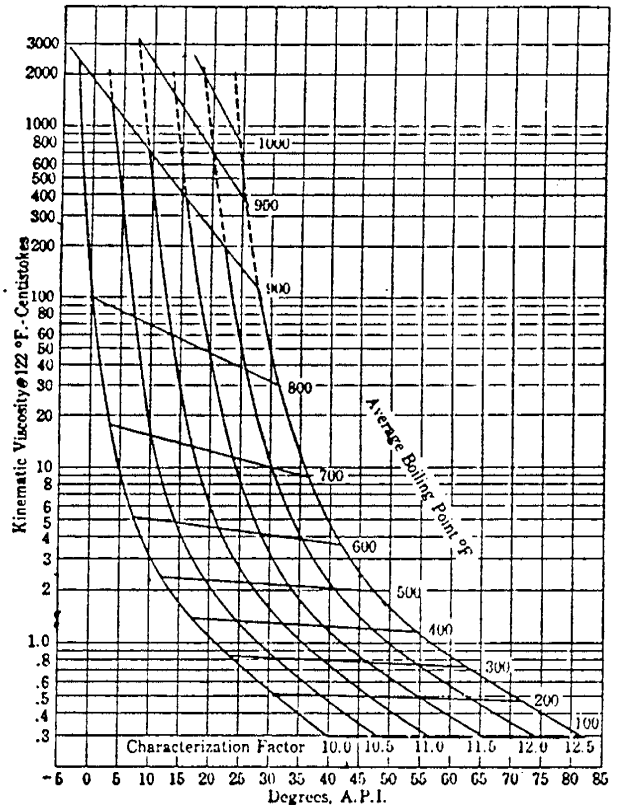

Figure 2.3.6 UOP Characterization Factor Correlation Chart

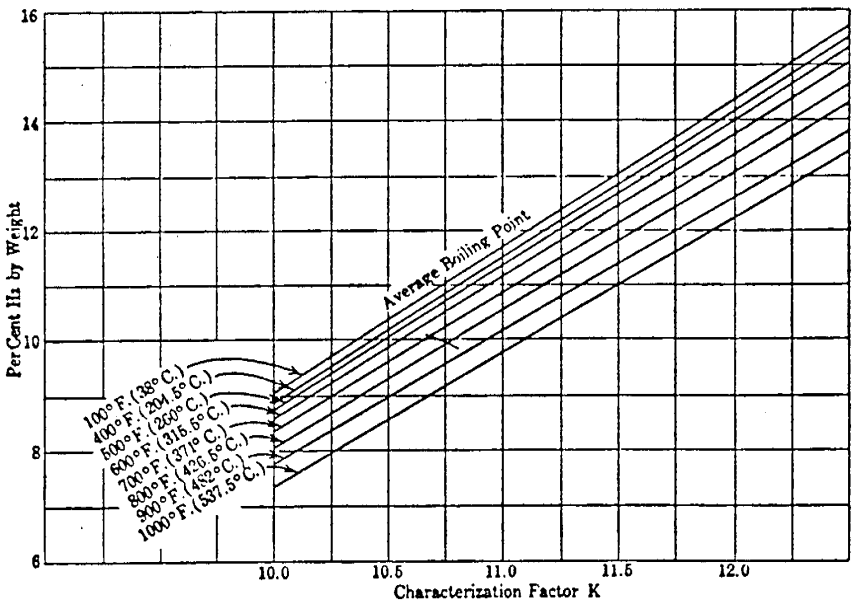

Figure 2.3.7 Characterization Factor vs. Weight % H_2

(Source: Hougen et. al., "Chemical Process Principles -- Part I")

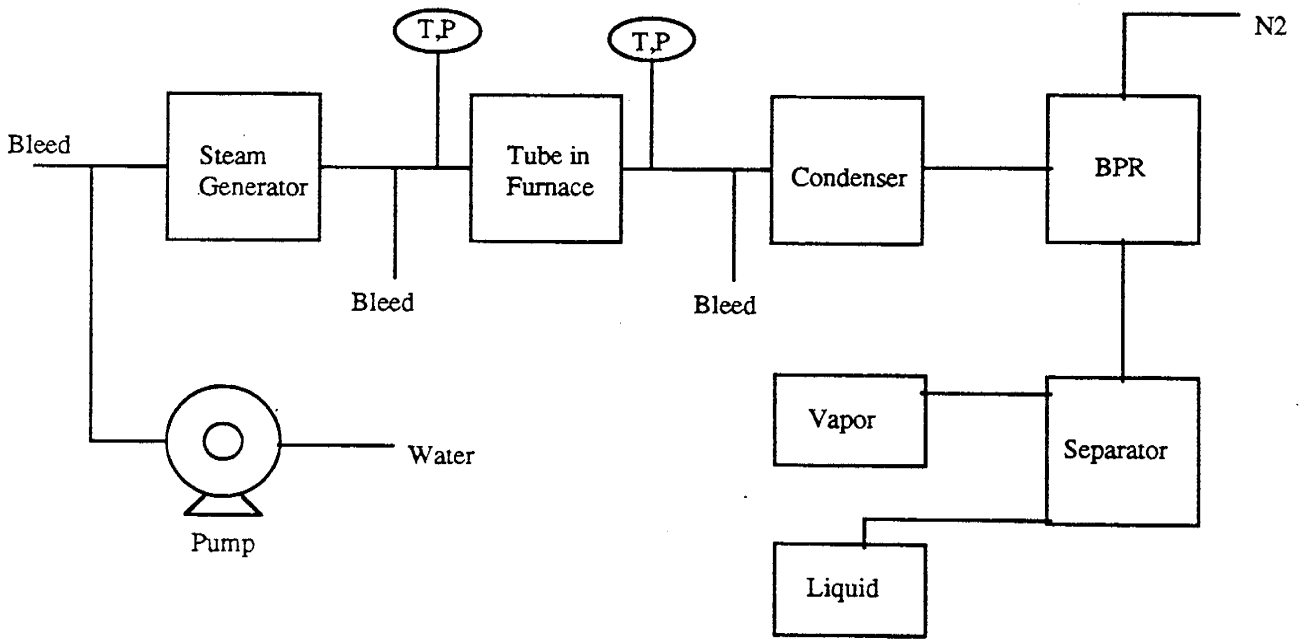

Figure 2.3.8 Schematic of Experiment Setup

2.3.10 FUTURE WORK

Future works on this subject will comprise the following.

1. Material balance studies, using experimental and field data.
2. Steamflooding experiments.
3. Verification and further development of correlations and concepts.
4. Application of results of this study to field projects.

ANALYSIS OF TRANSIENT FOAM FLOW IN 1-D POROUS MEDIA WITH COMPUTER TOMOGRAPHY

by

D. Liu

Stanford University
Petroleum Research Institute
Stanford, California

3.1 ANALYSIS OF TRANSIENT FOAM FLOW IN 1-D POROUS MEDIA WITH COMPUTED TOMOGRAPHY
(D. Liu)

3.1.1 ABSTRACT

Transient behavior is likely to dominate over most of the duration of a foam injection field project. Due to the lack of experimental data, little is presently known about transient foam flow. Foam flow does not follow established models such as the Buckley Leverett theory and no general predictive model has been derived. Therefore, experimental data are badly needed. Transient foam flow is being studied in a simple linear porous medium.

Foam is injected at a constant volumetric rate into a one-dimensional sandpack of 1-inch diameter and 24-inch length, initially saturated with distilled water. The system is placed in a CAT-Scanner. Data are accumulated at low temperature and pressure including the pressure field and saturations obtained by scanning. The liquid saturation can be obtained at each point of a cross section of the pack with less than 1% error over the range of interest. Calculations from the numbers obtained from the scanner show that the best spacial resolution available is a volume element (voxel) of 0.5×.5×5 mm. Hence a relationship can be found between saturation and pore volume injected for each location in the sandpack. Pressure profiles show that the pressure drop along the sandpack is not evenly distributed and varies with time. The pressure gradient is much greater between the injection end and the foam front than it is ahead of that front. Moreover, the pressure gradient keeps changing as the foam advances in the sandpack. It is this behavior that differs from the standard Buckley-Leverett theory. The CT-scan results demonstrate that foam displacement is not piston-like. Gas channeling appears near the front, and eventually the foam blocks all channels. The foam flows through the sandpack by continuously breaking and reforming. It takes several pore volumes of foam injection to reach residual liquid saturation.

The saturation versus pore volumes injected relationships for a given section of the sandpack have been matched with power law formulas. In general, the matches are satisfactory, however the exponents and constants in the formulas vary as a function of the position of the section considered. Graphing the data as saturation versus equivalent pore volumes injected reduces the range of these variations but does not eliminate them. We are unable to model this behavior to date.

Techniques of measurement of saturations by X-ray cat-scanning as well as interpretation of CT data were also presented this past year. This year we have focused on an attempt to model the process.

3.1.2 THEORETICAL AND COMPUTER MODELING

Basically, the idea is to treat foam as an infinite number of gas slugs with various viscosities displacing the in-situ fluid (water). The theory behind this is the fractional flow curve construction method (Lake, 1989). A computer program for this theory was written to facilitate the understanding and to incorporate the experimental data in to the model in the future.

To obtain the fractional flow curves, the relative permeabilities have to be determined first. In this case, the semi-empirical model is used as in the following equations:

$$k_{rw} = k_{rw}^{o} \left[\frac{S_w - S_{wc}}{1 - S_{wc} - S_{gr}} \right]^{n_w}$$

$$k_{rg} = k_{rg}^{o} \left(\frac{S_g - S_{gr}}{1 - S_{wc} - S_{gr}} \right)^{n_g}$$

where

k_{rw} --- water relative permeability
k_{rg} --- gas relative permeability
k_{rg}^{o} --- endpoint relative permeability for water at residual gas saturation
k_{rw}^{o} --- endpoint relative permeability for gas at irreducible water saturation
S_w --- water saturation
S_g --- gas saturation
S_{gr} --- residual gas saturation
S_{wc} --- irreducible water saturation
n_w --- relative permeability index for water
n_g --- relative permeability index for gas

Then the fractional flow of gas is calculated as:

$$f_g = \frac{M^o \, S^{n_g}}{M^o \, S^{n_g} + (1 - S)^{n_w}}$$

$$S = \frac{S_g - S_{gr}}{1 - S_{wc} - S_{gr}}$$

$$M^o = \frac{K_{rg}^{o} \, \mu_w}{K_{rw}^{o} \, \mu_g}$$

where

f_g --- fractional flow for gas
S --- reduced gas saturation
M^o --- gas-water endpoint mobility ratio
μ_w --- water viscosity
μ_g --- gas viscosity

As an example, the fractional flow curves are shown in Fig. 3.1.1 for a series of gas slugs displacing water with gas viscosities ranging from 0.02 cp to 20 cp. In between, the viscosities are calculated so that the later saturation profile is smooth. Here for numerical limits, only 20 different viscosities are considered.

Since the surfactant adsorption is significant at the foam (gas) front, it can not be neglected. The frontal advance loss can take a variety of forms. At this stage, Langmuir-type isotherm (Langmuis, 1915) is chosen as the basis, it will be modified if experimental data require it. Combining the fractional flow curve construction method and the frontal advance

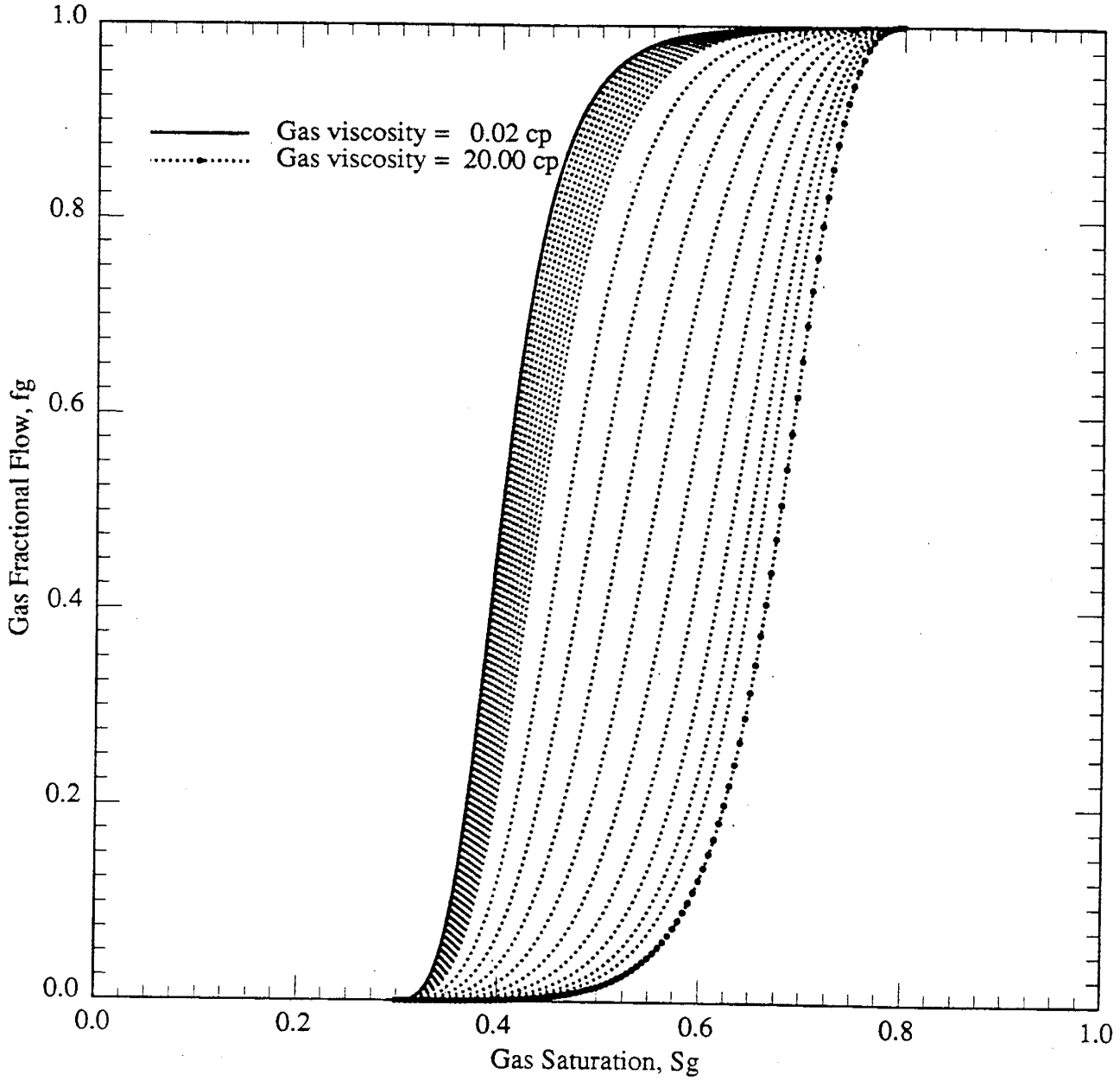

Figure 3.1.1 Fractional Flow Curves

loss, the first gas shock velocity is calculated as:

$$\upsilon_1 = \frac{f_{g_1} - f_{g_\phi}}{S_{g_1} + D_1} = f_{g_1}'$$

$$D_1 = \frac{a}{1 + bC_1}$$

where

υ_1 --- first gas shock viscosity
f_{g_1} --- gas fractional flow at first shock
f_{g_o} --- gas fractional flow at initial condition
f_{g_1}' --- tangent of first fractional flow curve
S_{g_1} --- gas saturation at first shock
D_1 --- frontal advance loss of surfactants
a,b --- Langmuir constants
C_1 --- Surfactant concentration at first shock

The second and subsequent shocks are:

$$\upsilon_2 = \frac{f_{g_2} - f_{g_1}}{(S_{g_2} + D_2) - (S_{g_1} + D_1)} = f_{g_2}'$$

$$D_2 = \frac{a}{1 + bC_2}$$

where

υ_2 --- second gas shock velocity
f_{g_2} --- gas fractional flow at second shock
f_{g_2}' --- tangent of second fractional flow curve
$6S_{g_2}$ --- gas saturate at second shock
D_2 --- frontal advance loss at second shock
C_2 --- surfactant concentration at second shock

According to the above two equations for shock velocities, the first shock velocity is equal to the slope of the tangent to the first fractional flow curve (the lowest gas velocity) starting from $f_g = 0$ and $S_g = -D_1$. As shown in Fig. 3.1.1, the tangential point on the curve gives rise to the gas flow fraction and the gas saturation for the first shock. The second shock velocity is the slope of the tangent to the second fractional flow curve (the next higher gas viscosity) starting from f_g (first shock) and S_g (first shock)-$(D_2 - D_1)$. The rest of the shocks

are treated the same way. Then the material balance is taken into account to modify the shock velocities. Figure 3.1.2 shows the velocities for each shock represented by the dimensionless quantities: dimensionless distance X_D and dimensionless time t_D.

For a given time, the saturation profile can readily be obtained from the velocities of each shock, as shown in Fig. 3.1.3 at the time of 0.5. For comparison, the saturation profiles are also calculated for the cases of pure gas displacements at viscosities 0.02 cp and 20 cp, respectively.

Figure 3.1.3 is redrawn in Fig. 3.1.4 to enlarge the middle part by using reduced gas saturation vs. dimensionless distance.

The saturation profile can also be shown as the saturation vs. equivalent pore volume at a given location. Figure 3.1.5 is shown in the liquid saturation-EPV relationship at the outlet ($X_D = 1$).

The above theory is capable of explaining the gas channeling and adsorption observed in the experiments (discussed in the 1989 annual report). However, this is still in the category of Buckley-Leverett theory whereas foam flow is not. So it does not explain why experimental saturation profiles stretch differently at different locations.

3.1.3 FUTURE WORK

1. More experiments will be conducted.
2. Mixing theory will be added to the above-mentioned model to take care of the saturation profile stretching observed in the experiments.
3. Experimental data will be incorporated into the model.
4. Hopefully, a semi-analytical model can be derived from the computer modeling investigation combined with experimental data.

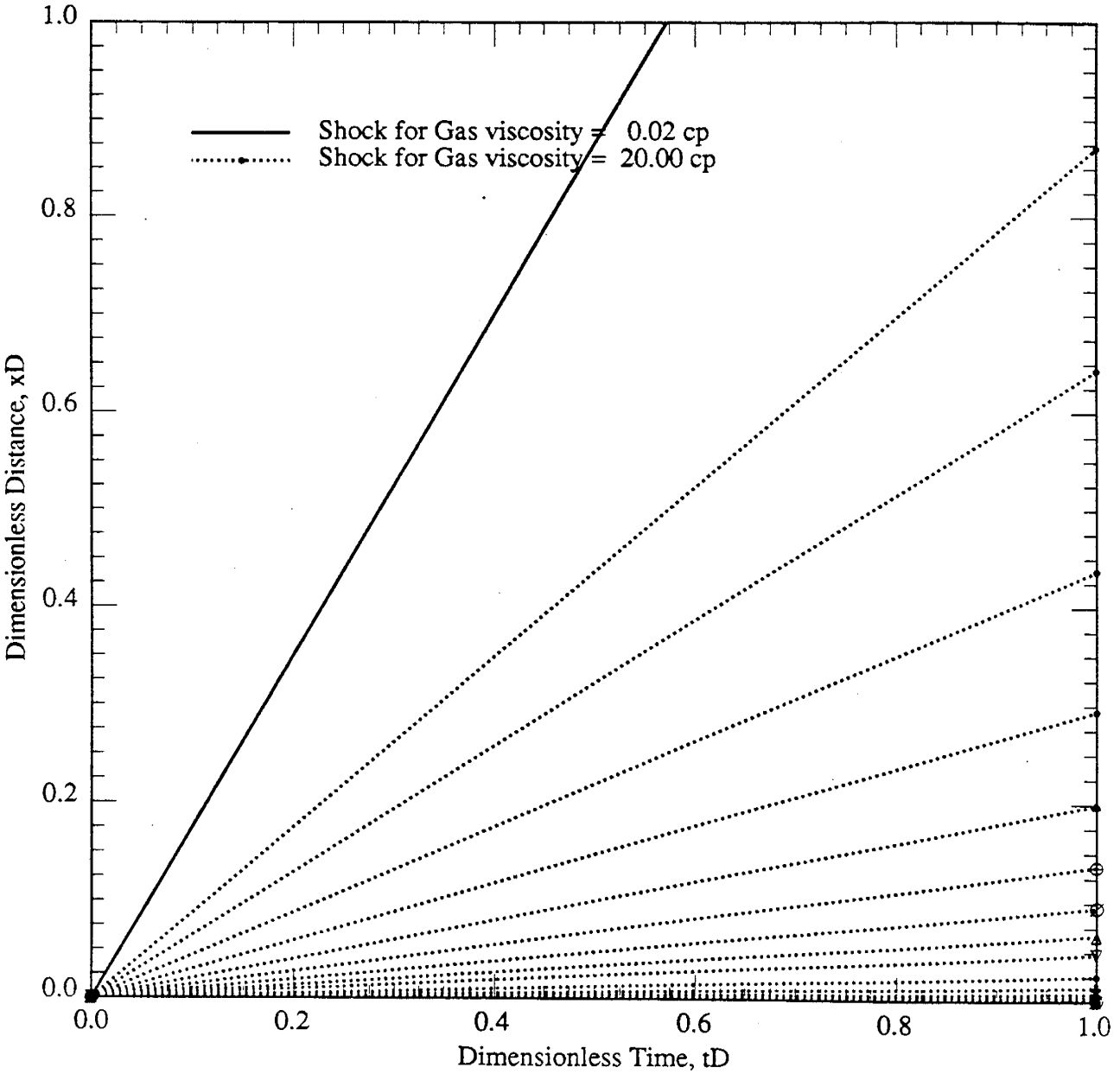

Figure 3.1.2 Shock Velocities

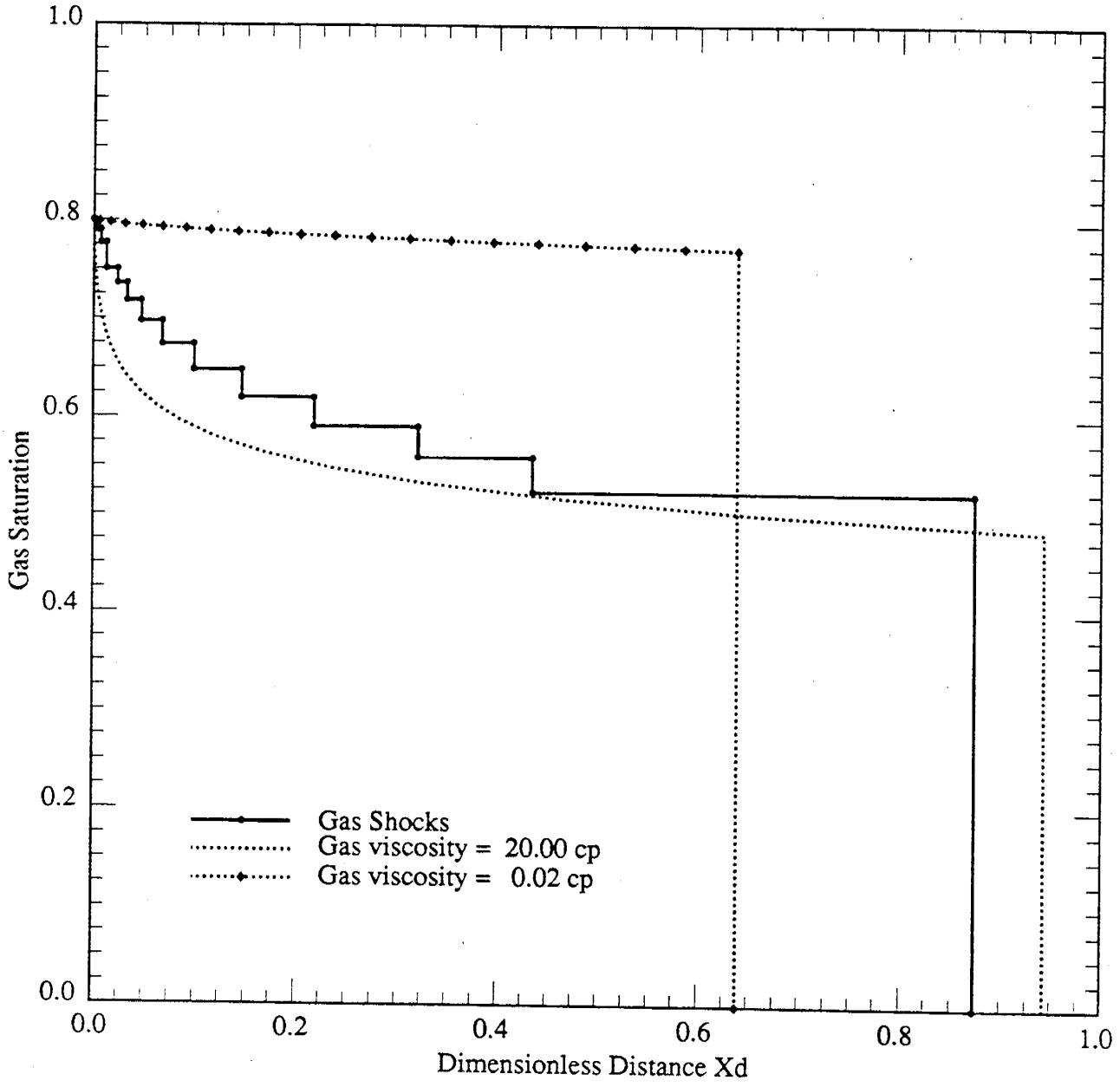

Figure 3.1.3 Saturation Profiles at $t_D = 0.5$

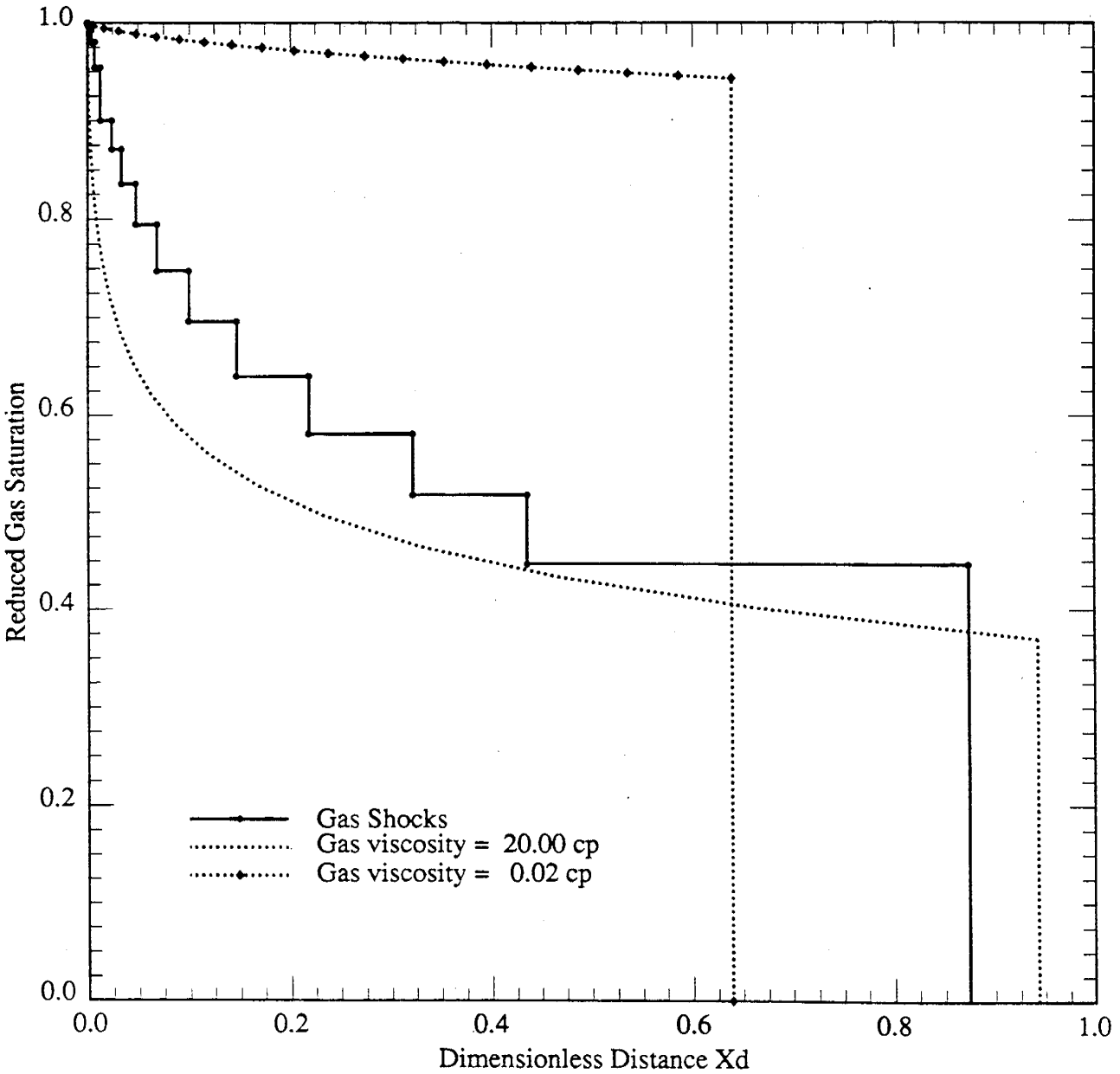

Figure 3.1.4 Saturation Profiles at $t_D = 0.5$ (Reduced Gas Saturation)

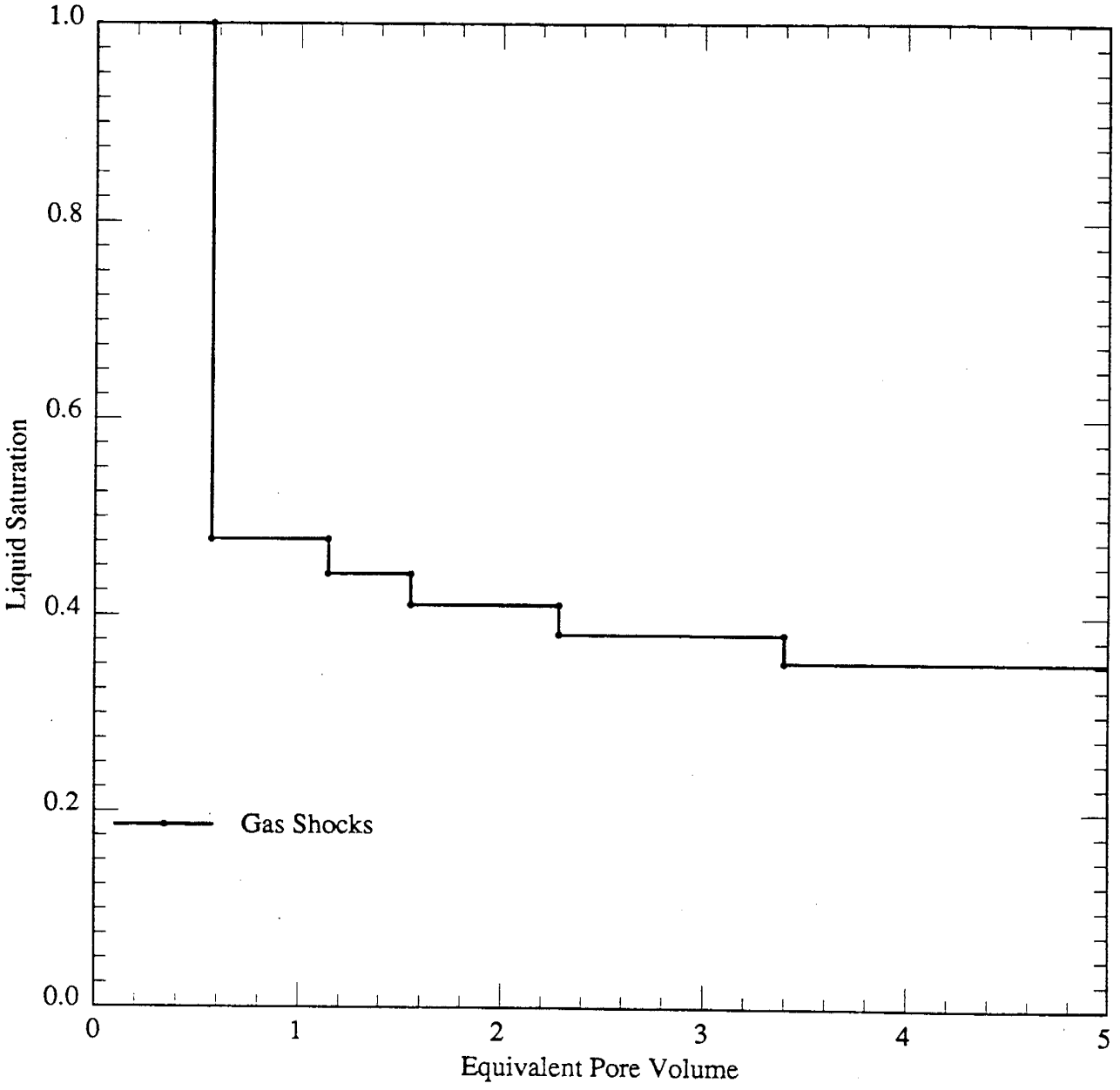

Figure 3.1.5 Saturation Profile at Outlet

STEAM-FOAM STUDIES IN THE PRESENCE OF RESIDUAL OIL

by

D. A. Hutchinson

Stanford University
Petroleum Research Institute
Stanford, California

3.2 STEAM-FOAM STUDIES IN THE PRESENCE OF RESIDUAL OIL
(D. A. Hutchinson)

3.2.1 ABSTRACT

The efficiency of a steamflood can be increased by the addition of surfactants which produce foam. The generation of a steam-foam reduces the steam mobility and forces the steam to seek a path to the producer not previously taken and, therefore, to displace unswept oil.

Since the principal purpose of a steam-foam is to divert steam to previously unswept areas, it is important to understand the behavior of surfactant in the presence of oil. However, since surfactant use is generally applied only after stream breakthrough, the focus of this research is to understand foam behavior in the presence of residual oil.

The results show that foam can be generated in the presence of residual oil when an alternating injection technique — surfactant slug followed by steam and nitrogen — is used. Additionally, the results indicate that the slug size may be reduced without any apparent reduction in the pressure response, hinting that an optimum may be determined.

3.2.2 EXPERIMENTAL SET-UP

LINEAR MODEL: A schematic of the linear model being used is shown in Figure 3.2.1. The model is a cylindrical stainless steel [ss#321] tube having a 6 ft. length, a 2.16 in. inside diameter, and a 2.25 in. outside diameter. The 21 thermocouples used to monitor temperature are separated between 2 in. (near the inlet) to 5 in. (near the outlet). Their location within the sandpack alternates between being at the center of the pack or being 0.5 in. from the top of the pack. The 5 pressure taps located at 16, 32, 52, and 72 in. from the inlet allow for monitoring of pressure changes within four separate sections of the model. The 5 heat flux sensors are used to measure the heat losses, obtain the overall heat transfer coefficient and, eventually, the steam quality along the sandpack. One of the heat flux sensors is located at the top of the tube, 38 inches from the inlet. The other 4 are located at the top, bottom, and sides of the tube at a distance of 25.5 inches from the inlet. The clean sand used to pack the model resulted in a system having 35% porosity and 85 Darcy permeability.

SUPPORTING EQUIPMENT: A simplified schematic of the experimental set-up is shown in Figure 3.2.2. Two Constametric Model III pumps are for fluid injection, with one being used exclusively for supplying distilled water to the steam generator, while the other is used for both surfactant injection and cleaning fluid injection. In addition, a Marshall Model #1056 tubular furnace is used to generate steam, a Matheson Model 8141 mass flowmeter is used to control the nitrogen injection rate, and an IBM-XT computer via an HP Model 3497A data-acquisition system is used to record temperature and pressure data from the 21 thermocouples and 5 pressure transducers.

3.2.3 PRIOR WORK

FRED WANG (1986): The linear model herein described was built and first used by Fred Wang. He examined one surfactant, SUNTECH IV, and found that a reduction in steam mobility could be obtained with as little as 0.1 wt% of surfactant in a 10% pore volume (PV) slug. The linear model in all cases was water saturated. A significant result from his work is that simultaneous injection of steam and nitrogen lessened the amount of surfactant needed to obtain a given pressure increase when compared with injection of steam alone.

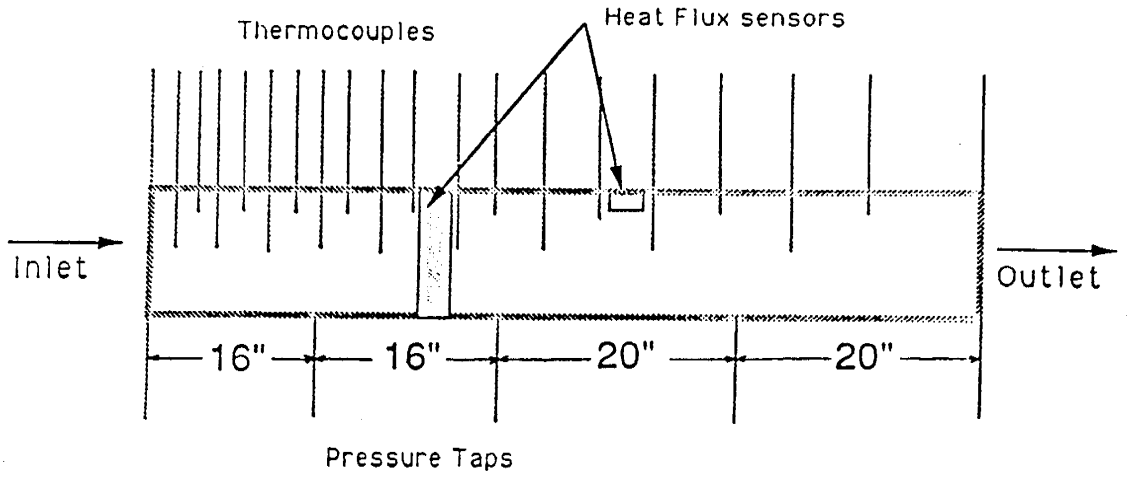

Figure 3.2.1 Linear Sandpack Model

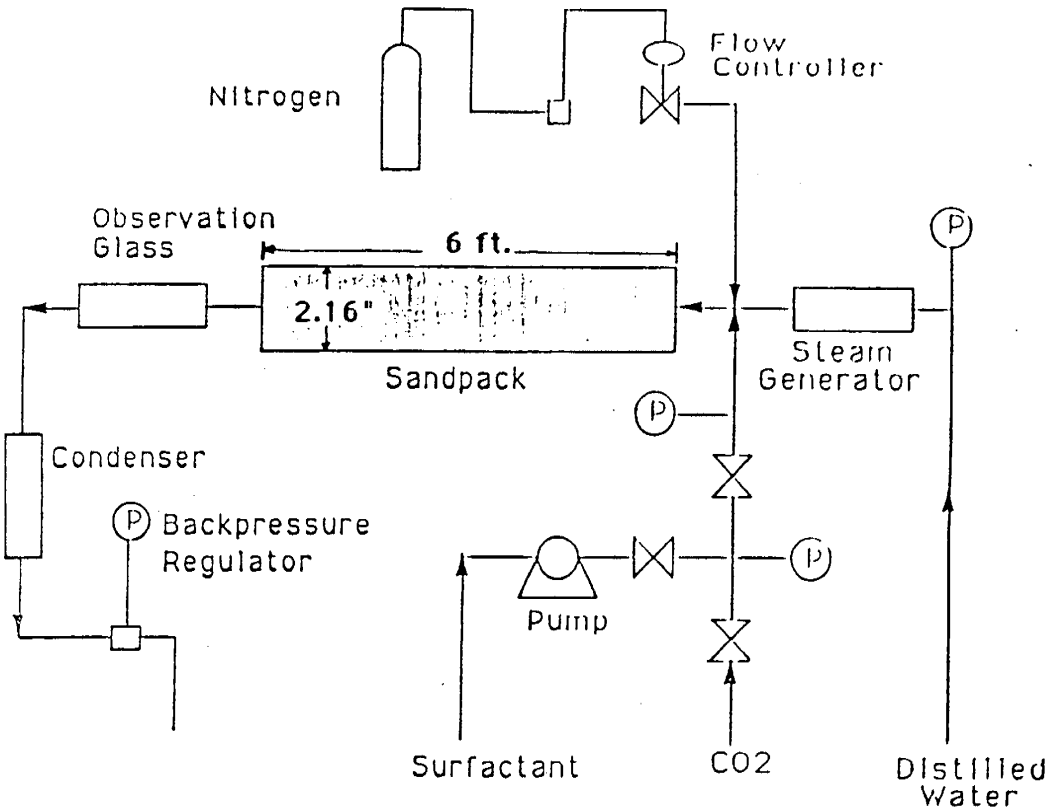

Figure 3.2.2 Experimental Set-Up

DAVID SHALLCROSS (1988): Extensive work was done by David Shallcross who tested seventeen surfactants, at various injection concentrations, rating their relative strengths based upon the size of the pressure increase resulting from their injection into the linear model. A summary of his results is given in Table 3.2.1. Inspection of the table shows that, for a given chemical group, there is a trend favoring larger molecular weight surfactants. As with the work of Fred Wang, the work of David Shallcross was for a 100% water saturated system.

FARID HAMIDA (1990): Farid Hamida, duplicating some of the Shallcross work, tested the top seven surfactants listed in Table 3.2.1. An additional surfactant, AOS2024DE, having an increased disulfonate content as compared with AOS2024, was also tested in the water saturated linear model. A comparison between these two surfactants indicates that increasing disulfonate content will reduce foam strength. The results regarding alkyl chain length were the same as those obtained by Shallcross, that is, the foam strength exhibited by surfactants in a given chemical group increased with increasing molecular weight. Further surfactant tests were made with residual oil in the model, however, the surfactants in all such tests were unable to cause a pressure increase.

3.2.4 RECENT WORK

A troubling result from the Hamida report was the complete surfactant failure in the presence of residual oil even though some of the surfactants used had been successfully field tested (Patzek and Koinis, 1988) and lab tested (Demiral and Okandan, 1987) in the presence of oil. No obvious explanation was forthcoming, however, Demiral did observe that most of the successful oil runs were those where steam and nitrogen were injected only after the surfactant-slug injection was completed. Such an alternating injection scheme (AIS) can be contrasted with the simultaneous injection scheme (SIS) used by Hamida, where the surfactant slug, steam, and nitrogen were all injected together. Recently the AIS method was applied to a residual-oil system and gave positive results, with pressure increases across the sandpack of about 20 psi (Figure 3.2.3). Although the observed pressure response is relatively small in comparison with the 100% water saturated runs, such an attenuated response is in accordance with results obtained by other investigators (Bernard et al. (1964), Duerken (1986), Robin (1987), Olsen (1989), Lau and Borchard (1989), and somewhat to be expected since oil partitioning of the surfactant will occur.

The reasons for the success of the AIS method over the SIS method is not understood, but a possible explanation is that different surfactant concentrations are seen by the steam depending upon the method used. In the AIS method, the slug has displaced oily water with distilled water that is surfactant full. Thus, when steam first enters the model, it encounters a surfactant concentration identical to what was injected in the original slug. Any injected steam must make a path through a surfactant rich volume of liquid. However, for the SIS method the entering steam initially encounters a surfactant-free solution. Should the steam take a specific path not followed by the fluid, it is possible that the steam never sees a sufficiently high surfactant concentration to produce foam. This presupposes that a higher surfactant concentration is needed to initiate foam production for residual oil systems vs 100% water saturated systems, but such an assumption is not unreasonable since oil can destabilize foam bubbles.

An additional observation from the residual-oil runs suggests that work is needed to optimize the slug size and injection frequency. Preliminary results show that a larger pressure response is obtained with less overall surfactant when the slug size is decreased but the slug injection-frequency increased (Figure 3.2.3). This result would be in agreement with the above mentioned hypothesis since, almost regardless of the slug size, if the AIS method is used the entering steam and nitrogen see a high surfactant concentration immediately, thus a large slug size is not needed. This could have important economic implications concerning proper field application.

Table 3.2.1 Results for Seventeen Surfactants (Shallcross 1988)

Surfactant	Manufacturer	Minimum Foaming Concentration (wt %)	Maximum Pressure Drop (psi)	Duration of Pressure Response (min)
Enordet AOS 2024	Shell	0.10	234	85
Enordet AOS 1618	Shell	0.10	132	68
Enordet LTS 18	Shell	0.10	58	> 120
Chaser SD 1000	Chevron	0.10	6	29
Enordet IOS 1720	Shell	0.25	217	79
Enordet IOS 2024	Shell	0.25	209	83
Hostapur OS fl	Hoechst	0.25	65	45
Hostapur SAS 60	Hoechst	0.50	> 215	76
Enordet IOS 1517	Shell	0.50	161	100
C 1416 AOS	Shell	0.50	71	> 118
Enordet LTS 1618D	Shell	0.50	42	> 206
Enordet LXS 18	Shell	1.00	246	> 85
Enordet LXS 16	Shell	1.00	230	87
Enordet LXS 1314	Shell	1.00	201	> 126
Enordet LXS 1112	Shell	Foaming did not occur at 1.00 wt %		
Enordet LXS 814	Shell	Foaming did not occur at 1.00 wt %		
Chaser SD 1020	Chevron	Foaming did not occur at 1.00 wt %		

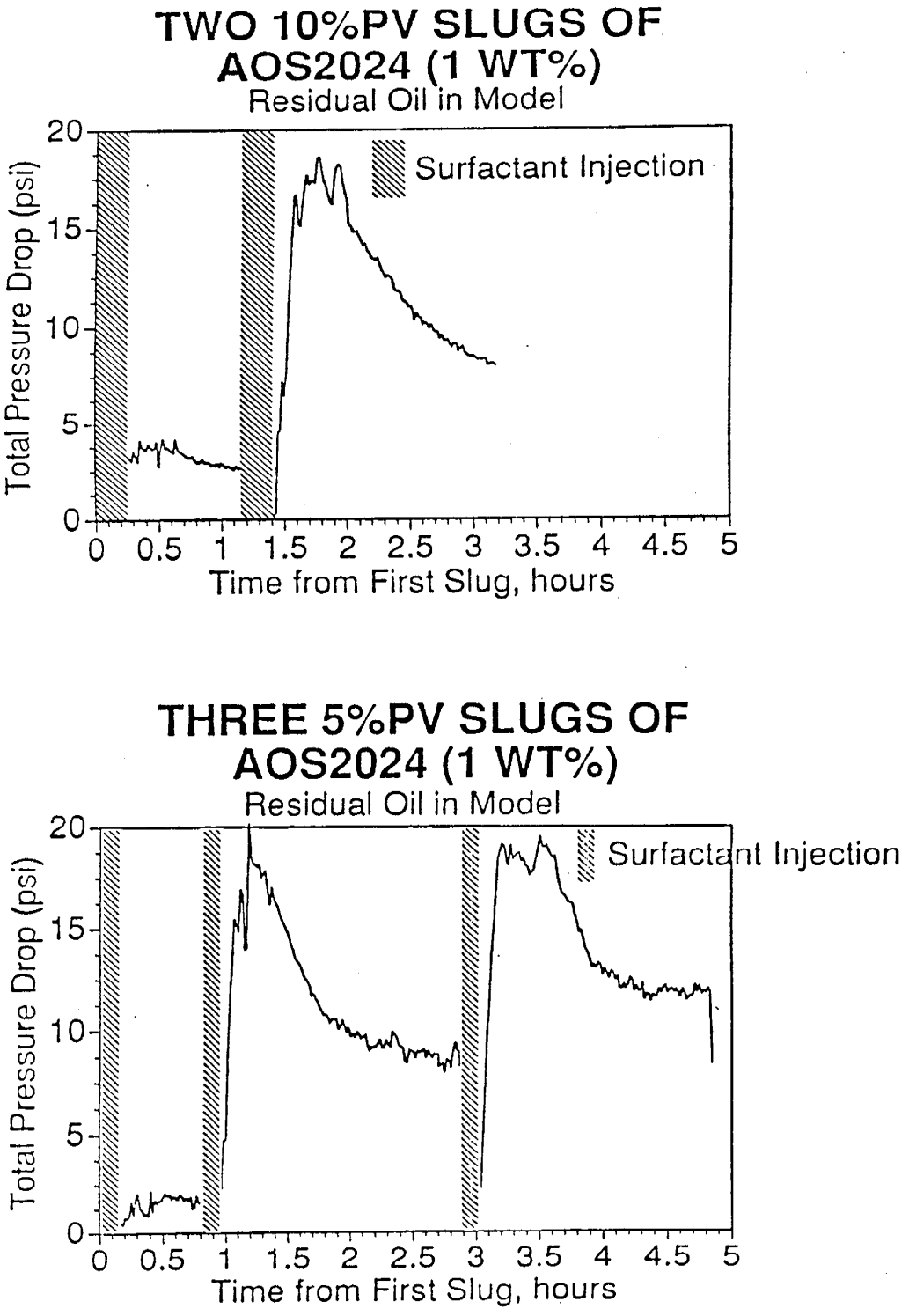

Figure 3.2.3 Pressure Response to Various Slug Sizes

3.2.5 FUTURE WORK

The direction of future work is aimed at better understanding steam-foam flow in the presence of residual oil. Initially, this will involve comparing the AIS and SIS injection schemes under various inlet steam qualities. Later, an attempt will be made to optimize the injection procedure in general.

The sequence of the planned work is the following:

1) With residual oil in the model and using the AIS method, make two separate runs for each of the following surfactants:

   AOS202 4LTS18 IOS1720

   The two runs will a include a low and a high steam quality. These three are the strongest foamers within their respective groups as determined by Shallcross.

2) Pick the strongest of the three surfactants and, using a low steam quality, make a run using the SIS method. If a pressure response is obtained then several runs will be made at various steam qualities.

3) Repeat step (2) but with the AIS method. Depending upon the results, several runs may be made at various steam qualities.

4) Do several runs with the idea of optimizing the slug size, injection frequency, and nitrogen rate.

MICROVISUALIZATION OF FOAM FLOW IN A POROUS MEDIA

by

D. Hornbrook

Stanford University
Petroleum Research Institute
Stanford, California

44-83

3.3 MICROVISUALIZATION OF FOAM FLOW IN A POROUS MEDIUM
(J. Hornbrook)

3.3.1 INTRODUCTION AND OBJECTIVES

Since the late 1950's foam has been recognized as a fluid possessing oil production enhancement capability. Foam may be used to improve the mobility characteristics of an oil reservoir or it may be used as a selective blocking agent to reduce the effects of fingering induced by permeability streaks in the producing formation. Additionally, the surfactants used to produce foams may aid in the production of heavy oils by partially dissolving the oil or by helping to separate oil blobs from the rock in mixed-wet systems.

Study of the flow of foam in porous media may be roughly divided into three broad areas. 1) Foam properties. This area includes studies of the fluid properties of foam, the most important of which is foam viscosity and how it varies with shear rate. 2) Foam flow mechanisms. This area is made up of research into the means of propagation of foam in porous media. Snap-off events and bulk propagation of the gas and liquid fractions of foam are studied in this area. 3) Foam interactions with oil. This area, obviously, concerns itself with the way foams react with oil. The ways in which foam increases the mobility of oil and the mechanisms by which oils destroy foam are of particular interest. Research within the three broad research areas has been undertaken at the field pilot project level, the macroscopic level in laboratory core floods, and at the microscopic level in micromodel studies.

The current research focuses on the third broad area of foam research (foam interactions with oil) and is carried out at the microscopic level. Background work designed to validate experimental procedure was completed in homogeneous micromodels. Presently, the construction of an exact two-dimensional replica of Berea sandstone is being attempted. Upon completion of the replica micromodel, the effects of foam injection procedure upon foam stability in an oil filled micromodel will be studied.

3.3.2 LITERATURE REVIEW

The study of foam with application to petroleum engineering application began with the pioneering work of Bond and Holbrook (1958). Their work concentrated on the mobility effects of injected foam and it pointed out the benefits to foam injection as a method of enhancing oil reservoir performance. Over the next thirty years much research and several field experiments have attempted to understand the flow of foam in porous media on both a qualitative and quantitative level.

Many papers have been written on the fluid properties of foam. The results of these papers are rarely in agreement on the nature of foam and are often contradictory. A chronological review of foam research was carried out by Marsden (1986). In his review, Marsden outlines the major advances in the understanding of foam flow and points out shortcomings and contradictions in existing work. A brief summary of foam fluid properties is: 1) foam is a fluid of high apparent viscosity, 2) foam viscosity is a function of the surfactant concentration, 3) foam viscosity is a function of flow rate (non-Newtonian flow), and 4) the flow history of foam affects its viscosity.

Foam flow mechanisms, the means by which foam propagates through a porous medium, have been studied in numerous papers as well. Most of this work, however, has focused on a

qualitative description of foam rather than a quantitative one. Most recently, the research of Owete (1984), and Radke (1988) have attempted to extend the understanding of foam flow mechanisms beyond the description of observed phenomena. Owete studied the flow of foam in the following two areas: 1) the propagation of foam and its components, and 2) the mobility of gas in the presence of foam. Owete carried out his work in micromodels with homogeneous and heterogeneous flow paths and, although most of his conclusions are qualitative, some quantitative results were obtained.

Owete's results for a homogeneous micromodel have been verified as a part of the background work in my research. The quantitative aspects of Owete's work will be extended to include the effects of foam injection procedure on oil displacement. Future research will be carried out in two-dimensional replicas of Berea sandstone.

Research on the effects of oil on foam has been carried out by Manlowe and Radke (1988) and by Sanchez and Hazlett (1989). The work of Manlowe and Radke was most applicable to this project. Manlowe and Radke studied the foam breaking tendency of oil on foam and described the stability of a pseudo-emulsion film as the determinant of foam stability in the presence of oil. This work will involve the study of the pseudo-emulsion film under different foam injection schemes.

Research involving flow of foam through micromodels is relatively new. In addition to the micromodel research mentioned above, several studies on the usefulness of micromodels as a research tool have been carried out. Sarathi (1986) points out the advantages in studying pore level events afforded by micromodels but warns against extrapolating pore level events to a large scale without additional information. He also points out several disadvantages inherent in commonly used micromodels, most of which will be eliminated by the construction process outlined in this report. Sarathi lists the following as important problems with micromodel research: 1) difficulty in obtaining a continuous specific etch depth, 2) introduction of microscopic heterogeneity into the model in the etch procedure, 3) difficulty in replicating reservoir Peclet number due to enlargement of the pores, 4) loss of three-dimensional continuity, and 5) loss of detail - heterogeneity, pore geometry, connectivity, and surface roughness - due to the anealling process used in most micromodel construction processes. Except for the loss of three dimensional continuity, all of the disadvantages listed above are eliminated in the micromodels described in this report.

Huh et al. (1989) point out the importance of differences in heterogeneity on foam generation in porous media, further supporting the need for accurate replication of a porous medium of interest in a micromodel study.

3.3.3 EQUIPMENT

An experimental apparatus has been constructed that will allow the flow of foam through a micromodel to be simultaneously observed, videotaped, and photographed, and will allow for monitoring of the pressure drop across the micromodel. The micromodels used are two-dimensional representations of porous media made by etching a flow path into a silicon wafer and then bonding the wafer to a flat piece of glass (Fig. 3.3.1), thus creating a self contained flow path. Two homogeneous micromodels were used in the background portion of the foam flow research. The homogeneous micromodels were used to verify that the experimental apparatus worked as designed and to replicate Owete's results to verify that the experimental procedure was correct. Both homogeneous micromodels were etched to a depth of 30 microns. One micromodel represented cubic packing of spheres of radius 100 microns while the other micromodel represented rhombohedral packing of spheres of radius 30 microns. A heterogeneous model which is an exact two-dimensional replica of Berea sandstone is being constructed. A detailed description of the construction of the Berea replica micromodel follows.

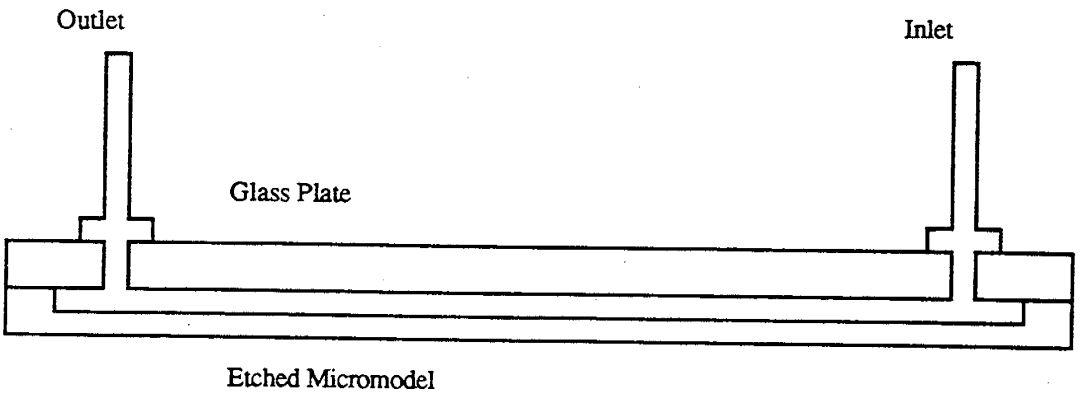

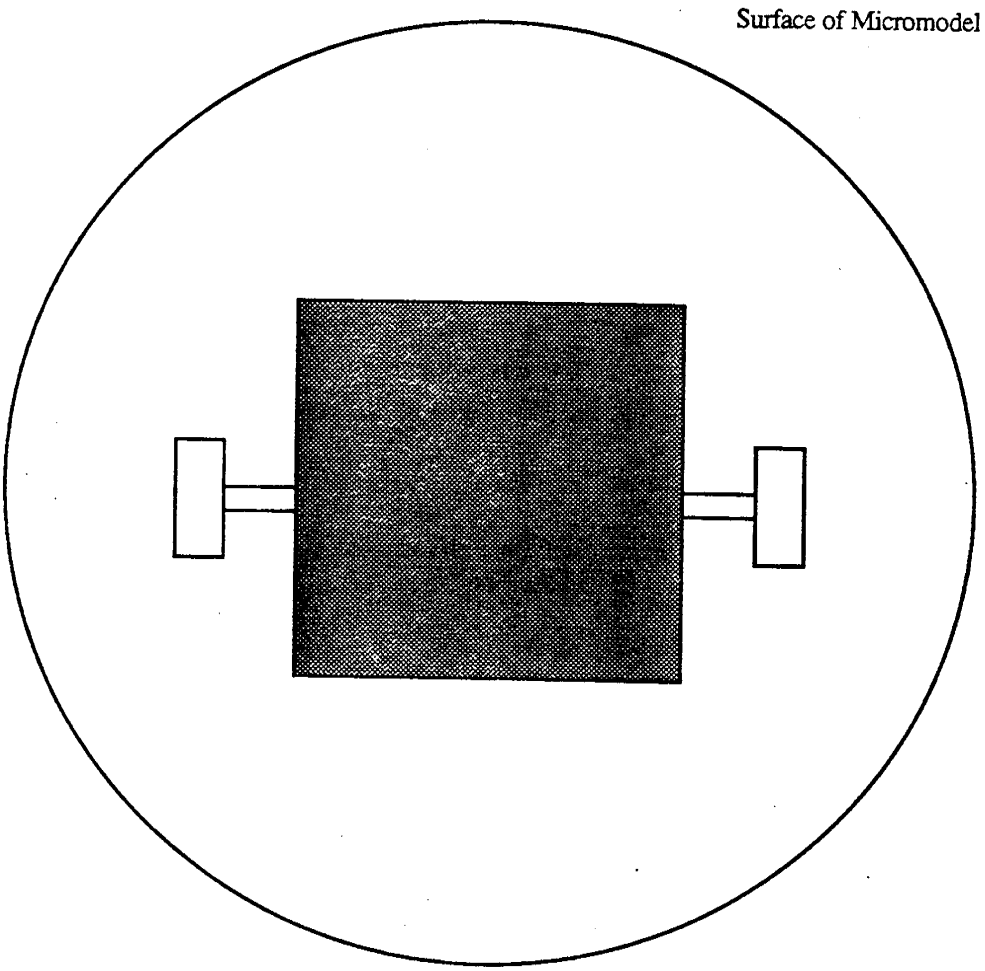

Figure 3.3.1 Micromodel Schematic

A thin section of clean Berea sandstone was prepared with the pore spaces filled with blue-dyed epoxy. A color photograph of the thin section was taken at 40 times magnification. The result is a photograph in which pore spaces appear blue and the sand grains appear black to grey. Professional slide film was used to get a true color image. The film was then sent to a photography lab where, after the development with the use of color filters, the blue was transformed to white. After this transformation, the pore spaces are white while the sand grains are still black and grey. Finally, a lithograph of the photograph is made. In the lithograph, the pore spaces appear white and the sand grains are strictly black - - there are no grey scales. Now the lithograph image must be transferred to the computer.

The lithograph of the thin section was put into PICT format by using a Macintosh digital scanner. The image was then analyzed by using a digital analysis package called Ultimage (1988). It was noticed that at various points in the image, pore spaces that should have been continuous were blocked off. This is an artifact of the loss of one dimension in transferring the three-dimensional flow path to two-dimensions. By use of the digital analysis package, a small number of pixels were removed to allow for a continuous flow path through the micromodel. When pixels were removed, the nature of the flow path was always maintained, so after manipulation of the digital image, a computer image of a continuous Berea flow path was obtained (Fig. 3.3.2).

The most difficult problem in obtaining a Berea micromodel is in the next step -- moving the computerized image of the sandstone (PICT format) to MEBES (1988) format which is the format used at Stanford's Center for Integrated Systems to transfer complicated images to silicon wafers. First, an ASCII bit map of the image is generated with black pixels given a value of 1 and white pixels given a value of 0. The bit map is then restructured into columnar form with each pixel given an address and size based on its location in the image. Finally, using modified transferring software available at Stanford CIS, the image is transferred to MEBES format. Once the image is put into MEBES format, the final steps are trivial.

A permanent chrome-on-glass mask of the Berea pore space is constructed by the electron beam imaging group at Stanford. Once the mask is complete, the silicon wafer model construction is carried out as in more conventional models (the process will be described in detail). Presently, I am attempting to get an accurate description of the Berea image in MEBES format, a rather complicated problem.

When the image mask has been completed, the following steps are used to generate the etched silicon flow path:

1. Oxidize one side of a silicon wafer (5 cm. diameter).
2. Coat one side of the oxidized wafer with a photoresist material.
3. Position the sample mask on the photoresist side of the wafer.
4. Expose the sample mask to ultra-violet light. The structure of the photoresist is destroyed by contact with ultra-violet light so, since the sample mask is a negative of the sample, the photoresist is destroyed where pores exist.
5. Etch the wafer with hydrofluoric acid to the desired depth.

Only the parts of the wafer not coated with photoresist will be etched, so after etching, the pores and flow channels of the Berea sample will be etched away while the grains will be intact. After etching, the wafer is anodically bonded to a flat glass plate. The process of anodic bonding is uncomplicated and is easy to carry out. The silicon wafer, in contact with the glass plate, is sandwiched between two electrodes (the negative electrode contacting the glass plate) and the entire system is placed on a hot plate (Fig. 3.3.3). The system is heated to

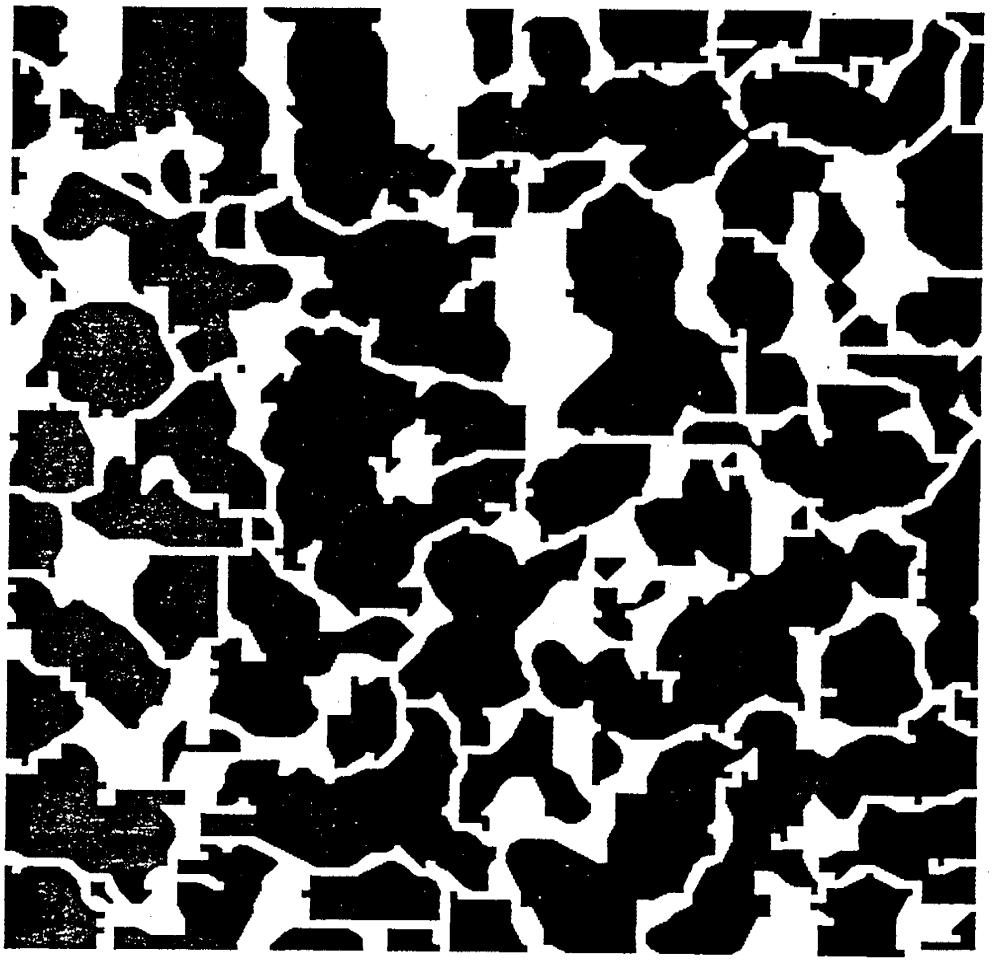

Figure 3.3.2. Digital Image of Flow Path in Brea Sandstone
(40 Times Magnification)

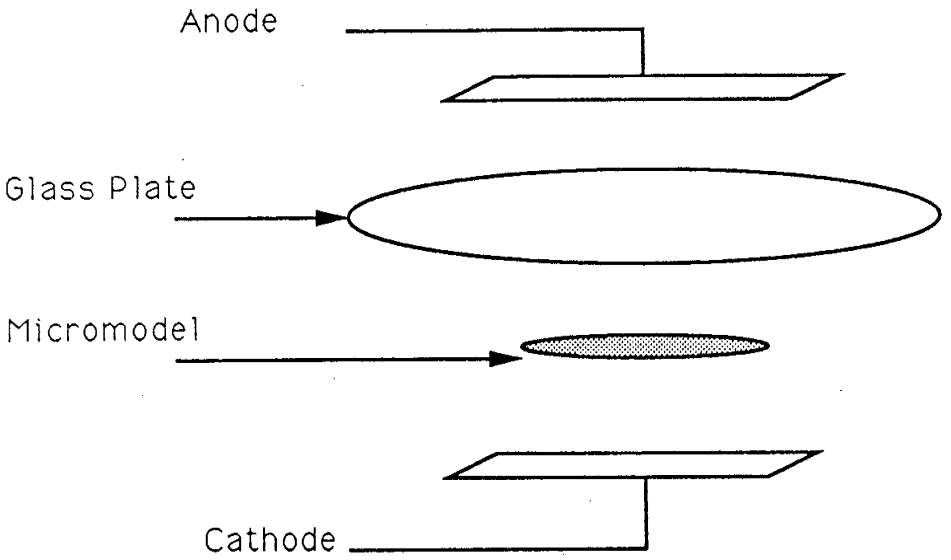

Figure 3.3.3 Anodic Bonding Schematic

400 C and a potential drop of 600 V is applied across the electrodes. Bonding between the wafer and the glass plate is immediate and is irreversible. The glass plate must be absolutely flat so the small flow channels end up as distinct and separate flow channels.

Figure 3.3.4 is a schematic of the flow visualization apparatus. A syringe pump will be used to either independently or simultaneously inject a surfactant solution and air which may be mixed in a foam generation cell and observed through a view port. While the foam is passing through the view port, it will be photographed and/or described at regular intervals so a record of foam texture may be kept throughout the run. Next, the foam will pass through the micromodel described in detail above. While in the micromodel, video and still cameras will record the movement of the foam (Fig. 3.3.5). After leaving the micromodel the foam will pass through another view port.

Here, the foam will again be observed and compared to the inlet foam to determine if any structural changes have taken place in the foam during the displacement process. The pressure drop across the micromodel will be monitored with the use of a pressure transducer, and the pressure data will be recorded on a chart recorder.

3.3.4 RESULTS AND PLANNED WORK

At this point, only the preliminary work using homogeneous micromodels has been carried out. Air was injected into a surfactant saturated micromodel at a flow rate of 2.5×10-4 cc/s and the general flow characteristics observed were found to be identical to those observed by Owete. The flow rate used was on the order of 100 ft/s which is much higher than normal reservoir rates which are on the order of 1 ft/s. Attempts were made to reduce the flow rate to around 1 ft/s, but no precise procedure was found to do this.

As soon as the Berea replica micromodel is constructed, the following work will be carried out.

1. Foam flowing properties in the micromodel will be compared to results obtained by Owete and others to determine if foam behaves the same in models of the same pore size and configuration of real reservoir rock as it does in the larger pore size micromodels commonly used. Flow rates equivalent to about 100 ft/s will be used in these runs as well.

2. The oil displacement efficiency of foam will be investigated under two different injection schemes. First, the micromodel at residual oil saturation will be injected with 0.5 pore volumes of surfactant solution. The model will then be injected with nitrogen and the foam/oil interactions at the fluid interface will be observed. Then, the same micromodel, again at residual oil saturation will be injected with foam produced in the foam generation cell. The foam/oil interactions will again be observed, and results from the two different injection schemes will be compared. Macroscopic experiments at Stanford have indicated that the former injection scheme is significantly more efficient and a microscopic study of the phenomena may yield useful information.

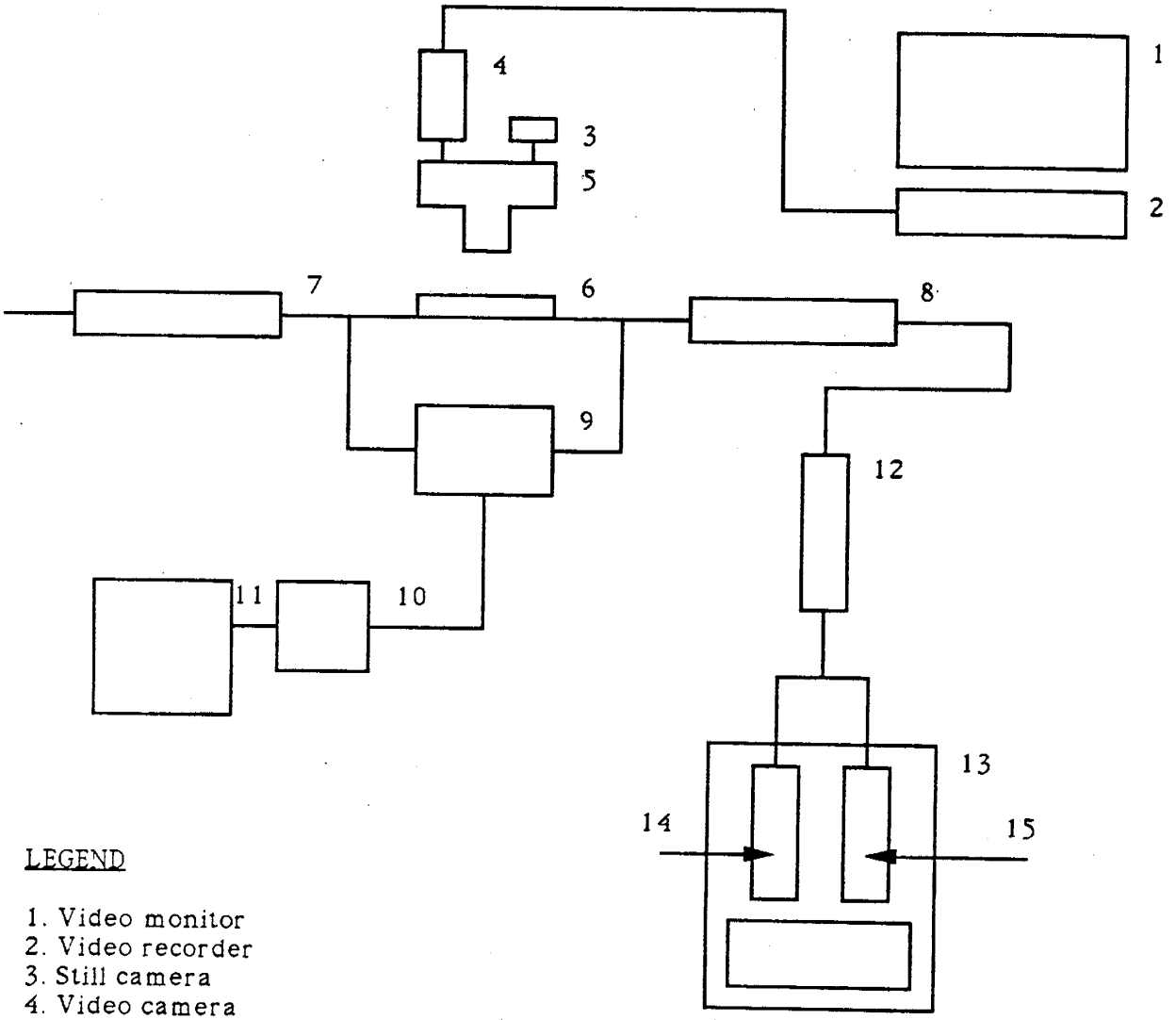

LEGEND

1. Video monitor
2. Video recorder
3. Still camera
4. Video camera
5. Microscope
6. Micromodel
7,8. Foam view port
9. Pressure transducer
10. Voltmeter
11. Chart recorder
12. Foam generation cell
13. Syringe pump
14. Surfactant solution
15. Air.

Figure 3.3.4 Schematic of Experimental Equipment

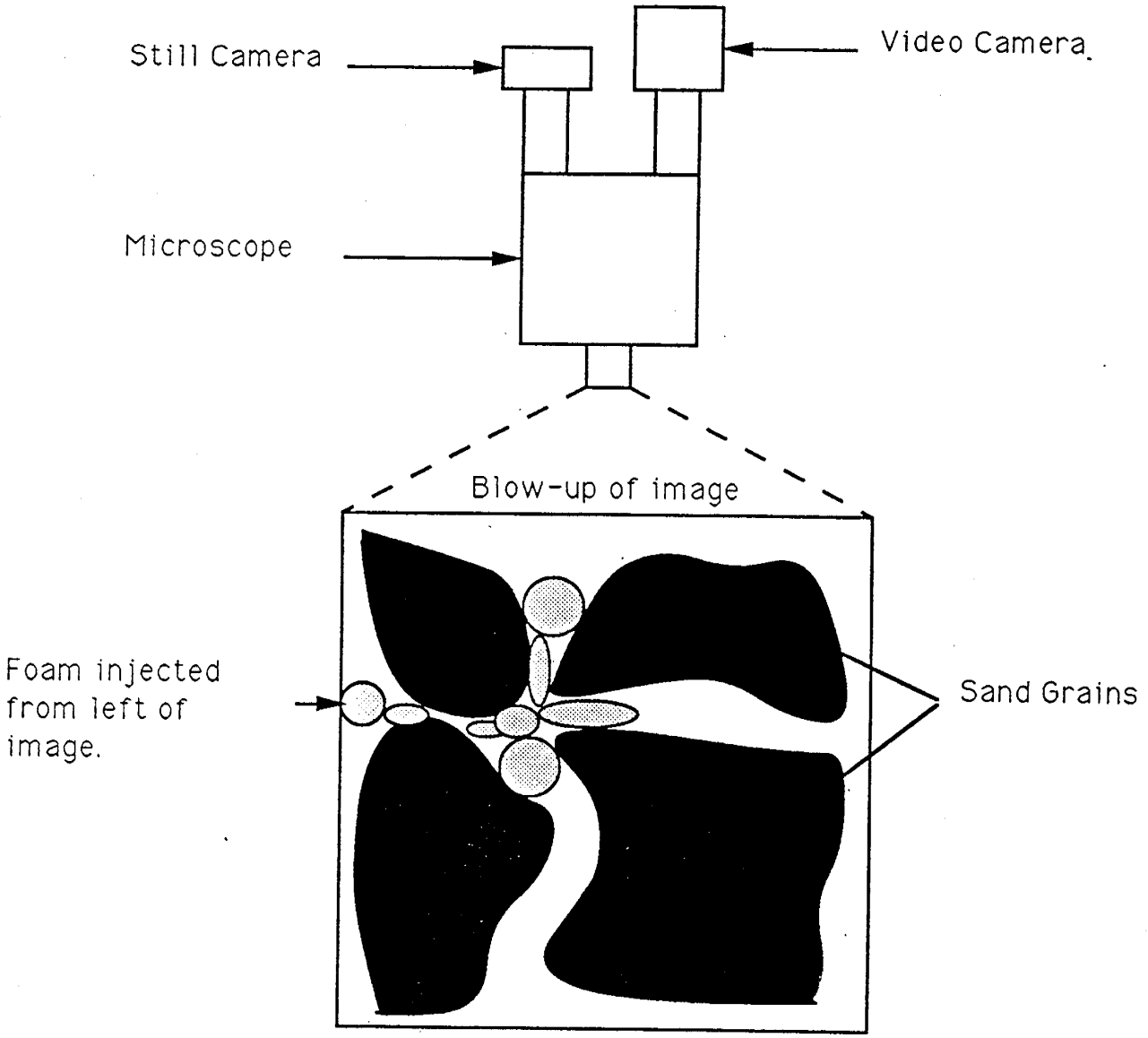

Figure 3.3.5 Foam Observation Process

THREE-DIMENSIONAL LABORATORY STEAM INJECTION MODEL

by

B. Demiral

Stanford University
Petroleum Research Institute
Stanford, California

3.4 THREE-DIMENSIONAL LABORATORY STEAM INJECTION MODEL
(B. Demiral)

3.4.1 SUMMARY

The objectives of this project are to observe the oil recovery mechanisms of steamflood and steam-foam injection in a 3-D laboratory model by using Computer Aided Tomography (CT Scanning). A stepwise approach has been followed to achieve this goal: 3-D model development, and steam and steam-foam injection experiments using CT Scanning.

3.4.2 3-D MODEL DEVELOPMENT

A three-dimensional laboratory steam injection model which is able to be scanned under CT scanner was developed. During the design period, different geometries that could be the best representative of radial flow and fit the dimensions of the scanning field of SUPRI-A CT scanner were examined in terms of their advantages and disadvantages. As a result of this analysis a 3-D box with dimensions $20 \times 20 \times 7.5$ cm was constructed. This box simulates a 1/4th of a five spot pattern. Aluminum, teflon and fiberfrax were chosen as supporting and insulating materials respectively. As can be seen from the injector producer diagonal cross-section of the model, Figure 3.4.1, the heat insulator (Teflon) is in first contact with the porous medium. Teflon was placed between the porous medium and the aluminum so that one could assume that the rate of heat transfer in the porous medium would be much faster than that in the aluminum during a steam injection run. Aluminum was necessary to back up the Teflon for strength under the proposed pressure and temperature conditions and was chosen as construction material since it absorbs less x-ray energy than other materials. The Teflon box was to be sealed against any gas or liquid leaks by using Chemgrip, a special epoxy which bonds Teflon to Teflon or Teflon to metal. Fiberfrax, a ceramic fiber insulating material which is inexpensive and can be applied as a wet putty which air dries to a semi-permanent cast, was chosen as a secondary insulating material around aluminum construction. As seen from Figure 3.4.1:

a) A top cover was introduced such that the porous medium can be compressed to assure there is no gas cap above it,

b) The injection well system is designed to allow injection of 100% steam through the total depth of the well. This is done by introducing a heater cartridge within an aluminum rod through which the steam flows, as shown in Figure 3.4.2,

c) The thermocouple and pressure tap locations are chosen as seen in Figure 3.4.3. Scanning will be done through the clear area, which has a width of 1.5 cm between these locations, and

d) The positioning tables were modified as seen in Figure 3.4.4. By using these two tables the 3-D model can be precisely positioned at the proper locations within the scan field.

A schematic flow diagram of the experimental apparatus can be seen in Figure 3.4.5. The set up consists of three parts: injection port, 3-D steam injection model, and production port. Each of these parts of the system are discussed next.

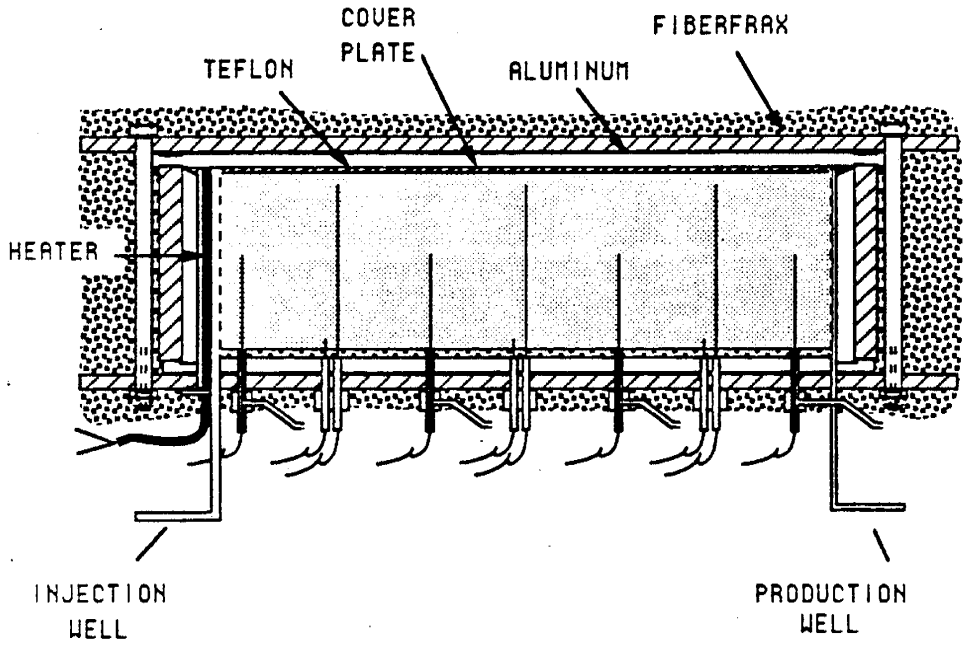

Figure 3.4.1 Injector-Producer Cross-section of the 3D Model

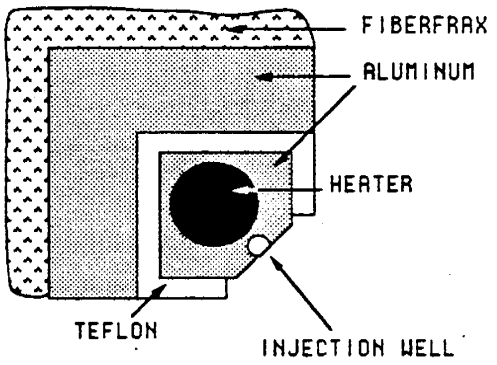

Figure 3.4.2 Cross-section of the Injection Well

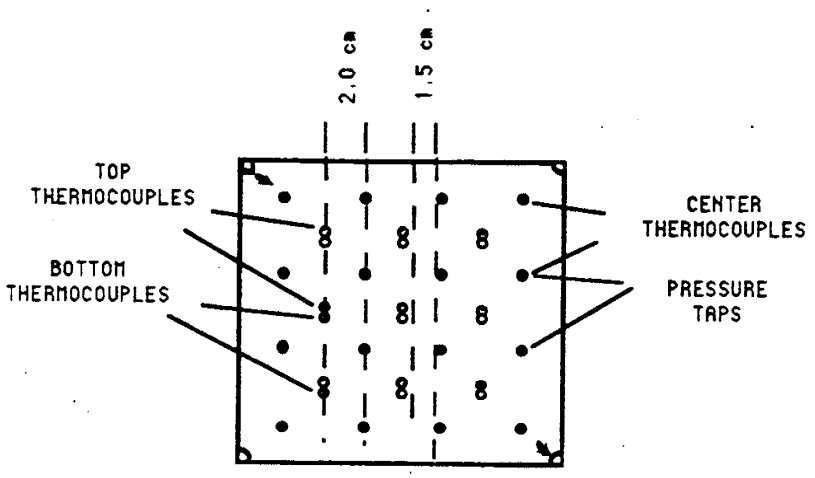

Figure 3.4.3 Thermocouple and Pressure Tap Locations in the 3D Model

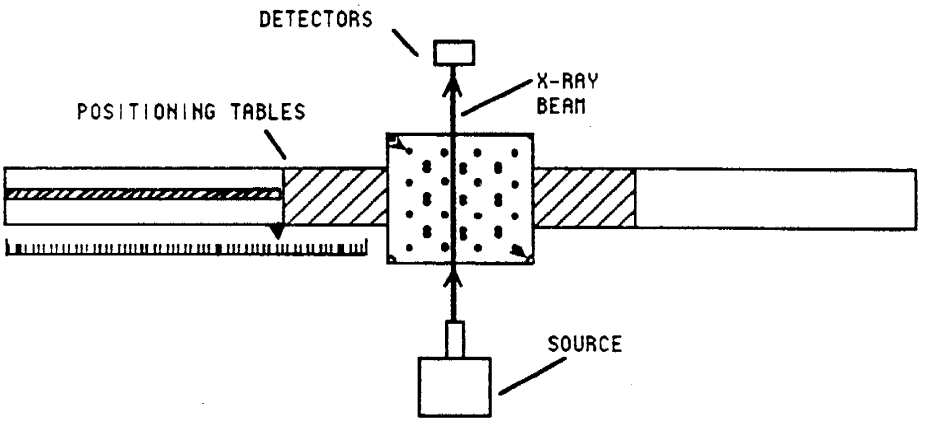

Figure 3.4.4 Positioning Tables

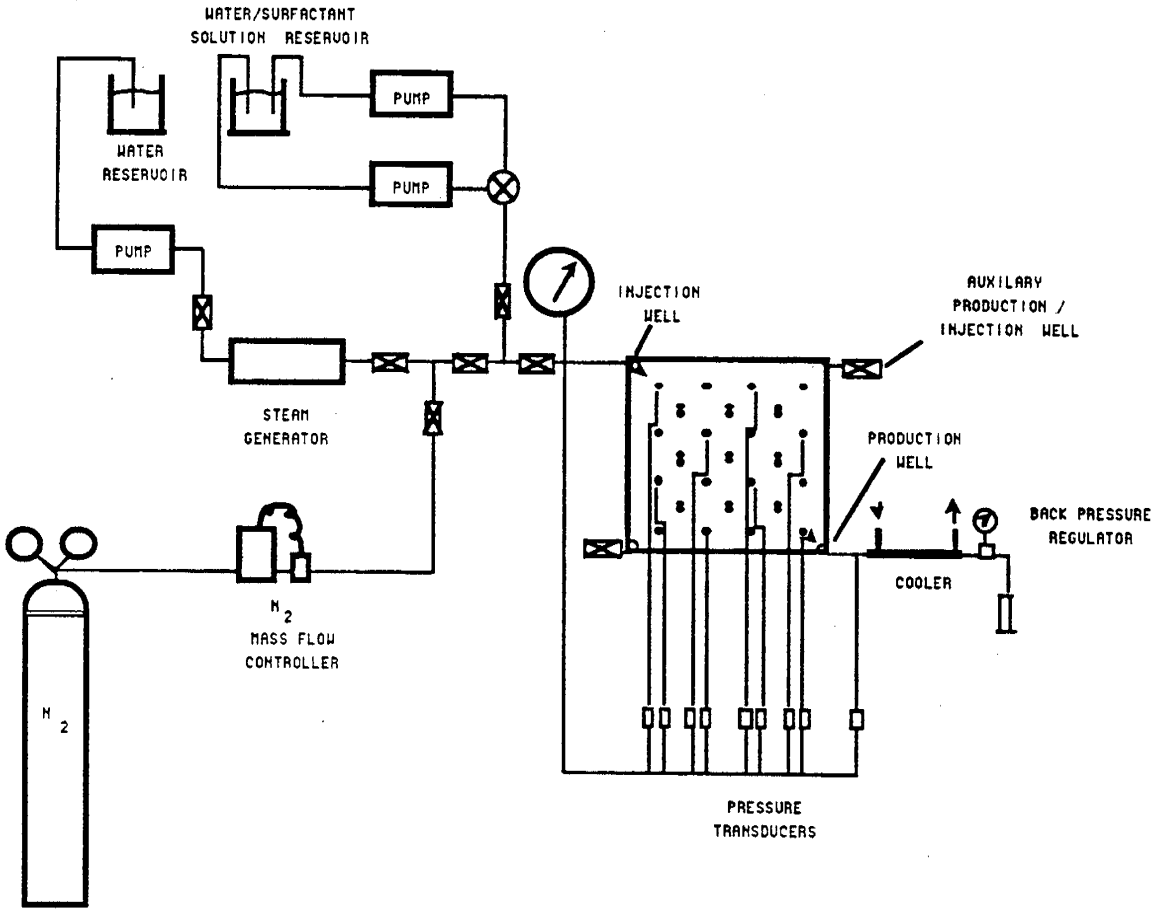

Figure 3.4.5 Schematic Flow Diagram of the 3D Laboratory Steam Injection Model

Injection Port

In the injection port there are two liquid chromatography pumps. One of them is to be used to inject water or surfactant solution and the other one is to feed the steam generator with distilled water. There is also a gas mass flow controller which will be used to inject nitrogen at a constant rate into the model during the experiments.

3-D Steam Injection Model

The 3-D steam injection model has a total of 38 J-type thermocouples which are located at three different levels in the model. Sixteen of them, center thermocouples, are placed at a level of 1.5 in. from the bottom of the model. Eleven top and eleven bottom thermocouples are placed at 2.75 in. and 0.25 in. from the bottom respectively. Sixteen pressure taps (only eight of them are used during the experiments) are located at the same places as the center thermocouples.

Production Port

A back pressure regulator maintains a constant pressure at the producing corner of the model. A cooler is used to condense the produced steam.

3.4.3 PRELIMINARY SCANS

Some preliminary work was done to understand the saturation determination by CT scan. To do this the model was scanned under different combinations of scan speeds, photomultiplier and detector levels, scan modes and energy levels. These preliminary runs showed that CT scanning technology could be applied to petroleum recovery processes in the laboratory and add another analysis tool to the classical temperature-pressure monitoring during steam injection experiments. Figures 3.4.6 and 3.4.7 show sample scan pictures from these runs. In these figures the top one shows the model filled with dry sand and shows settling in the top portion of the model. The bottom one represents the same cross-section after adding more sand to the model and injecting water from the left hand side. According to the theory (Withjack, 1988), there must be a 200 CT unit difference between the dry sand and the wet sand. As can be seen this difference was verified in both attempts at two different energy levels. This showed that it would be possible to differentiate saturating fluids in the model by comparing their CT numbers as well as by comparing them visually.

As an addition to these preliminary scans of 3-D model, some calibration works were also performed. A linear model, 1 in. in diameter and 24 in. in length, was used for that purpose. The model was filled with Berea sand and saturated with water, then NaI solutions at different saturations were injected to displace water. After reaching 100% NaI solution saturation scan pictures at six different locations along the model were taken. These pictures were compared later to see the difference between the average CT numbers as seen on Figure 3.4.8. As it can be seen from this figure there is a linear relationship between the NaI solution concentration and average CT numbers such that by increasing the concentration, one can obtain the optimum contrast between the NaI solution and the distilled water. This property will be used in future experiments.

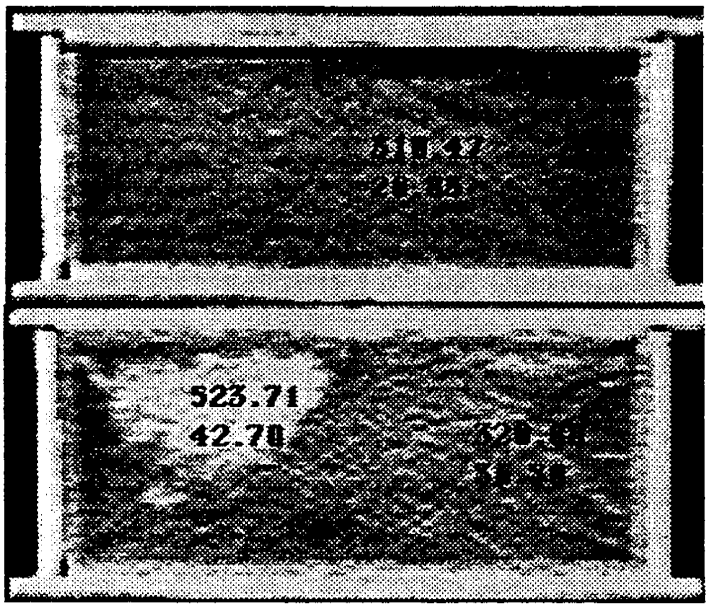

Figure 3.4.6 Scan Pictures of the 3D Model Before and After Water Injection (140 keV)

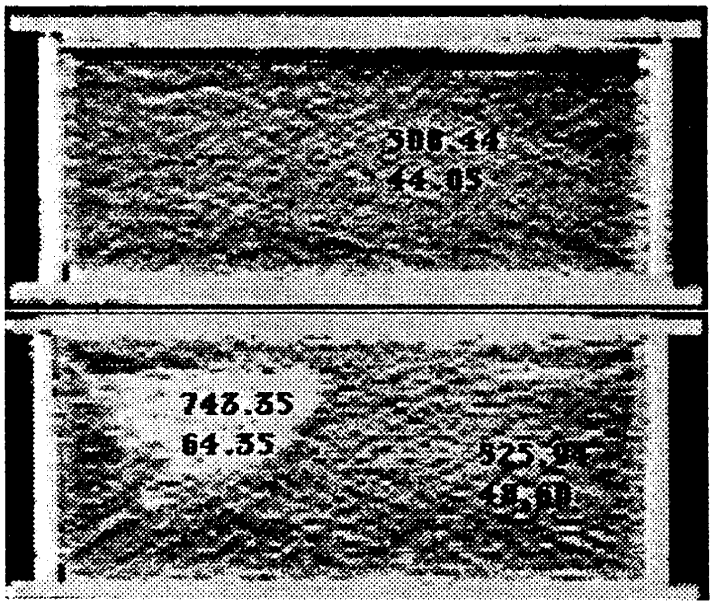

Figure 3.4.7 Scan Pictures of the 3D Model Before and After Water Injection (100 keV)

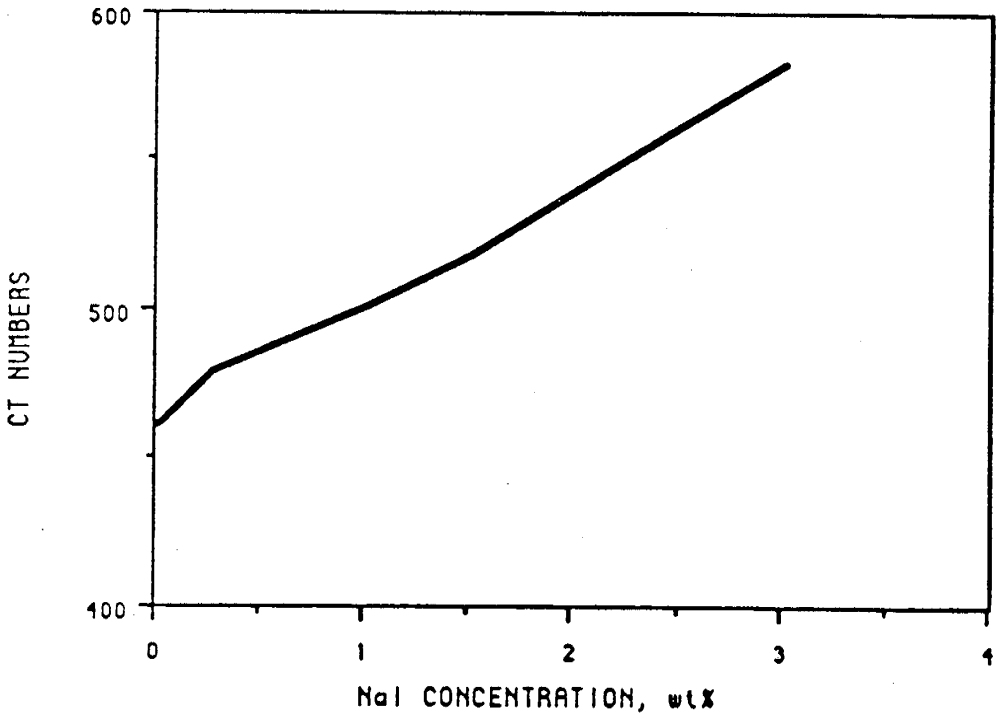

Figure 3.4.8 Change of CT Numbers with NaI Concentration

3.4.4. DETERMINATION OF SATURATIONS

Saturations in the model will be determined by using the basic principles of Computerized Tomography (CT). Basically CT measures the linear attenuation coefficients across an object within the x-ray scanning field. The linear attenuation coefficient which is dependent upon the nature of the attenuating material is defined by Beer's law:

$$I / I_s = e^{-\mu x} \tag{3.4.1}$$

where:

I_s = the source x-ray intensity
I = the intensity measured by the detectors
μ = the attenuation coefficient, and
x = the thickness of the material

The linear attenuation coefficient depends on electron density (bulk density), atomic number and energy level. The linear attenuation coefficient is expressed as (Evans, 1955):

$$\mu = \rho \left(a + bZ^{3.8} / E^{3.2} \right) \tag{3.4.2}$$

where:

ρ = electron density
a = Klein-Nishina coefficient
b = 9.8×10^{-24}
E = energy level in kV, and
Z = atomic number

If the subject contains a mixture of components, the overall mass attenuation coefficient of the mixture will be (Vinegar and Wellington, 1987):

$$\mu_{mix} = \sum_i \mu_i \, S_i \tag{3.4.3}$$

If the components are not miscible, S_i is the saturation of the phase i, that is, water, oil or gas in our case.

Since in petroleum recovery problems one mostly deals with 2 or 3 phase systems, Equation 3.4.3 is applicable to petroleum engineering research without changing the basic CT technology. The only requirement here is to calibrate it for different phases. For two-phase saturation Equation 3.4.3 can be written as:

$$\mu = \mu_1 S_1 + \mu_2 S_2 \tag{3.4.4}$$

Here μ_1 and μ_2 are the attenuation coefficients for the medium fully saturated with phase 1 and 2 respectively and since they are known from the calibration scans, using

$$S_1 + S_2 = 1 \tag{3.4.5}$$

one can easily calculate S_1 and S_2.

This analysis can be expanded to three-phase saturation. The additional unknown requires an additional, independent measurement. This is done by scanning at a different energy level. Supposing the phases are water (w), oil (o), and gas (g), the system of equations will then become:

$$S_o + S_w + S_g = 1 \tag{3.4.6}$$

$$\mu_1 = \mu_{o1} S_o + \mu_{w1} S_w + \mu_{g1} S_g \tag{3.4.7}$$

at energy level 1, and

$$\mu_2 = \mu_{o2} S_o + \mu_{w2} S_w + \mu_{g2} + S_g \tag{3.4.8}$$

at energy level 2.

The CT output is not the classic linear attenuation coefficient. Instead, the CT computer converts attenuation coefficients into corresponding numerical values in units of Hounsfields (H or CT numbers). The scale is usually defined by two points: water = 0 and air = - 1000 and behaves as shown in Figure 3.4.9. CT number is defined as:

$$N_{CT} = K\ (\mu - \mu_b)/\mu_b \tag{3.4.9}$$

where:

μ = attenuation coefficient of material occupying volume element (voxel) during scan
μ_b = coefficient for reference material, and
K = constant (typically K = 1000)

During the experiments CT computer will compute the CT numbers for each voxel in the scanning area. The voxel has a volume of $0.5 \times 0.5 \times 5$ mm^3. Then the corresponding saturations for every voxel will be calculated by replacing attenuation coefficients in previous equations and using Equations 3.4.4 through 3.4.8.

3.4.5 A TRIAL RUN: CO_2 INJECTION

We decided to make a trial run to see the possible difficulties before making a real steam injection run. In order to do this a immiscible CO_2 injection run was conducted. The experimental procedure is given below.

Experimental Procedure:

1. saturate with distilled water
2. scan each section shown on Figure 3.4.10
3. start CO_2 injection
4. scan each section every 12 minutes
5. process scan pictures for each section at selected times of injection
6. compare scan pictures

The scan pictures at selected times of CO_2 injection at every sections of the model are given in Figures 3.4.11-14. As it can be seen from these figures, injected CO_2 (light color)

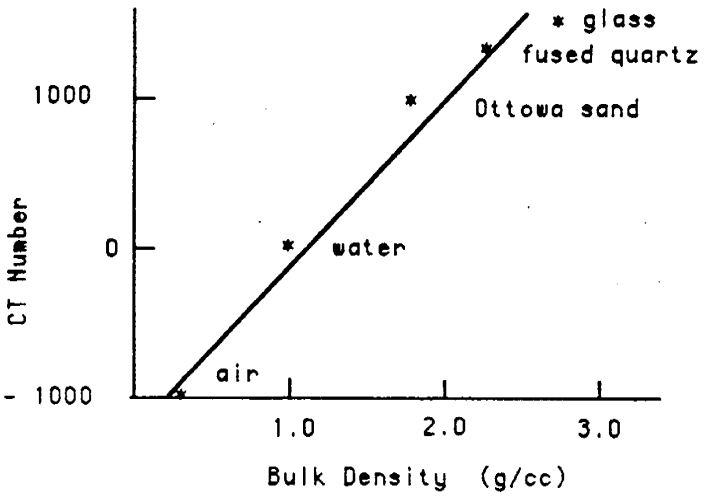

Figure 3.4.9 Effect of Density on CT Number

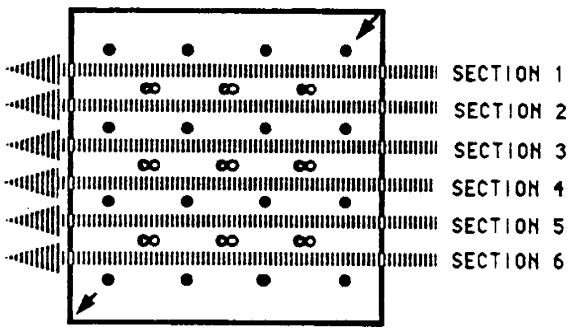

Figure 3.4.10 CT Scanning Sections Through the 3D Model

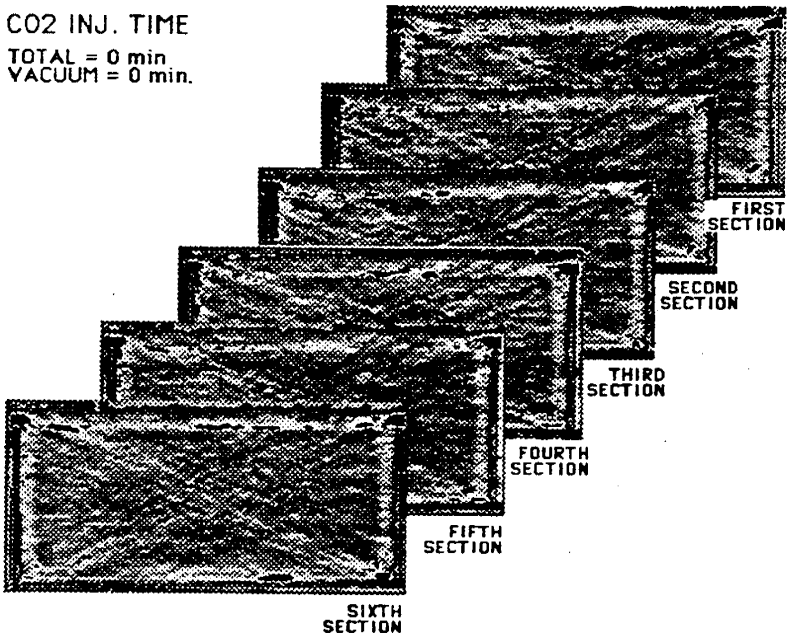

Figure 3.4.11 Saturation Distribution at Each Scanning Section of the 3D Model Before CO_2 Injection Started

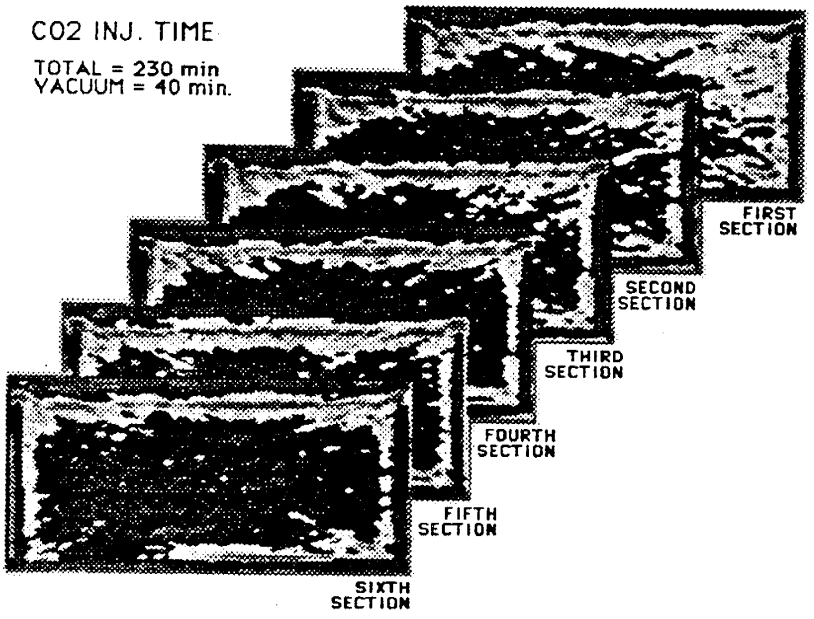

Figure 3.4.12 Saturation Distribution at Each Scanning Section of the 3D Model After 330 min. of CO_2 Injection

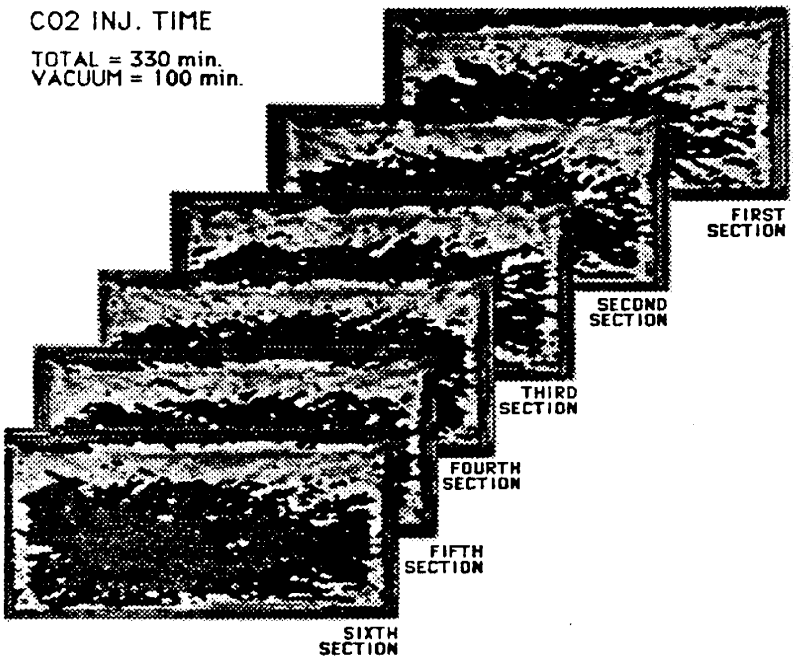

Figure 3.4.13 Saturation Distribution at Each Scanning Section of the 3D Model After 330 min. of CO_2 Injection

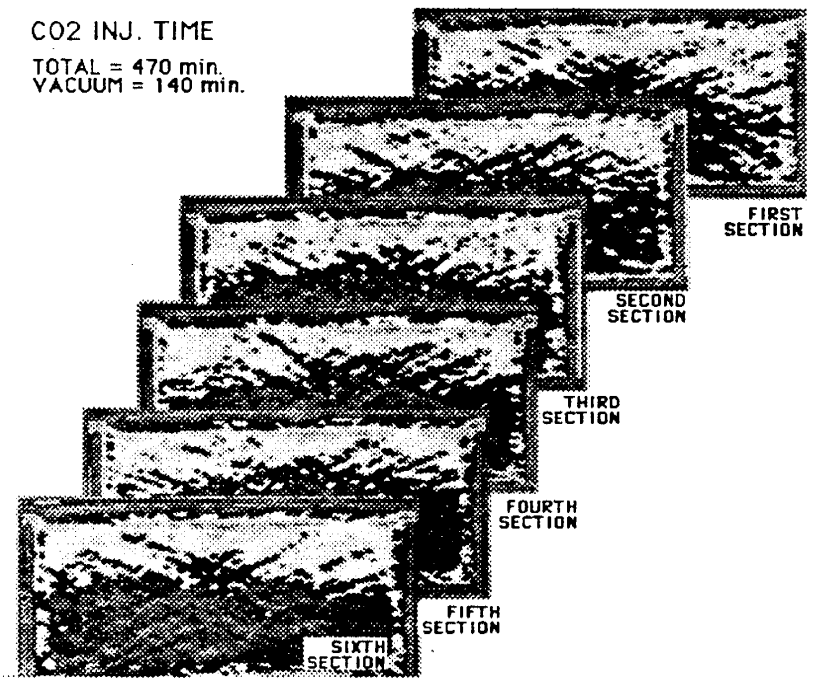

Figure 3.4.14 Saturation Distribution at Each Scanning Section of the 3D Model After 470 min. of CO_2 Injection

tried to reach the production corner from the top of the model. After breakthrough it started displacing water from the rest of the model behaving as a chest. Although these pictures are raw and unprocessed it is very easy to follow the propagation of CO_2 visually. In future work these pictures will be processed and the noise strikes from corner to corner at each picture will be taken care of by subtraction.

3.4.6 FUTURE WORK

First of all some calibration experiments will be carried out according to the following procedure:

1. The 3-D model will be scanned dry,
2. The 3-D model will be saturated with water,
3. The initial saturation distribution will be scanned. Water injection will be continued until 100% water saturation is achieved.
4. Continuous steam injection will be started, during which:
   a) temperature and pressure data will be taken at one minute intervals,
   b) scan data will be recorded every 12 minutes at each of the 6 sections at two different energy levels,
   c) production will be measured to make overall material balance calculations.
5. The scan data will be analyzed to calibrate CT numbers at two different energy levels, for air, water and steam saturated sand. After measuring these CT numbers, the future scan pictures and CT values can be easily analyzed in terms of saturations within the model at a given time.
6. Steam and steam-foam injection experiments will be run in water saturated model.

NUMERICAL SIMULATION OF WELL-TO-WELL TRACER FLOW TEST AT NONUNITY MOBILITY RATIO

by

D.A. Alvarado

Stanford University
Petroleum Research Institute
Stanford, California

4.2 NUMERICAL SIMULATION OF WELL-TO-WELL TRACER FLOW TEST AT NONUNITY MOBILITY RATIO
(D. A. Alvarado)

A numerical simulation of tracer flow was carried out for a nonunity mobility ratio flood in a five-spot pattern. The UTCHEM simulator from the University of Texas at Austin was used to model physical dispersion phenomena and, also, to study numerical dispersion phenomena associated with the finite difference solution of the convection-dispersion equation. New correlations were found which relate some properties of the dimensionless tracer concentration after breakthrough for a tracer slug test in a nonunit mobility ratio displacement, to the same properties defined for the unit mobility case. Also for the zero dispersion case, a new correlation was developed for the continuous tracer injection at favorable mobility ratios. We have found that the numerical solution obtained by using UTCHEM is sensitive to the values of cell Peclet number, i.e., the ratio of the grid size to the dispersity constant. From our results we can conclude that, for cell Peclet number greater than 8.33, the numerical solution based on Leonard's third order convective difference scheme as used in UTCHEM does not give an acceptable answer to the test problem. Hence, we decided to perform our computations for cell Peclet number lower than or equal to 8.33. More research has to be done with UTCHEM to investigate the behavior of this model under mesh refining and time step considerations, to study other mobility ratio injection conditions, and to consider other patterns of wells.

4.2.1 OBJECTIVES OF THE STUDY

In any enhanced oil recovery (EOR) project, it is important to detect reservoir heterogeneities, for the overall efficiency of the project depends on the nature of the flow from well to well. So, there is a need for a detailed description of the reservoir to be exploited. Traditional studies include geology, geophysics, coring, well logging and single well testing to help define reservoirs and their heterogeneities. Two additional types of test which have become popular in recent years are well-to-well transient pressure tests and well-to-well tracer tests. These two tests complement each other, for they measure different characteristics. The pressure transient test tends to measure average properties between wells. The tracer tests have the ability to indicate the extent of heterogeneity that exists in the region tested.

When well-to-well tracer tests are used, usually a small slug of tracer is injected and this in turn is followed by tracer free fluid. Several methods have been presented in the literature (Yuen et al. 1979; Brigham and Abbaszadeh-Dehghani, 1987; and Mishra, 1987) to analyze the tracer concentration data recorded at the production well, in order to obtain qualitative and quantitative information about the characteristics of the reservoir region tested. Indeed, the main objective of these studies was to examine the sensitivity of test responses to the presence of heterogeneity and to extract layer parameters from an overall tracer breakthrough profiles.

In most cases, quantitative analysis of well-to-well tracer tests has been performed for a multilayer five-spot pattern. However, Abbaszadeh-Dehghani and Brigham (1982) developed equations for computing tracer breakthrough curves in several flooding patterns (five-spot, direct drive line, staggered line drive and seven-spot) by analytically formulating tracer slug concentration in a general streamtube. Since the exact equations for streamlines of repeated patterns are known (Abbaszadeh-Dehghani and Brigham, 1982; Aronosky and Heller, 1957; and Brigham and Abbaszadeh-Dehghani 1987) the velocity of the fluid at any point in the system can be calculated by differentiating the streamline functions and by using the Cauchy-Riemann relationships. At any injected pore volume of displacing fluid, the production well concentration is the sum of concentrations from the streamtubes, which are computed at the production well. To simplify the analysis, tracer breakthrough curves for different patterns were correlated into a single set of curves. The five-spot system was chosen as a reference for correlation. Finally, a computer program was developed, based on a method presented by

Yuen, et al. (1979) to decompose a tracer profile form a multilayered reservoir into several responses from individual layers.

In the study of Abbaszadeh-Dehghani and Brigham (1982), the theory and analysis of tracer flow behavior was formulated on the assumption of unit mobility ratio, and exact analytical equations were obtained in the form of elliptic integrals which provided breakthrough curves for the different patterns. An attempt was made to define pattern breakthrough curves analytically for nonunit mobility ratio in a developed five-spot, but the results obtained contradicted experimental observations. This was because of the unrealistic assumption that streamlines are independent of the mobility ratio.

Because the streamtube procedure can not generate correct breakthrough curves at nonunity mobility ratio and because there is a need to describe tracer flow in such systems, we have pursued a numerical study of interwell tracer tests when mobility ratio contrast exists. Along the lines of the work of Abbaszadeh-Dehghani and Brigham (1982), a correlation will be sought between the curves from several patterns and mobility ratios. Proper numerical modeling is necessary for an accurate representation of these processes. Of importance are some features in the formulation of the problem, such as numerical dispersion and grid orientation effect associated with finite difference solutions of the convection-dispersion equation.

To reach these objectives, we decided to test the University of Texas UTCHEM simulator (User's Guide for UTCHEM-V.22, 1989). UTCHEM is a three-dimensional compositional chemical flooding simulator, adapted to describe tracer flow in different patterns, and also to control numerical dispersion and grid orientation effects. Several differencing schemes are available in the simulator. Of particular interest is a third-order scheme based on Leonard's method.

In the simulation of tracer studies conducted before and during many of the EOR projects for reservoir characterization, one of the main objectives is to determine the level of physical dispersion and heterogeneity. In numerical reservoir simulation, however, artificial numerical dispersion can further smear concentration fronts by increasing the level of dispersion. This numerical dispersion results in inaccurate predictions of both concentrations and breakthrough times. Therefore, accurate simulation of physical processes involved in EOR requires that numerical dispersion be essentially eliminated.

We will not describe the UTCHEM simulator in detail. The main features of this program have been the subject of several papers and theses (Datta Gupta, 1985; Datta Gupta et al., 1986; Descant III, 1989; and Saad, 1989). We will give some information about the principal characteristics of this simulator. Because of the need to simulate mixing phenomena, and, therefore, to minimize numerical dispersion, the four convective differencing schemes available in UTCHEM will be reviewed briefly.

Since it is possible to consider many recovery phenomena in the program, UTCHEM has many input options to specify which phenomena will be included. Therefore, one of the main difficulties for a user of UTCHEM is to define the input data choice correctly. Four input data files are needed. The first file is used to describe the run. The second file concerns the grid characteristics, initial conditions, and the output options. Injection/production data are specified in the third file, while the fourth one is related to physical properties.

The main assumptions made in UTCHEM are: isothermal reservoir, slightly compressible fluid and solid, Darcy's law applies, thermodynamic equilibrium, dispersion follows Fick's law for multiphase flow, and surfactants and polymer are treated as monospecies without a molecular weight distribution.

The derivation of the conservation equations and the slightly compressible formulation of the pressure equation are given in detail by Saad (1989) but some of the more important concepts on the mixing equations are reviewed here.

Most current reservoir simulators use single point upstream weighting to approximate the first order derivative of the convection term in the equations. This method has a first order local truncation error, and the global truncation error of an algorithm using this differencing

operator is also first order. This method suffers from artificial numerical dispersion and the results are implemented by grid orientation. This method is stable; furthermore, it can be cause dispersion that is considerably larger than the physical dispersion, leading to inaccurate results. For convection dominated flow, at high Peclet number, the hyperbolic nature of the equations produces oscillatory solutions.

A second order explicit method, proposed by Chaudhari and implemented in UTCHEM produces accurate results for chemical flooding applications when the cell Peclet number is kept below two (Saad, 1989); this is, unfortunately, a limiting factor in large scale or convection dominated applications. At low cell Peclet numbers, the two point upstream weighting method produces more accurate results than single point upstream weighting; however, at higher cell Peclet numbers (convection dominated flows), it too produces inaccurate results (Saad, 1989).

A third order convective differencing scheme based on Leonard's method is especially suited for convection-dominated flow problems. This method results in a minimal increase in storage or computation time per time step per grid block compared to the lower order methods. This method is referred to as the higher order method in this work.

The details on the finite difference operators and its implementation in UTCHEM are discussed thoroughly by Saad (1989).

4.2.2 RESULTS AND DISCUSSION

We have been using UTCHEM-V-4.22 released on September 1989. The first step of our research consisted of a learning period to run the simulators. A good description of how to deal with the input data is given in the User's Guide for UTCHEM-V-4.22 (1989). Although, the input information is well documented, the output information is poorly commented. The author is in the process of writing a summary about the characteristics of the output files.

Next, UTCHEM-V-4.22 was validated for one dimensional miscible displacements (tracer in aqueous phase). Figure 4.2.1 shows a one-dimensional problem. In this case we considered a linear reservoir initially saturated with water, and tracer injection is at unit mobility ratio. We used constant viscosity polymer as a tracer and the Leonard's third order scheme was used. Since we assumed zero physical dispersion, the Peclet number is infinite, and we have a purely convective displacement. The analytical solution to this problem is the unit step function. As can be seen from Figure 4.2.1, the solution oscillates after breakthrough.

Figure 4.2.2 shows dimensionless tracer concentrations for Leonard's third order scheme together with those of single-point upstream weighting, two-point upstream weighting and Chaudhari's method for a Peclet number of 1,000 (cell Peclet number, $P_\Delta = 10$). The agreement between the analytical solution and the higher order method for this convection dominated test problem is remarkable, especially when compared with the diffused solution of single-point upstream weighting and the oscillatory nature of the solution using Chaudhari's dispersion control.

At lower cell Peclet numbers, Chaudhari's method and two-point upstream weighting will also give an accurate solution to the model problem (Chaudhari, 1971; Saad, 1989). This illustrates that, for the model problem and the same degree of accuracy using the higher order method requires a much lower level of grid refinement than the two-point upstream weighting or Chaudhari's method. On the other hand, at a large cell Peclet number, the higher order method will also oscillate and the inaccuracies reappear. This is seen in Figure 4.2.4 which compares the higher order method and the exact solution at Peclet number of 10,000 ($P_\Delta = 100$).

Figure 4.2.3 presents a graph of normalized concentration as a function of normalized distance, for the analytical and numerical solutions for a linear reservoir. Initially, we have only water in the reservoir and we are injecting a tracer solution of the same mobility as the

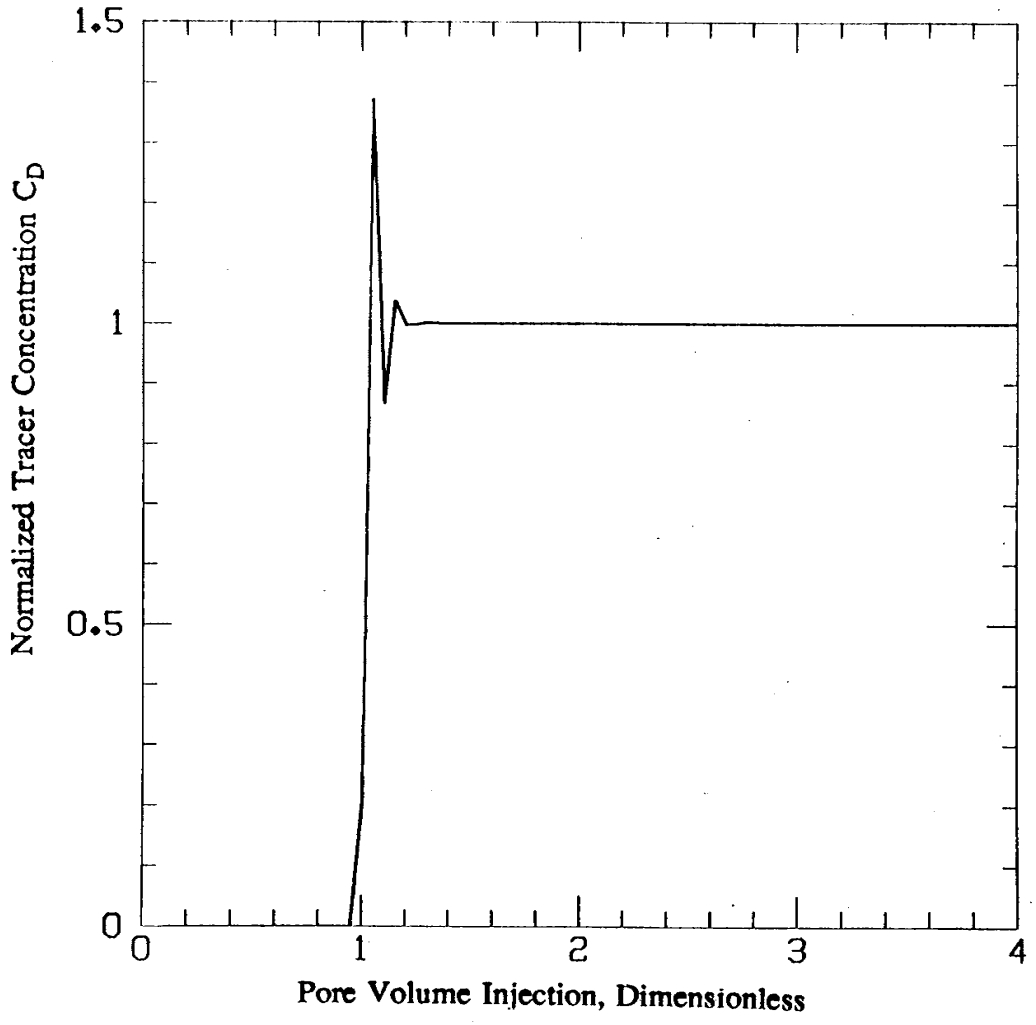

Figure 4.2.1 Tracer Concentration as a Function of Pore Volume Injected, 1 Dimension Case, Zero Physical Dispersion. Leonard's Method.

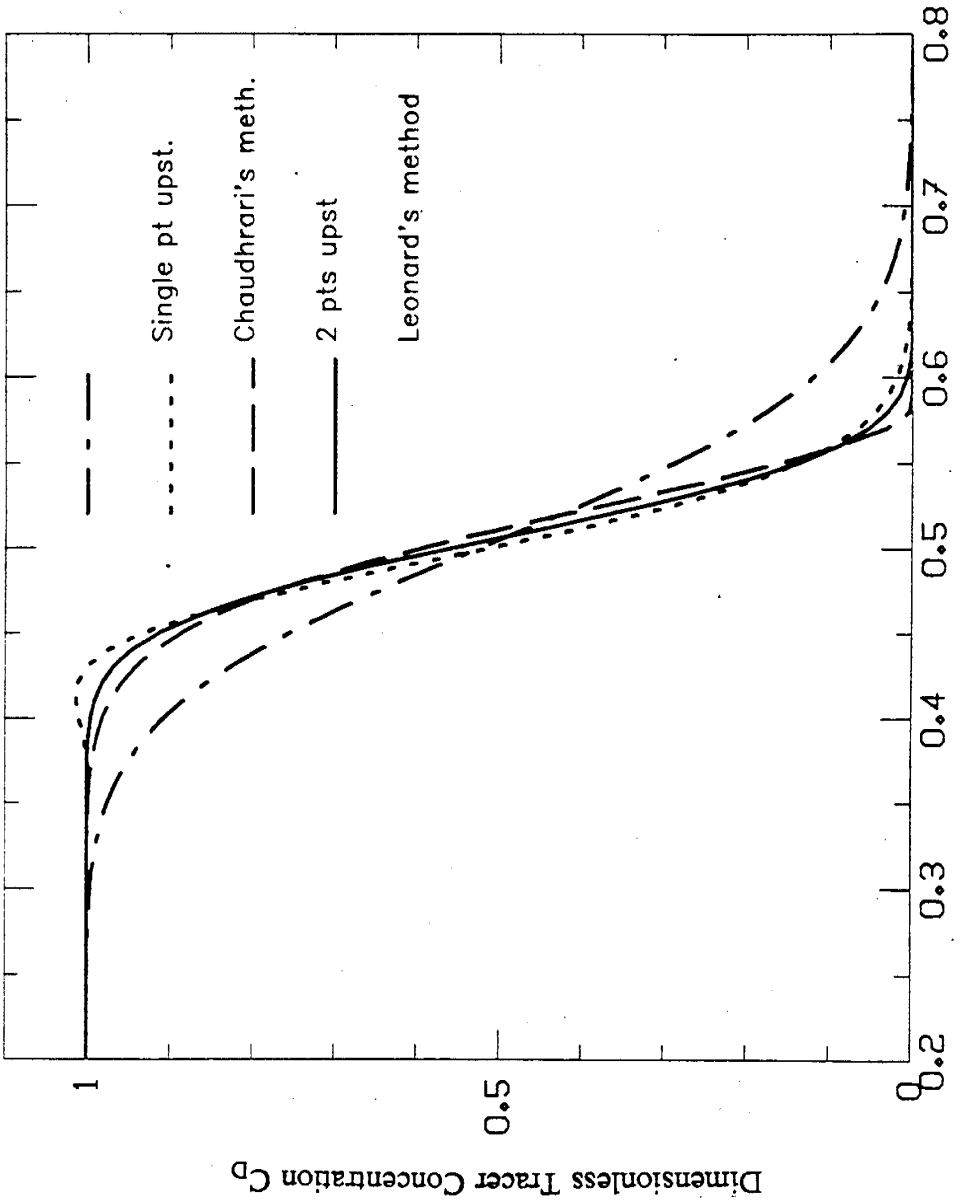

Figure 4.2.2 Tracer Concentration vs Dimensionless Distance Showing Numerical Dispersion. 0.5 Pore Volume Injected. Cell Peclet Number, $P_\Delta = 10$. $\alpha_L = 0.01$ ft.

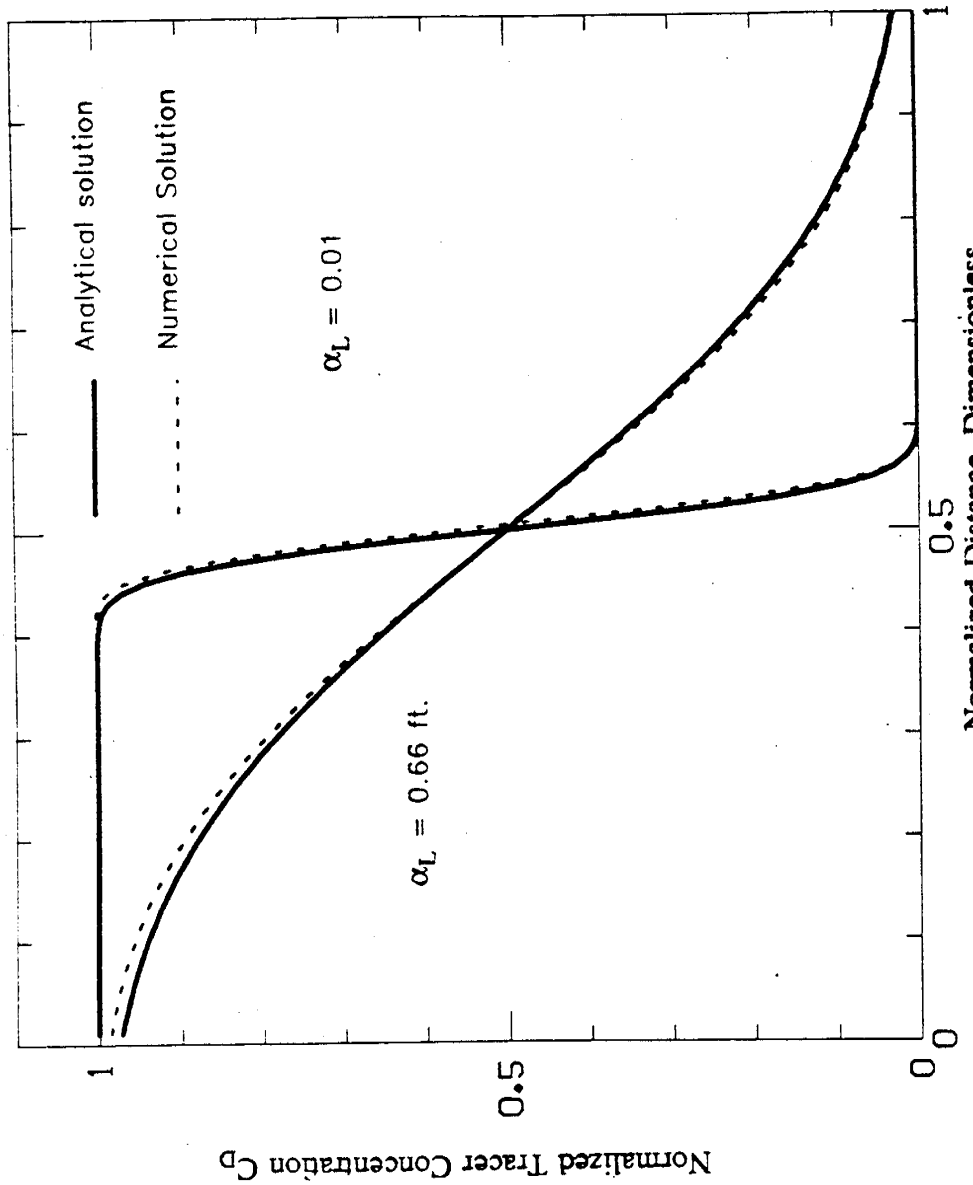

Figure 4.2.3 Comparison of the Numerical Solution with the Analytical Solution for Cell Peclet Number of 0.15 (α_L=0.66) and for Cell Peclet Number of 10 (α_L=0.01). Leonard's Method.

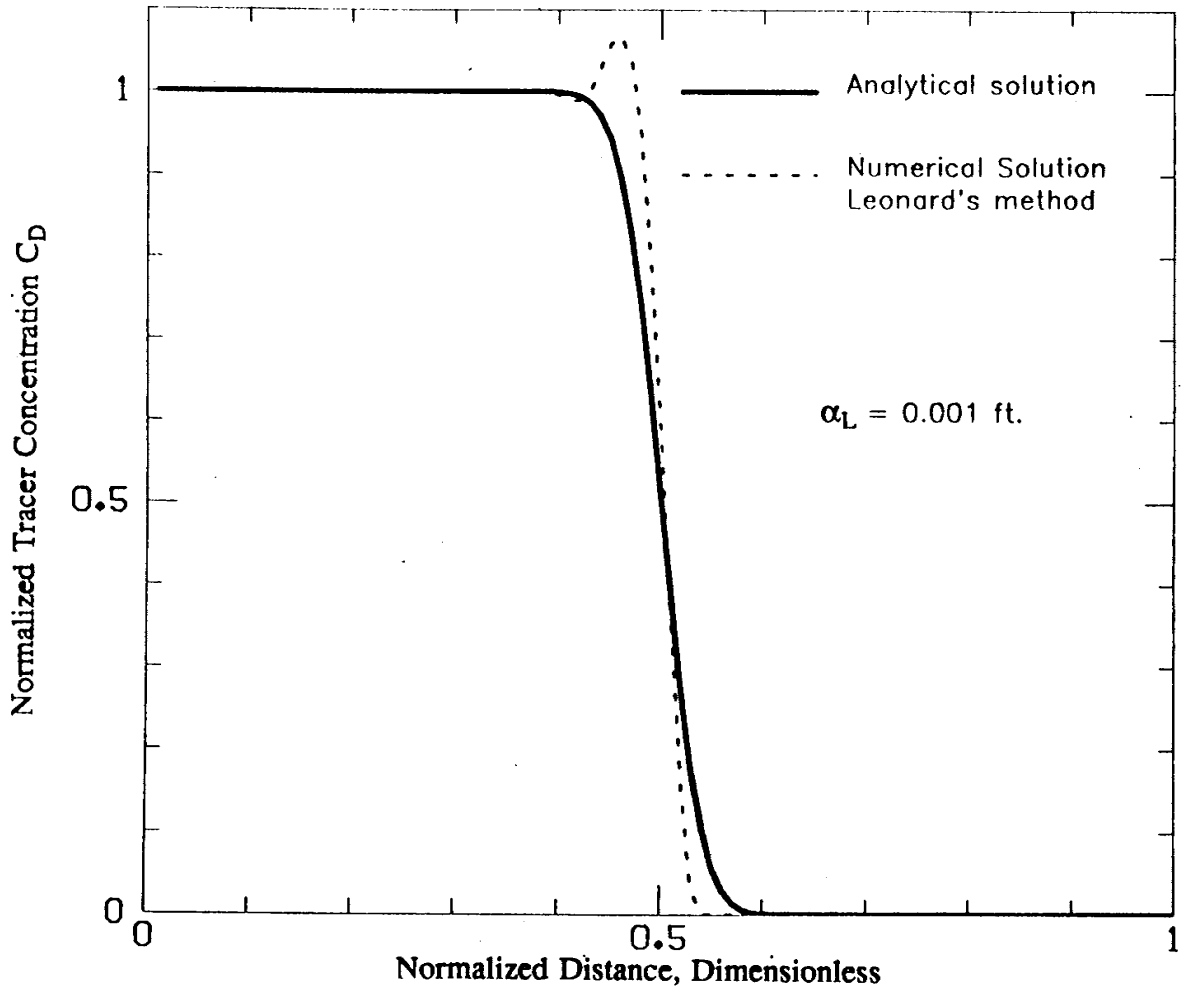

Figure 4.2.4 Comparison of the Numerical Solution Using the Higher Order Method (Leonard's method) with the Analytical Solution. Cell Peclet Number of 100. One Dimension. PV Injected=0.5.

initial fluids in the reservoir at constant flow rate. Two different values of the dispersion constant were considered α_L = 0.66 ft and α_L = 0.01 ft. As can be seen in Figure 4.2.3, the agreement between both solutions is adequate.

Next, we attempted to use UTCHEM to describe the tracer flow in a developed five-spot pattern. A unit symmetry area was chosen as a physical domain, the distance between like wells is 330 ft, so the unit symmetric area is a 165 ft square. Other data used are shown in Table 4.2.1.

Figure 4.2.5 shows a comparison of the numerical solutions for different methods of dispersion control in the five-spot pattern. We have plotted the normalized concentration as a function of the pore volume injection for zero dispersion. The injection rate is constant and the fluid injected is composed of water plus tracer. The mobility ratio of the displacing fluids to the displaced fluids is equal to one. Note that Chaudharis' method oscillates around the analytical solution. The single point upstream method and the two point upstream method both show appreciable differences from the analytical solution and from experimental results at, and shortly after breakthrough. The calculated pore volumes injected at breakthrough. are lower than the true value. Later, the numerical solutions converge to the analytical solution. The differences shortly after the breakthrough are due to numerical dispersion. Remember that this is a pure convection problem; there is no physical dispersion. The method which appears to have the least numerical dispersion is the Leonard's third order method, so we used the Leonard's method as a method henceforth.

Figure 4.2.6 is a graph of dimensionless tracer concentration as a function of pore volume injected, for continuous injection of tracer solutions of different viscosities. We considered mobility ratios of 0.2, 0.5, 0.8 and 1, i.e., favorable mobility ratios.

Figure 4.2.7 shows the basic information at m = 0.2 presented on Figure 4.2.6, plus the extrapolation of the maximum slope straight line to the x axis (pore volume injected axis). Experimental values presented by Caudle and Witte (1959), were taken from Figure 4.12, page 87 of "Mechanics of Secondary Oil Recovery," by C.R. Smith (1975). Table 4.2.2 shows the comparison between those values. A maximum difference of 2% was found for the breakthrough obtained numerically. Based on this fact, we take the value of the extrapolated maximum slope curve, as the pore volume injected at breakthrough. A FORTRAN program was written which computes the maximum slope straight line tangent to the given concentration curve; and then from the tangent point; the intersection of this line at concentration on the x axis is taken to be the pore volume injected at breakthrough. Next, we use this point to correct the curve of concentration vs pore volume injected, by setting the breakthrough point as the first point, the second being the tangent point, and the other points after these points remained unchanged.

Figure 4.2.8 presents the correlation which was obtained when we plotted the displacing water cut, dimensionless continuous tracer injection concentration, as a function of the dimensionless pore volume function, $(V_{pD} - V_{PDbt})/(1 - V_{pDbt})$, previously used by other investigators (Morales, 1975; Morgan, 1977; and Abbaszadeh-Dehghani and Brigham, 1982). As we can see from this figure, it appears that all the curves for different mobilities of the displacing phase, collapse into a single curve. The values used of pore volume injected at breakthrough are shown on Table 4.2.2, as compared with those obtained from experimental tests.

Figure 4.2.9 shows a comparison of the results of analytical solution and numerical solution for different values of Peclet number (a/α_L ratio) for tracer flow in a homogeneous developed five-spot pattern at unit mobility ratio. In Figure 4.2.9, for Peclet number greater than 500, the numerical solution does not match the analytical solution. On the other hand, for a/α_L ratio values 500 or lower, the analytical and numerical solutions are much closer, with only slight differences. Based on this test, we decided to investigate further the tracer flow behavior for different mobility ratios at the leading slug interface, but only by using values of a/α_L ratios equal to or lower than 500.

Table 4.2.1 Reservoir Simulation Data for the Two Dimensional Developed Five-Spot Pattern Tracer Flow Problem

Tracer slug size, % PV	2.00
Longitudinal dispersion, ft.	0.066-3.30
Transverse dispersivity, ft.	0.00
Cell peclet number, dimensionless	1.66-83.3
a/ α_L, dimensionless	100-5000
Simulated area, ft.	165x165
Number of grid blocks	30x30x1
Grid sizes, ft.	
$\Delta x = \Delta y$	5.50
Δz	5.00

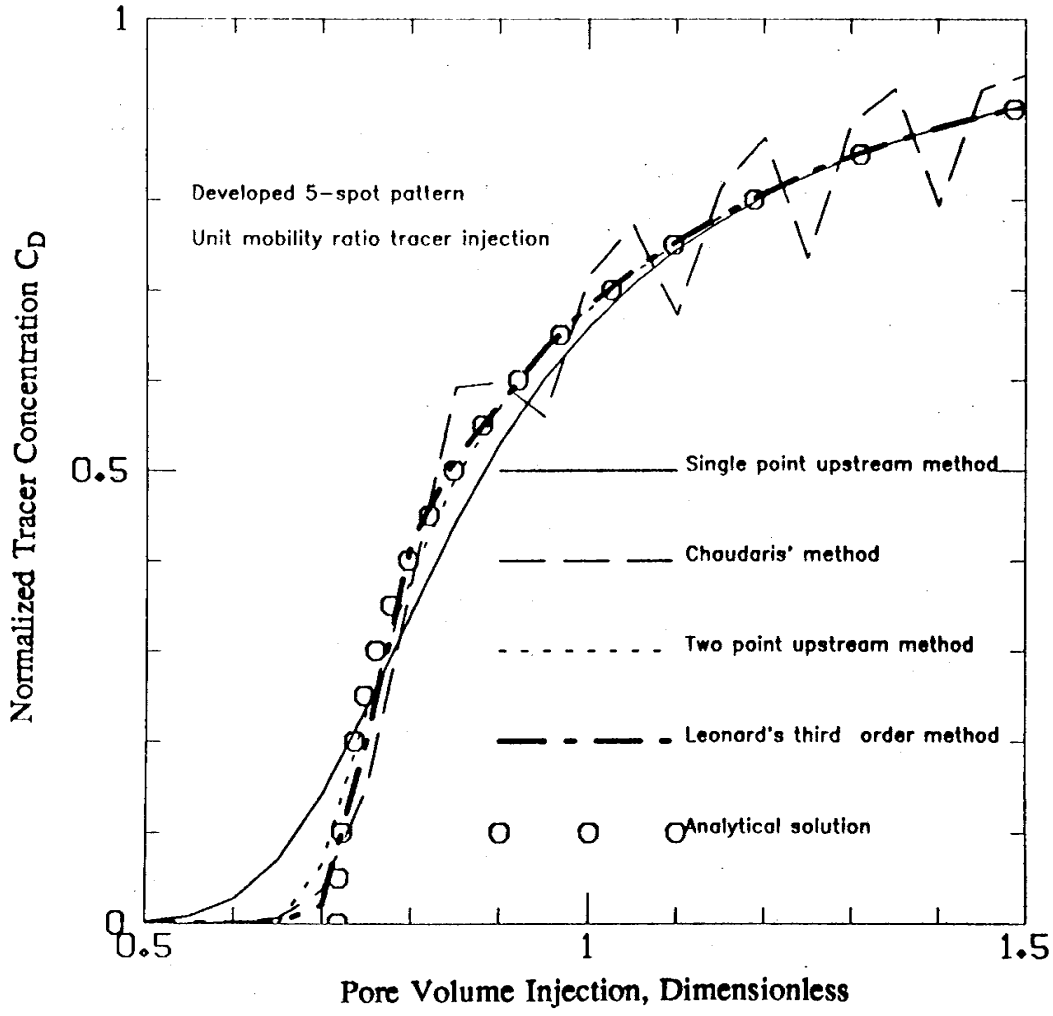

Figure 4.2.5 Comparison of Numerical Solutions by Using Different Methods of Numerical Dispersion Control for the Continuous Constant Rate Tracer Injection in a Developed Five-Spot Pattern.

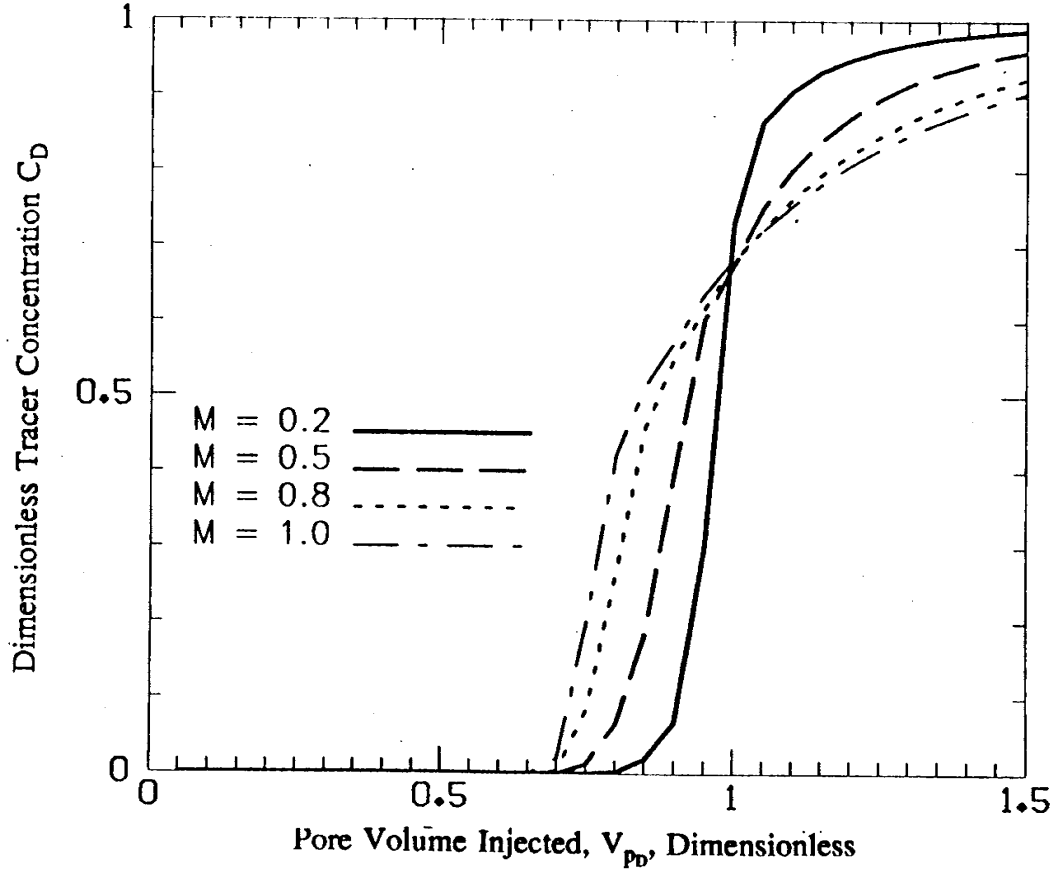

Figure 4.2.6 Tracer Concentration as a Function of Pore Volume Injected for Continuous Injection of a Tracer Slug. Mobility Ratios: 0.2 to 1.0. Leonard Method.

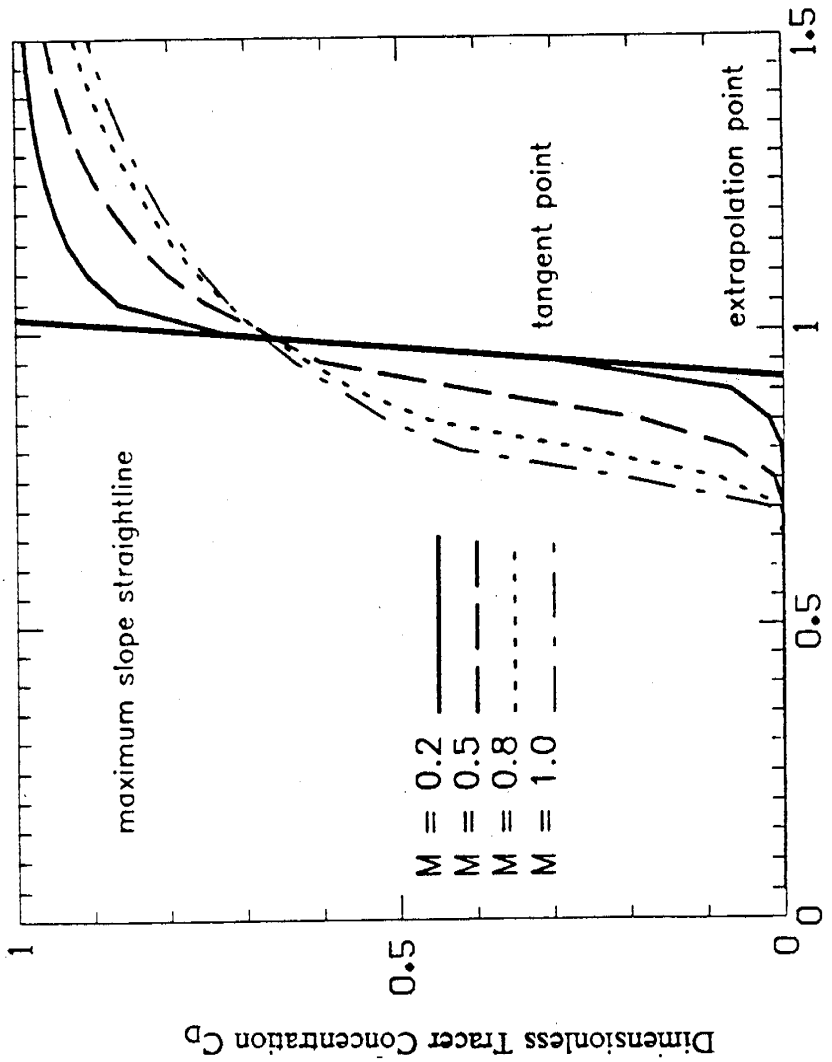

Figure 4.2.7 This is the Same Figure 4.2.6 Showing the Maximum Slope Straightline Tangent to the Breakthrough Concentration Curve Corresponding to Mobility Ratio Equal to 0.2. Zero Physical Dispersion.

Table 4.2.2 Comparison of Experimental Values of Pore Volume Injected at Breakthrough and Those Obtained by Extrapolating the Maximum Slope Straightline, for Different Values of Mobility Ratio

Mobility Ratio	Experimental (*) Value	Extrapolated Value
0.2	0.930	0.912
0.5	0.800	0.816
0.8	0.725	0.732
1.0	0.700	0.707

(*) After Caudle, B.H., and Witte, M.D., AIME Tech. Note 2047, J. Pet. Tech. (Dec. 1959) 63

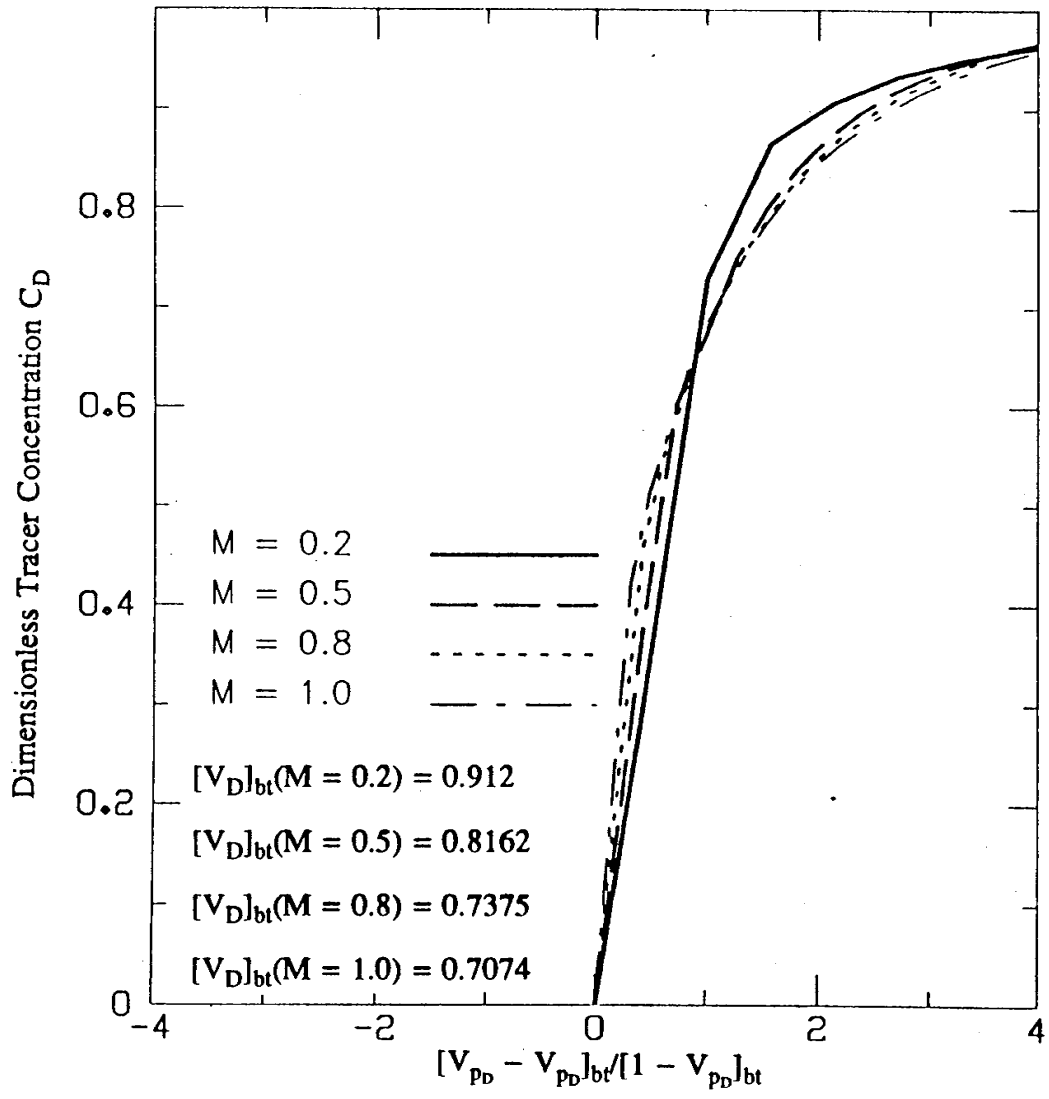

Figure 4.2.8 Dimensionless Tracer Concentration as a Function of the Dimensionless Pore Volume Function, (VpD-VpDbt)/(1.-VpDbt)

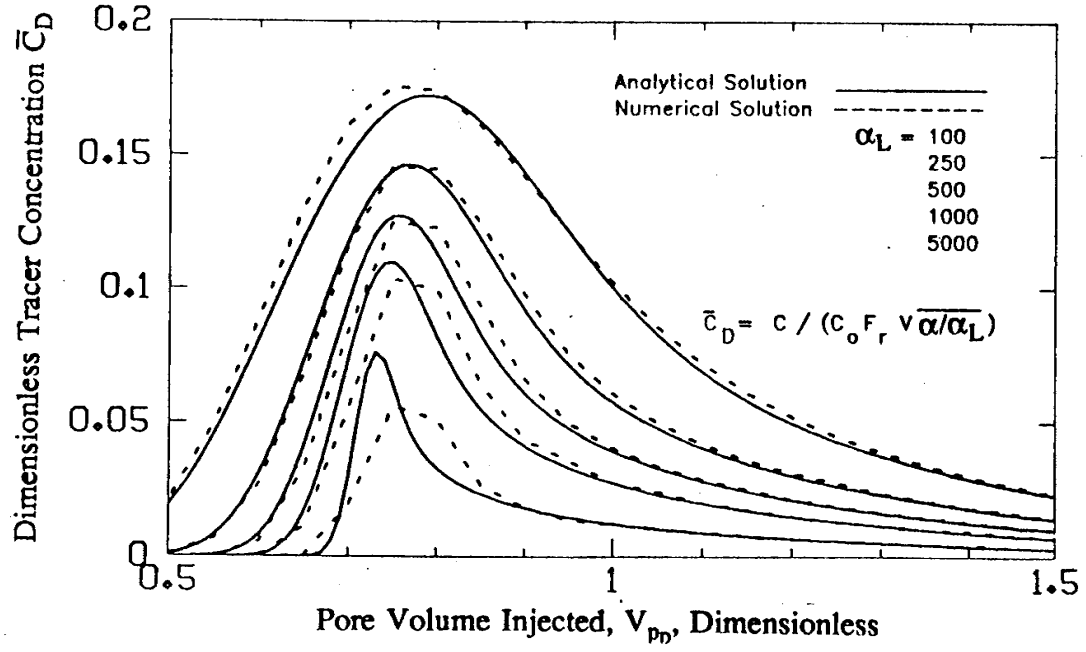

Figure 4.2.9 Comparison of the Results of Analytical Solution and Numerical Solution for Different Values of Peclet Number(a/α_L) for Tracer Flow in Homogeneous Five-Spot Pattern. Unit Mobility Ratio.

We try now to study the case of injecting tracer slug of different mobility ratios with respect to the initial fluid mobility. We consider only favorable mobility ratios, from 0.2 to 1. The tracer slug viscosity was varied by using polymer as a component in order to increase the viscosity of the slug. The mobility ratio of the interphase slug-injected fluid was kept equal to one.

Figures 4.2.10, 4.2.11 and 4.2.12 depict the dimensionless concentration, $\overline{C}_D$ (as defined by Abbaszadeh-Dehghani and Brigham, 1982), as a function of the pore volume injected, Vp_D for different values of the parameter a/α_L (100, 250 and 500). The three figures present some common features. First, for values of the mobility ratio greater than 0.50 (0.50 to 1.00) the peak concentration is approximately constant independent of the mobility ratio. For values of mobility ratios lower than 0.50 the peak height increased at higher mobility ratios. This means that if we are injecting a tracer slug with a mobility ratio lower than one, (favorable mobility ratio), but higher than 0.50 the peak concentration is approximately equal to the one for unit mobility ratio.

Figure 4.2.13 summarizes the peak height data of Figs. 4.2.10-4.2.12. This figure shows that the peak concentration, $\overline{C}_{D_{max}}$, is approximately constant for values of mobility between 0.5 and 1, and for mobility ratios lower than 0.5 the peak concentration increases slightly. Further research is required on this topic, because a mathematical analysis of the nature of this problem, indicates that the peak concentration height should increase as the mobility ratio is reduced. So, Figure 4.2.13 can be used to translate the results of a tracer test for favorable mobility ratios other than one to an equivalent developed five-spot pattern of unit mobility.

From Figures 4.2.10-4.2.12, we can see that the value of the pore volume injected V_{pD}, at the peak concentration is displaced to the right for the different mobility ratio considered with respect to the position of the peak concentration $\overline{C}_{D\,max}$ for the unit mobility ratio case. This effect was found for all of the a/α_L values studied. Figure 4.2.14 presents the pore volume injected at peak concentration, $V_{pD\,max}$ as a function of mobility ratio. By inspecting Figure 4.2.14, it appears that there is an approximately linear relationship between these variables. This means that the peak position of a given tracer slug test, could be translated into an equivalent developed five-spot pattern slug concentration, by applying Figure 4.2.14.

In summary, it appears that the variables we need in a slug tracer injection test for further calculations, i.e., the peak concentration, $\overline{C}_{D\,max}$, and the volumetric position at the peak, can be, in principle, translated into equivalent values to the unit mobility ratio injection condition. Thus, now, we can apply the procedure developed by Abbaszadeh-Dehghani and Brigham (1982) for analyzing a tracer injection test at a favorable mobility ratio.

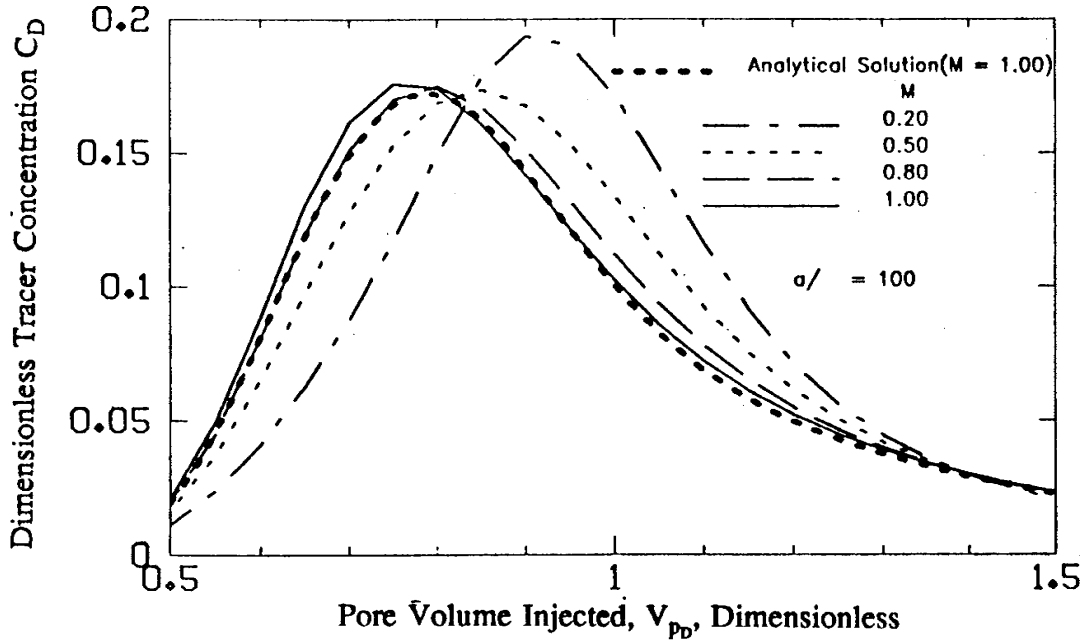

Figure 4.2.10 Dimensionless Slug Tracer Concentration, $\bar{C}_D$, as a Function of Pore Volume Injected, VpD, for Different Values of Mobility Ratio at the Front Interphase. a/α_L = 100.

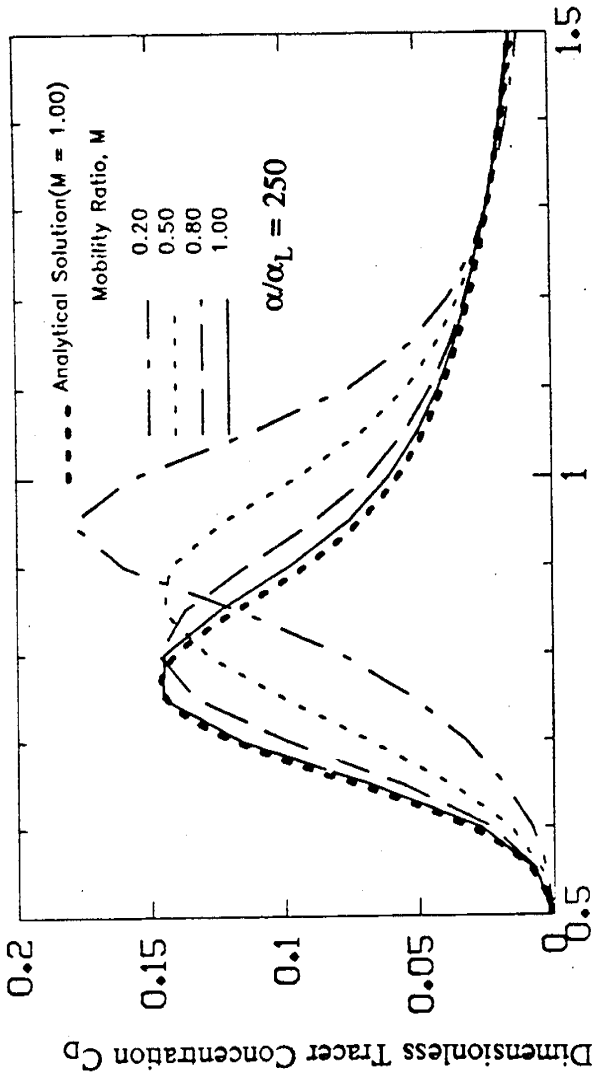

Figure 4.2.11 Dimensionless Slug Tracer Concentration, $\bar{C}_D$, as a Function of Pore Volume Injected, VpD, for Different Values of Mobility Ratio at the Front Interphase. a/α_L =250.

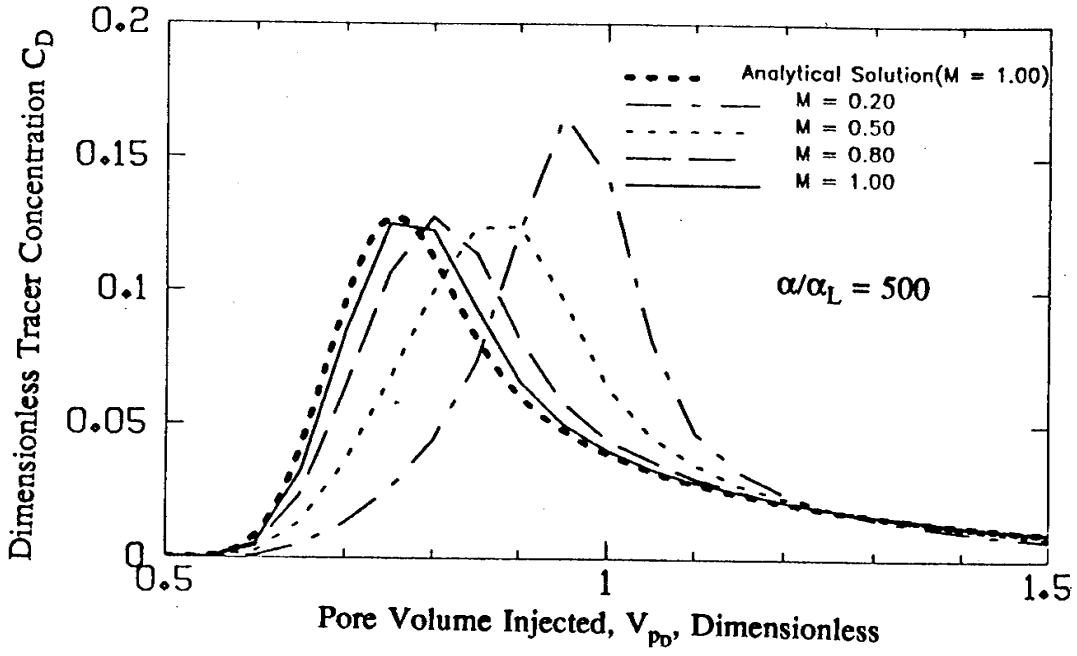

Figure 4.2.12 Dimensionless Slug Tracer Concentration, $\bar{C}_D$, as a Function of Pore Volume Injected, VpD, for Different Values of Mobility Ratio at the Front Interphase. a/α_L =500.

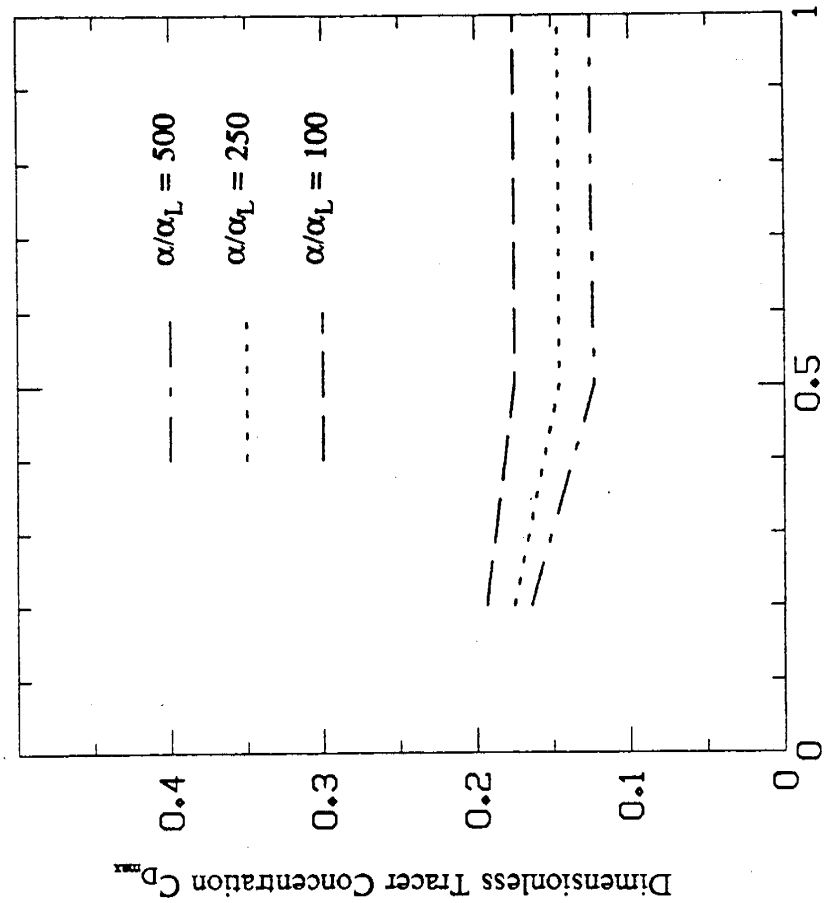

Figure 4.2.13 Peak Concentration, $C_{D\,max}$, as a Function of Mobility Ratio for Different Values of Peclet Number, a/α_L.

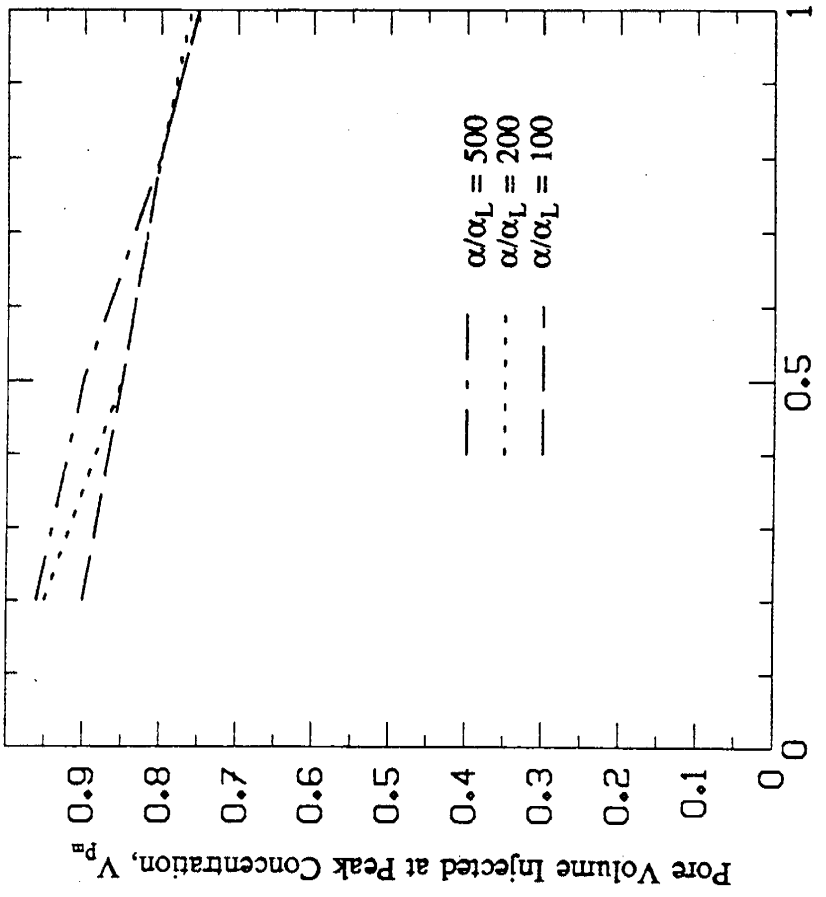

Figure 4.2.14 Pore Volume Injected at Peak Concentration, $V_{pD\,max}$ as a Function of Mobility Ratio for Different Values at Peclet Number, a/α_L.

Task 45 - INTEVEP shall provide DOE with information from two-dimensional laboratory displacements and numerical simulation studies on the influence of surfactants on steam injection profiles and oil production performance under conditions typical of steam drive and cyclic steam processes.

NUMERICAL SIMULATION STUDIES ON TWO-DIMENSIONAL LABORATORY DISPLACEMENTS - INFLUENCE OF SURFACTANTS ON STEAM INJECTION PROFILES AND OIL PRODUCTION PERFORMANCE

by Staff

INTEVEP, S.A.

Los Teques, Miranda

Venezuela

TABLE OF CONTENTS

LIST OF FIGURES

LIST OF TABLES

ABSTRACT

The first activity carried out to evaluate the STARS simulator capacity to model the process of heavy oil recovery through steam injection with surfactant was a simulation of the experimental information available[1] from laboratory tests. Said tests were intended to obtain a numerical model for estimating relative water/steam permeability curves under steady state conditions with and without surfactant.

The aim of this work is to predict the pressure drop along the pack, obtained once steady state conditions are reached, for eleven steam water displacement tests at steam injection flows of 2, 4 and 6 gr/min and injection pressures of 100, 200, and 300 psia, as well as for two steam injection tests with a 0.5% surfactant concentration at steam injection flows of 2 and 4 gr/min and at pressures of 237 and 222 psia respectively.

A simulation was conducted for each test and when numerical results were compared to experimental ones some small differences were found in the pressure drop values along the pack, which led to a change in the initial data in the simulator.

A second series of simulations was carried out by modifying, for each test, the relative permeability curves. This allowed to obtain almost the same results as those found in the laboratory.

1. INTRODUCTION

Steam injection is by itself an efficient method to displace and produce heavy and extra-heavy crude because crude viscosity is largely reduced when temperature increases in the reservoir zone affected by steam. Nevertheless, it is known that this process is less effective when steam, mainly due to gravitational segregation and high permeability channels, does not interact with large portions of the reservoir, thus leaving considerable amounts of crude undisturbed.

Additives have been injected along with steam to increase the basic process efficiency through a better control of steam sweep in the reservoir. The injection of surfactant-type foaming additives along with steam basically aims at blocking the zones of high steam permeability, and reducing the gravitational segregation of this fluid towards the formation top. This type of injection is increasingly used as an alternative to control gas phase mobility in steam injection processes[2,3,4], as well as CO2 injection processes. Under favorable circumstances, reductions have been reported[2,3,4] in gas phase mobility in approximately 100 times its initial value.

Several aspects have been considered[5,6] in the study of foam flow through a porous medium, namely surfactant adsorption in sand at low temperatures, thermal surfactant stability at high temperatures, the adverse effect of the cation exchange occurring between the surfactant solution and the formation porous medium on the surfactant active matter, and the mass transfer taking place from the surfactant solution to the oleic phase, which might be affected by temperature and ion concentration in the

formation water, even if it is normally considered to be insignificant, given the high surfactant solubility in the aqueous phase.

Traditional thermal simulators analyze gas and oleic phases according to the composition of their elements, based on the assumption that aqueous phase only consists of water. A simulator taking into account the aqueous phase composition and capable of evaluating additive-rock interactions is required to model the physical processes associated with the injection of water-soluble additives in a non-isothermal environment.

At present, Intevep has a STARS numerical thermo-compositional simulator (version 3.1.1) developed by Computing Modeling Group (CMG) for modeling both the basic mechanisms occurring in thermal oil recovery processes and those applications where steam is injected with additives such as surfactants or solvents.

Since this is a new simulator, it is necessary to become acquainted with the equipment in order to learn how to use it and evaluate all its predictive capabilities. Therefore, as a starting point, this work includes a series of simple runs to simulate water displacement in a unidimensional porous medium, through the injection of steam alone and with surfactant. Results were compared to experimental data available.

2. FOAM MODELING

STARS simulator has two models to estimate foam flow. The first one is the Mobility Reduction Model, a simple model based on the reduction of the gas phase mobility as a function of the amount of surfactant present in the aqueous phase. The second model, called "Lamella" Model, is based on the formation of a component in the gas phase through a water-surfactant chemical reaction. In the following paragraphs a short description will be made of the above- mentioned models.

2.1 Gas Phase Mobility Reduction Model

The Mobility Reduction Model is based on a change in the value of the gas phase mobility. The general assumption is that if there is some surfactant in the aqueous phase, there will be some foam in the gas phase. The gas phase mobility, λ_g, obtained through this model is a function of the mobility of said phase without foam, λ_{gm}, and a mobility factor, **FM**, and it is given by:

$$\lambda_g = \lambda_{gm} \text{ (without foam)} * FM \qquad (1)$$

where the mobility factor **FM** depends upon the surfactant concentration in the aqueous phase, the crude saturation, the gas flow rate, and the maximum value of the gas phase mobility reduction factor in the porous medium.

The mobility factor **FM** is a dimensionless interpolation value represented by the following expression:

$$FM = \{1 + MMR\,(Ws/Ws^{max})^{es} * ((So^{max}-So)/So^{max})^{eo} * (Nc^{ref}/Nc)^{ev}\}^{-1} \qquad (2)$$

where:

MMR is the maximum mobility reduction

Ws is the surfactant concentration in the aqueous phase

Ws^{max} is the maximum surfactant concentration in the aqueous phase

So is crude saturation

So^{max} is the maximum crude saturation for foam presence

Nc is the capillary number

Nc^{ref} is the capillary number with reference to the minimum gas flow rate

Superscripts **es**, **eo**, and **ev** are, respectively, the surfactant composition, crude saturation and capillary number contributions. The values therefore may vary for the first and the second one from 1.00 to 2.00, and for the third one from 0.3 to 0.7.

An analysis of the previous expression allows to observe that in order to obtain the highest reduction in the gas phase mobility the following conditions are required for the porous medium:

* Surfactant concentration in the aqueous phase must be the maximum one
* Crude saturation must be equal to zero.
* The capillary number must be equal to the reference capillary number corresponding to a minimum gas flow rate. It is also important to highlight that no foam will exist in the porous medium if any of the following conditions is present:

* No surfactant presence in the porous medium.

* Crude saturation is equal to or higher than the maximum saturation allowed for foam formation.

* The capillary number has the maximum value, which means that gas flow has no restriction.

The maximum mobility reduction, **MMR**, is the factor used to diminish the values of the gas-related permeability curve in the presence of foam and it is expressed as follows:

$$\textbf{MMR} = (\Delta P)\ \textbf{with foam} \ / \ (\Delta P)\ \textbf{without foam} \qquad (3)$$

where both pressure drops are obtained through experimental steam water displacement tests, in the absence of crude. In equation (3), the numerator represents the pressure drop obtained in this type of tests by using steam and surfactant at the concentration at which crude displacements through steam and surfactant injection were carried out. The denominator represents the pressure drop obtained when only steam is injected.

If there are no experimental values for a given simulation, field data should be used. Some typical values for these parameters are given hereinbelow:

MMR = from 5 to 1000

Ws^{max} = 0.00001 molar fraction

So^{max} = 0.2

Nc^{ref} = 0.0001

es = 1.0

$e_o = 1.0$

$e_v = 0.5$

As shown in equation (2), the mobility factor **FM** covers the interval from 1, if no foam exists in the gas phase, to close to zero, when there is a heavy foam presence in the gas phase

$$0 < FM \leq 1 \qquad (4)$$

The minimum mobility factor value is approximately the reciprocal of the maximum mobility reduction:

$$FM \approx (1/MMR) \approx 0 \qquad (5)$$

Surfactant data required to use this model are as follows:

Phase equilibrium constants, $K_{gas/oil}$ and $K_{oil/water}$:

Since surfactant is considered to be essentially nonvolatile, the gas-water phase equilibrium constant is considered to be null, $K_{gas/water} = 0.0$. On the other hand, foaming surfactants have a limited partitioning inside the crude. Therefore, it is necessary to obtain some values for the crude-water phase equilibrium constant, $K_{oil/water}$. Nevertheless, for foams at steam temperatures, initial Koil/water values are not necessary.

Maximum adsorption:

Surfactant adsorption usually diminishes as temperature increases (for foams in steam, the maximum initial adsorption value is not required at steam temperatures).

Surfactant mean life:

Surfactant decomposition generally increases with temperature (for foams in steam, initial decomposition rates at steam temperatures are not necessary). The model assumes a constant decomposition rate **kd** (at a basic **pH**), or its equivalent value, the surfactant mean life $t_{1/2}$ (**kd** values = $0.693/t_{1/2}$).

Besides the preceding information, additional data are required to use the Mobility Reduction Model:

K_{rg}, K_{rw}, K_{ro}, (without foam):

The two relative permeability curves of the gas-liquid and water-crude phases are used together with Stone Model. These curves define the basic flow pathways that the phase is likely to follow in the presence of foam.

Maximum mobility reduction factor **MMR**:

It is obtained in foam-water displacement tests at a maximum surfactant concentration Ws^{max}, at a reference rate (or capillary number Nc^{ref}), and in the absence of crude in the pack (see equation 3).

Interpolation parameters:

Ws^{max}: A maximum surfactant concentration is necessary to obtain a heavy foam formation (usually about 1.0% by weight)

So^{max}: Maximum crude saturation in which foam is not produced (normally 10% to 30%, depending on the surfactant selected).

Nc^{ref}: Reference capillary number (equivalent to gas phase flow rate in the presence of heavy foam) in the experiment.

Main advantages of the Mobility Reduction Model:

* Relatively few data are required, which may be promptly obtained through laboratory tests.
* A single additional equation is used (for the surfactant) to describe the fluid flow through the porous medium, which means a small increment in simulation costs.
* Field and laboratory steam injection simulations with surfactant are allowed.

2.2 "Lamella" Model

Another model used by STARS simulator to describe the foam flow is the so-called "Lamella" Model. The "Lamella" approach is a modeling type consisting of dispersing components, where "Lamella" is a gas phase component whose concentration determines the gas phase flow properties, viscosity, relative permeability, and resistance factor.

The preformed foam injected into the porous medium has the same characterization as the capture process for the component dispersed in the flow of stable emulsions, polymers and fines. This trapping mechanism may be seen as being quasi-static (polymer adsorption) or kinetic (emulsion or fine capture). Said capture process affects the "Lamella" propagation rate and local density that is associated with the stable foam movement. Besides, foam generation and coalescence affect not only the "Lamella" local density, but also foam properties and propagation rate. As a result, these processes are modeled through mass transfer expressions under non-equilibrium conditions.

A mean "Lamella" is defined as a combination of the water and

surfactant amounts existing in the aqueous medium in the following chemical reaction:

$$(H_2O)_w + b(S)_w \rightarrow (L)_g \qquad (6)$$

where the stoichiometric coefficient **b** is small (it defines the number of surfactant moles per water mol. in the mean "Lamella"), approximately equal to 10^{-5}. The exact value of **b** depends on a series of factors including the assumed "Lamella" shape, the molar water volume/specific surfactant surface area ratio, etc. It is noteworthy that **b** is small, but not negligible, which means that the "Lamella" physical properties are related to those of water, and "Lamella" formation requires a sufficient amount of surfactant.

The "Lamella" model is a complex scheme and the parameters necessary for its application are not easy to obtain. Besides, they are similar to those employed in the modelings of emulsion flow and chemical equations.

Therefore, the use of this model is limited to the simulation of very important aspects in laboratory foam experiments and very small-scale field simulations.

3. STEAM INJECTION SIMULATION

The initial phase of this study focused on simulating simple laboratory experiences for which experimental data[1] were already available, with the aim of validating the effectiveness of the numerical STARS simulator option in the modeling of steam injection processes with additives.

In the experiences to be simulated some water was displaced in a (unidimensional) cylindrical porous medium by continuously injecting steam alone or with surfactant. The variables for these tests were as follows: injection pressure in the order of 100, 200, and 300 psia, and steam injection flow of 2, 4, and 6 gr/min.

The experimental equipment consisted of an ATICA sandpack, 92% quartz, 4% Al_2O_3, and 4% Fe_2O_3, completely covered with an insulating fiber to minimize environmental heat losses. The pack was initially saturated with water and then heated until a temperature close to the boiling point corresponding to the preset outlet pressure was obtained. Afterwards, saturated steam was injected with and without surfactant, and once steady state conditions were reached, inlet and outlet pressures and temperatures were measured in three points along the cell. Inlet and outlet water and steam flow rates were also measured in the pack.

Pressure profiles along the pack obtained in these tests are compared to those predicted by the simulator using the Mobility Reduction Model, in order to lay down the foundations for discussing how effective is STARS simulator the modeling of these experiences.

As a starting point, the curves reported by Barboza et al[1] were used in the simulation for relative permeability with and without surfactant (see Figures 1 and 11), keeping constant the following parameters in all runs:

Pack length:	30.00 cm
Pack diameter:	3.80 cm
Porosity:	0.3
Inlet steam quality:	0.80
Absolute permeability:	4.00 Darcy
Room temperature:	30.00 C

where the injectivity index was calculated by means of the transmissibility of the first block in the mesh, which is used by STARS simulator when wells are located in the end walls in a unidimensional cell. Peaceman equation[7] does not give correct values for this type of array, thus generating values lower than those obtained experimentally, due to homogeneous and radial flow approximations.

Table 1 shows outlet pressure and steam injection rate conditions, as well as the

type of experience, with and without surfactant, and the identification of the figure number where a comparison is made of the pressure drops along the cell resulting from the different simulator runs with the corresponding experimental values for each test.

It was impossible to make a historical comparison between the injection and the saturated steam production because the experimental data reported only provide the pressure drop values along the pack obtained once steady state conditions were reached.

3.1 Analysis of Results

The following aspects were observed when analyzing results:

* Runs gave, on the average, a steam surge at the cell outlet after 18 seconds, and steady state conditions were reached before 2 minutes had elapsed, after steam injection had started. Unfortunately, the corresponding experimental information is not available to compare these two times.

* As shown in Figures 2 to 13, the results given by the STARS simulator runs are slightly different (lower than 5.6%) from those obtained in the experimental tests.

* In general, it was observed that for steam injection tests alone (see Figures 2 to 10) the difference between simulated and experimental results decreased as injection rate increased and, except for tests at 100 psia with 4 and 6 gr/min, pressure values predicted by the simulator were lower than the experimental measurements.

* A comparison of the simulator results during steam injection with and without surfactant (see Figure 14), for 200 psia at a 4 gr/min rate, allows to observe that the pressure drop predicted for steam with surfactant is higher than that for steam without surfactant. However, when comparing simulated and experimental results (see Figures 10 and 11), the simulator pressures for the 2 gr/min rate are slightly higher that the experimental ones (maximum difference = 1.2%). On the contrary, for a 4 gr/min rate, experimental results are higher than the simulated ones (maximum difference = 5.26%).

4. CHANGES IN RELATIVE PERMEABILITY

With the aim of studying how variations in the relative permeability curves influence upon results obtained with the model, a new series of runs was carried out varying said curves, until the pressure drops estimated by the simulator fitted into those obtained experimentally

Table 2 shows the conditions of steam injection rate, outlet pressure, and the localization of figures in which modified gas-related permeability curves are presented, as well as the localization of the figures corresponding to experimental and simulated pressure profiles along the cell for each test.

4.1 Analysis of Results

An analysis of the results obtained in the new runs highlights the following aspects:

* It was necessary to decrease gas-related permeability values by almost 70% to have equivalent simulated and experimental pressures, except for tests 2 and 3 (unmodified) and test 10 where gas-related permeability values doubled with surfactant.

* The modified gas-related permeability values in steam injection tests alone (except for tests 2 and 3) are very close to values reported in the literature, Counsil [8].

* The runs for steam injection with surfactant (see Figures 32 and 34) showed that gas-related permeability increased for an injection rate of 2 gr/min, but decreased for a 4 gr/min rate. This could indicate the presence of tests carried out in porous media having different permeabilities.

* Water saturation values are similar along the cell, in all simulations, and very close to the residual water saturation value because heat losses are very small and saturations are found in a steady state process.

- Water- and steam-related permeability values observed in the simulations correspond to those of a water saturation process which is about to become irreducible. As a result, water-related permeability is almost zero and steam-related permeability is almost reaching its maximum value.

- Pressure and temperature decrease very little along the cell in all simulations because of the experiment conditions, the presence of very low heat loss levels, and the measurement of steady state pressures. Therefore, it is an adiabatic process.

5. CONCLUSIONS

- Experiments to determine relative steam-surfactant and steam-water permeability curves under steady state conditions provide little information to evaluate the whole STARS simulator capacity. Nevertheless, when using the Mobility Reduction Model for steam injection with surfactant, this simulator predicted with a good approximation the experimental results obtained in a unidimensional pack.

- Under steady state conditions, and in an adiabatic process, large differences in steam-related permeability values do not considerably affect the pressure drop values along the cell, due to the high steam compressibility and the low steam viscosity.

- The evaluation of a numerical simulator in the process of steam injection with additives has to be effected by using experimental information that will allow to fully utilize the simulator capacity.

6. RECOMMENDATIONS

- STARS simulator effectiveness in reproducing the results obtained in crude displacement tests through steam injection with surfactant should be evaluated before using it for modeling, on a small scale, steam injection processes involving the use of additives.
- Unidimensional tests should be carried out in tubes being long enough to neglect final effects. Besides, a well defined pressure distribution along the tube is recommended, as well as two-dimensional tests to assess the gravitational segregation effect, and tests in the presence of crude allowing an analysis of capillary pressure effects.

REFERENCES

1. BARBOZA, M. and MONSALVE, A.. Determination of Steam -Water Relative Permeabilities From Experimentally Observed Pressure Profiles. Third Admenment And Extension To Annex IV Enhanced Oil Recovery Thermal Processes, Task 29, Los Teques, Venezuela, July 1986.

2. DILGREN, R.E., DEEMER, A.R., OWENS, K.B., The Laboratory Development and Field Testing of Steam/Noncondensible Gas Foams for Mobility Control in Heavy Oil Recovery, SPE 10774, California Regional Meeting, San Francisco, CA., March 1982.

3. PLOEG, J.F. y DUERKSEN, J.H., Two Successful Steam/Foam Field Tests, Midway-Sunset Field, SPE 13609, California Regional Meeting, Bakerfield, Ca., March 1985.

4. MOHAMMADI, S.S., VAN SLYKE, D.C., GANONG, B.L., Steam-Foam Pilot Project in Dome-Tumbador Midway-Sunset Field, SPE Res. Eng., February 1989.

5. HOLM, L.W., and GARRISON, W.H., CO_2 Diversion with Foam in an Immiscible CO_2 Field Project, SPE Res. Eng., February 1988.

6. FRIEDMAN, F., CHEN, W.M., GAUGLITZ, P.A., Experimental and Simulation Study of High Temperature Foam Displacement in Porous Media, SPE/DOE 17357, Enhanced Oil Recovery Symposium, Tulsa, OK., April 1988.

7. PEACEMAN, D.W., Interpretation of Well-Block Pressures in Numerical Reservoir Simulation with Non-square Grid Blocks and Anisotropic Permeability, SPE 10528 presented in Sixth SPE Symposium on Reservoir Simulation, New Orleans, February 1982.

8. COUNSIL, J.R., Steam-Water Relative Permeability. PhD. Thesis, Stanford University, 1979.

LIST OF SYMBOLS

eo	= oleic phase contribution factor
es	= surfactant contribution factor
ev	= gas rate contribution factor
FM	= dimensionless interpolation factor
kd	= decomposition rate
kr_g	= gas-related permeability
kr_o	= oil-related permeability
kr_w	= water-related permeability
K	= phase equilibrium constant
MRF	= maximum mobility reduction factor
Nc	= capillary number
Nc^{ref}	= reference capillary number
pH	= alkalinity or acidity degree
r_g	= gas resistance factor
So	= oil saturation
So^{max}	= maximum oil saturation
$t_{1/2}$	= mean lifetime
Ws	= surfactant concentration

Ws^{max} = maximum surfactant concentration

Greek Symbols:

λ_g = gas mobility

λ_{gm} = foamless gas mobility

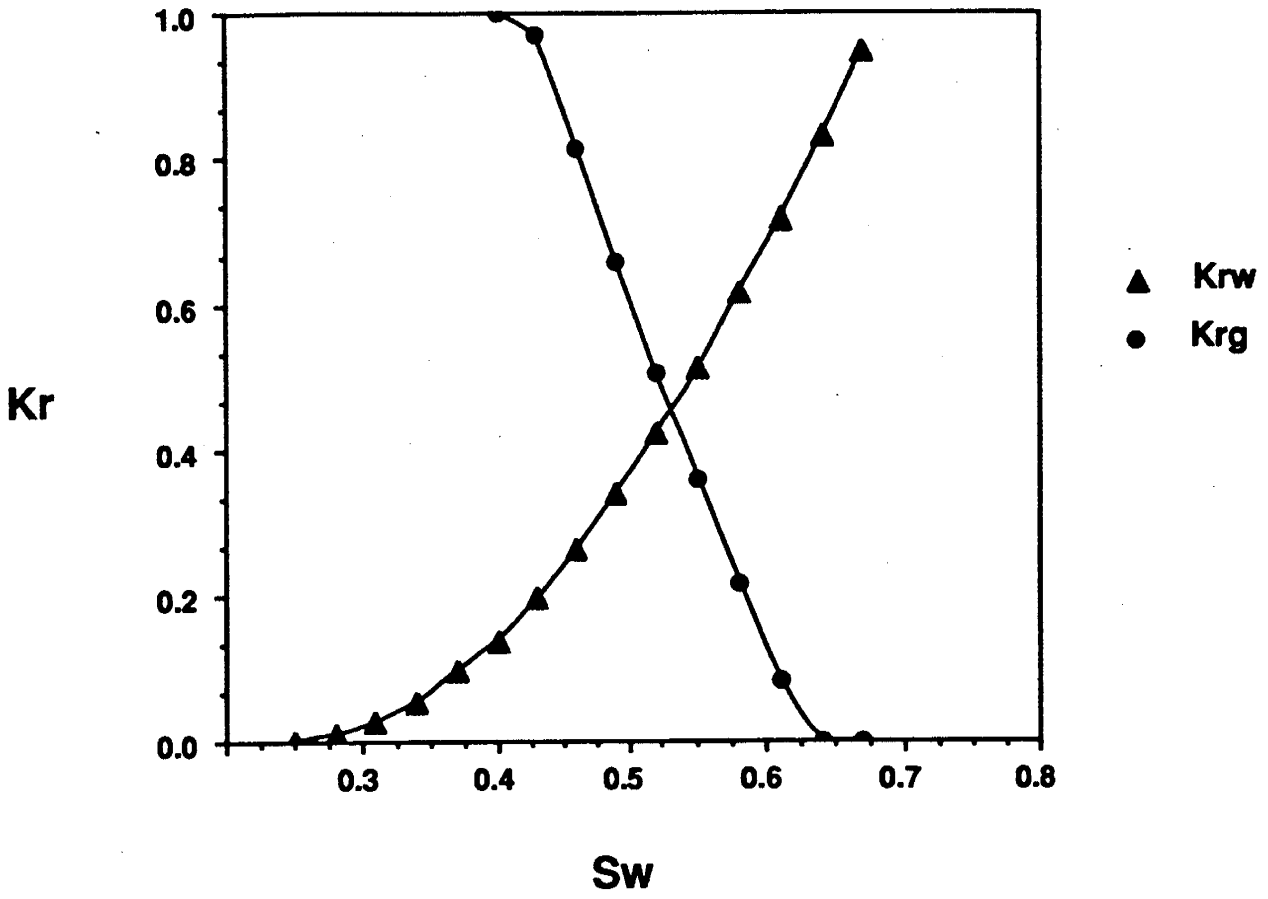

Fig. 1 INITIAL RELATIVE WATER/STEAM PERMEABILITY CURVES

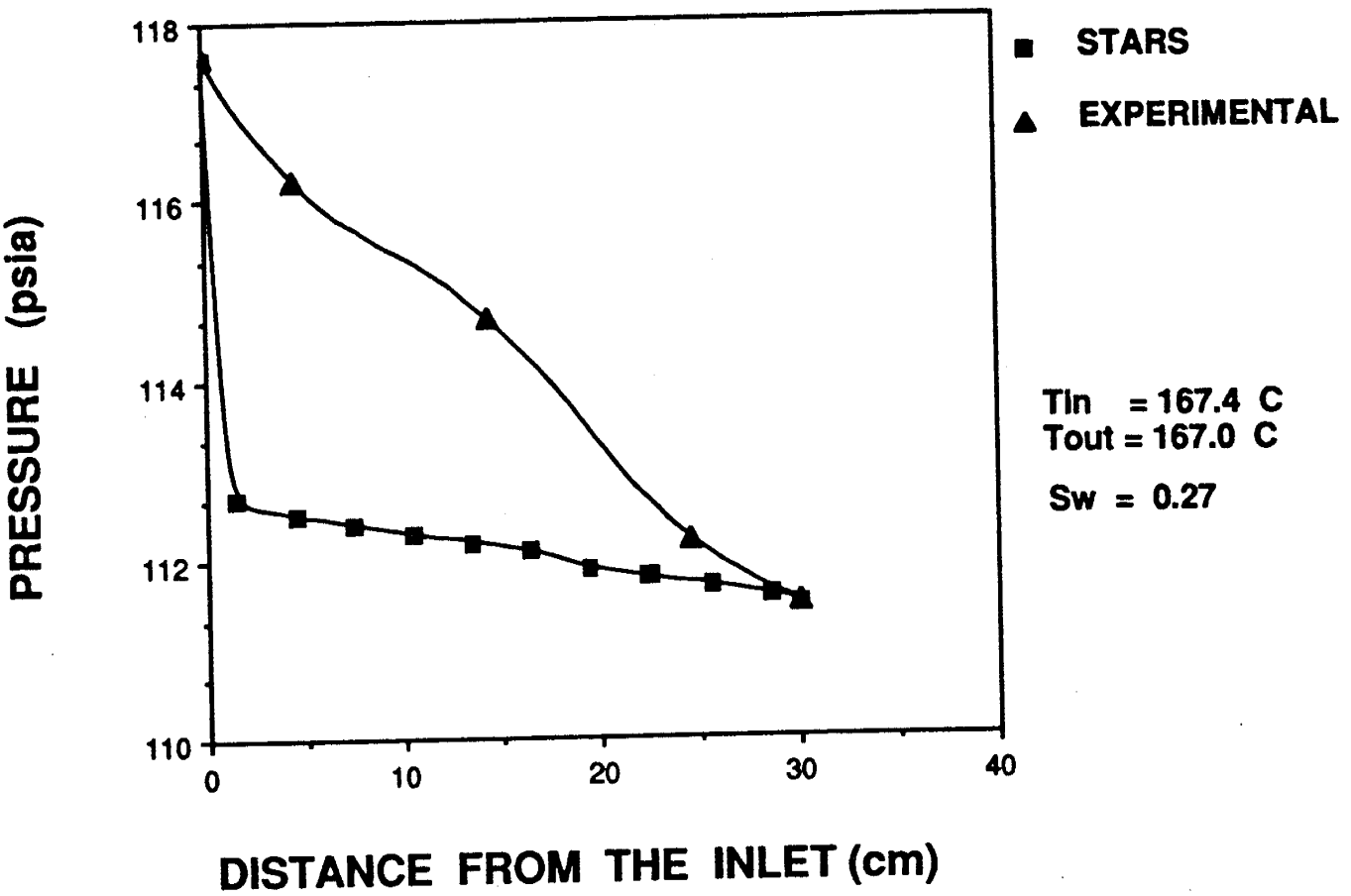

Fig. 2 EXPERIMENTAL PRESSURE PROFILES SIMULATED FOR 100 psia AND 2 gr/min

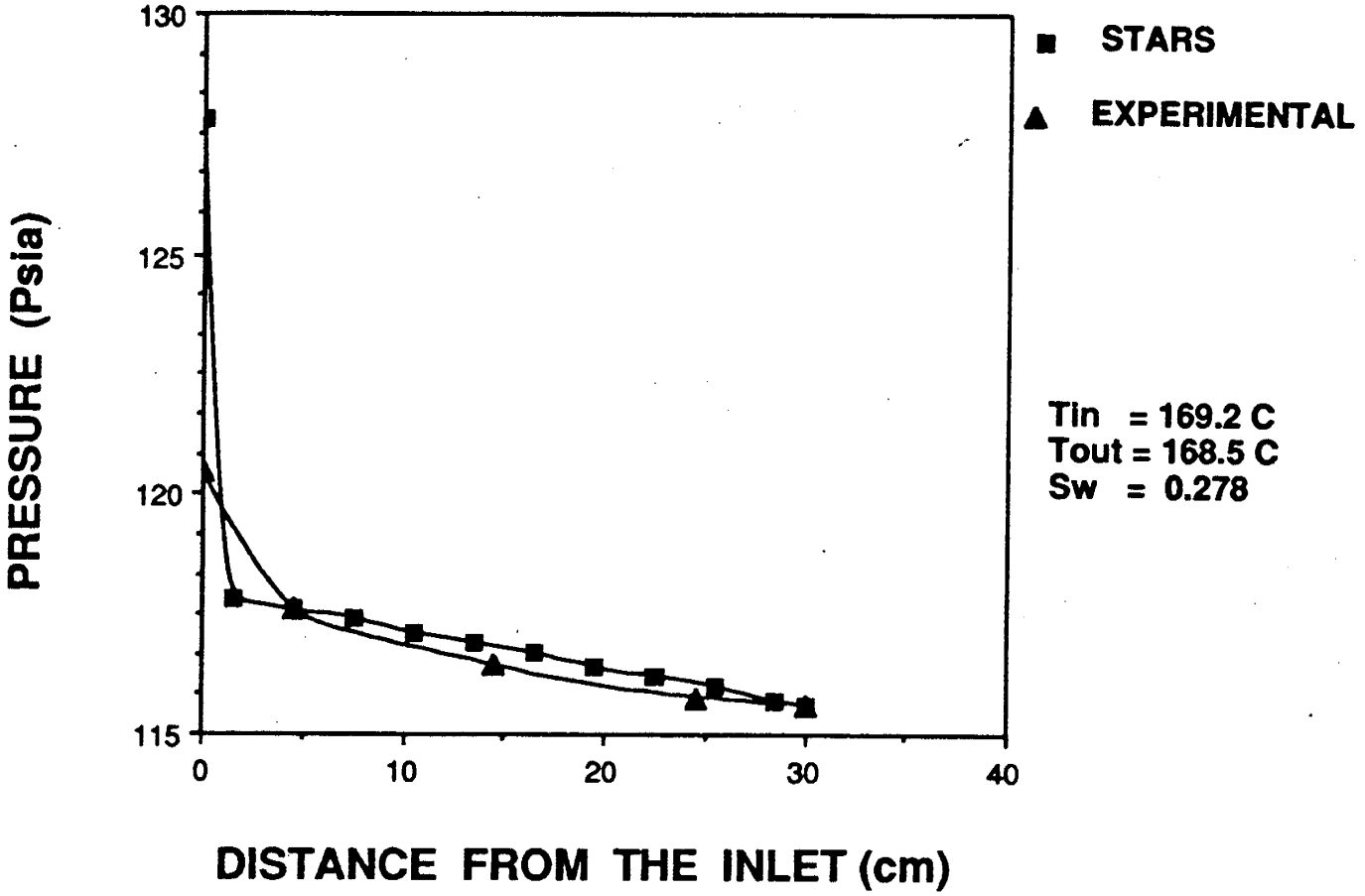

Fig. 3 EXPERIMENTAL PRESSURE PROFILES SIMULATED FOR 100 psia AND 4 gr/min

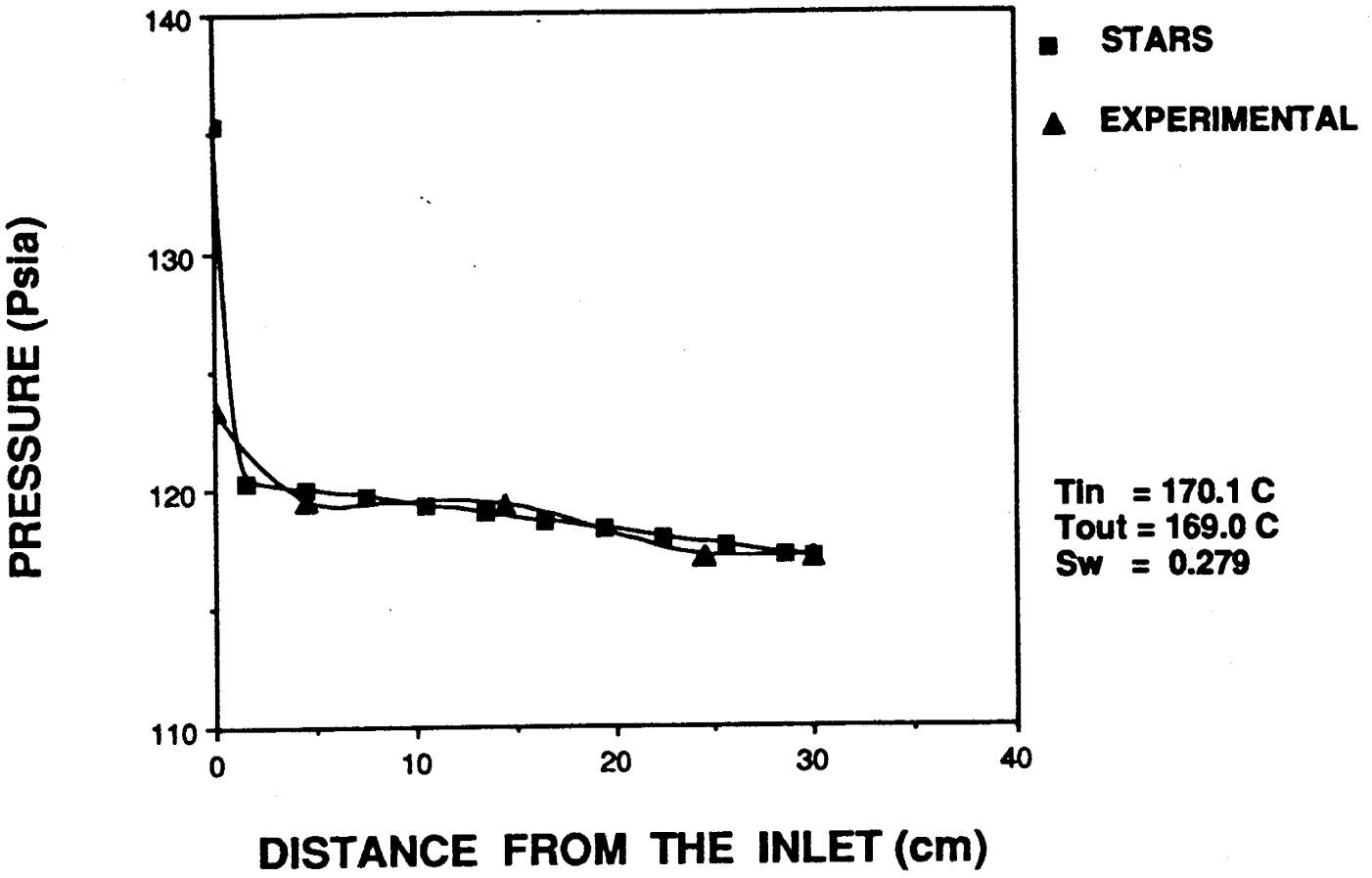

Fig. 4 EXPERIMENTAL PRESSURE PROFILES SIMULATED FOR 100 psia AND 6 gr/min

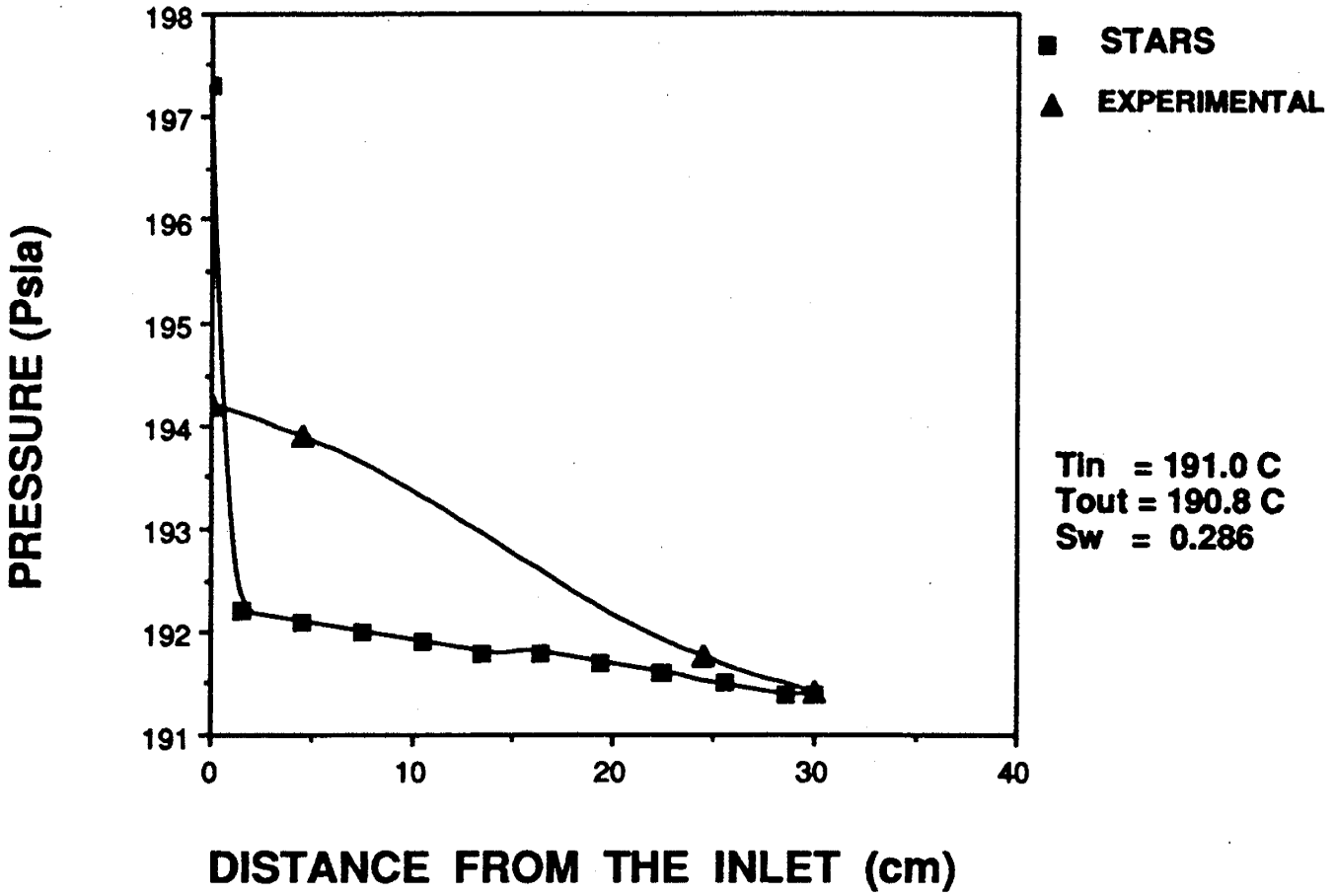

Fig. 5 EXPERIMENTAL PRESSURE PROFILES SIMULATED FOR 200 psia AND 2 gr/min

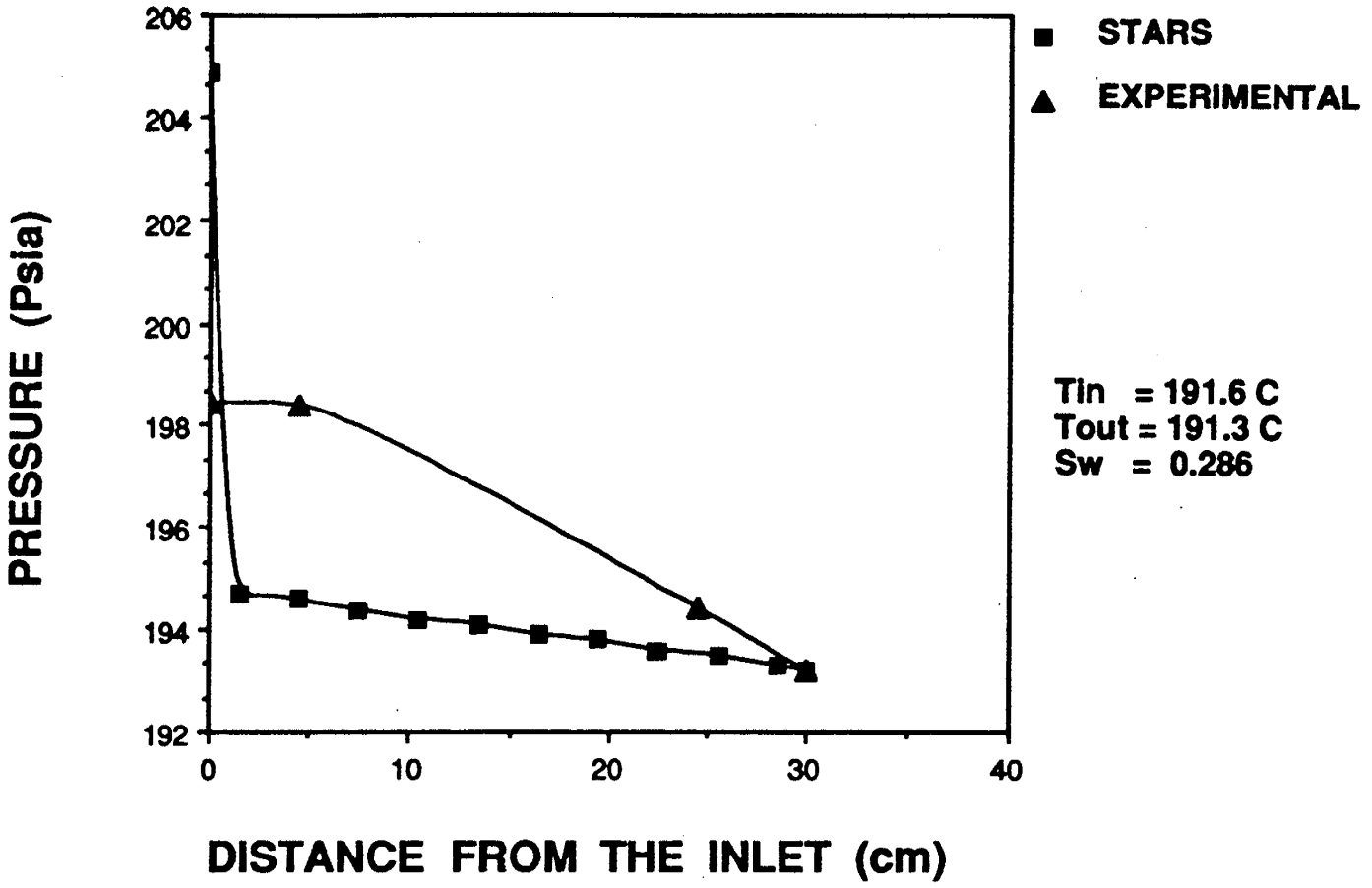

Fig. 6 EXPERIMENTAL PRESSURE PROFILES SIMULATED FOR 200 psia AND 4 gr/min

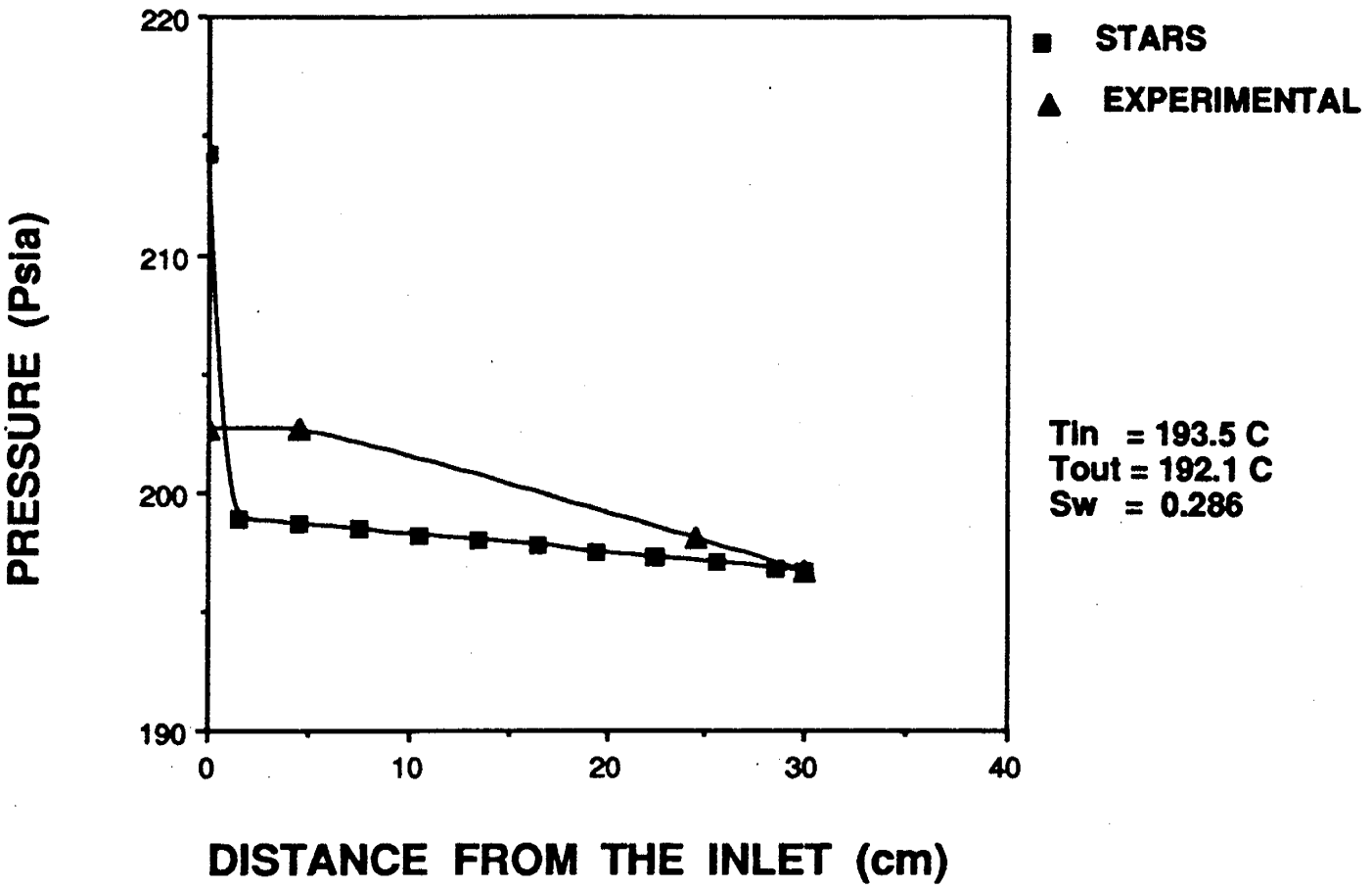

Fig. 7 EXPERIMENTAL PRESSURE PROFILES SIMULATED FOR 200 psia AND 6 gr/min

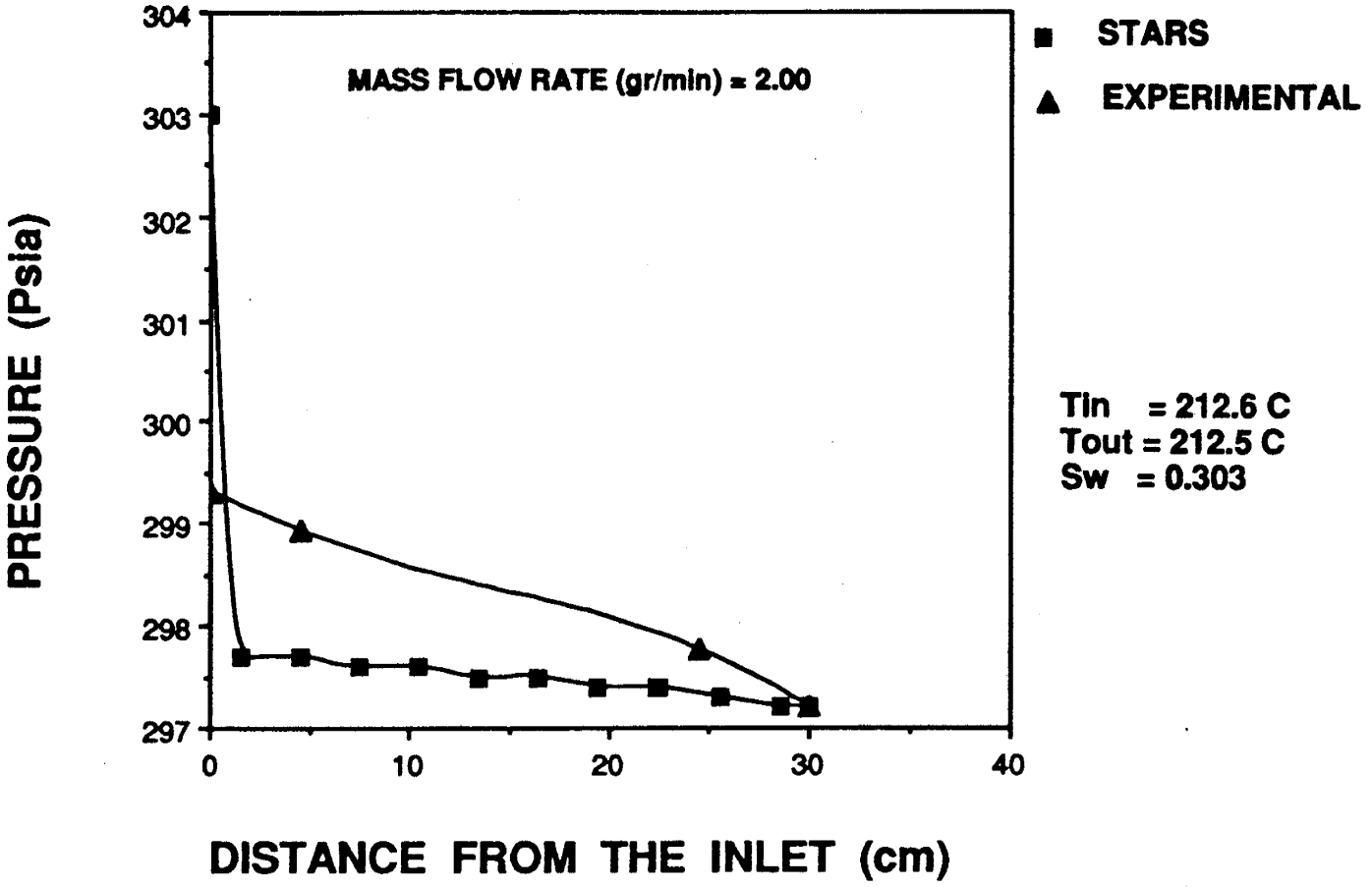

Fig. 8 EXPERIMENTAL PRESSURE PROFILES SIMULATED FOR 300 psia AND 2 gr/min

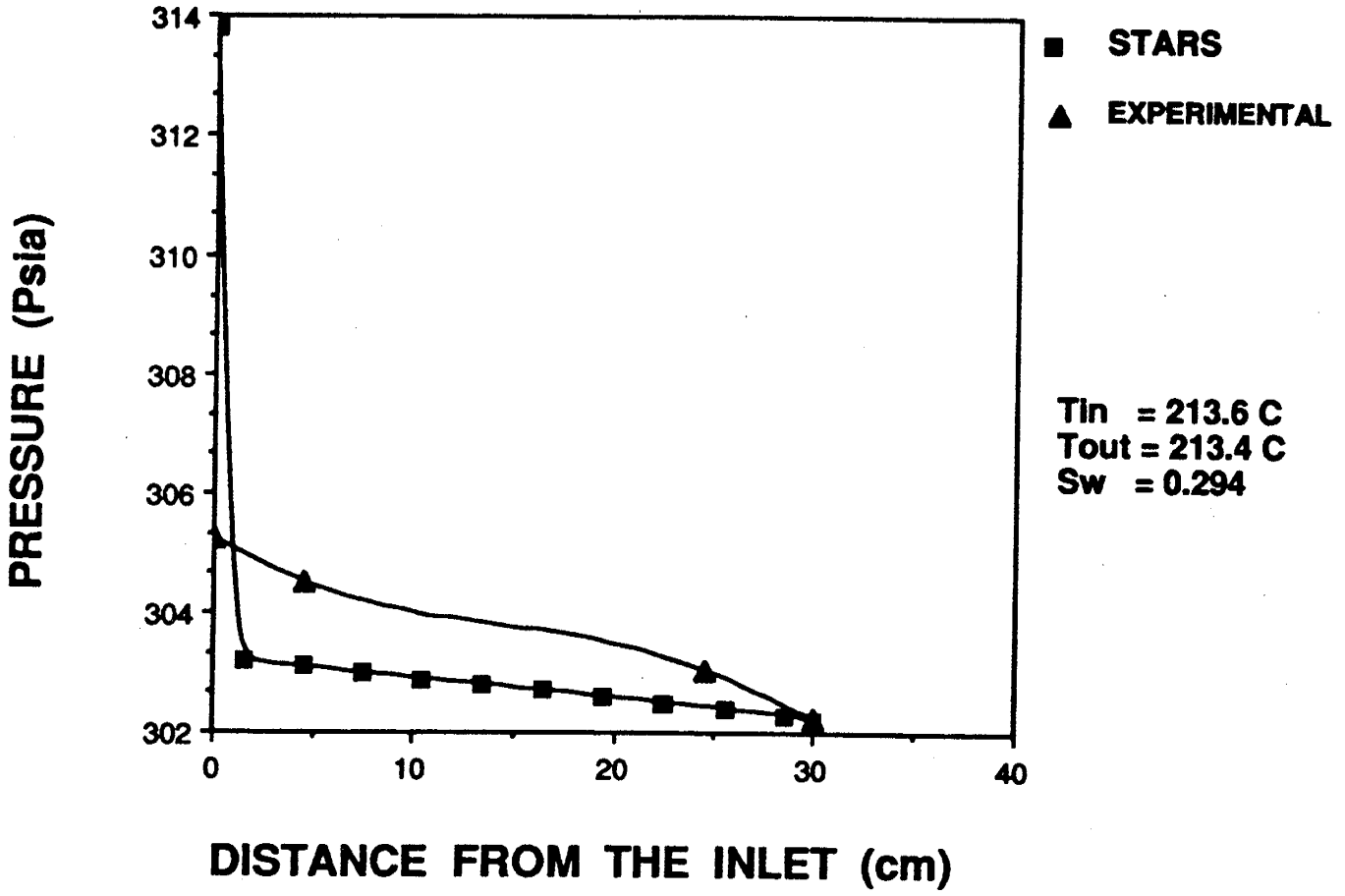

Fig. 9 EXPERIMENTAL PRESSURE PROFILES SIMULATED FOR 300 psia AND 4 gr/min

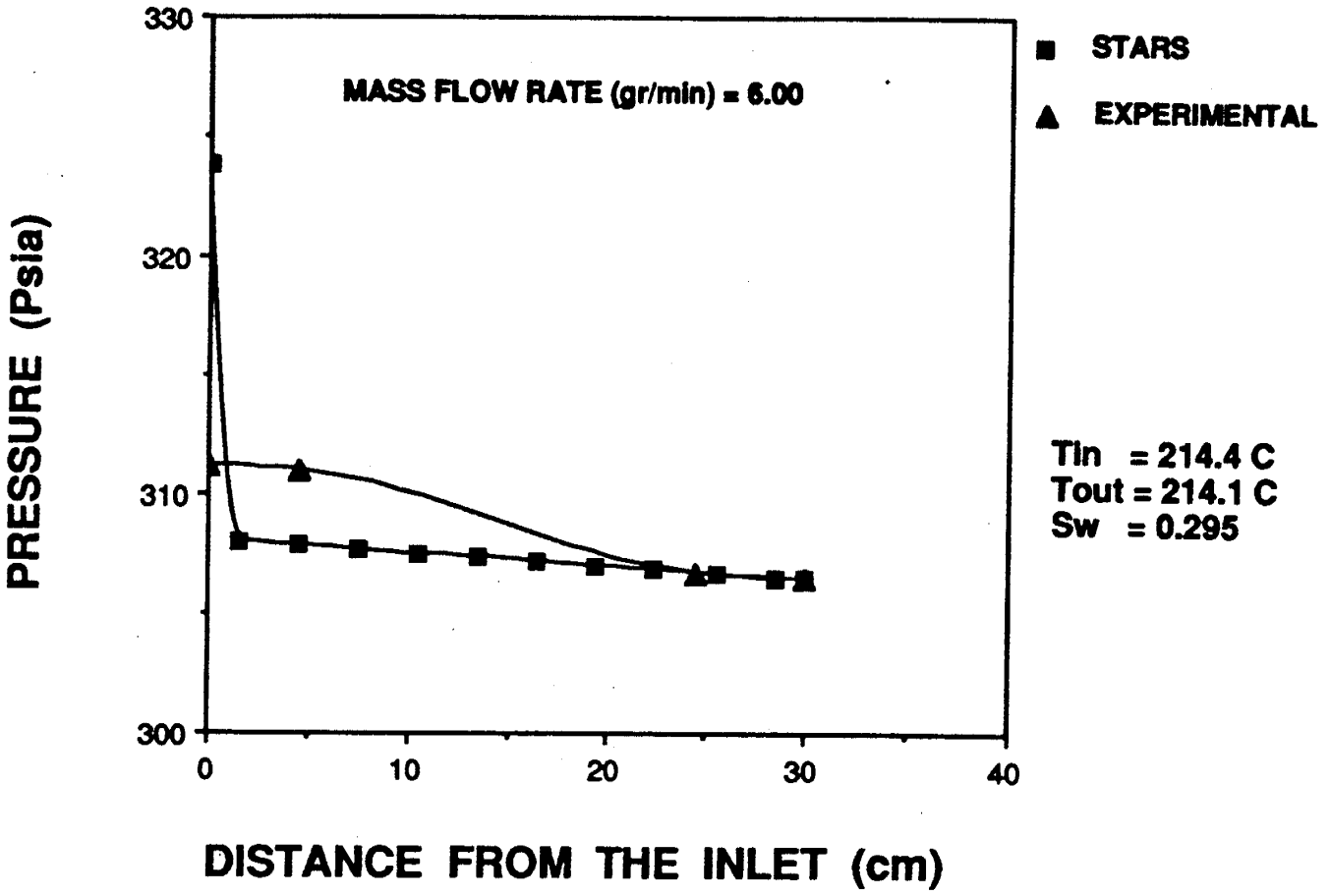

Fig. 10 EXPERIMENTAL PRESSURE PROFILES SIMULATED FOR 300 psia AND 6 gr/min

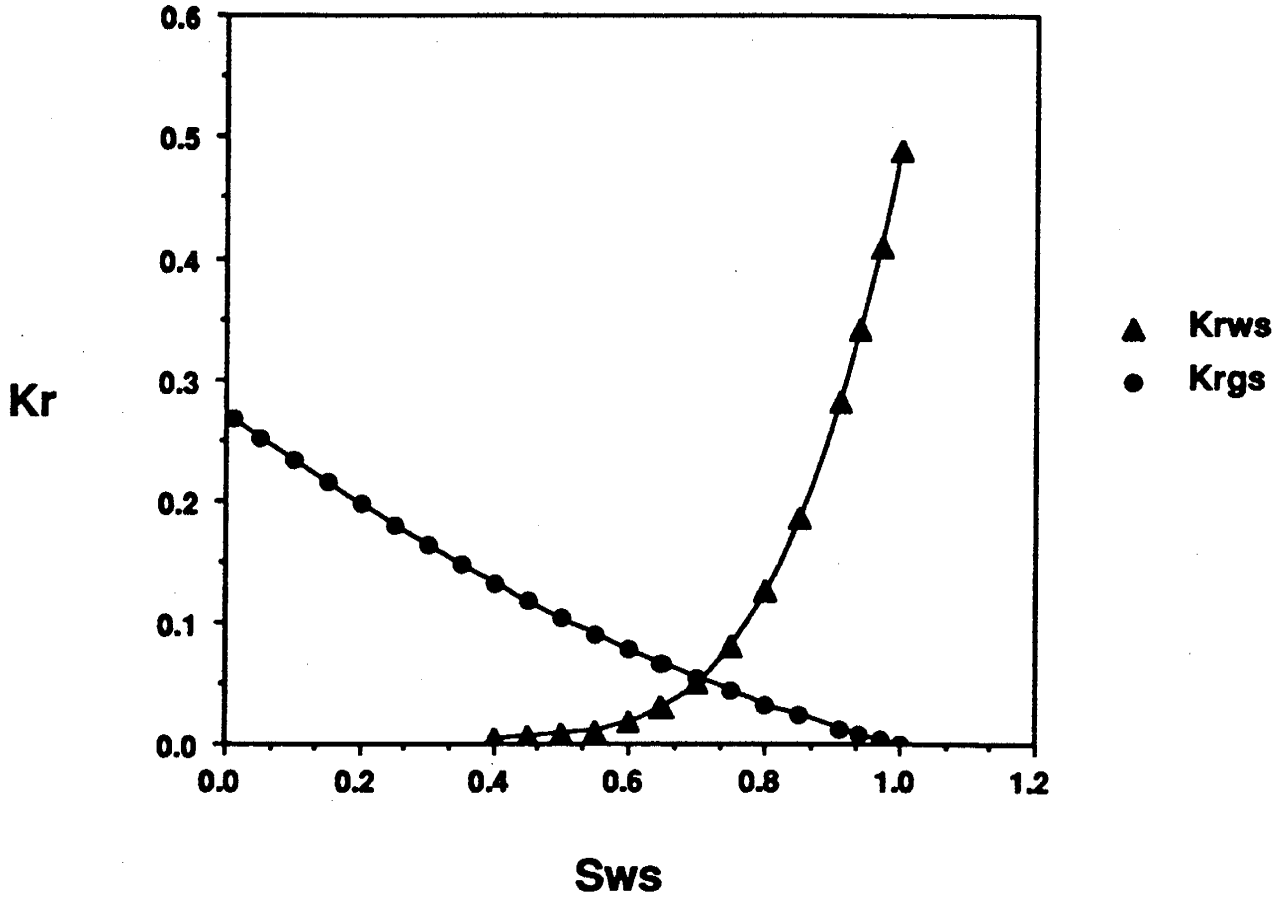

Fig. 11 RELATIVE WATER/STEAM PERMEABILITY CURVES WITH SURFACTANT

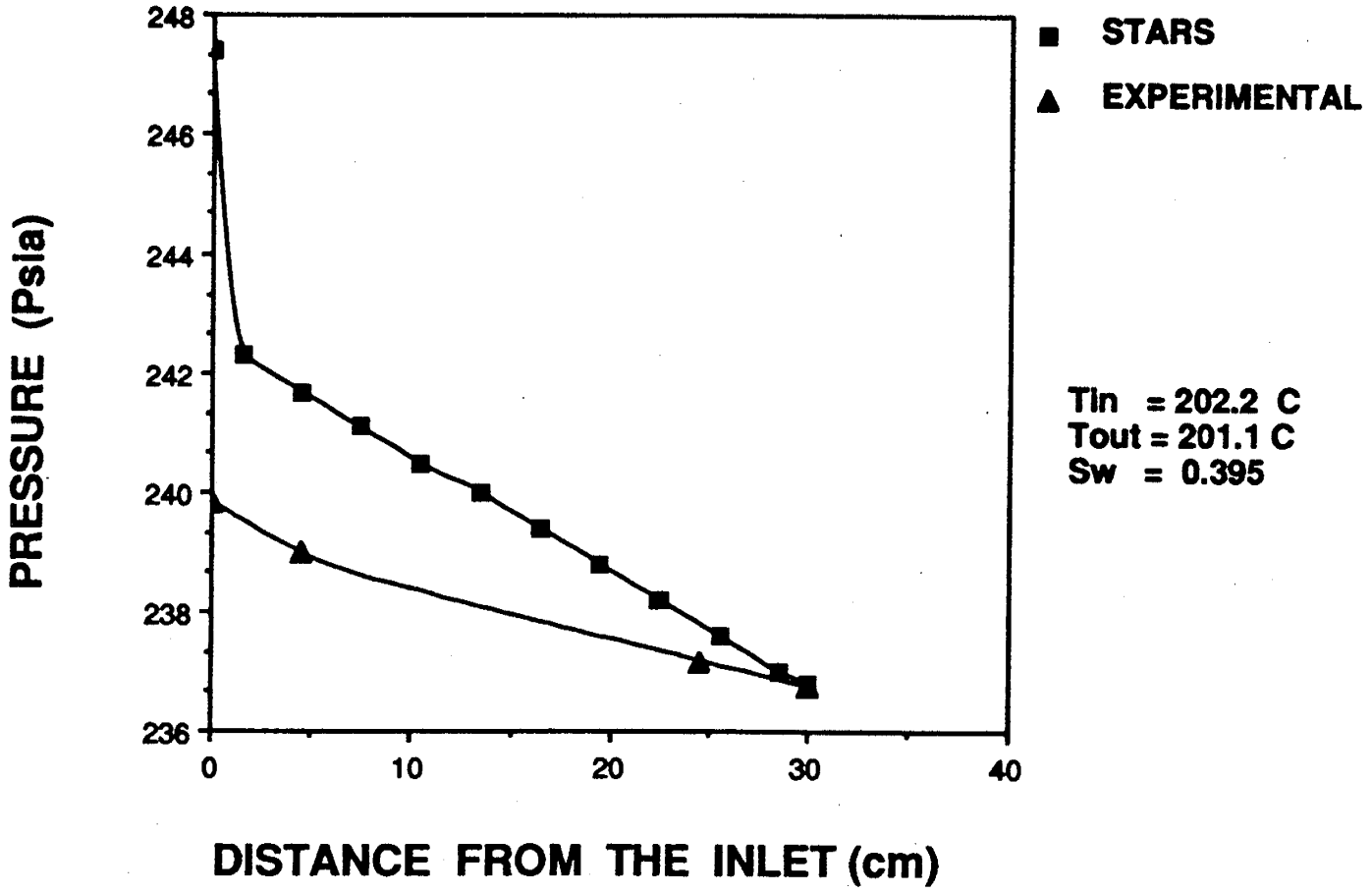

Fig. 12 EXPERIMENTAL PRESSURE PROFILES SIMULATED FOR 200 psia AND 2 gr/min WITH 0.5% SURFACTANT

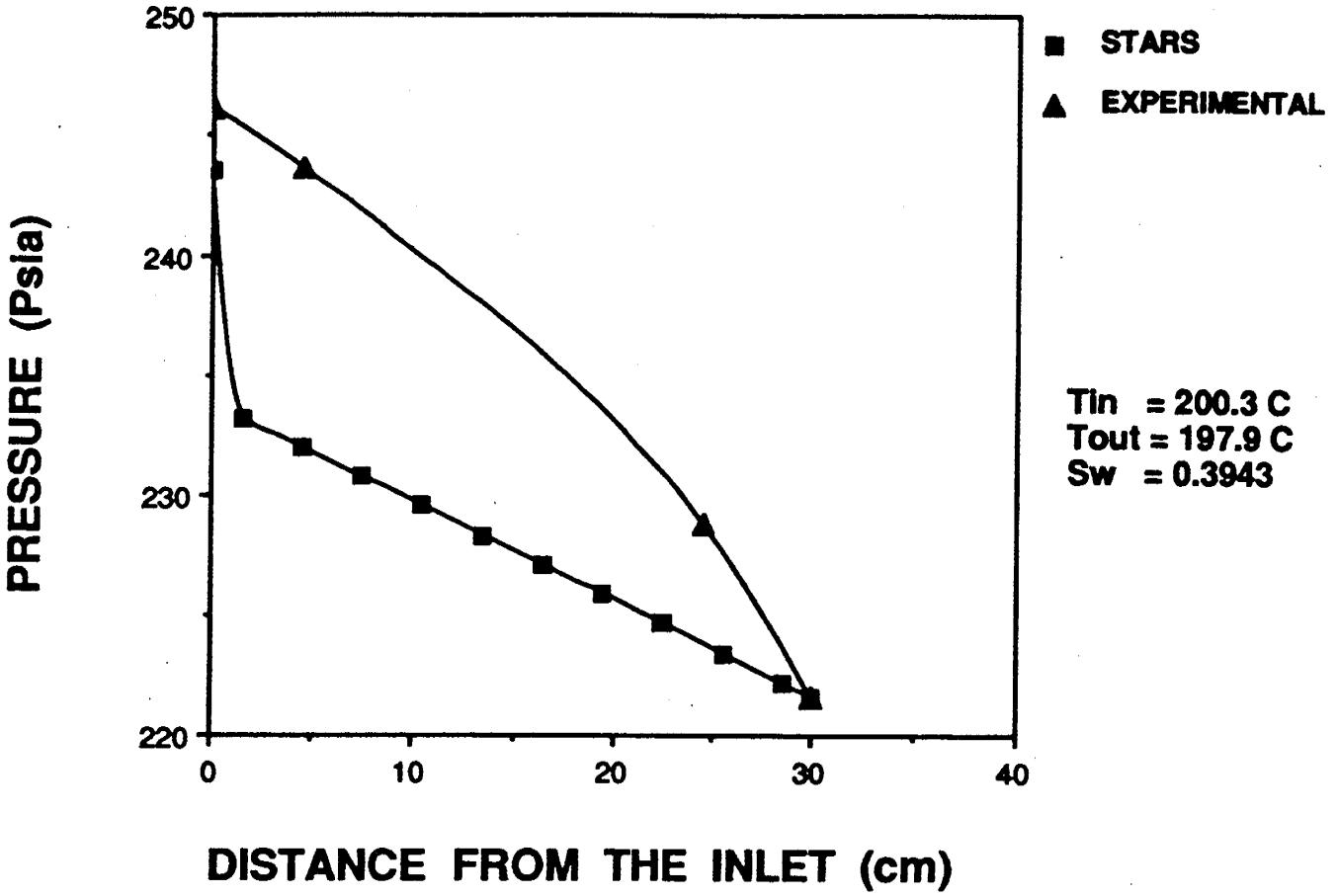

Fig. 13 EXPERIMENTAL PRESSURE PROFILES SIMULATED FOR 200 psia AND 4 gr/min WITH 0.5% SURFACTANT

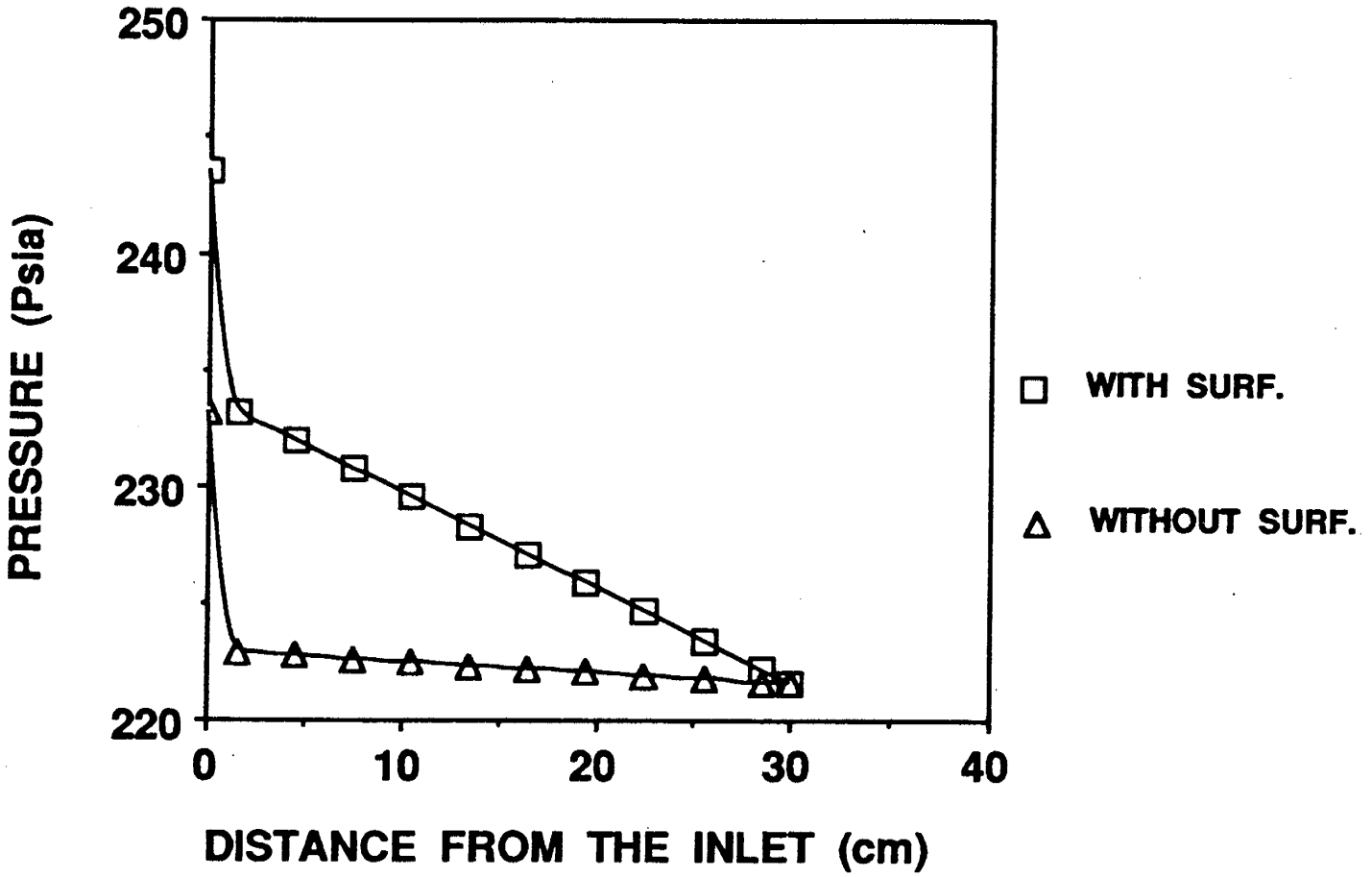

Fig. 14 PRESSURE PROFILES SIMULATED FOR 200 psia AND 4 gr/min WITH AND WITHOUT SURFACTANT

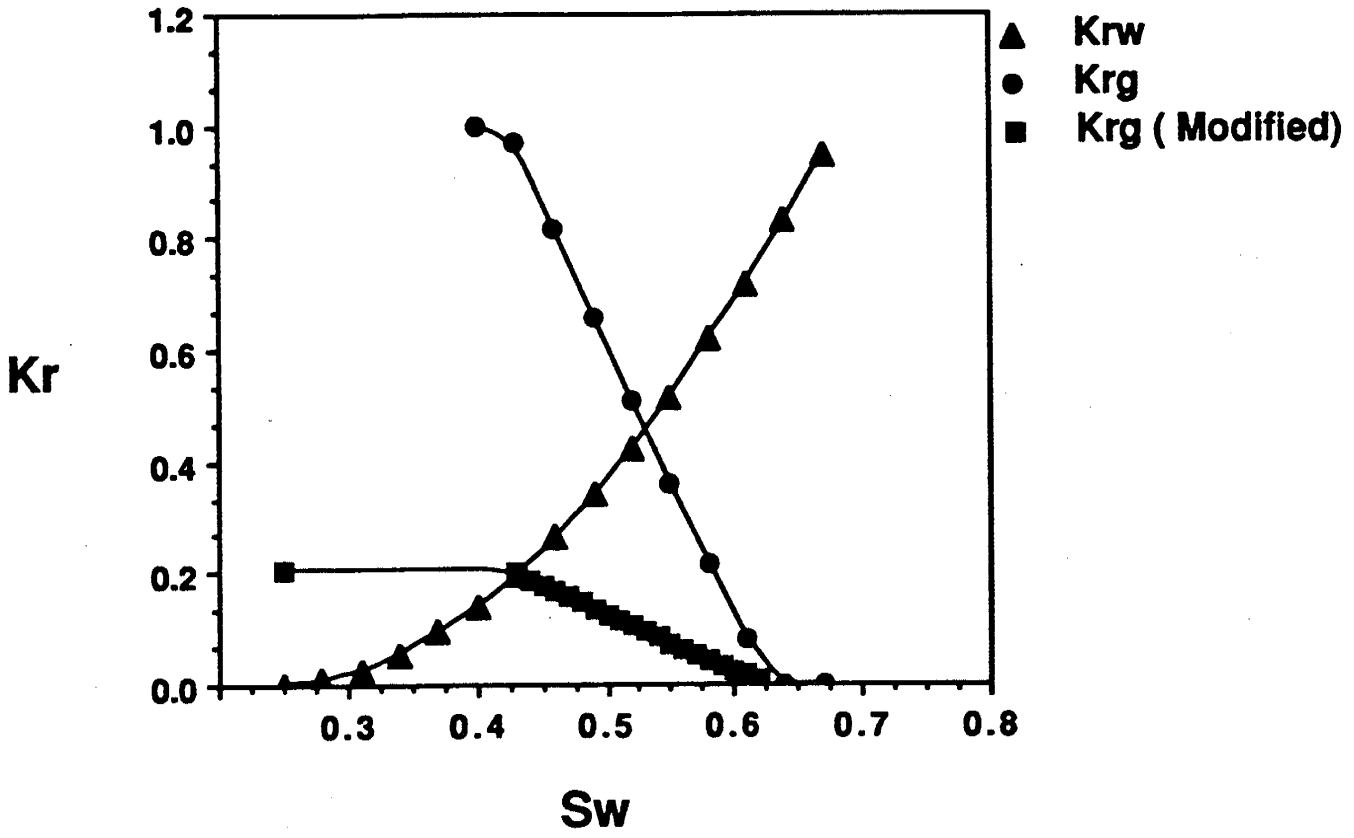

Fig. 15 RELATIVE WATER/STEAM PERMEABILITY CURVES MODIFIED FOR 100 psia AND 2 gr/min

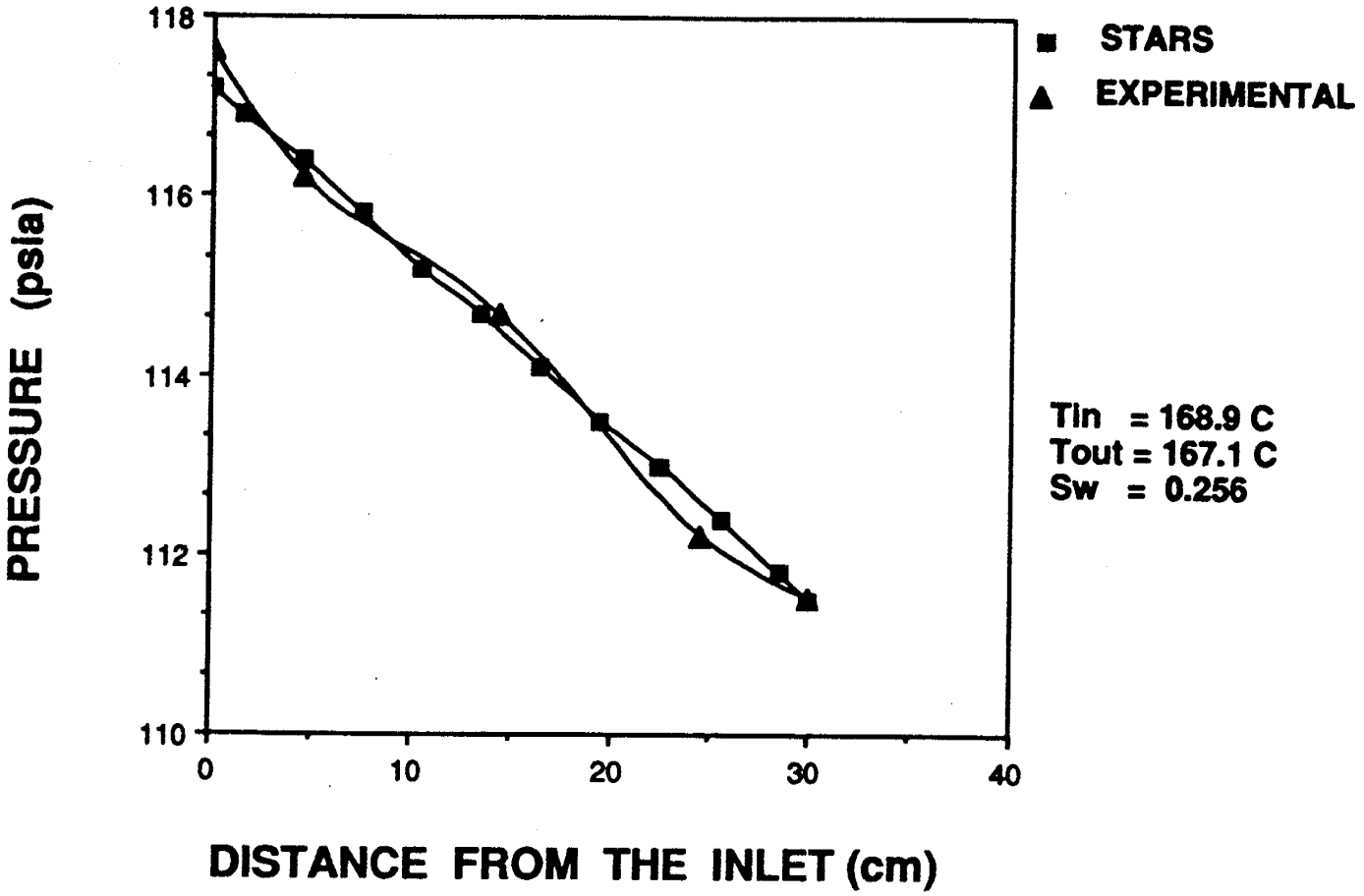

Fig. 16 EXPERIMENTAL PRESSURE PROFILES SIMULATED FOR 100 psia AND 2 gr/min WITH MODIFIED DATA

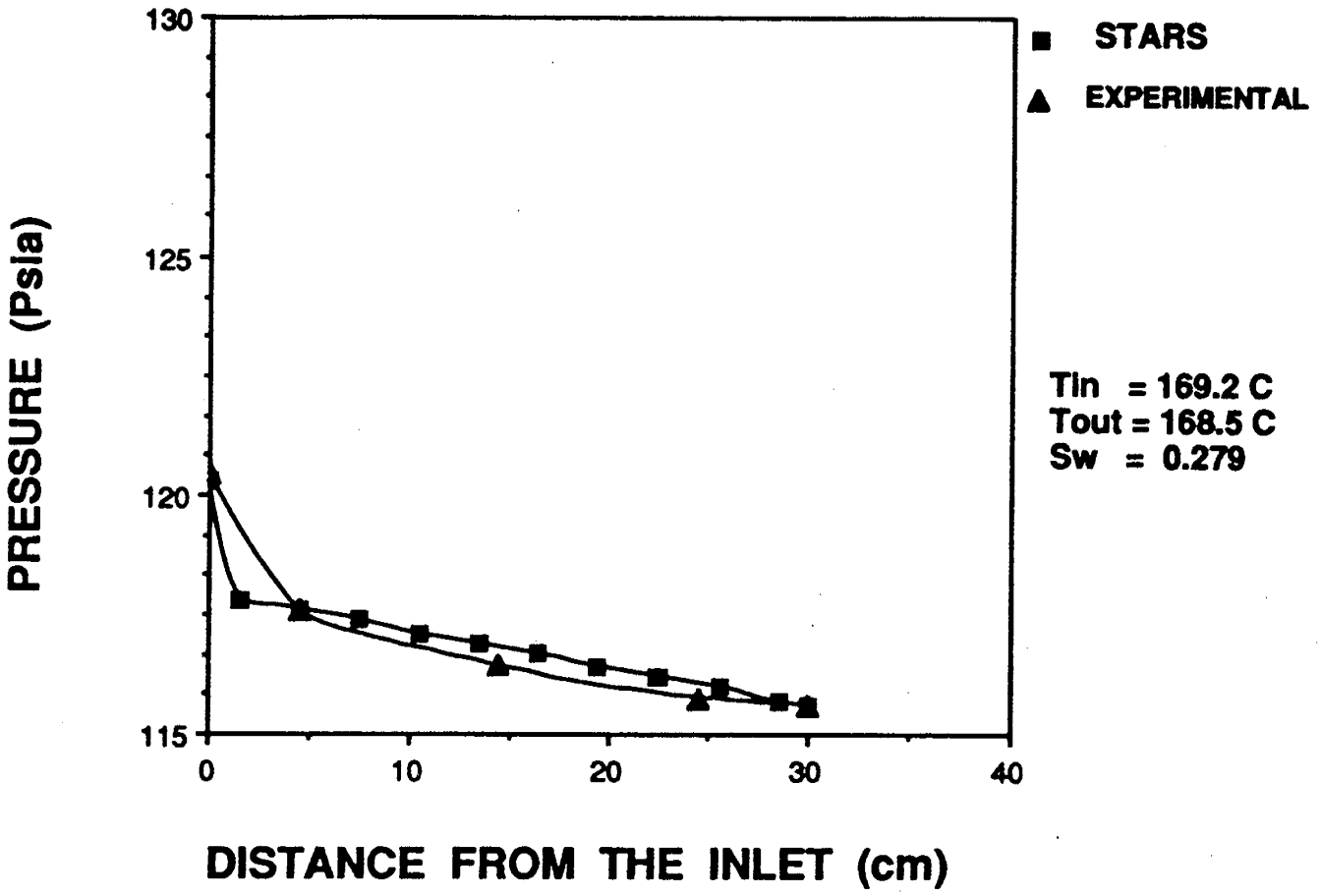

Fig. 17 EXPERIMENTAL PRESSURE PROFILES SIMULATED FOR 100 psia AND 4 gr/min WITH MODIFIED DATA

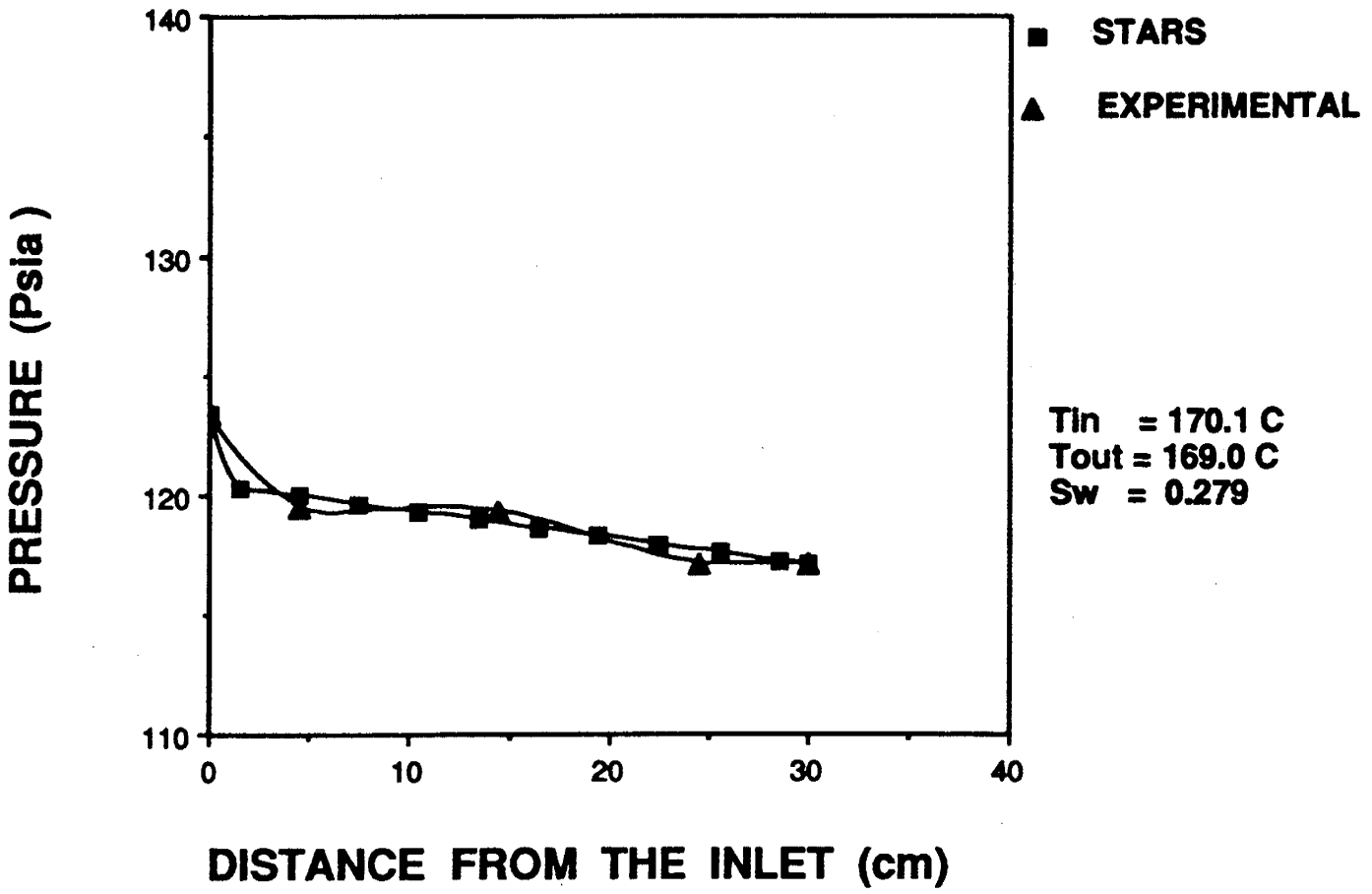

Fig. 18 EXPERIMENTAL PRESSURE PROFILES SIMULATED FOR 100 psia AND 6 gr/min WITH MODIFIED DATA

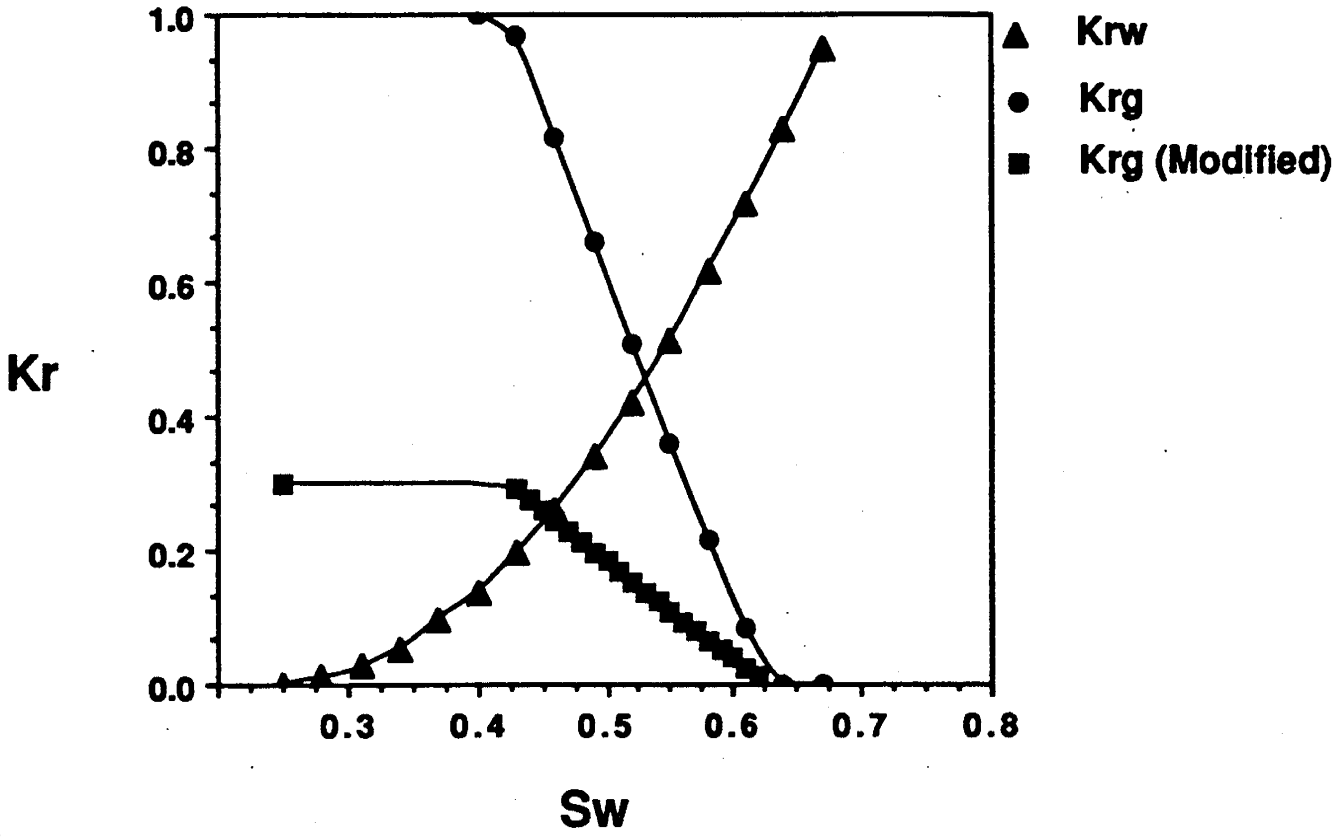

Fig. 19 RELATIVE WATER/STEAM PERMEABILITY CURVES MODIFIED FOR 200 psia AND 2 gr/min

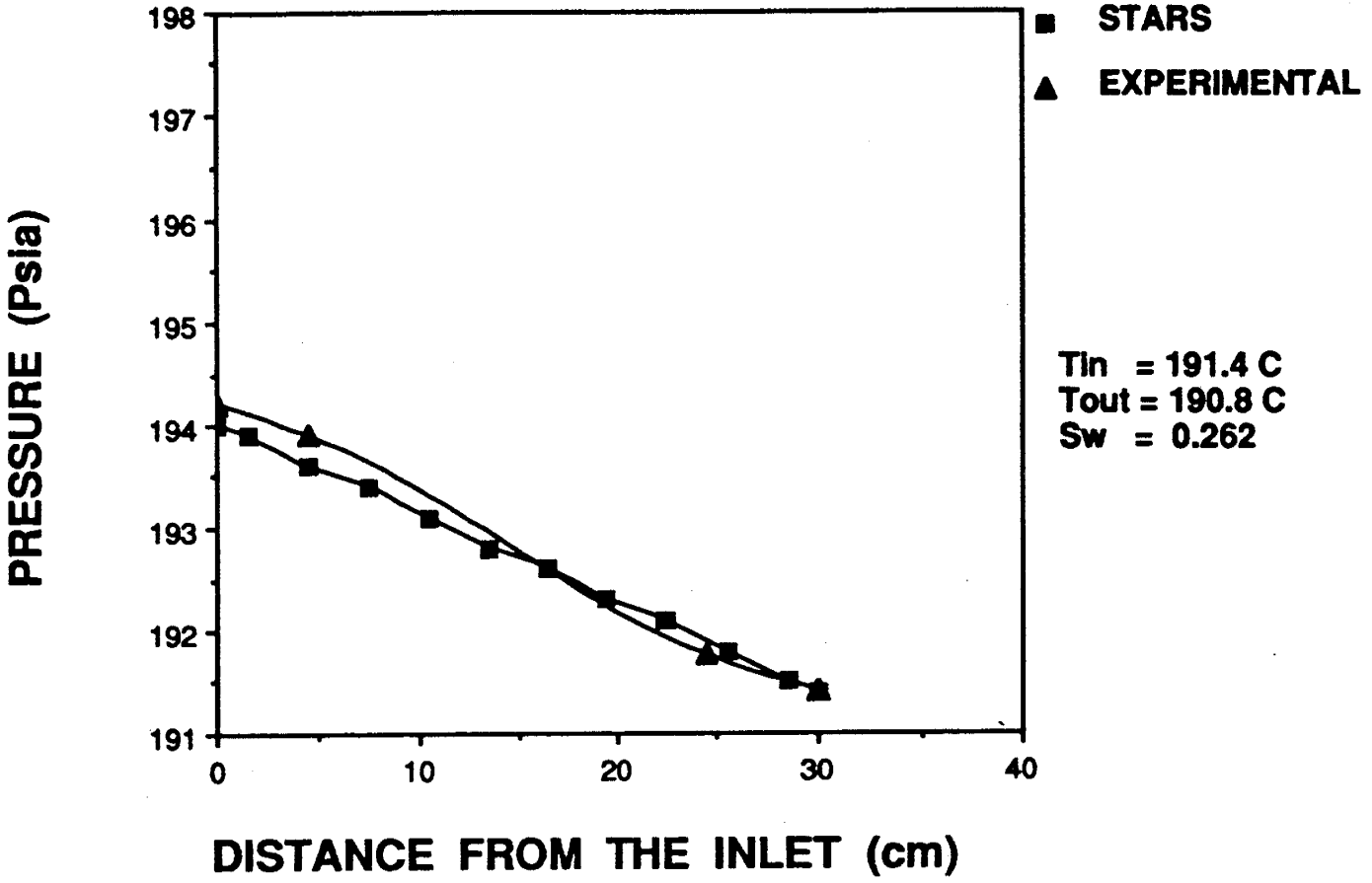

Fig. 20 EXPERIMENTAL PRESSURE PROFILES SIMULATED FOR 200 psia AND 2 gr/min WITH MODIFIED DATA

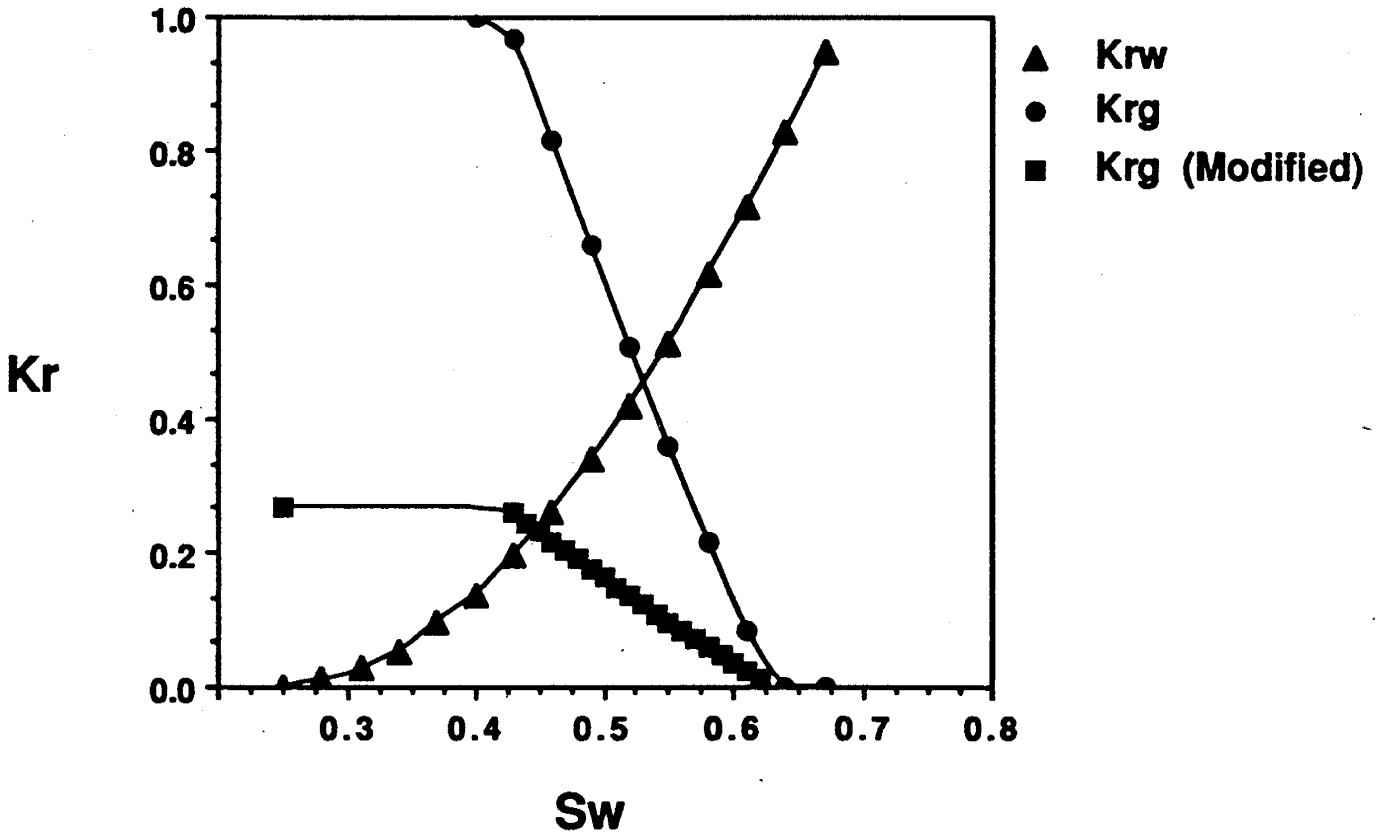

Fig. 21 RELATIVE WATER/STEAM PERMEABILITY CURVES
MODIFIED FOR 200 psia AND 4 gr/min

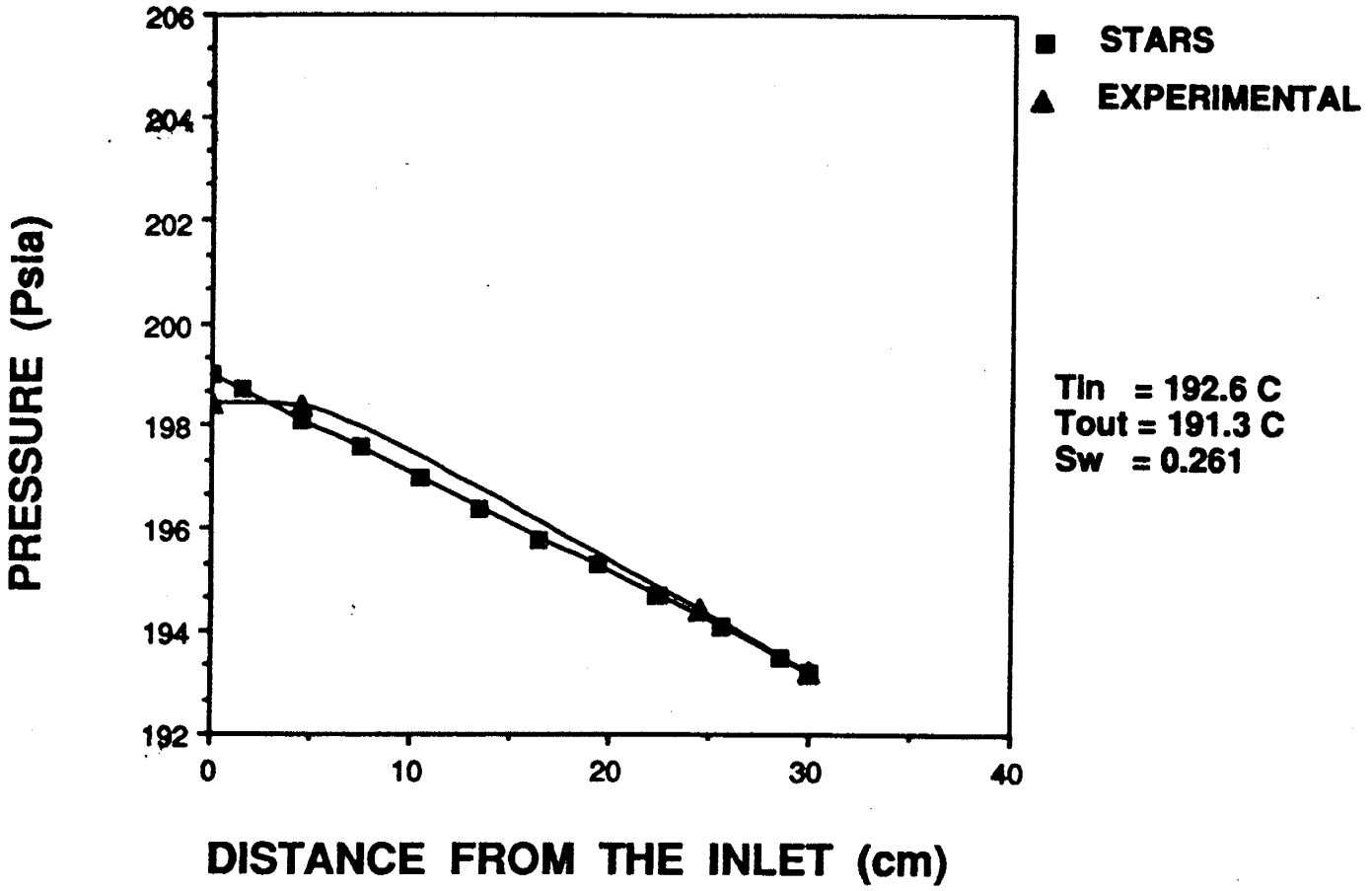

Fig. 22 EXPERIMENTAL PRESSURE PROFILES SIMULATED FOR 200 psia AND 4 gr/min WITH MODIFIED DATA

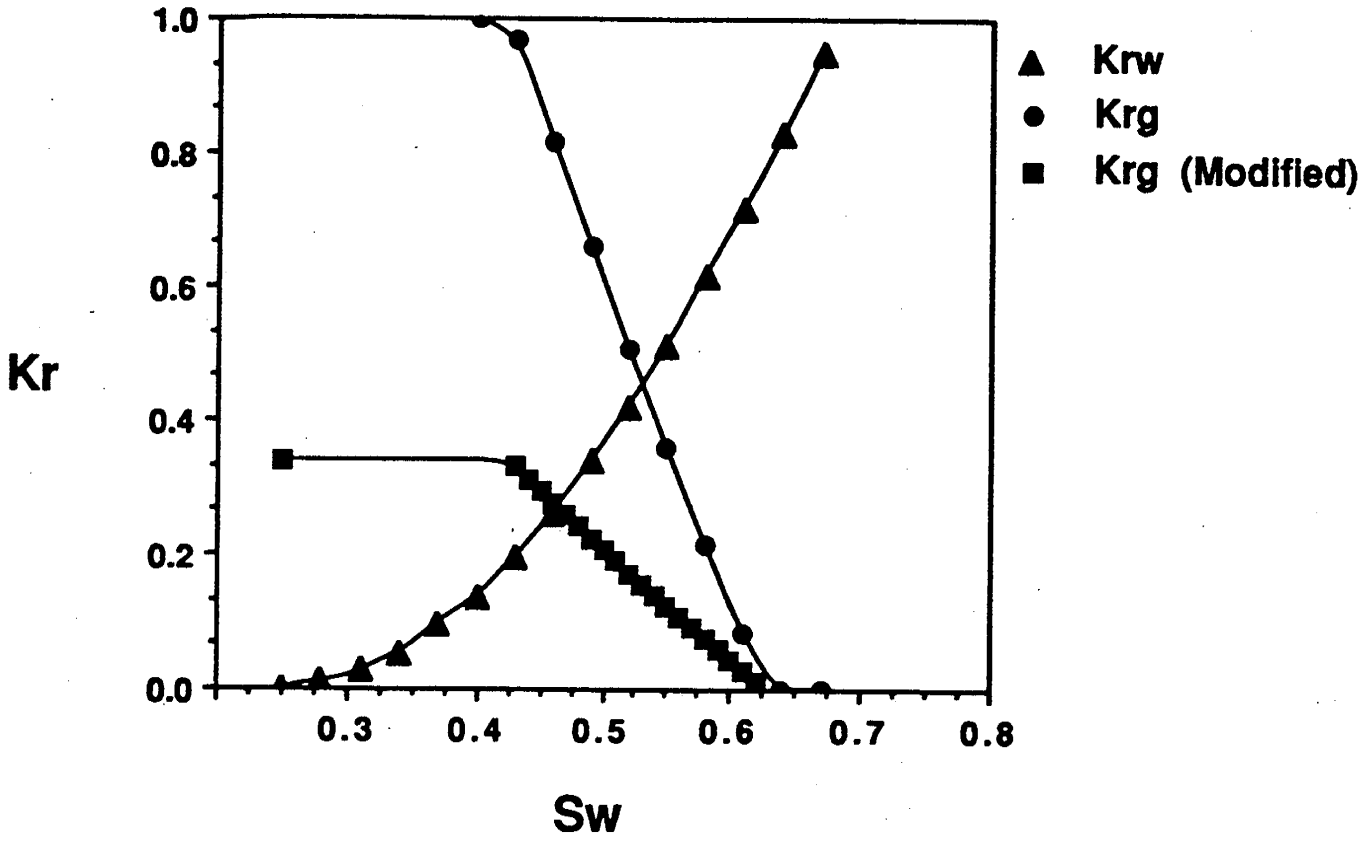

Fig. 23 RELATIVE WATER/STEAM PERMEABILITY CURVES
MODIFIED FOR 200 psia AND 6 gr/min

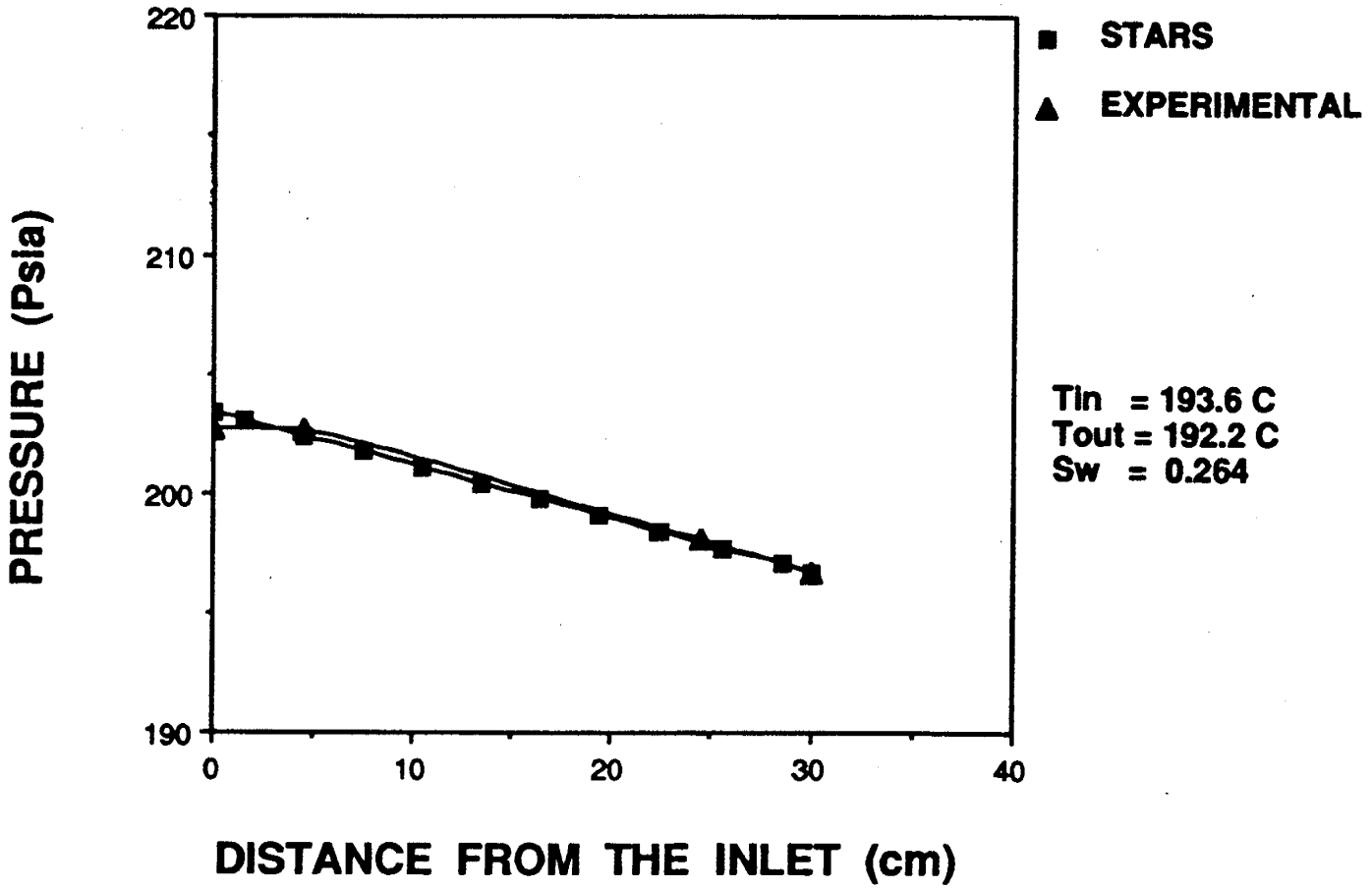

Fig. 24 EXPERIMENTAL PRESSURE PROFILES SIMULATED FOR 200 psia AND 6 gr/min WITH MODIFIED DATA

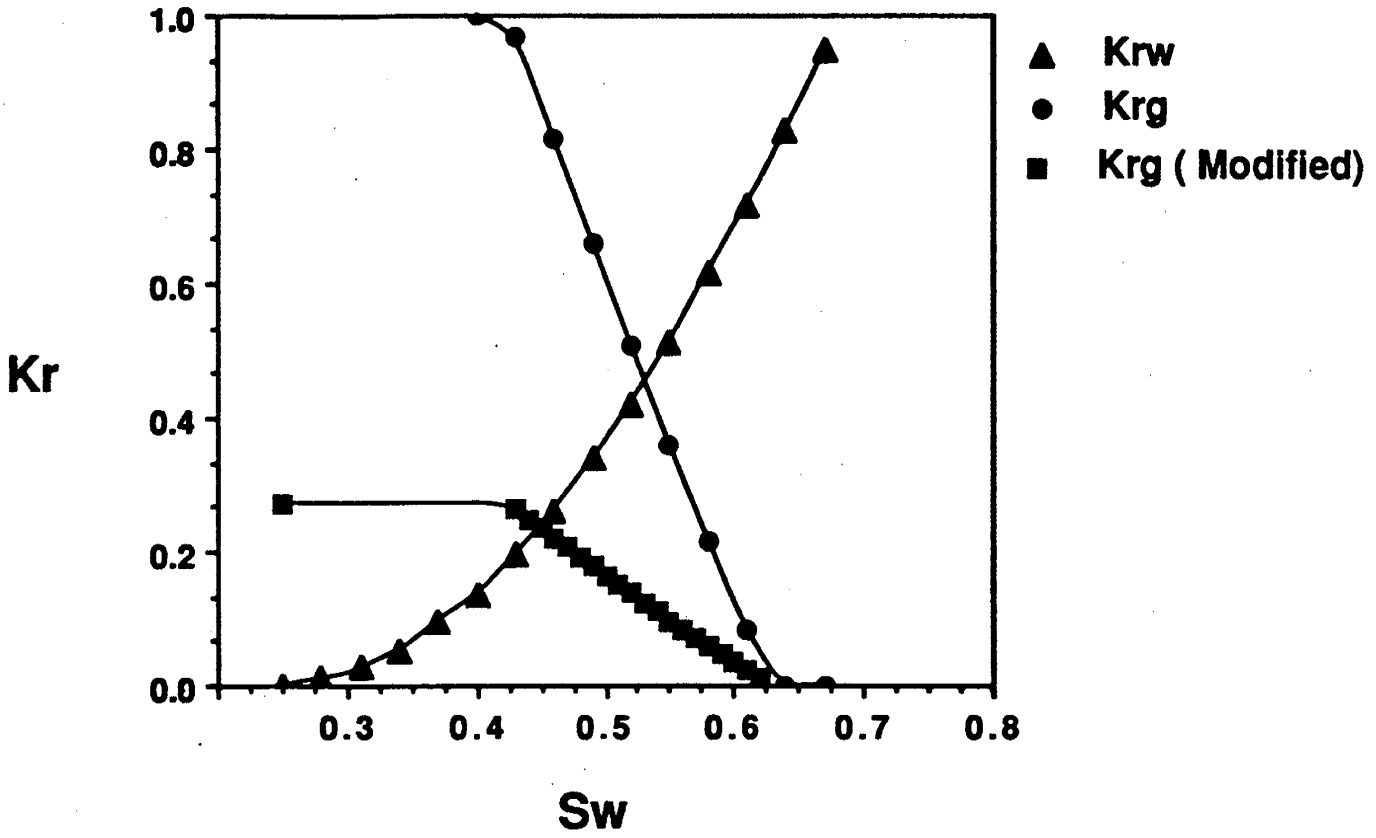

Fig. 25 RELATIVE WATER/STEAM PERMEABILITY CURVES
MODIFIED FOR 300 psia AND 2 gr/min

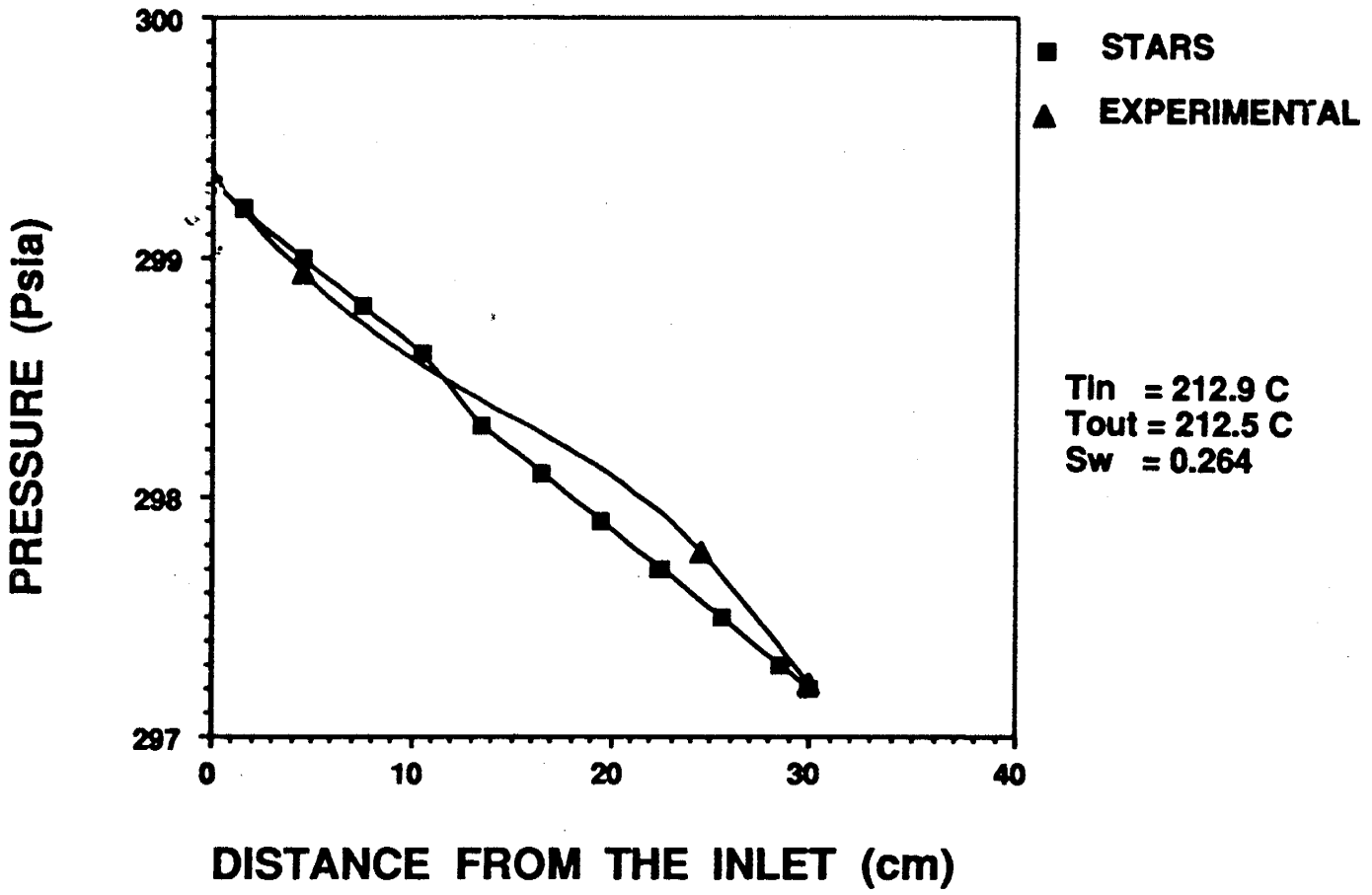

Fig. 26 EXPERIMENTAL PRESSURE PROFILES SIMULATED FOR 300 psia AND 2 gr/min WITH MODIFIED DATA

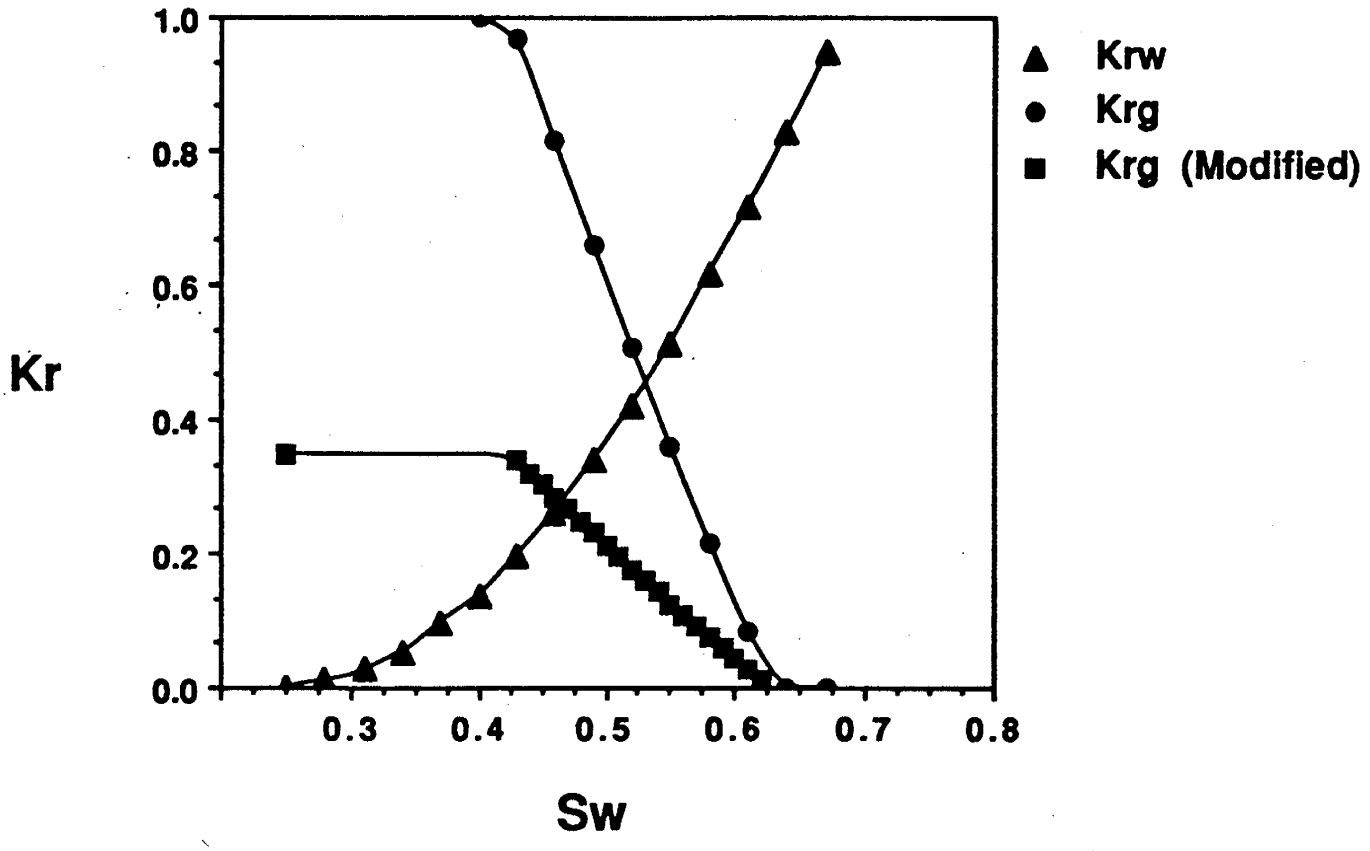

Fig. 27 RELATIVE WATER/STEAM PERMEABILITY CURVES
MODIFIED FOR 300 psia AND 4 gr/min

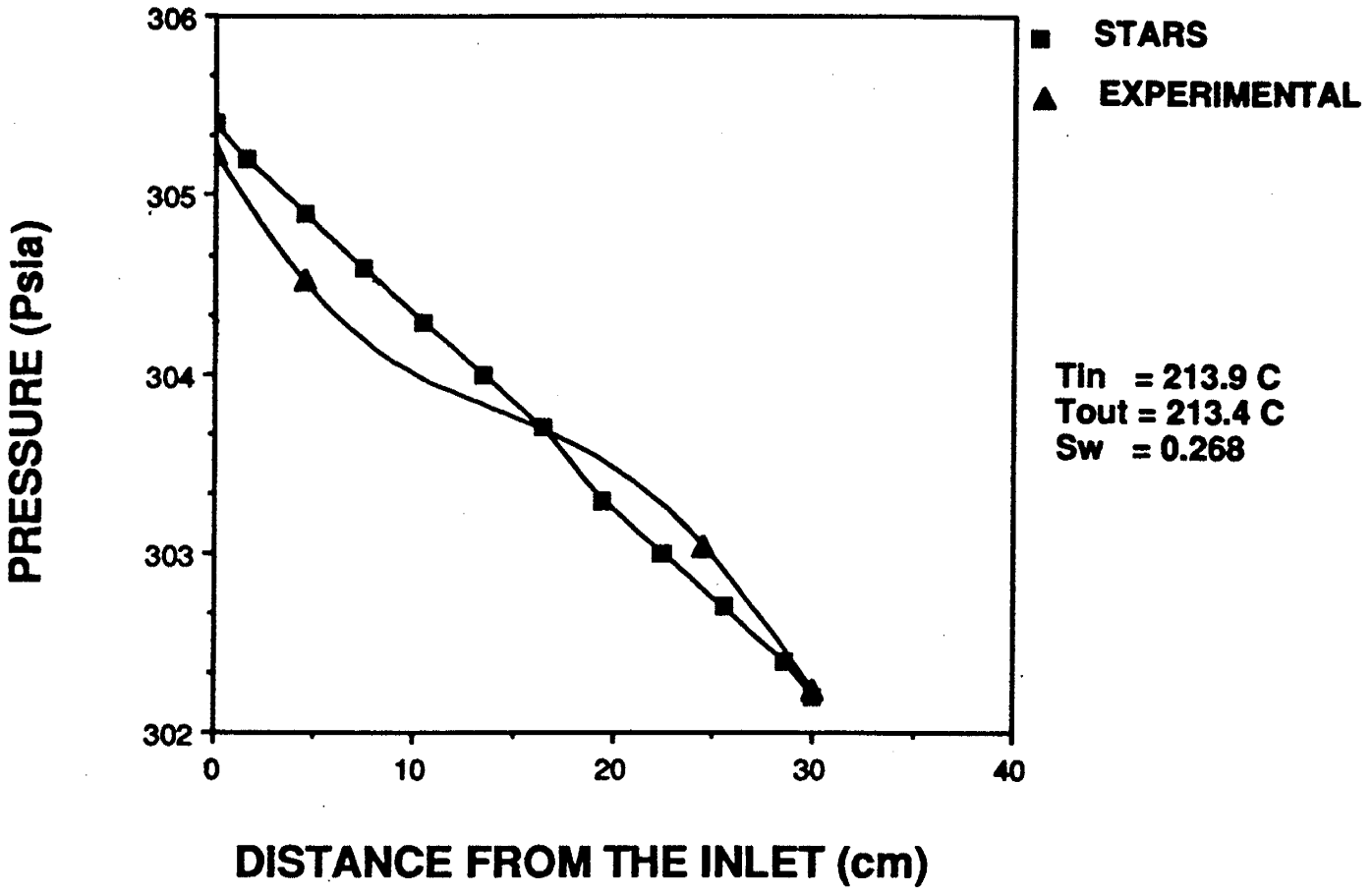

Fig. 28 EXPERIMENTAL PRESSURE PROFILES SIMULATED FOR 300 psia AND 4 gr/min WITH MODIFIED DATA

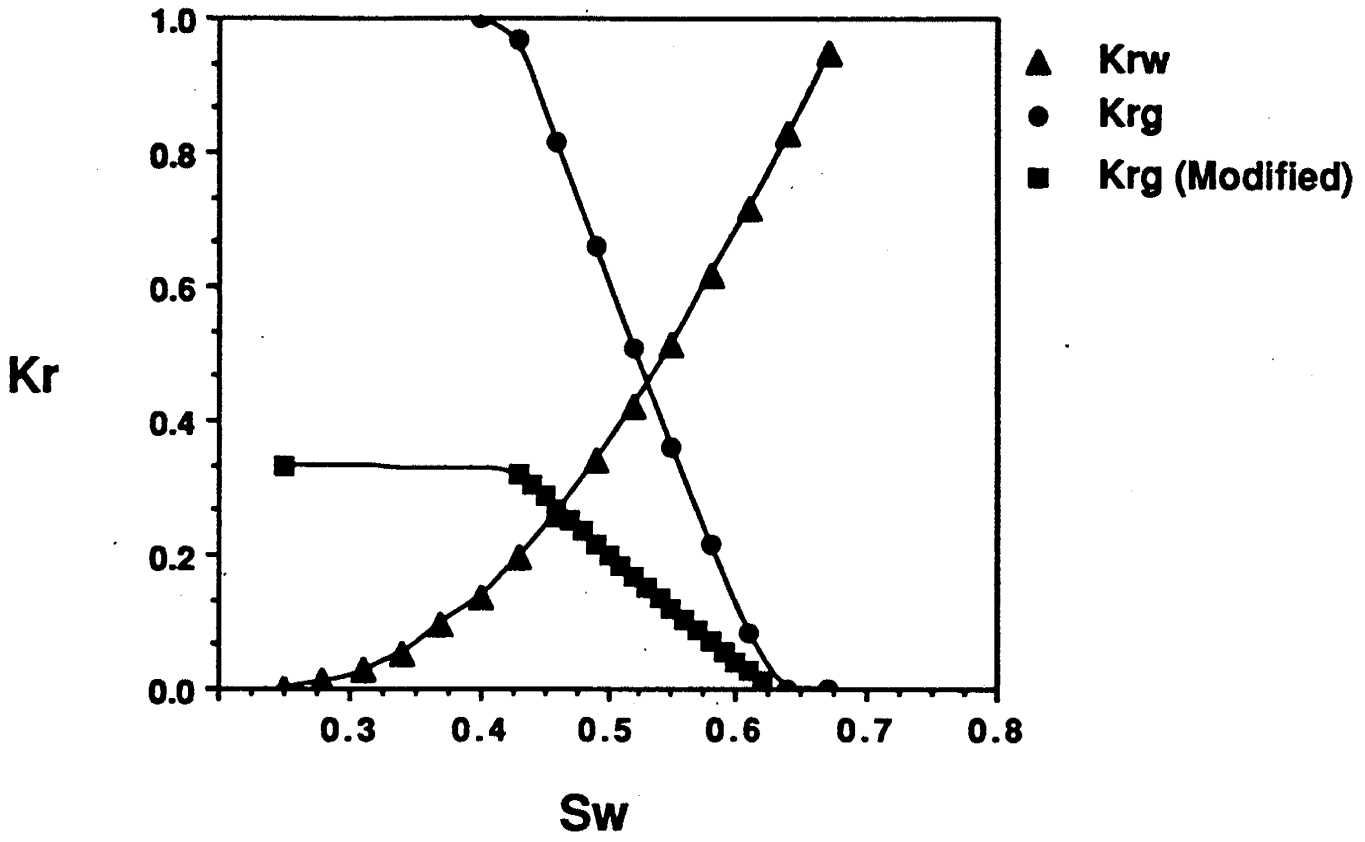

Fig. 29 RELATIVE WATER/STEAM PERMEABILITY CURVES
MODIFIED FOR 300 psia AND 6 gr/min

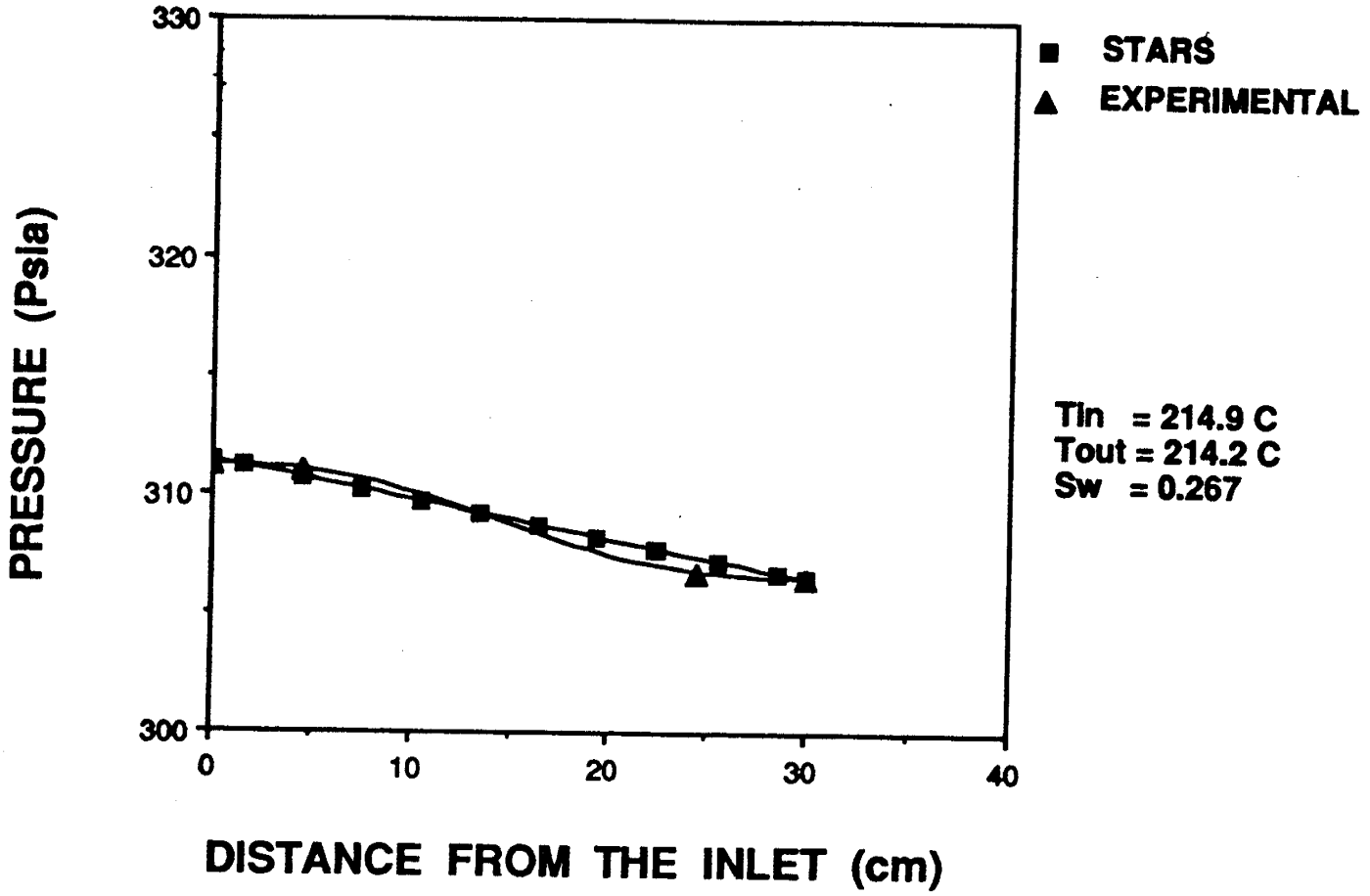

Fig. 30 EXPERIMENTAL PRESSURE PROFILES SIMULATED FOR 300 psia AND 6 gr/min WITH MODIFIED DATA

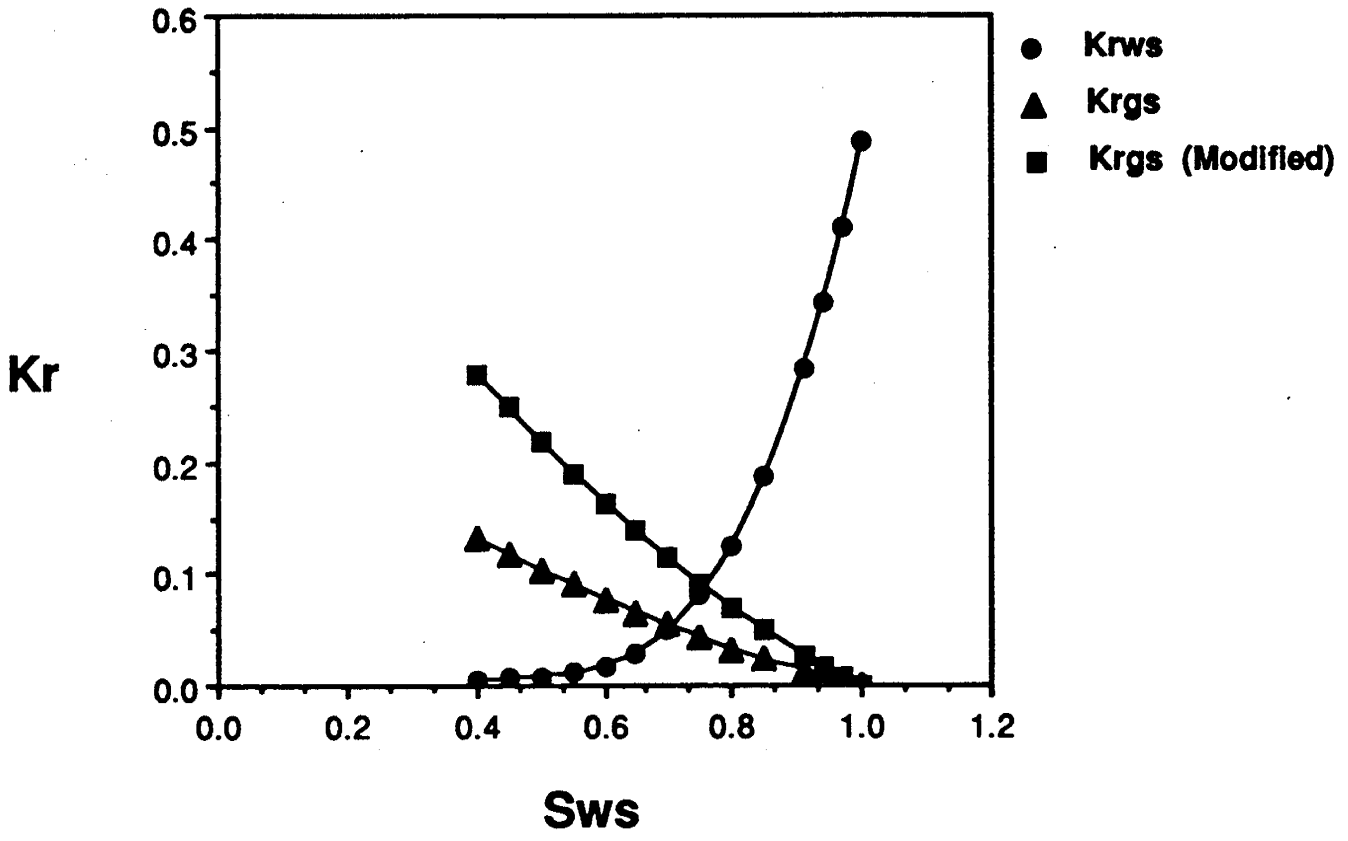

Fig. 31 RELATIVE WATER/STEAM PERMEABILITY CURVES WITH SURFACTANT MODIFIED FOR 200 psia AND 2 gr/min

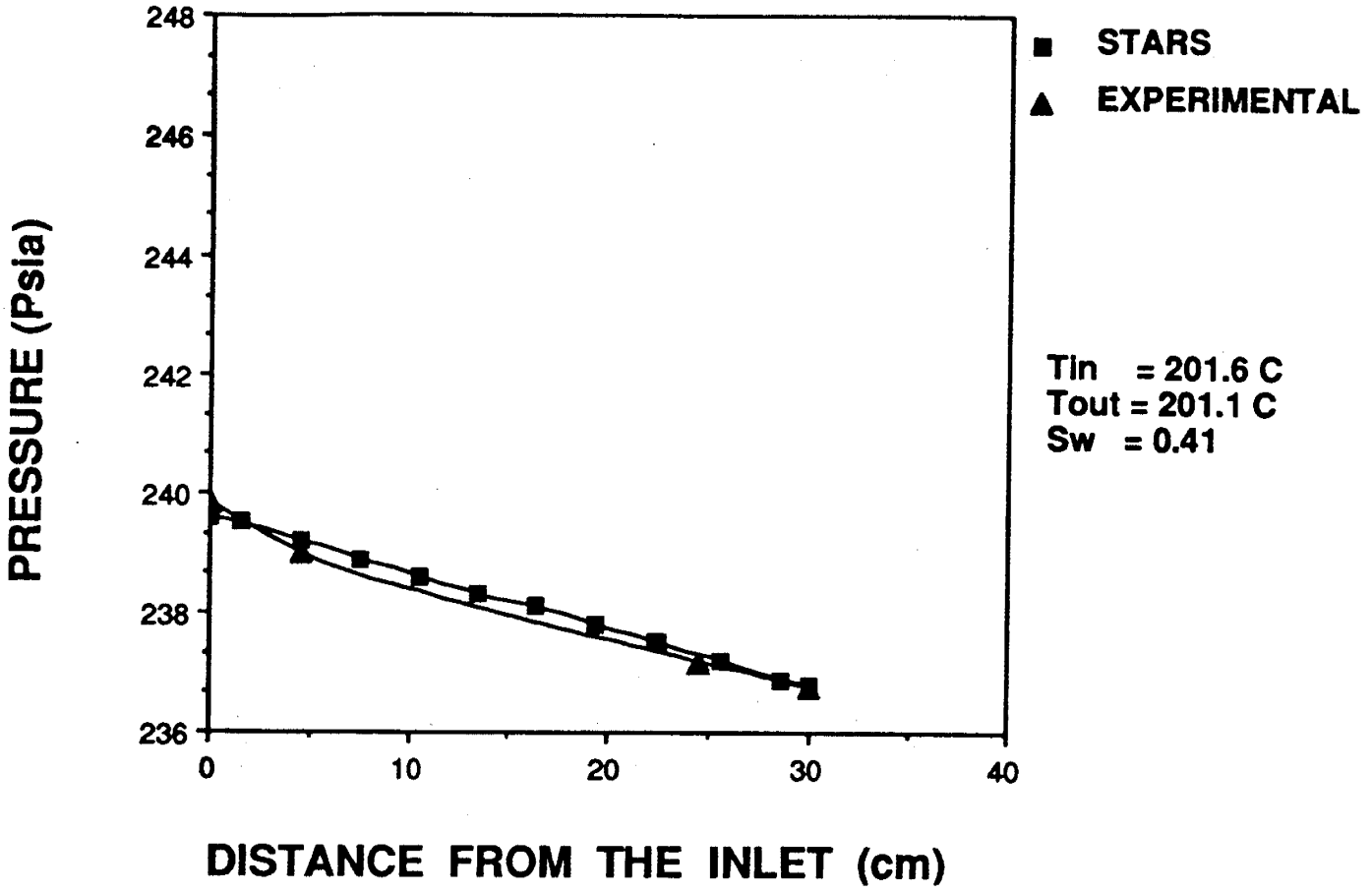

Fig. 32 EXPERIMENTAL PRESSURE PROFILES SIMULATED FOR 200 psia AND 2 gr/min WITH 0.5% SURFACTANT WITH MODIFIED DATA

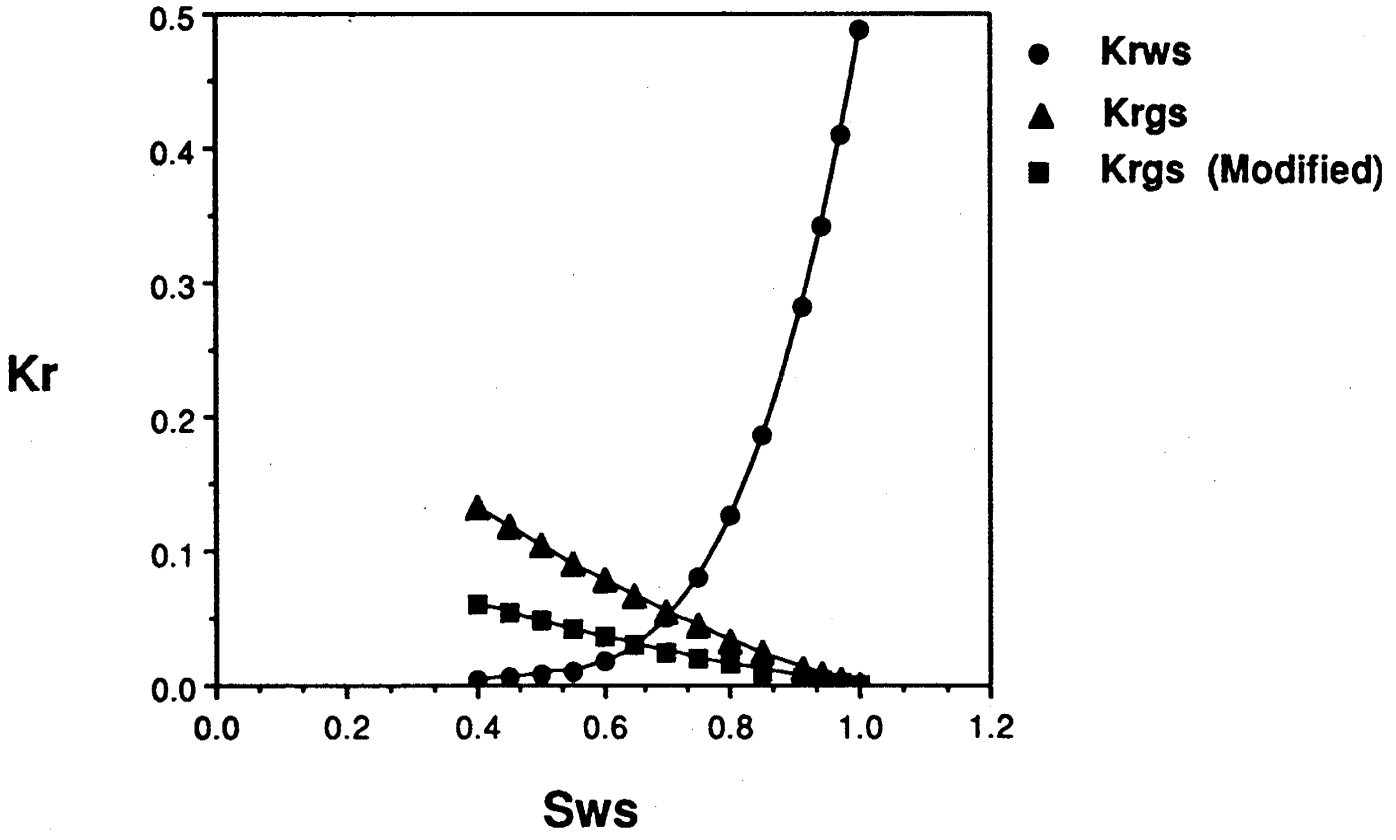

Fig. 33 RELATIVE WATER/STEAM PERMEABILITY CURVES WITH SURFACTANT MODIFIED FOR 200 psia AND 4 gr/min

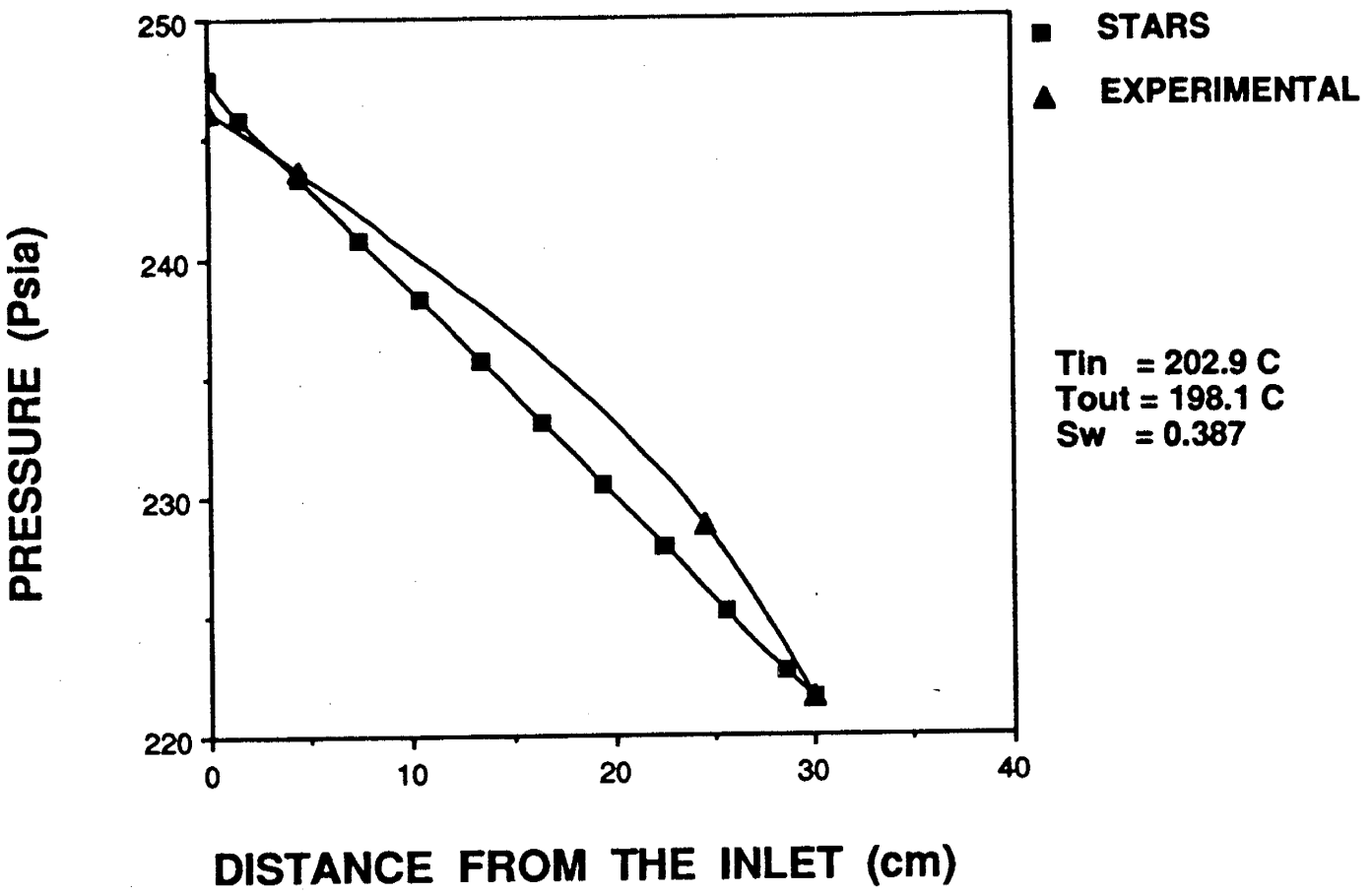

Fig. 34 EXPERIMENTAL PRESSURE PROFILES SIMULATED FOR 200 psia AND 4 gr/min WITH 0.5% SURFACTANT WITH MODIFIED DATA

64

Table 1. Operational Conditions and Result Localization for Simulations with Original Data

TEST (N°)	INJECTION RATE (gr/min)	OUTLET PRESSURE (Psia)	RESULTS (Fig. N°)
1	2.00	111.52	2
2	4.00	115.62	3
3	6.00	117.06	4
4	2.00	191.41	5
5	4.00	191.18	6
6	6.00	192.02	7
7	2.00	297.22	8
8	4.00	302.24	9
9	6.00	306.46	10
10	2.00	236.75	11 *
11	4.00	221.56	12 *

* with 0.5% of surfactant

Table 2. Operational Conditions and Result Localization for Simulations with Adjusted Data

TEST (N°)	INJECTION RATE (gr/min)	OUTLET PRESSURE (Psia)	K_{rg} MOD. (Fig. N°)	RESULTS (Fig. N°)
12	2.00	111.52	15	16
13	4.00	115.62	NM	17
14	6.00	117.06	NM	18
15	2.00	191.41	19	20
16	4.00	191.18	21	22
17	6.00	192.02	23	24
18	2.00	297.22	25	26
19	4.00	302.24	27	28
20	6.00	306.46	29	30
21	2.00	236.75	31	32 *
22	4.00	221.56	33	34 *

NM: Non-modified permeability

* = with 0.5% of surfactant

Task 46 - DOE shall provide INTEVEP with information from laboratory studies on light oil steamflooding conducted by NIPER. The research is to describe the influence of reservoir rock and its wettability, its composition, brine and steam temperature on oil recovery from light oil reservoirs.

NIPER-552
Distribution Category UC-122

LIGHT OIL STEAMFLOODING - EFFECT OF WETTABILITY ON STEAMFLOOD PERFORMANCE

Report For Annex IV—Task 46

By David K. Olsen

Work performed for
U.S. Department of Energy
Under Cooperative Agreement
DE-FC22-83FE60149

Thomas B. Reid, Program Manager
U.S. Department of Energy
Bartlesville Project Office

DISCLAIMER

IIT Research Institute
NATIONAL INSTITUTE FOR PETROLEUM AND ENERGY RESEARCH
P.O. Box 2128
Bartlesville, Oklahoma 74005
(918) 336-2400

TABLE OF CONTENTS

TABLES

ILLUSTRATIONS

ABSTRACT

This report summarizes research presented as part of the ANNEX IV report for Task 46, Light Oil Steamflooding. Four interrelated topics are described: the methodology for measuring capillary pressure and wettability at elevated temperature, the use of silylating agents to convert water-wet Berea sandstones or unconsolidated quartz sands to oil-wetted surfaces, the evaluation of the thermal and hydrolytic stability of these oil-wet surfaces for possible use in laboratory studies using steam and hot water to recover oil, and the effect of porous media of different wettabilities on oil recovery where the porous media is first waterflooded and then steamflooded.

All elevated temperature capillary pressure evaluations with various fluid/porous media systems yielded similar results. The capillary pressure curves were similar in shape, but irreducible brine saturations were found to increase as run temperatures increased. Wettability values were found to increase (become more water-wet) as run temperatures were increased. Artificially oil-wet porous media were produced by treatment with asphaltenes or polar crude oil components, and by silylation using both liquid-phase and vapor-phase treatments. Thermal stabilities and hydrolytic stability of the oil-wet surfaces were evaluated by observing changes in the wettability index as cores were subjected to hot water or steam displacements, with or without crude oil coating the porous media. Cores treated with asphaltenes or polar crude oil components failed to produce a lasting oil-wet surface. Liquid-phase silylation of silica surfaces yielded oil-wet surfaces that reverted to water-wet upon exposure to hot water. Vapor-phase silylation using bis(dimethylamino)dimethylsilane resulted in a bidentate bound $Si(CH_3)_2$ group chemically bonded to the silica surface. This artificially oil-wet surface was more inert and resisted changes in wettability. Laboratory oil recovery experiments, using steam in one-dimensional Berea sandstone cores of various wettabilities, showed that oil-wet sandstones responded to steam faster than water-wet sandstones, but both attained final residual oil saturations of less than 12%.

A series of steamflood experiments was conducted in a two-dimensional model using water-wet, intermediate-wet, and oil-wet porous media to investigate the steamflood potential for light oil production after waterflooding. The study evaluated the effects of changes in wettability on steamflooding light oils. New London crude oil (32° API) was used in the study. Comparisons of the oil saturation profiles of the sandpacks indicated higher initial oil saturations in oil-wet sandpacks. However, waterflooding recovered less oil at a slower rate and lower oil-water ratio from oil-wet sands. Oil-wet sands showed much higher residual oil saturation after reaching waterflood residual. Steamfloods initiated at this point displaced little oil from water-wet sandpacks. However, significant oil was displaced from oil-wet sandpacks. This study indicated that final oil saturation after steamflooding is independent of initial wettability.

OBJECTIVE

The purpose of this research was to evaluate specific changes in oil recovery by hot water and steam as a function of changes in wettability of porous media/fluid systems. To conduct this research, methodology was needed to determine changes in capillary pressure and wettability with increasing temperature.

ACKNOWLEDGMENTS

This work was performed by the IIT Research Institute, National Institute For Petroleum and Energy Research (NIPER) and sponsored by the U.S. Department of Energy (DOE) under cooperative agreement DE-FC22-83FE60149. The author wishes to thank P.S. Sarathi, M. E. Crocker, D. Roark, C. Robertson, S. M. Mahmood and E. B. Ramzel, all of NIPER, and J. Betancourt, visiting INTEVEP engineer at NIPER, for their research and analysis, and A. Strycker and M. K. Tham of NIPER and T. B. Reid of the DOE Bartlesville Project Office for their helpful reviews. This report summarizes research presented as part of the ANNEX IV report for task 46, Light Oil Steamflooding, as part of the technology exchange between the U. S. Department of Energy and the Ministry of Energy and Mines of the Republic of Venezuela. More complete descriptions of this research are given in the following references: (Olsen and Crocker, 1991), (Olsen, Crocker, Sarathi and Betancourt, 1991), and (Olsen, Sarathi, Roark, Ramzel and Mahmood, 1992).

BACKGROUND

Thermal recovery, by cyclic steam and steamdrive, is a commercial oil recovery technology that contributes nearly 454,000 barrels of oil per day (BOPD) or about 6% of the total daily United States oil production (Moritis, 1990). This oil is predominantly heavy oil, 10° to 20° API. Only two light oil steamfloods (LOS) are operating in the United States at the present time and both floods are in DOE-managed Naval Petroleum Reserve (NPR) fields. One flood is being conducted in the Shannon sandstone formation at NPR No. 3, Teapot Dome (WY) field. This test is in a highly fractured, consolidated, tight (63 mD) sandstone at a depth of 325 to 500 ft. The second LOS is in the Shallow Oil Zone (SOZ) at NPR No. 1, Elk Hills (CA) field. The SOZ pilot is being conducted in a highly calcareous, unconsolidated, multisand sandstone at a depth of 2,800 ft. Both steamfloods test LOS technology in very different adverse environments.

One target of LOS within the last 10 years has been previously waterflooded reservoirs (Chu, 1988; Hanzlik, 1981; Hong, 1986; Strycker 1988). Oil-wet reservoirs may be a more attractive, economic target for LOS because the oil saturation at the beginning of a LOS may be considerably higher in oil-wet reservoirs than in water-wet reservoirs (Olsen, 1990). In strongly water-wet

porous media, oil recovery at water breakthrough is high, with little additional production after water breakthrough. In strongly oil-wet porous media, water breakthrough occurs much earlier, and most of the oil recovered is slowly swept out during an extended waterflood with a low oil-water ratio. This parallels what is observed in waterfloods of most sandstone reservoirs. Waterfloods are less efficient in oil-wet reservoirs than in water-wet reservoirs, because more water must be injected to recover the same amount of oil. As the wettability index increases (more water-wet), the water relative permeability increases, and oil relative permeability decreases. Consequently, water flows more easily than oil causing progressively earlier breakthrough and lower oil recovery (Anderson, November and December 1987).

NIPER has been investigating the recovery of light oil by steamflooding for several years. Strycker and Sarathi (1988) presented a critical review of previous LOS studies. The economics of steamflooding require that the product of oil saturation times permeability be high (Chu, 1983; Chu, 1988; Farouq Ali, 1978; Farouq Ali and Meldau, 1978). However, most waterfloodable light oil reservoirs have already been waterflooded to a relatively low oil saturation; thus, the porosity-saturation product may be unfavorable, and subsequent steamflooding of such reservoirs may be uneconomic. Injection of steam or any other gas into these previously waterflooded reservoirs would tend to follow previously waterflooded channels and result in poor sweep efficiency. In addition, heat loss to the water phase may be excessive (water has a higher heat capacity than oil). Oil-wet light oil reservoirs, which often exhibit poor waterflood recovery, may have sufficient oil saturation to make light oil steamflooding technically and economically feasible.

NIPER needed porous media that was significantly more oil-wet than very strongly water-wet to evaluate specific changes in oil recovery by treatments with hot water and steam as a function of wettability of porous media/fluid systems. Both strongly oil-wet and intermediate-wet porous media were needed. Several methods were tried to provide these media including precipitation of asphaltene and polar fractions on porous media, treatment of porous media with siloxane and silylating agents in the liquid phase, and finally silylation of the porous media using reagents in the gas phase to attain more uniform coverage of the surface and potentially more stable oil-wet surfaces. The thermal and hydrolytic stability of these oil-wet surfaces needed to be determined to see if the surface was degrading and reverting to a water-wet condition. The surface needed to be sufficiently inert to permit observing the effect of steam on changing the wettability of the surface in laboratory oil displacement tests.

RESULTS AND DISCUSSION

Effect of Temperature on Capillary Pressure and Wettability

The effect of elevated temperature on capillary pressure has been previously studied (Samaroo and Guerrero, 1981; O'Kandan et al., 1974; Sanyal et al., 1973; Sinnokrot et al., 1971). Samaroo and Guerrero (1981) indicated that increases in irreducible water saturation with elevated temperature should correspond with increased oil recovery.

As part of this study, NIPER modified a centrifuge and test cells to evaluate capillary pressure and wettability at elevated temperature (Olsen, Crocker, Sarathi and Betancourt, 1991). The effect of elevated temperature on core saturation was evaluated in a series of experiments using different porous media-fluid systems including mineral oil and New London crude (32 °API, from the site of a proposed LOS in south-central Arkansas). The results of capillary pressure determinations for a simple porous media-fluid system, nitrogen/brine (2% NaCl)/Berea sandstone at 75°, 150°, 250°, and 350° F are shown in figure 1. The capillary pressure curves were calculated based upon the method of Rajan (1986) and show an increase in irreducible water saturation at each temperature at which the centrifuge measurement was conducted. Figure 2 shows the trend of increasing irreducible water saturation for two different fluid systems in Berea sandstone. Both figures show increasing irreducible water saturation with increasing temperature. These results are in agreement with the literature (Samaroo and Guerrero, 1981; Sanyal et al., 1973; Sinnokrot et al., 1971; O'Kandan et al., 1974), where similar capillary pressure experiments have shown increases in irreducible water saturations with increasing temperature. The increase in irreducible water saturation with increasing temperature has been postulated to arise from a wettability change in the core towards a more water-wet state (Samaroo and Guerrero, 1981; O'Kandan et al., 1974; Sanyal et al., 1973; Sinnokrot et al., 1971). Another possible cause postulated is a reduction in the oil-water viscosity ratio (Honarpour et al., 1986).

To evaluate the effect of temperature on wettability, a series of experiments was conducted (fig. 3) with a number of fluid systems in Berea sandstone. The wettability index was calculated using the USBM method (Donaldson et al., 1969). The results show increasing wettability (more water-wet) with increasing temperature. The USBM method uses the ratio of the areas under the imbibition and drainage capillary pressure curves to calculate a wettability index (W), where $W = \log(A_1/A_2)$ and where A_1 and A_2 are areas under the oil and brine-drive capillary pressure curves, respectively. The USBM wettability index typically ranges from -1.0 (highly oil-wet) to +1.0 (highly water-wet) for most reservoir rock. It is possible to exceed these values if the area under one capillary pressure curve is much greater than the other.

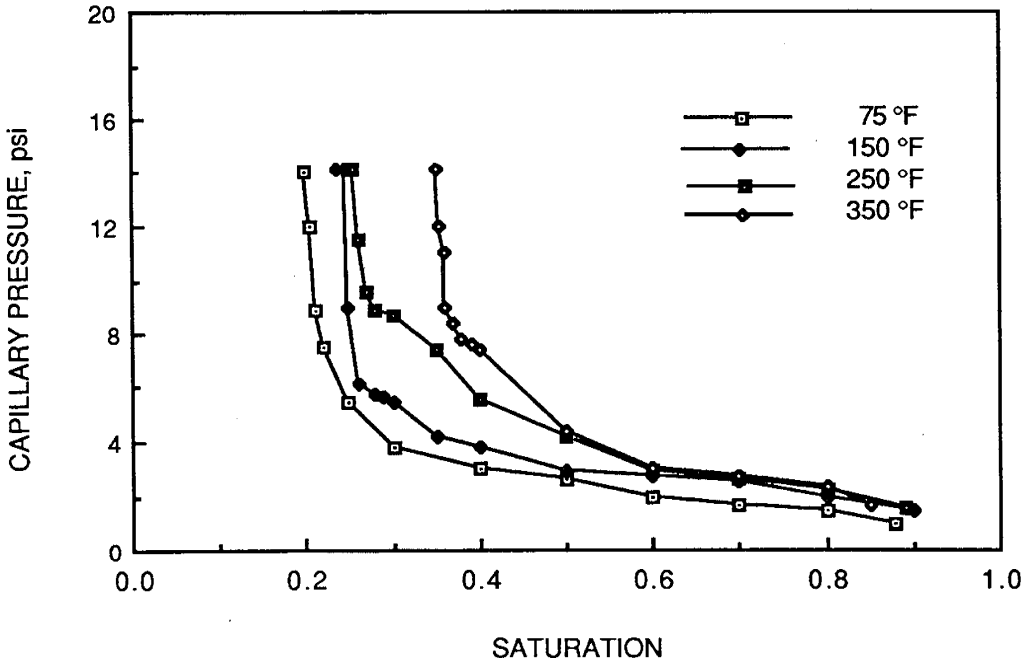

FIGURE 1. - Capillary pressure curves for nitrogen/brine/Berea sandstone.

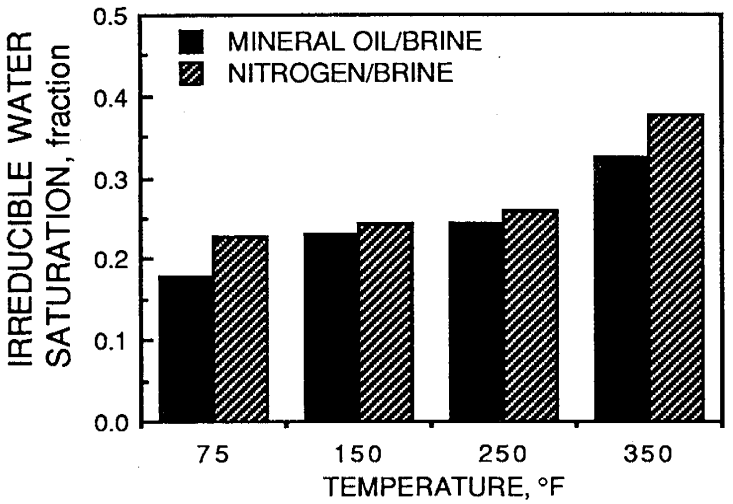

FIGURE 2. - Final irreducible water saturations for nitrogen/brine/Berea sandstone and mineral oil/brine/Berea sandstone.

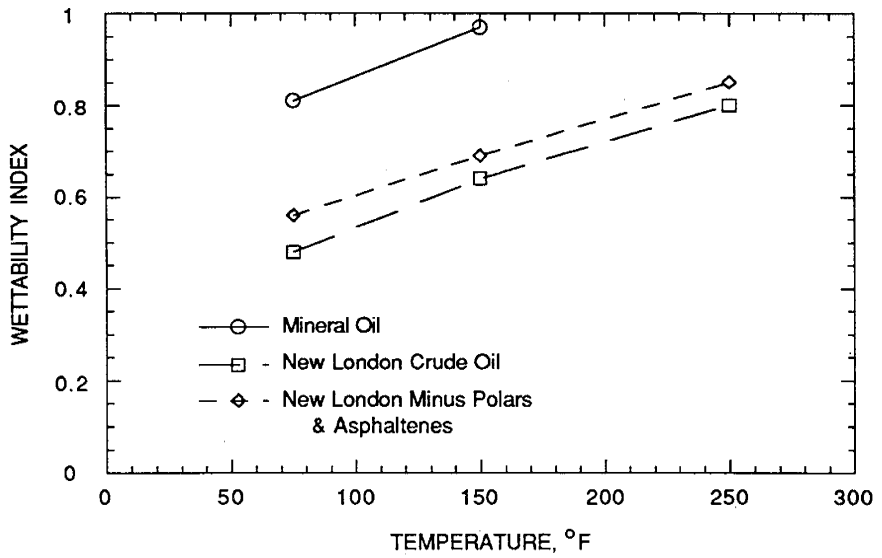

FIGURE 3. - Comparison of wettability values at various temperatures.

Preparation and Evaluation of Artificially Oil-Wet Surfaces

Laboratory studies of fluid displacement in porous media are often used to model oil production occurring in the field. Tests in native-state, preserved cores would be preferred, but this step in the design process is often not feasible because of the high costs of acquiring field core. Outcrop core from numerous areas throughout the world have been used. The literature reveals that very strongly water-wet Berea sandstone is the porous matrix material most often used in the United States for evaluating oil recovery systems designed for sandstone reservoirs. However, oil recovery from Berea sandstone cores is often twice that of native-state cores. The high oil recovery is due to more homogeneous rock than most formations, the low clay content and very strongly water-wet nature of the surface of Berea sandstone. Many oil reservoirs are not very strongly water-wet, but rather are of intermediate wettability (Cuiec, 1990; Willhite, 1986). The effect of wettability on waterflood oil recovery is well known and has been the subject of recent reviews by Morrow (1990) and Anderson (1987).

Fired cores are often used to minimize laboratory problems by simplifying operating problems caused by fines migration, ion exchange, adsorption, and clay swelling. Firing cores increases reproducibility of many tests used to evaluate process variables, but this is at the expense of changing other phenomena occurring in the displacement. Each simplification or modification of the porous media tends to remove the modeling of the field away from the native state. Scaled physical experiments often limit the choice of porous media and the wettability of the surface of the

media. The importance of porous media selection depends upon what process is modeled, the information needed, and the extent of detail and time that can be expended to scale the oil recovery process.

Physical models are widely used to simulate chemical and physical phenomena in steamflood displacement. In low-pressure, scaled-model studies, the porous media has typically been very strongly water-wet glass beads (Doscher et al., 1982; Doscher, 1981; Sufi, 1990; Ahner and Sufi, 1990; Lookeren, 1977; Farouq Ali, 1985). High-pressure models have used unconsolidated field sand of intermediate wettability (Quettier and Corre, 1988; Green and Isaacs, 1986), very strongly water-wet quartz sands (Butler and Yee, 1986; Ozen and Farouq Ali, 1967; Coats, et al., 1974), or very strongly water-wet consolidated sandstone, such as Berea sandstone (Ozen and Farouq Ali, 1967; Sarathi et al., 1990; Madden and Sarathi, 1985), or crushed Berea sandstone (Madden and Sarathi, 1985; Wu and Fulton, 1971) as the porous media in their laboratory studies of thermal oil recovery processes.

In recent years, NIPER has conducted light oil steamflood displacement tests using each of the above porous media, but our capillary pressure/wettability measurements have indicated that oil-wet or intermediate-wet field sands became more water-wet during steamflooding (Olsen et al., 1991; Sarathi et al., 1989). Crocker and Marchin (1988 and 1986) conducted a series of laboratory studies to produce stable wettabilities in core samples using both asphaltenes and polar fractions of crude oils and organosilane agents applied in the liquid phase. They found that the wettability change was not permanent and could be reversed by soaking in brine. Recently, Takach, et al. used gas-phase silylation to obtain an oil-wet surface on glass plates (Takach et al., 1988) and cores (Takach et al., 1989) for their study of waterflood and chemical flooding EOR.

Silylation involves chemical modification of the silica surface (replacement of the H-atoms of the surface hydroxyl groups by covalently bound organosilyl groups) to produce a hydrophobic surface and is used extensively in the manufacture of chromatographic column packings to produce a reverse phase or hydrophobic surface. There are several different ways that the Si-O-H functional group on a silica surface can be capped, as shown by the series of reactions in figure 4. The most common method uses a monofunctional silylation agent that forms a single bond, such as with hexamethyldisilazane. Monofunctional endcapping gives a very reproducible surface and controlled coverage. Polyfunctional silylation agents can form multiple bonds to the silica surface such as obtainable with dichlorodimethylsilane or bis(dimethylamino)dimethylsilane which form bidentate molecules covering the surface.

NIPER prepared cores, plugs, and unconsolidated sand used for oil-wet displacement tests or wettability measurements by two different techniques: liquid-phase and vapor-phase silylation.

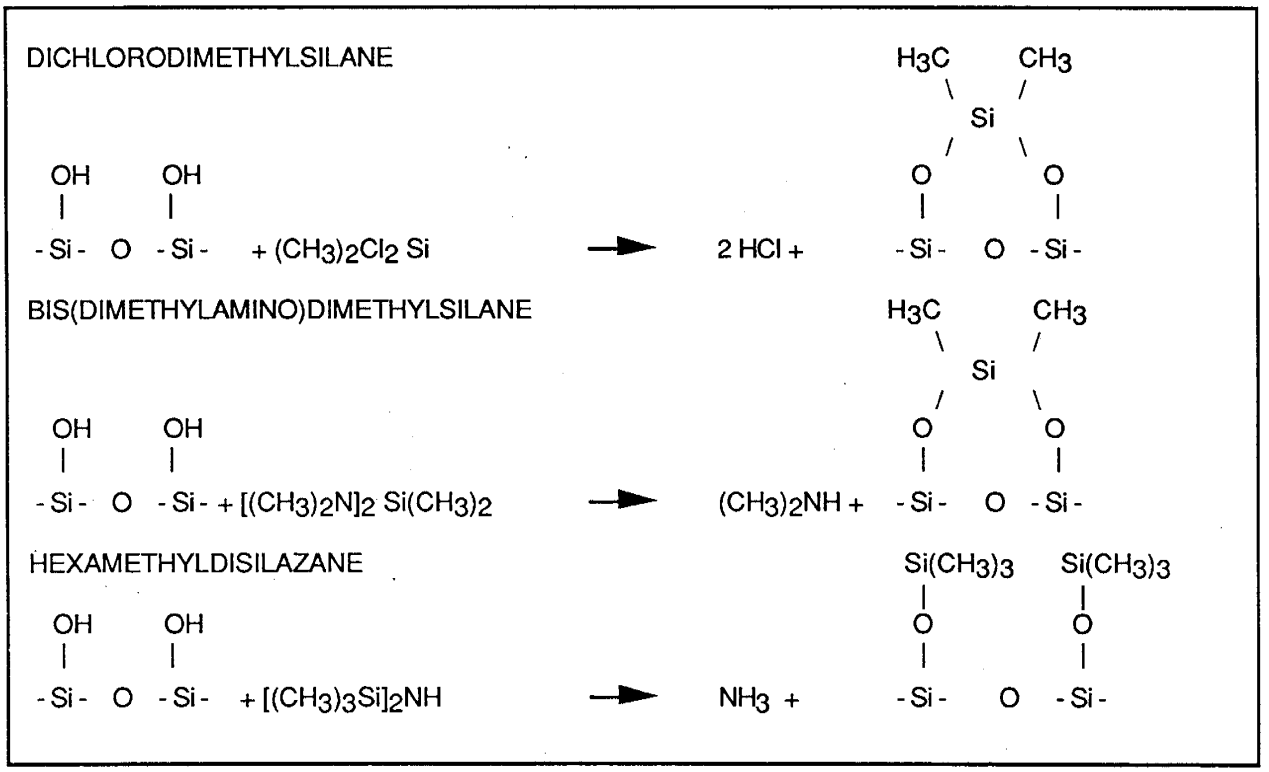

FIGURE 4. - Schematic of chemically bound organo silanes on silica surface.

The liquid phase procedure has been described by Olsen and Crocker (1991) using either of two silylating agents, trioctylchlorosilane $(C_8H_{17})_3$ Si Cl or dimethyldichlorosilane$(CH_3)_2Cl_2Si$ in toluene. Vapor-phase silylation of silica surfaces has been used to convert water-wet glassware used in analytical laboratories to a hydrophobic surface or for making hydrophobic packings for high-performance liquid chromatography (Deyhimi and Coles, 1982). Vapor-phase laboratory silylation with bis(dimethylamino)dimethylsilane, $[(CH_3)_2N]_2Si(CH_3)_2$ or hexamethyldisilazane, $[(CH_3)_3Si]_2NH$ were used to prepare oil-wet porous media (Takach et al. 1988, 1989; and Olsen and Crocker 1991).

Several tests were conducted to evaluate the thermal and hydrolytic stability of porous materials prepared by liquid or gas-phase silylation and of surfaces treated with crude oil fractions precipitated on the surface. The stability of the surface coating was evaluated by measuring the wettability of plugs using the USBM method with mineral oil (table 1) or New London crude oil as the wetting phase (tables 2 and 3). The use of crude oil fractions (asphaltene or polar fractions) from a number of crude oils, dispersed in mineral oil allowed the preparation of less water-wet surfaces and tended toward intermediate-wettability. However, the surface lost its intermediate-wettability upon flushing with crude oil (100 PV) or extensive waterflooding (>100PV).

TABLE 1. - Wettability changes of Berea sandstone with crude oil fractions

Wettability of Berea core with mineral oil	Source of Oil (Formation, State)	Wettability of Berea core with mineral oil/ asphaltenes	Wettability of Berea core with mineral oil/ polars
+0.81	Stevens, CA	+0.21	-0.06
+0.81	Anadarko, OK	+0.38	+0.25
+0.81	Woodbine, TX	+0.35	+0.21

TABLE 2. - Changes in wettability of silylated Berea sandstone and Quartz sands

		Liquid-Phase		Vapor-Phase
Silylation treatment	None	$Si(C_8H_{17})_3$	$Si(CH_3)_3$	Bidentate $Si(CH_3)_2$
Untreated (Berea Sandstone)	+0.48[1]			
Silylated (Initial)		-0.82[2]	-0.78[1]	-0.66[3]
After 48 hr at water reflux	+0.51[3]	+0.32[3]	+0.47[3]	-0.45[3]
After 8 hr steam from 285° to 335° F				-0.29[3]
After 8 hr steam from 335° to 365° F				+0.09[3]
1-D steamflood at 350° steam injection end of oil saturated core after 10 hrs of steaming				-0.42
1-D steamflood at 350° production end of oil saturated core after 10 hrs of steaming				-0.52
Untreated Quartz sand	+0.53[3]			
Silylated Quartz sand (Initial)				-0.39[3]
After 8 hr steam from 335° to 365° F				-0.21[3]

[1] Average of 3 tests. [2] Average of 2 tests. [3] Average of 6 tests.

TABLE 3. - Wettability increase with temperature for various systems.

	75° F		150° F		250° F	
	O/W	W/W	O/W	W/W	O/W	W/W
Wettabilities of consolidated Berea sandstone cores						
Brine/mineral oil	-0.51	+0.75	-0.30	+0.92		
Brine/New London	-0.66	+0.40	-0.47	+0.78	-0.14	+0.95
Wettabilities of unconsolidated quartz sand						
Brine/New London	-0.39	+0.53	-0.21	+0.75	+0.27	+1.06
Wettabilities of unconsolidated Berea sandstone cores						
Unextracted New London crude	-0.45	+0.52	-0.15	+0.85	+0.03	
		+0.18				+0.81
Brine/mineral oil		+0.60		+0.87		+1.21

A comparison of the porous media prepared by the two silylation techniques is shown in table 2, where New London crude oil/1% NaCl solution was used in the centrifuge method for determining wettability. Unsilylated Berea sandstone was water-wet (+0.48). The surfaces produced by liquid-phase silylation, giving bonded $Si(CH_3)_3$ and $Si(C_8H_{17})_3$ groups, and vapor-phase silylation with bis(dimethylamino)dimethylsilane producing a bidentate bonding of $Si(CH_3)_2$ to the silica surface, produced oil-wet surfaces whose wettability indices were -0.82, -0.78, and -0.66, respectively. Selected plugs were refluxed in water in a Dean Stark extractor at atmospheric pressure. Untreated Berea sandstone increased in wettability to +0.51, and both sets of plugs prepared by liquid-phase silylation reverted to a more water-wet condition, +0.32 and +0.47, respectively. Only the plugs prepared by vapor-phase silylation with bis(dimethylamino)-dimethylsilane remained oil-wet, -0.45. The bidentate bonded silylated cores were then subjected to more severe temperature and hydrolysis conditions. They were mounted in Hassler sleeves and subjected to steam injection (two different steam temperature conditions) for 8 hours. More than 100 PV of cold water equivalent steam was injected in each experiment. This resulted in decreasing the oil wettability and a shift to intermediate-wettability, -0.29 and +0.09. Wettability analysis was also conducted on plugs obtained after 10 hours of steamflooding oil-saturated cores. Plugs from the injection and production ends of a 1-D steamflood showed some decrease in oil wettability, but the surface of the core still remained oil-wet, -0.42 and -0.52. There was almost a direct correlation between the severity of the steam treatment and the increase in water-wetness in these experiments. Saturation with crude oil reduced the rate of change in wettability. Silylated cores steamed at higher temperatures or with more pore volumes of steam or longer time periods became more water-wet. Silylated porous media prepared with bis(dimethylamino)dimethylsilane have been used in NIPER laboratories for hot water floods in the presence of crude and refined oils

at 190° F (hot waterfloods where <4 PV of hot water was injected) without any detectable change in wettability.

A series of experiments was conducted on very strongly water-wet Berea sandstone or quartz sand and on oil-wet Berea sandstone or quartz sand, prepared by vapor-phase silylation with bis(dimethylamino)dimethylsilane (table 3) to confirm the effect of temperature on wettability. In each system, the wettability index increased (became more water-wet). At 250° F, the initially water-wet porous media has a USBM wettability index greater than one. This is due to the area under one capillary pressure curve being much greater than the other.

Steamflood Performance of Water-Wet, Intermediate-Wet and Oil-Wet Porous Media

Laboratory waterfloods of water-wet systems behave very differently from those of oil-wet systems. In strongly water-wet porous media, oil recovery at water breakthrough is high, with little additional oil production after water breakthrough. In strongly oil-wet porous media, water breakthrough occurs much earlier, and most of the oil recovered is slowly displaced during an extended waterflood with a low oil/water ratio. This parallels what is observed in waterfloods of most sandstone reservoirs; waterfloods are less efficient in oil-wet reservoirs than in water-wet reservoirs because more water must be injected to recover the same amount of oil. As porous media becomes more oil-wet, the water relative permeability increases, and the oil relative permeability decreases. Water flows more easily than oil causing progressively earlier breakthrough and lower economic oil recovery (Anderson, 1987).

A pair of duplicate 1-D steamfloods was conducted with New London crude oil, using fired strongly water-wet Berea sandstone cores and oil-wet cores obtained from vapor-phase silylation using bis(dimethylamino)dimethyl silane. These 1.5 in. x 28 in. cores were vacuum water saturated, flooded with >25 PV of 1% NaCl brine, and then oil saturated with New London crude oil. Backpressure on the system was set to 150 psi, and the cores were steamflooded (no preliminary waterflood). The production histories are shown in figure 5. Energy input (steam rate) was maintained as constant as possible for both runs, although the steam injection rate and back pressure were reduced to maintain constant injection pressure. Steam breakthrough occurred about 7 hours into each flood.

Oil-wet cores, because of their preferential affinity for oil, exhibited a higher initial oil saturation and a higher residual oil saturation at the termination of the steamflood than water-wet cores. The slope of the oil production curve during the first part of the steamflood was less steep for a water-wet core than for an oil-wet core because the water-wet core had a higher initial water saturation and a greater percentage of energy was consumed in bringing the connate water to steam

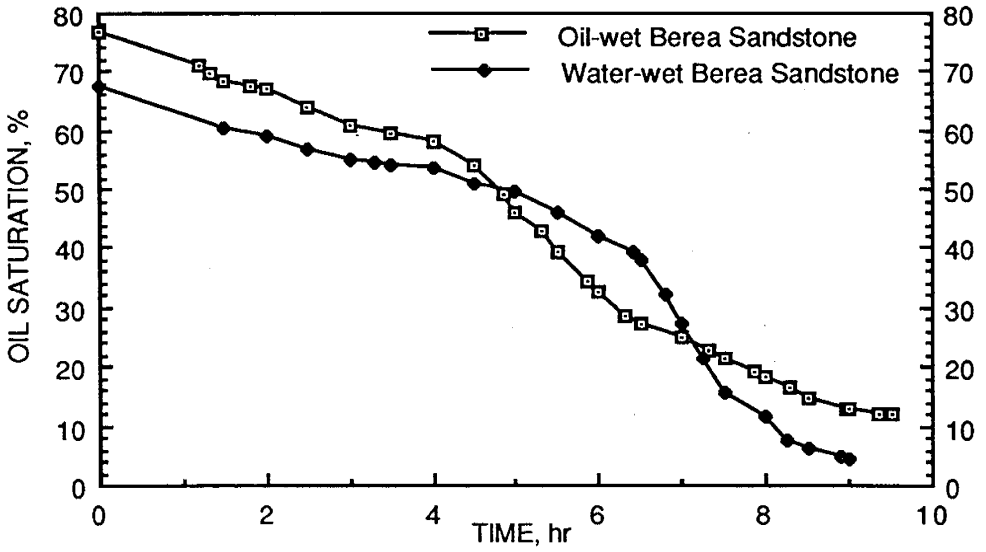

FIGURE 5. - Oil production from steamflooding oil-wet and water-wet Berea sandstone in a 1-D model.

temperature. Consequently, less energy was available to heat the oil. The kick in oil production occurred at different times in these experiments. The sudden kick in oil production in the case of the oil-wet core after about 5 hours of steam injection might have resulted from gradual shifting of the wettability of core toward water-wet and banking of the oil. The sudden kick in oil production in the water-wet core which occurred after about 6-1/2 hours of steam injection can be attributed to the decrease in the consumption of energy for bringing in situ water to steam temperature and the availability of more energy for oil production. After steam breakthrough, the water-wet core continued to produce greater amounts of oil because of a lower affinity for oil as compared to the oil-wet core.

Light Oil Steamflood Displacements in 2-D Sandpacks

Most light oil reservoirs are waterflooded after primary production. To investigate the steamflood oil recovery potential after waterflooding, a series of experiments was conducted in a 2-D sandpack packed with quartz sands of various wettabilities. The experiments incorporated strongly oil-wet porous media (silylated quartz sand prepared from vapor-phase silylation with bis(dimethylamino)dimethyl silane), quartz sand that had been silylated to yield a surface of intermediate wettability, and untreated very strongly water-wet quartz sand. The effects of wettability are illustrated by the oil production and decline curves in figures 6 through 9. The oil-wet quartz sand yielded a high initial and high waterflood residual oil saturation (figs. 6 and 9). Quartz sands of intermediate wettability showed lower initial and intermediate waterflood residual

oil saturation, but they were steamflooded to a low residual oil saturation (figs. 7 and 9). Water-wet quartz sand resulted in the lowest initial oil saturation, the lowest oil saturation after waterflood, and the lowest oil production by steamflooding (figs. 8 and 9). In each experiment, waterfloods were conducted until the water cut was greater than 97% before the start of steam injection. In the case of the oil-wet sand, the oil saturation continued to drop as steam was injected and the water, sand, and oil were heated. The oil-water ratio abruptly increased just before steam breakthrough in the cases of intermediate and oil-wet sands. During the steamflood, the most significant oil production was seen in those sandpacks which were more oil-wet. When compared with intermediate wet sands, the oil saturation decline curve for the oil-wet sands did not decrease as sharply as expected. Comparison of the oil saturation profiles of these sandpacks indicates that waterflooding recovers more oil from sands that are more water-wet. These results from 2-D sandpacks indicate that oil recovery by steamflooding of oil-wet sands looks very promising.

Economic Target of Light Oil Steamflooding

One of the principal advantages of steamflooding oil-wet light oil reservoirs, in addition to possible high oil saturation, is that the crude oil sells for a light oil price. Heavy oils, such as Kern River California crude, 13° API, sell for only about two-thirds of the price of West Texas Intermediate crude oil, figure 10 (Maples, 1990). Thus, the economics of light oil steamflooding in oil-wet reservoirs that have high oil saturation and have appropriate geology and mineralogy along with high permeability may be attractive.

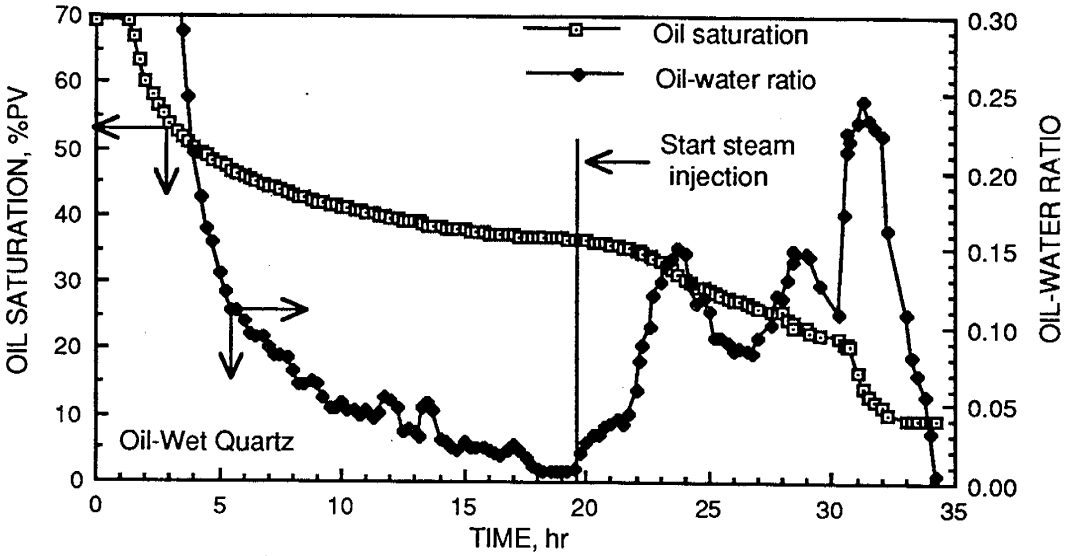

FIGURE 6. - Oil production from a 2-D model packed with strongly oil-wet quartz sand, waterflood followed by steamflood.

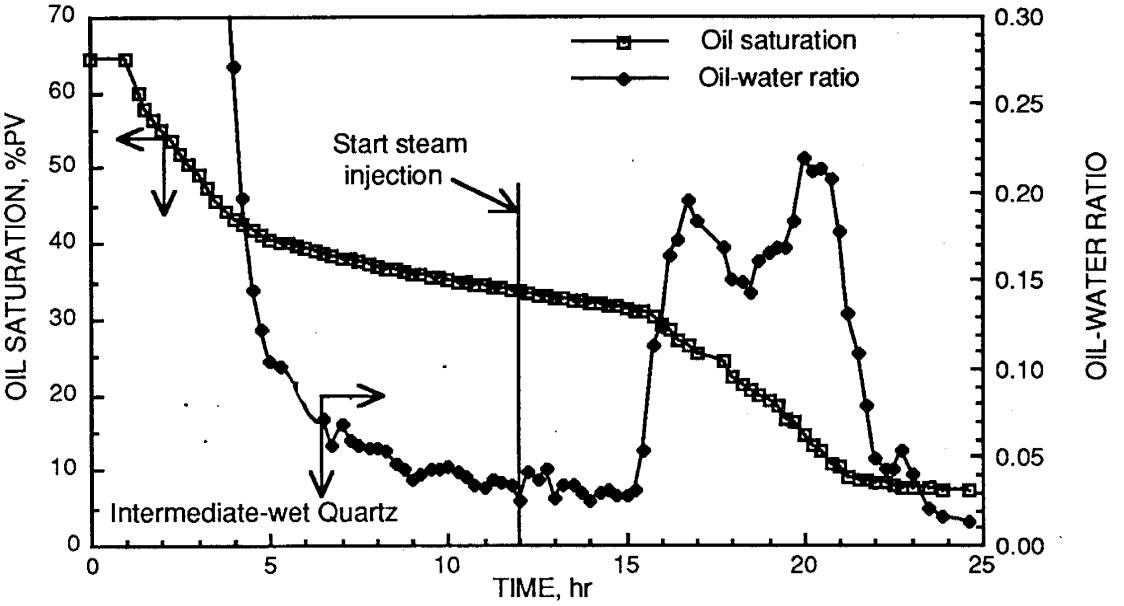

FIGURE 7. - Oil production from a 2-D model packed with intermediate-wet quartz sand, waterflood followed by steamflood.

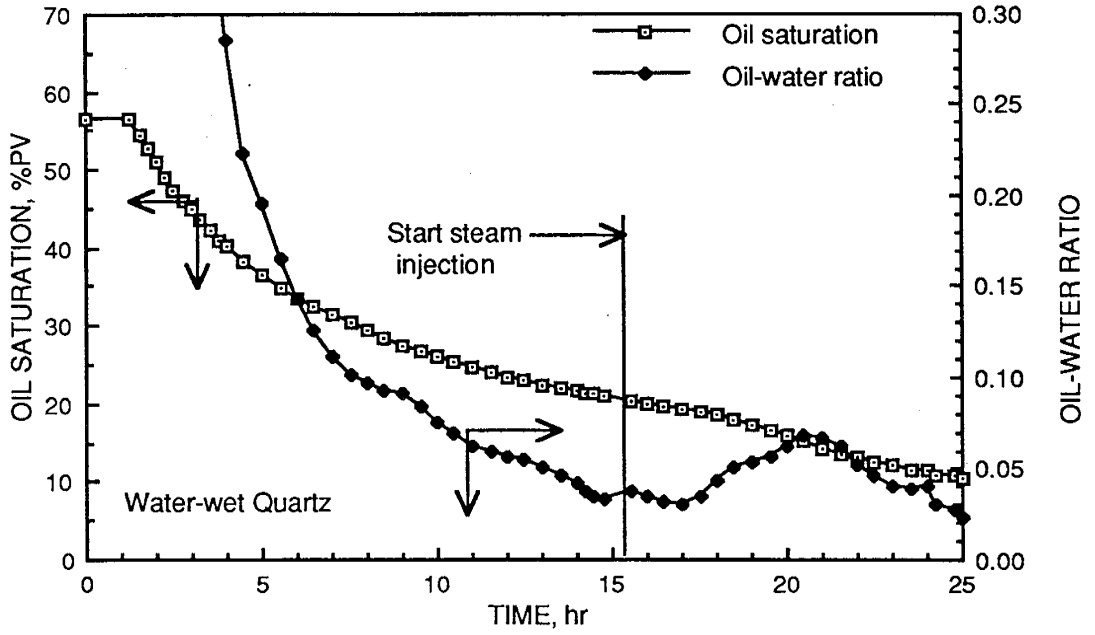

FIGURE 8. - Oil production from a 2-D model packed with water-wet quartz sand, waterflood followed by steamflood.

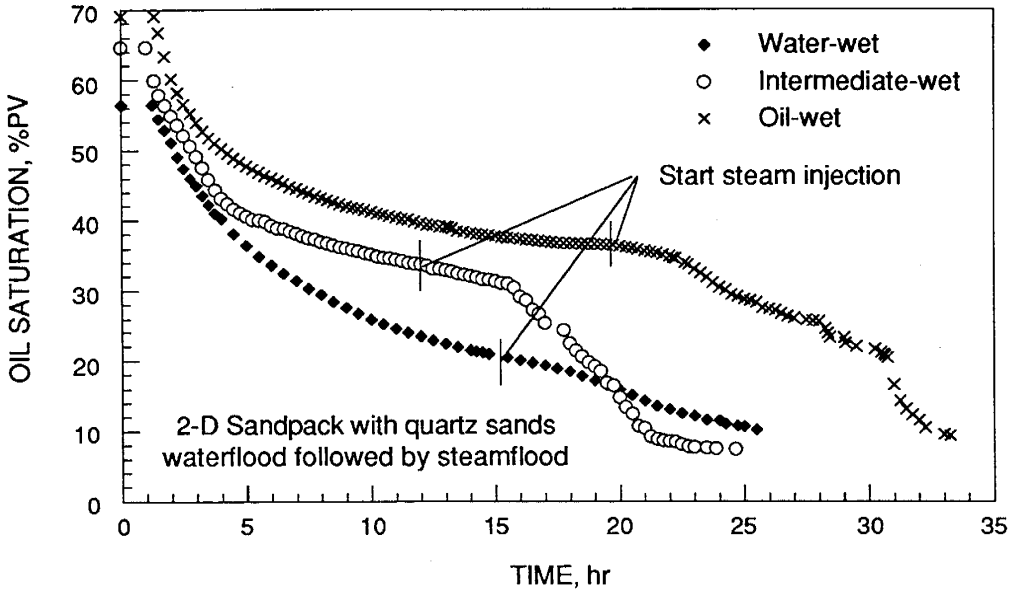

FIGURE 9. - Comparison of oil production from 2-D models, waterflood followed by a steamflood, in oil-wet, intermediate-wet, and water-wet quartz sandpacks.

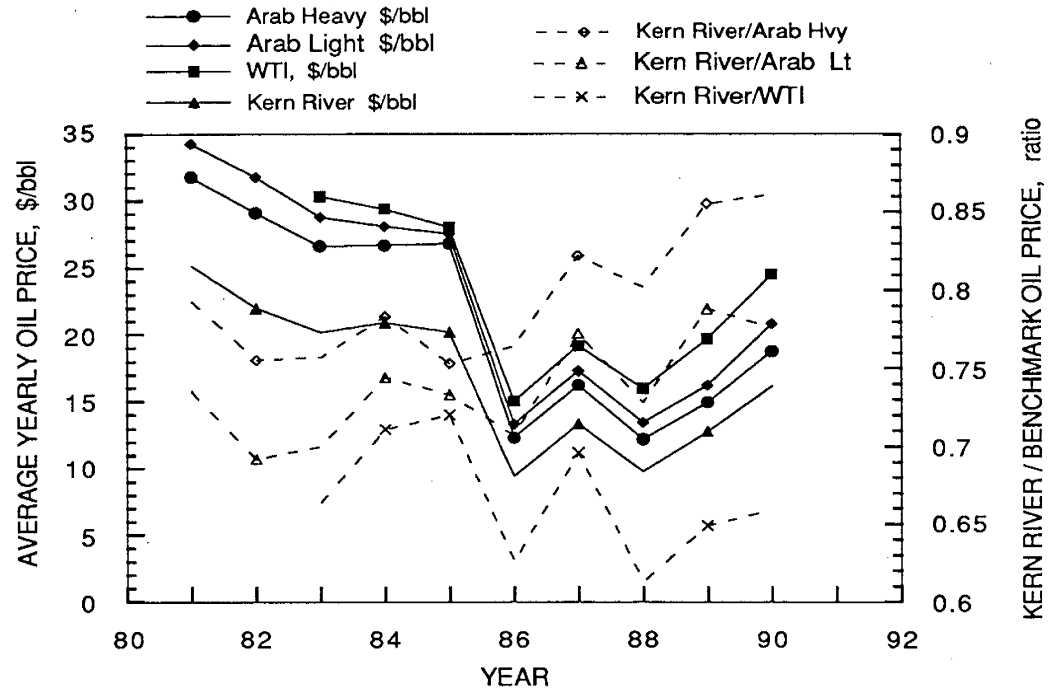

FIGURE 10. - Comparison of average yearly oil price of benchmark crude oils with Kern River 13°API gravity oil (from Maples, 1990).

SUMMARY AND CONCLUSIONS

The use of Berea sandstone as a porous media matrix in preliminary evaluations or screening of oil recovery processes has been widely practiced. This report summarizes the use of silylating agents in both the liquid and the vapor-phase to convert hydrophilic, very strongly water-wet Berea sandstones or unconsolidated quartz sands, to hydrophobic, oil-wetted, surfaces for use in laboratory studies of oil recovery with steam and hot water. The thermal and hydrolytic stability of the oil-wet surfaces were evaluated by measuring changes in the wettability index of cores after they were subjected to hot water or steam, both in the presence and absence of crude oil.

The vapor-phase silylation process using bis(dimethylamino)dimethylsilane to treat silica surfaces has yielded oil-wet surfaces with more uniform coverage that were more hydrolytically and thermally stable, but they were still transformed to water-wet surfaces upon extended steaming and higher steam temperatures. This process produces an oil-wet surface that is more thermally and hydrolytically stable than previous liquid-phase silylation processes. However, we have not been able to decouple degradation of the silylated surface from any change in surface properties. In the presence of crude oil, the oil-wet surface prepared from vapor-phase silylation using bis(dimethylamino)dimethylsilane to treat silica surface resists changes in wettability under hot water and low temperature steamflood conditions and allows its use in laboratory studies of steam and hot water oil recovery. The stability of the surface is expected to degrade with more severe (higher steamflood temperatures) conditions.

Capillary pressure/wettability measurements indicate that oil-wet or intermediate-wet sands become more water-wet with increasing temperature and that the irreducible water saturation increases as the temperature increases.

Oil production and oil saturation profiles from 2-D sandpacks of water-wet, intermediate-wet, and oil-wet porous media, have been compared where a light crude oil is displaced by a waterflood followed by a steamflood. These data indicate that oil-wet sandpacks oil have a higher initial oil saturation and waterflood (to an economic limit) to much higher waterflood residual oil saturation than either intermediate-wet or water-wet sandpacks. Steamfloods initiated at this point displace little oil from water-wet sandpacks and displace increasingly greater amounts of oil from more oil-wet sandpacks. This behavior is anticipated based upon water displacement of oil from porous media of varying wettability. The steamfloods required increasing response times (steamflood rate and injection pressure were maintained as constant as possible in each of the three experiments) to produce an oil kick in the order: oil-wet, intermediate-wet and finally water-wet. The oil-wet system responded the quickest because there was less water in the sandpack. Since water has a higher heat capacity than oil, more energy (steam) was required to heat the system and steam distill the oil from a water-wet system. This study also indicates that final oil saturation,

after steamflooding, were nearly independent of initial wettability as oil saturations were 8 to 10 % PV at the conclusion of the steamflood.

Steamflooding light oil, oil-wet reservoirs, may be an attractive economic target in the appropriate geologic setting. In addition to light oil commanding a much higher price than heavy oil, the response time between steam injection and oil production is short, making economic payback more attractive.

REFERENCES

Ahner, P. F. and Sufi, A. H.: "Physical Model Steamflood Studies Using Horizontal Wells." SPE/DOE paper 20247 presented at SPE/DOE 7th Symp. on EOR, Tulsa, OK, Apr. 22-25,1990.

Anderson, W. G.: Wettability Literature Survey—Part 5 "Effects of Wettability on Relative Permeability." J. Pet. Tech., November 1987, pp. 1453-1468.

Anderson, W. G.: Wettability Literature Survey—Part 6. "Effects of Wettability on Water-flooding." J. Pet. Tech., December 1987, pp. 1605-1622.

Butler, R.M. and Yee, C. T.: "An Experimental Study of Steam Condensation in the Presence of Non-Condensible Gases in Porous Solids." AOSTRA J. of Research, Vol. 3, No. 1 (1986) pp. 15-23.

Chu, C.: "A Comprehensive Simulation Study of Steamflooding Light-Oil Reservoirs After Waterflood." J. Petroleum Technology, 894, July 1988.

Chu, C.: "Examination of the Confined-Pattern Concept in Steamflood Simulation." SPE Reservoir Engineering, 559, November 1987.

Chu, C.: "State-of-the-Art of Steamflood Field Projects." SPE paper 11733 presented at the 1983 California Regional Meeting, Ventura, CA, Mar. 23-25, 1983.

Chu, C.: "Prediction of Steamflood Performance in Heavy Oil Reservoirs using Correlations Developed by Factorial Design Method." SPE paper 20020 presented at the 60th Annual California Regional Meeting, Ventura, CA, April 4-6, 1990.

Coats, K.H., George, W.D., Chu, C. and Marcum, B.E.: "Three-Dimensional Simulation of Steamflooding." SPEJ, December 1974, pp. 573-592.

Crocker, M. E. and Marchin, L. M.: "Wettability and Adsorption Characteristics of Crude Oil Asphaltene and Polar Fractions." J. Pet. Tech., April 1988, pp. 470-474.

Crocker, M. E. and Marchin, L. M.: "Experimental Studies to Produce Stable Wettabilities in Core Samples." Dept. of Energy Report NIPER-184, August 1986.

Cuiec, L. E.: "Evaluation of Reservoir Wettability and Its Effect On Oil Recovery." Interfacial Phenomena in Oil Recovery, N. R. Morrow (ed.), Marcell Dekker, New York, N. Y. (1990) pp. 319-375.

Deyhimi, F. and Coles, J. A.: "Rapid Silylation of a Glass Surface: Choice of Reagent and Effects of Experimental Parameters on Hydrophobicity." Helvetica Chimica Acta,Vol 65, (1982) 1752-1759.

Donaldson, E. C., Thomas, R. D. and Lorenz, P. B.: "Wettability Determination and Its Effect on Recovery Efficiency." SPEJ, March 1969, pp. 13-20.

Doscher, T. M., Omoregie, O. S., and Ghassemi, F.: "Steam Drive-Definition and Enhancement." J. Pet. Tech. (July 1982) pp. 1543-45.

Doscher, T. M.: "Steam Drive - An Ultimate Recovery Process for High-Gravity Crudes After Waterflooding." *Oil & Gas. J.* (November 9, 1981) 234-38.

Farouq Ali, S.M.: "Steam Injection Experiments in a Scaled Physical Model." Final Report, Oct. 1, 1983 - June 30, 1985. AOSTRA contract DSS EMR OST83-00212.

Farouq Ali, S. M. and Meldau, R. F.: "Current Steamflood Field Experience." SPE paper 7546 presented at the 53rd Annual Fall Technical Conference and Exhibition of the Society of Petroleum Engineers of AIME, Houston, TX, Oct.. 1-3, 1978.

Green, M.K. and Isaacs, E. E.: "Laboratory Investigation on The Use of Foam Forming Surfactants During Steam Injection," Petroleum Society of CIM, paper no.86-37-02 presented at the 37th Annual Technical Meeting held in Calgary, June 8-11, 1986, pp. 11-24.

Hanzlik, E. J.: "Steamflooding as an Alternative EOR Process for Light Oil Reservoirs." SPE paper 10319 presented at the SPE Annual Technical Conference, San Antonio, TX, Oct. 5-7, 1981.

Honarpour, M., DeGroat, C., and Manjinath, A.: "How Temperature Affects Relative Permeability Measurements." World Oil, May 1986, p. 116.

Hong, K. C.: "Numerical Simulation of Light-Oil Steamflooding in the Buena Vista Hills Field, California." SPE paper 14104 presented at the 1986 SPE Intl. Meeting on Petroleum Engineering, Bejing, Mar. 17-20, 1986.

Lookeren, J. Van: "Calculation Methods for Linear and Radial Steam Flow in Oil Reservoirs." SPE paper 6788 presented at the SPE 52nd Annual Fall Technical Conference and Exhibition, Denver, Colorado, Oct. 9-12, 1977.

Madden, M. P. and Sarathi, P.: "Light Oil Steamflooding - Core Flood Experiments." Topical Report, Dept. of Energy Report NIPER-44, 1985.

Maples, J. W.: "Crude Oil Prices 1990." Kern County Assessor, Oil and Gas Properties Division, Kern County, California, February 1991.

Moritis, G.: "Annual Production Report, CO_2 and HC Injection Lead EOR Production Increase." *Oil and Gas J.*, Apr. 23, 1990.

Morrow, N. R.: "Wettability and Its Effect on Oil Recovery." J. Pet. Tech. (December 1990) pp. 1476-1484.

O'Kandan, E., Marsden Jr., S. S., and Ramey Jr., H. J.: "Capillary Pressure and Contact Angle Measurements at Elevated Temperatures." Presented at AIChE meeting, Tulsa, OK, Mar. 12, 1974.

Olsen, D. K.and Crocker, M. E.: "Evaluation of Artificially Wetted Surfaces for Use in Laboratory Steamflood Experiments," presented as paper 109 at UNITAR/UNDP V International Conference on Heavy Oil and Tar Sands, Caracas, Venezuela, Aug. 4-9, 1991.

Olsen, D. K.,Crocker, M. E.,Sarathi, P. S. and Betancourt,J.: "Effects of Elevated Temperatures on Capillary Pressure and Wettability," presented as paper 110 at UNITAR/UNDP V International Conference on Heavy Oil and Tar Sands, Caracas, Venezuela, Aug. 4-9, 1991.

Olsen, D. K., Sarathi,P. S., Roark,S. D., Ramzel, E. B. and Mahmood,S. M.: "Light Oil Steamflooding: A Laboratory Study of Oil Recovery from Water- and Oil-Wet Porous Media in 2-D Sandpacks." SPE paper 21769 to be presented at SPE Latin American II Meeting, Mar. 8-11, 1992, Caracas, Venezuela.

Olsen, D. K. "National Institute for Petroleum and Energy Research Quarterly Technical Report for Oct. 1 - Dec. 31, 1989 v. II, Energy Production Research." Dept. of Energy Report No. NIPER - 463, February. 1990, p. 64.

Ozen, A.S. and Farouq Ali,S.M.: "An Investigation of the Recovery of the Bradford Crude by Steam Injection." SPE paper 1972 presented at the SPE 4th Annual Eastern Regional Meeting, Pittsburgh, PA, Nov. 2-3, 1967.

Quettier, L. and Corre, B.: "Hot-Water and Steamflood Laboratory Experiments Under Reservoir Conditions." SPE Res. Eval., February 1988, pp. 149-157.

Rajan, R. R.: "Theoretically Correct Analytical Solution for Calculating Capillary Pressure-Saturation From Centrifuge Experiments." Presented at the 27th Annual Logging Symposium of SPWLA, Paper O, Houston, TX, June 9-12, 1986.

Samaroo, B. H. and Guerrero, E. T.: "The Effect of Temperature on Drainage Capillary Pressure in Rocks Using a Modified Centrifuge." SPE paper 10153 presented at the 56th SPE of AIME Annual Fall Technical Conference, San Antonio, TX, Oct. 5-7, 1981.

Sanyal, S. K., Ramey, H. J., and Marsden, S. S.: "The Effect of Temperature on Capillary Pressure Properties of Rocks." SPWLA 14th Annual Logging Symp., Lafayette, LA, pp. N1-N16, May 6-9, 1973.

Sarathi, P.S., Roark, S.D. and Strycker, A.R.: "Light-Oil Steamflooding: A Laboratory Study." SPE Res. Eng., May 1990, pp. 177-184.

Sarathi, P., Roark, S. D. and Strycker, A.: "Two-Dimensional Steamflood Laboratory Studies of Light Crude Oil Saturated Sandpack—Comparison of Waterflooded with Non-Waterflooded Porous Media," presented at the 3rd International Symposium on Enhanced Oil Recovery, Maracaibo, Venezuela, Feb. 19-22, 1989.

Sinnokrot, A. A., Ramey, H. J., and Marsden, S. S.: "Effect of Temperature Level Upon Capillary Pressure Curves." SPEJ., (March 1971) 13-22.

Strycker, A. "Thermal Recovery of Light Crude Oils Using Steam—A Laboratory Study Using a Two-Dimensional Physical Model." Dept of Energy Report No. NIPER-347, June 1988.

Strycker, A. and Sarathi, P.: "Steamflooding Light Crude Oil Reservoirs -- A State-of-the-Art Review." Dept. of Energy Report NIPER-338, 1988.

Sufi, A. H.: "A Method of Alternating Steam and Water Injection for Recovering Heavy Oils." SPE/DOE paper 20246 presented at SPE/DOE 7th Symp. on EOR, Tulsa, OK, Apr. 22-25, 1990.

Takach, N. E., Bennett, l. B, Douglas, C. B. Andersen, M. A. and Thomas, D. C.: "Wettability Alteration of Model Sandstone Surfaces by Vapor-Phase Treatments with Organosilanes," presented at ACS Division of Petroleum Chemistry, Los Angeles Meeting, Sept. 25-30, 1988, p. 525.

Takach, N. E., Bennett, L. B, Douglas, C. B. Andersen, M. A. and Thomas, D. C.: "Generation of Oil-Wet Model Sandstone Surfaces." SPE paper 18465 presented at Soc. Pet. Eng. International Symposium on Oilfield Chemistry, Houston, TX, Feb. 8-10, 1989.

Willhite, G. P.: "Waterflooding," SPE Textbook Series, Vol. 3, SPE Richardson, TX, 1986 p 33.

Wu, C.H. and Fulton, P.F.: "Experimental Simulation of the Zones Preceding the Combustion Front of an In-Situ Combustion Process." SPEJ, March 1971, pp. 38-46.

Task 47 - INTEVEP shall provide DOE with information from laboratory work and field experience on methods to minimize heat losses in steam injection wells. Information will include well completion and injection strategies as well as types of insulating materials used.

HEAT LOSSES IN STEAM INJECTION WELLS

BY

Oswaldo Saab

Belkis Fernandez

INTEVEP, S.A.

Los Teques, Miranda

Venezuela

1 SUMMARY

The purpose of this work is to show the results obtained with an analytical model called PERCAL which was developed to analyze heat losses in steam injection tubing based on the calculation of the global resistance.

PERCAL was introduced some routines allowing to calculate the properties of natural gas, which consists of methane, ethane, propane, carbon dioxide and nitrogen, at different compositions and in a temperature and pressure interval covering field operation conditions.

2 INTRODUCTION

Steam injection as a process for recovering heavy oils has been successfully applied in the western and eastern areas of Venezuela. With the aim of introducing in the reservoir the highest steam-derived caloric content, several types of insulators have been developed. Said insulators are to be used in pipelines and tubing transporting steam both at surface level and inside the injection well. Nevertheless, due to the operational problems posed by subsurface works, the techniques to insulate tubing in these wells have generated great interest. As a result, many insulators have been tested to this end.

Depending on pressure, temperature and depth conditions in the reservoir, three basic types of insulators are used for avoiding any heat loss from the tubing to the porous medium surrounding the well: solid-type insulators represented by calcium or sodium silicate shells placed around the external tubing walls, liquid insulators based on high viscosity and thermal resistance oil, and gas insulators such as air or nitrogen occupying the well annulus.

In Venezuela, various strategies for steam injection tubing insulation have been used in the last thirty years. They have been selected according to reservoir conditions, operators' policies, and market conditions for selling heavy oil.

For instance, since 1967, calcium silicate has been successfully used in more than 2000 wells in Costa Bolívar, in the western area of the country, for cyclic steam injection projects dealing with reservoirs having a depth of up to 3000 feet, steam injection rates and pressures ranging from 100 to 500 tons/day and 1000 to 1300 psi (1). Fig. 1 indicates the number of wells having calcium silicate (wo/Ins) and lacking this insulator (w/SiCa) in Costa Bolívar wells from 1988 to 1990. In the eastern area of the country, Bunker C, a 16 API and 6000 cp-viscosity residual crude has been used in some cases since

FIG. 1 NUMBER OF WELLS AND KIND OF INSULATOR BOLIVAR COAST FIELDS (1988–1990).

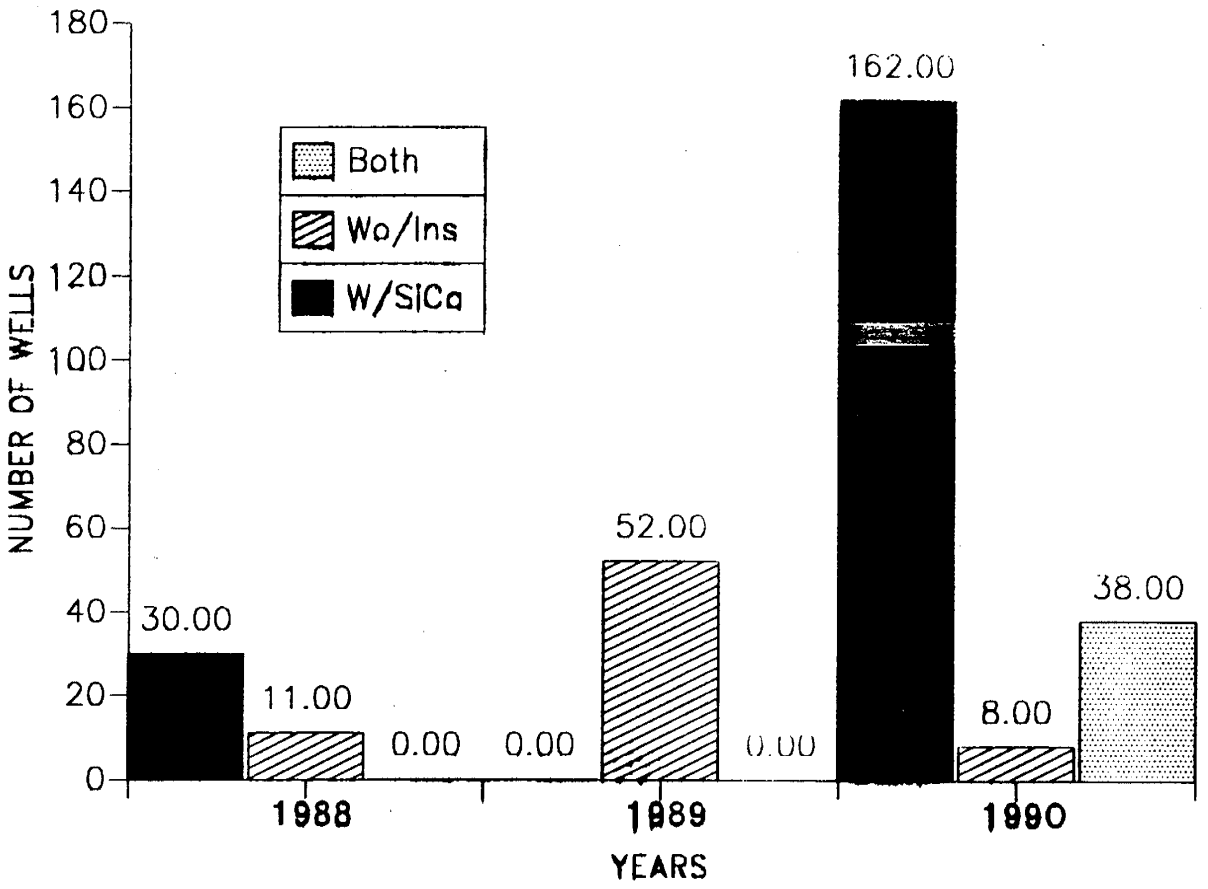

1978, as well as Ken-Pack, a commercial product having tixothropic properties which has been injected in the annulus.

Figures 2 and 3 present the theoretical results obtained from the maximum temperatures reached by casing as a function of time, for tubing with none insulator. In this case, Ken-Pack has been used and a preinsulation has been made with 1/4 inch sodium silicate and 1 inch calcium silicate. The evaluation was made for 7 inch (Fig. 2) and 9 5/8 inch (Fig. 3) casing diameters (1). As one may observe, in all cases the tubing preinsulated with calcium silicate gave the best results.

In the last 7 years, heavy crude production in Venezuela was affected by a major support given to medium and light crude production. A large amount of steam injection projects were then suspended. Nevertheless, during this period, those areas that still produced heavy crudes used silicates and some variations thereof, such as the use of only 400 to 600 feet of silicate-insulated tubing, the rest remaining naked, and a tendency to use only nitrogen or air in the annulus to insulate some wells in the western area of the country.

In 1986, INTEVEP develops Gel-Int, whose properties are similar to Ken-Pack's. In 1988, Gel-Int is first used in the Orinoco Oil Belt wells. Figures 4 and 5 indicate the number of wells in the Belt and in the eastern area of the country where Gel-Int, Ken-Pack and air were used in the 1986-1990 period.

Since there was a growing tendency to use nitrogen in the annulus of those wells, INTEVEP undertook a conceptual study in 1990 in order to determine the best conditions for applying this gas and the theoretical feasibility of using natural gas instead.

A review of the techniques available at INTEVEP to evaluate heat losses in steam injection tubing showed that the WELMOD numerical simulator WELMOD (2), devel-

Fig. 2 MAXIMUN TEMPERATURE VS. INJECTION TIME 7" CASING.

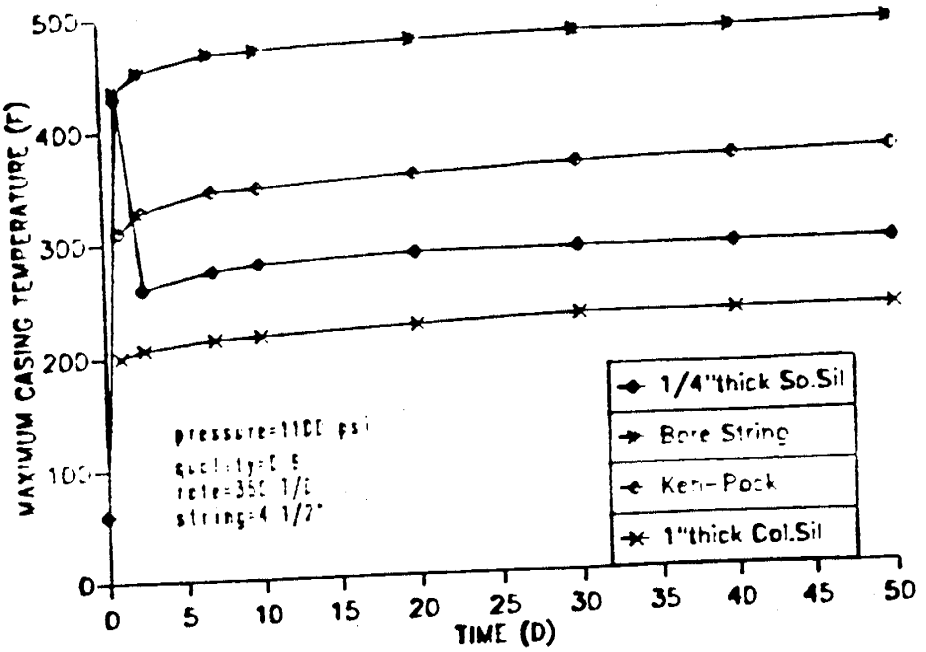

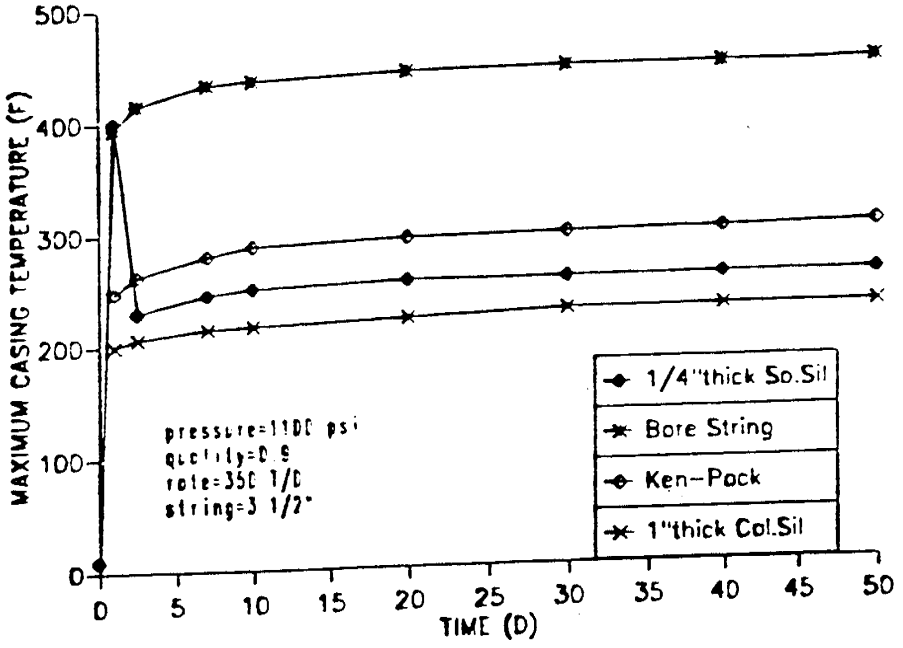

Fig. 3 MAXIMUN TEMPERATURE VS. INJECTION TIME 9 5/8" CASING.

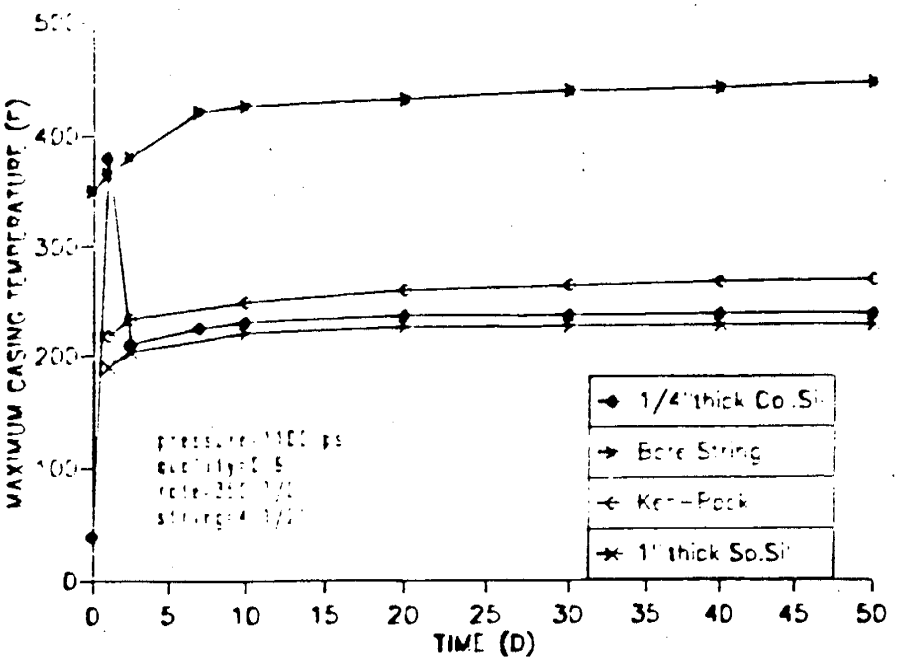

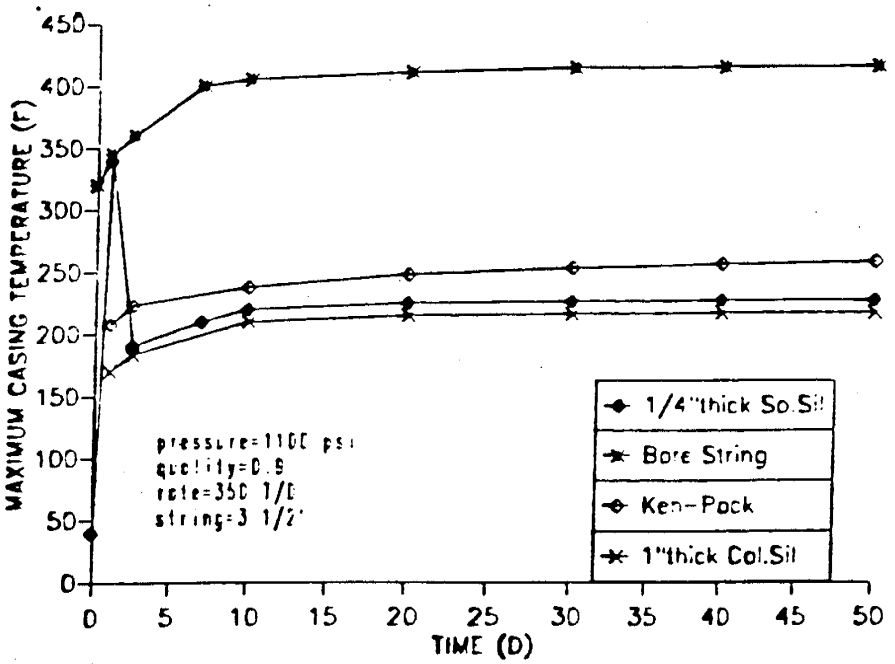

Fig. 4 NUMBER OF WELLS AND KIND OF INSULATOR ORINOCO BELT FIELDS (1988–90).

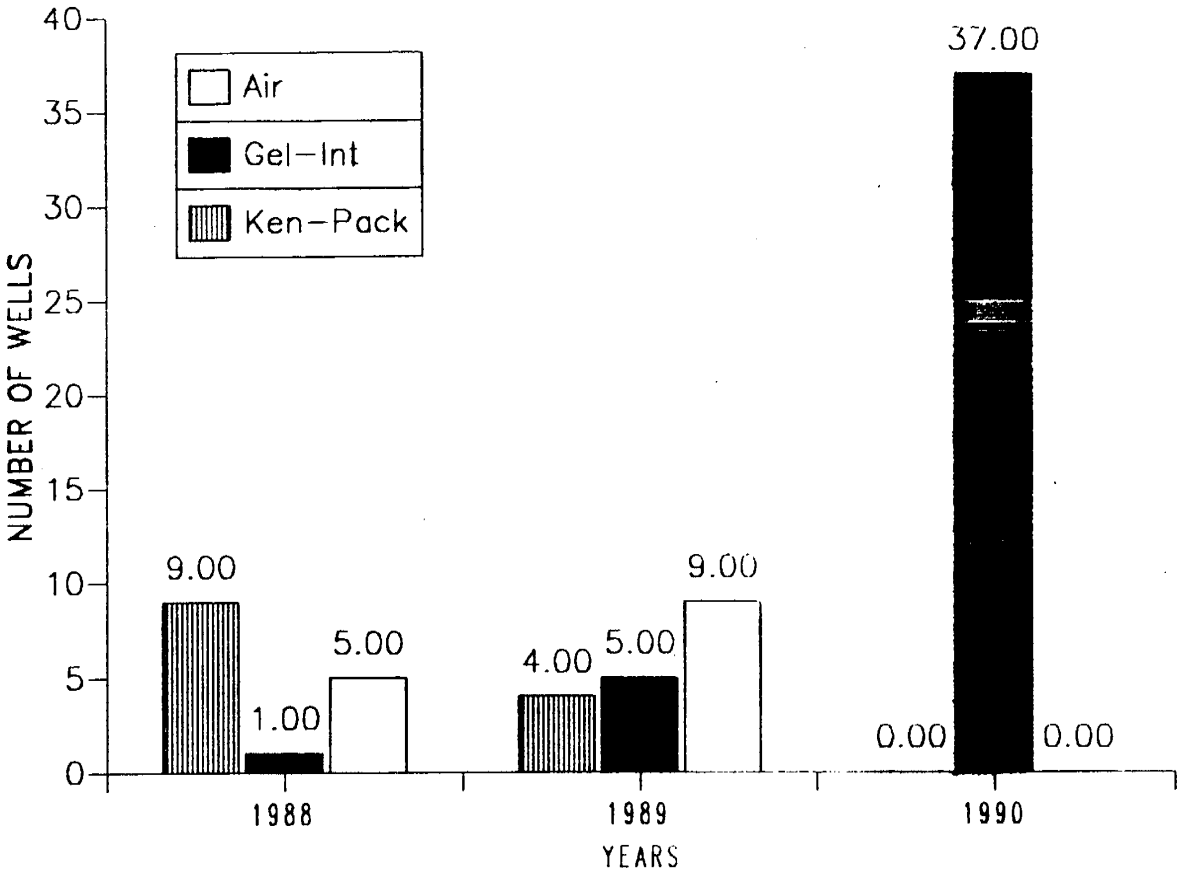

Fig. 5 NUMBER OF WELLS AND KIND OF INSULATOR, SAN TOME FIELDS (1986–90).

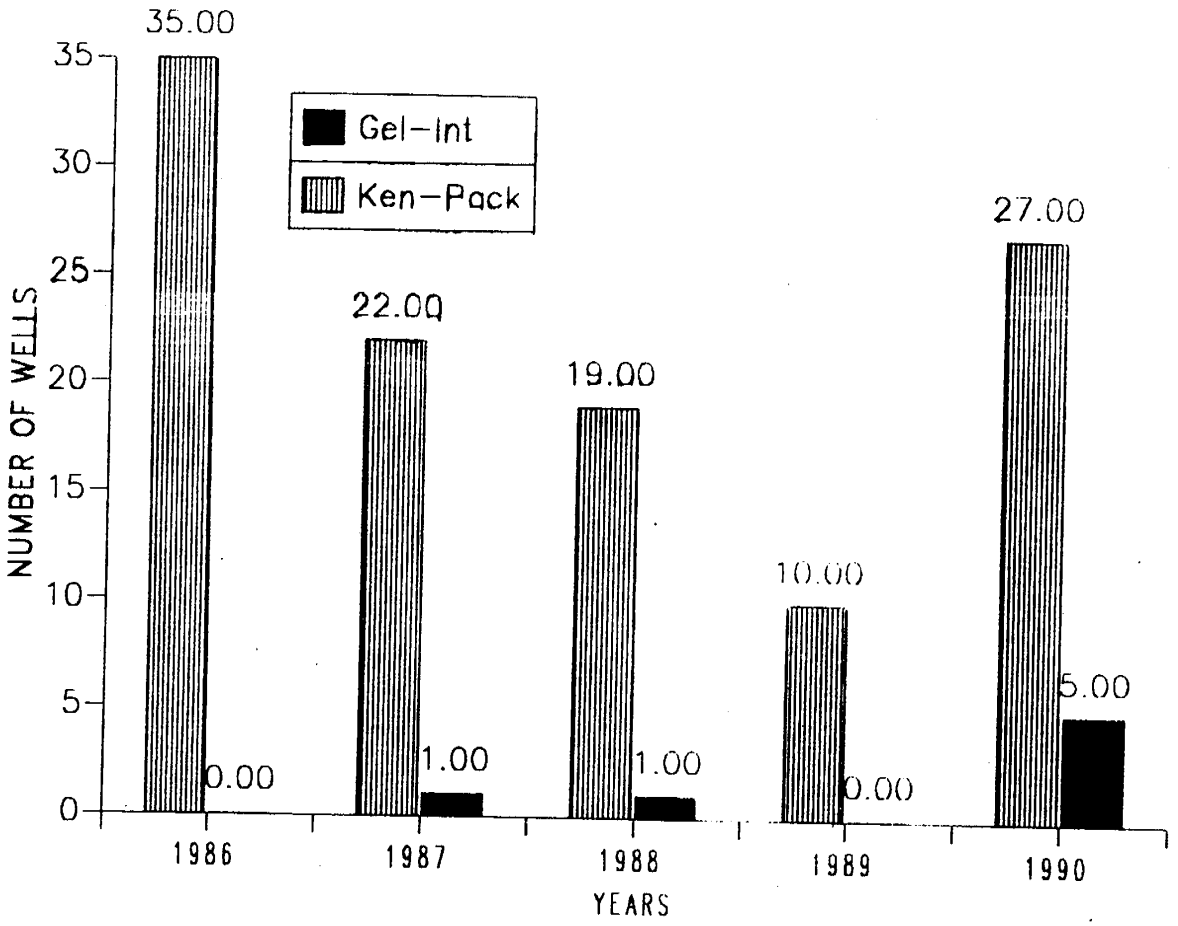

oped at INTEVEP in 1984, could be a good tool in this area. However, air could only be evaluated at atmospheric pressure and pure nitrogen and methane at atmospheric pressure and 1500 psi, which was a limiting factor. As an alternative, an analytical model called PERCAL was developed to analyze heat losses in steam injection tubing based on the calculation of the global resistance imposed by existing materials and fluids between the steam flowing inside the tubing and the porous medium surrounding the injecting well.

PERCAL was introduced some routines allowing to calculate the properties of natural gas, which consists of methane, ethane, propane, carbon dioxide and nitrogen, at different compositions and in a temperature and pressure interval covering field operation conditions. This routines will be eventually loaded to WELMOD simulator for improvement reasons.

This report briefly presents the WELMOD simulator and the results obtained from the nitrogen and methane evaluation as insulating fluids in the annulus of a steam injecting well. Following, the analytical simulator PERCAL is presented. A detailed explanation is given of the most important aspects of the algorithm thereof, the results obtained with this simulator being compared with those given by the WELMOD simulator. Finally, the corresponding conclusions, recommendations and future activities are stated.

3 NUMERICAL ANALYSIS AND PERFORMANCE OF NITROGEN AND NATURAL GAS

A detailed study has been conducted on the problem of how to calculate heat losses through the injecting well, as one may observe in the bibliographical review by Bernard and Vaca (2). Nevertheless, few works have studied the specific performance of gases such as air, nitrogen and natural gas in the annulus of wells for thermal activities.

3.1 WELMOD Numerical Simulator

In 1984, INTEVEP developed the WELMOD numerical model to estimate pressure, temperature and steam quality conditions along a hot water or steam injecting well. This model is a valuable tool for thermal projects designed to select the tubing and characteristics in corrosion studies and stress calculations both for tubing and casing. Besides, it allows to obtain steam conditions in the well bottom as an input datum for numerical simulators of thermal processes at reservoir level.

In order to calculate heat losses along the well as a function of injection time, the WELMOD simulator includes the following effects:

1. Phase change (steam/liquid) and mass transfer between them.
2. Simultaneous treatment of different biphase flow rates in the tubing.
3. Pressure drop for biphase flow.
4. Heat losses around the formation.

The basic hypotheses on which the mathematical model was developed to describe heat transfer through the injecting well were as follows:

1. The formation is a symmetric and opaque solid having constant thermal properties compared to orthogonal coordinate axes.
2. The formation limits are perpendicular to the O-Z symmetry axis.

3. Flow through the tubing is unidimensional and steady- state. In the case of biphase flow, steam and water are in thermodynamic equilibrium.
4. Heat transfer from the fluid to the formation is radial, taking into account conduction mechanisms (tubing, insulator, cement), convection (annular fluid), and radiation (annulus filled with a transparent fluid).

The model includes the thermal properties of the materials used as tubing insulators, such as silicates, diesel, Ken-Pack, cement and water, as well as the annulus filling with air, nitrogen, and methane at atmospheric pressure and at 1500 psi. The fluids' properties were included as tables for a wide range of temperatures at the two pressures mentioned above. Water and steam properties were included through routines comprising, among other things, data from steam tables ASME (3), the Juza and Mares equation of state for water (4), and Watson's water viscosity correlations (5).

The fluid's movement and energy balances are solved through a numerical integrator. A complete description for this simulator is provided in the work by Bernard and Vaca.

3.1.1 Presentation and discussion of results

In order to evaluate the insulating performance of nitrogen and methane as to heat losses at the formation and the maximum temperature reached by the casing, a series of runs were effected while the well's characteristic parameters specified in Table 1 were kept constant. It is noteworthy to clarify that since gases can only be evaluated at two pressures, it will be convenient to use the acronyms LP to refer to atmospheric conditions and HP for 1500 psi.

The insulators studied were as follows:

1. Nitrogen (LP and HP).
2. Methane (LP and HP).

TABLE 1 INJECTION WELL CHARACTERISTICS

I. LENGTH (ft): 3000

II. DIAMETERS (inch):

- Tubing: 3.5
- Casing: 7
- Well: 12

III. STEAM PROPERTIES:

- Quality (Well Head) (%): 80
- Temperature (°F): 600
- Injetion Rate (ton/d): 400

IV. INJECTION PERIOD (d): 15

3. Tubing insulated with a 1-inch thickness calcium silicate shell and an annulus filled with nitrogen (S. Ca/N2) or methane (S. Ca/NG).

Fig. 6 shows the maximum temperatures obtained in the casing, as well as total heat losses after steam had been injected for 15 days. These results lead to the following observations:

When the annulus is preinsulated with calcium silicate, heat losses and the temperature reached by the casing are the same, irrespective of the use of nitrogen and methane in the annulus.

Analyzing nitrogen results at high and low pressure, it is observed that at high pressures heat losses were 17% higher and the casing temperature increased by 10% compared to those obtained at atmospheric conditions. Similarly, methane shows a 21% increase in heat losses and a 13% rise in casing temperature.

3.2 PERCAL Analytical Model

As stated in the Introduction, this program was developed to evaluate nitrogen and natural gas effectiveness as thermal insulators in the annulus of steam injecting wells.

The basic program structure includes a division of the injecting well into cylindrical sections of equal size. For each section, an analytical calculation is made of outlet steam quality, pressure and temperature conditions, as well as of heat losses from each block to the formation.

The procedure starts in the surface block where inlet conditions are known and correspond to steam conditions in the well head. Coupling the expressions corresponding to energy balances, outlet steam conditions and energy losses in the block are obtained simultaneously. The procedure continues in the next lower block, where inlet conditions correspond to outlet conditions in the upper block. This process is repeated for each

Fig. 6 RESULTS NUMERICAL SIMULATOR

(HEAT LOSSES AND CASING TEMPERATURE).

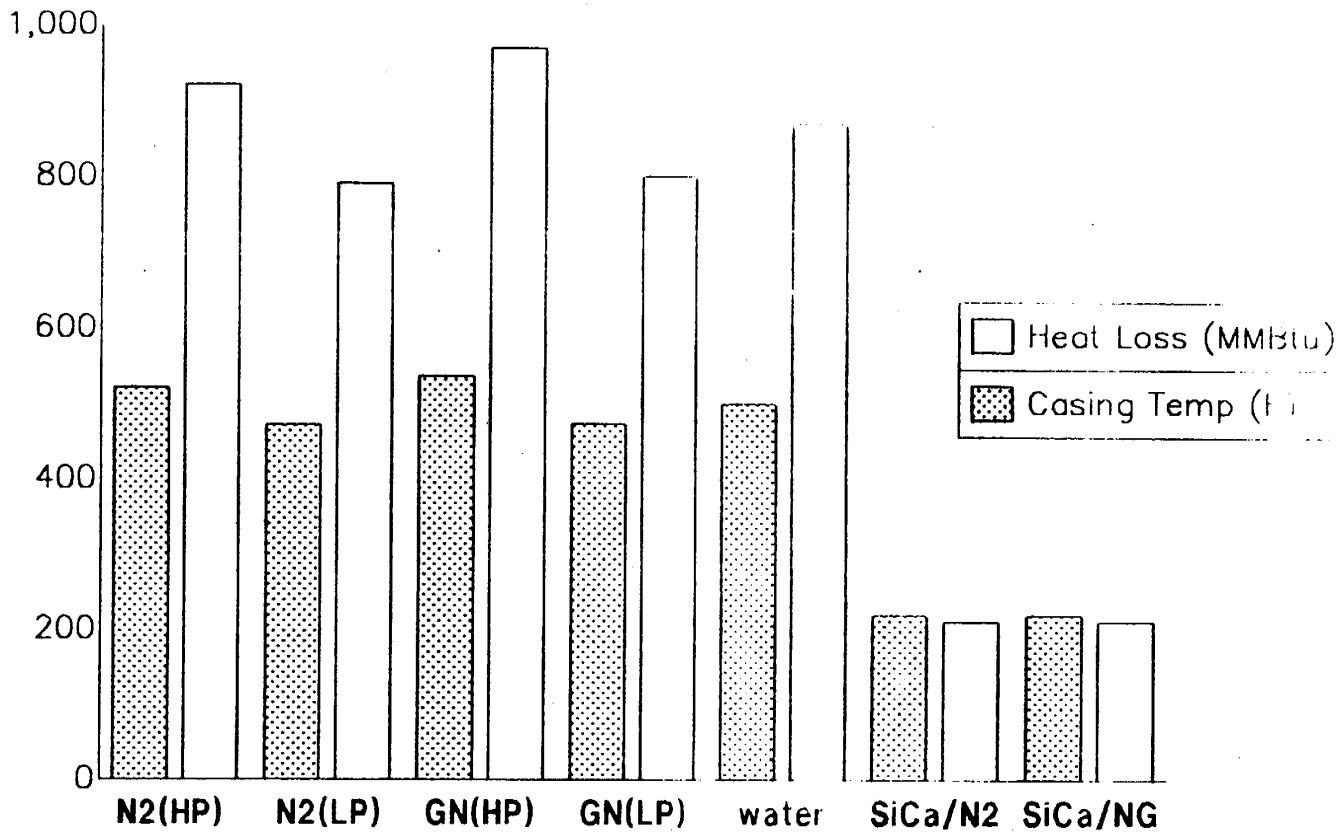

section until the well bottom is reached. A sum of the heat losses obtained in each block will result in the value of total heat losses towards the formation along the tubing and corresponding to the time interval evaluated.

PERCAL development was based on the following assumptions:

1. Heat flows radially from steam inside the tubing, crossing an insulating layer (optional), going through the fluid contained in the annulus, the casing, and the cement until formation is reached. Heat flow through surface films formed in the tubing and casing is taken into account (see Fig. 7).
2. Heat transfer is a function of steam injection time.
3. The length of each cylindrical cross section in the well is considered to be constant and equal at 100 feet.
4. The formation is a semi-infinite solid having constant properties.
5. Temperature variation in the formation with respect to depth is linearly dependent upon the geothermal gradient.
6. Steam is considered to be a monophase fluid whose properties are weighed by quality.
7. The pressure drop calculation assumes that steam is a monophase flow.

To estimate steam properties at each block outlet, as well as the corresponding heat losses towards the formation, the problem has been split into two parts:

3.2.1 Determining the Steam Pressure Drop

The total pressure drop in tubing is equal to the sum of pressure drop by gravity, acceleration and friction, namely:

$$\triangle P_{TOTAL} = |P_1 - P_2| = \triangle P_{friccion} + \triangle P_{gravedad} + \triangle P_{aceleracion} \quad \cdots\cdots\cdots (1)$$

Fig. 7

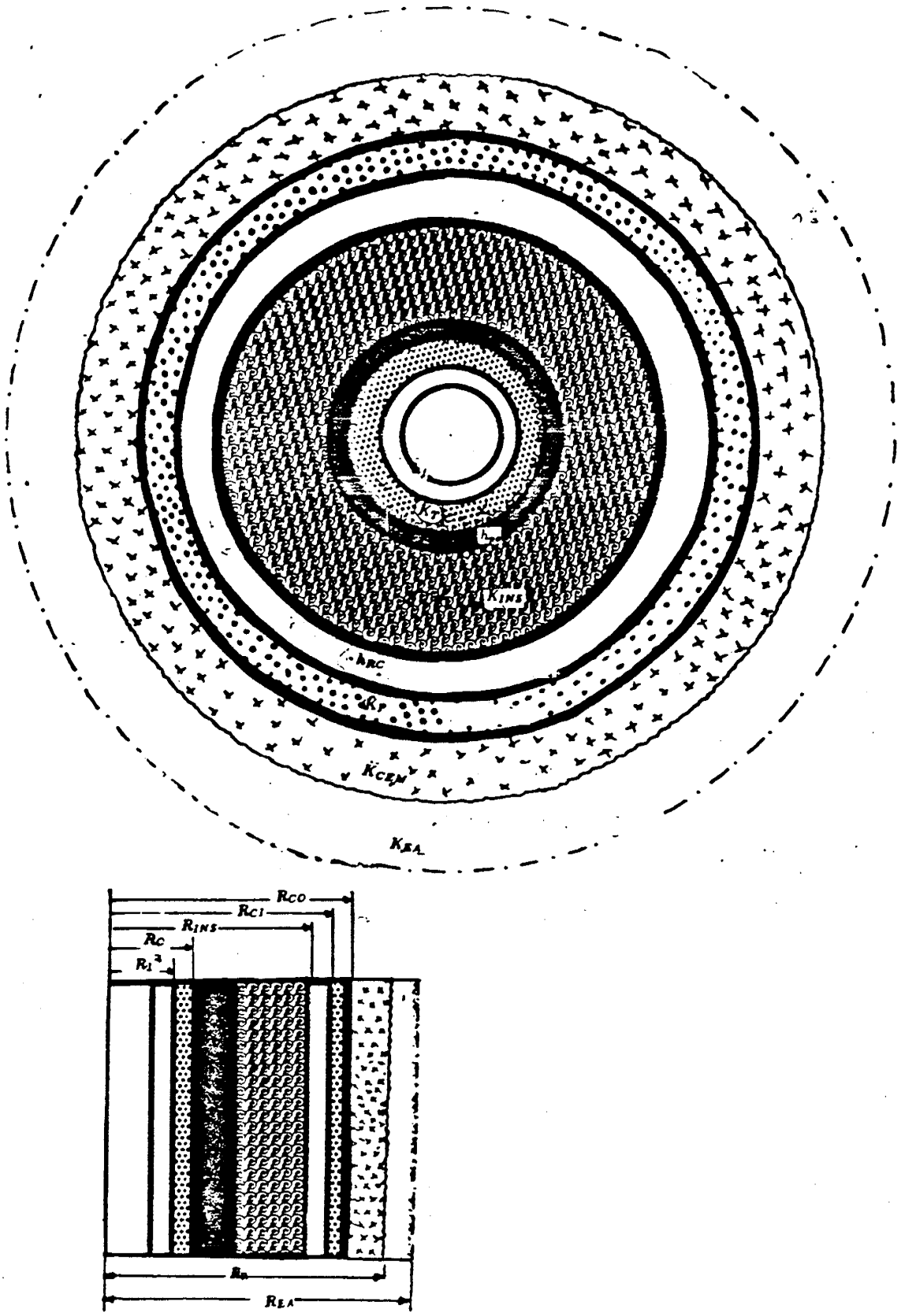

where pressure drops are obtained through Bernoulli simplified equation (6):

$$\triangle P_{friccion} = \frac{fLp\rho_v V_v^2}{2D_I g_c} \quad \ldots\ldots\ldots \quad (2)$$

$$\triangle P_{gravedad} = \rho_v . L . g \quad \ldots\ldots\ldots \quad (3)$$

$$\triangle P_{aceleracion} = \frac{V_i^2 - V_f^2}{2g_c} \quad \ldots\ldots\ldots \quad (4)$$

where:

f = friction factor, (dimensionless)

Lp = tubing length, (foot)

ρ = mean fluid density, (lbm/foot3)

Vv = mean fluid velocity, (foot2/s)

Vi = fluid velocity at block inlet, (foot/s)

Vf = fluid velocity at block outlet, (foot/s)

DI = tubing diameter, (foot)

g = gravity acceleration, (foot/s2) and gc = conversion factor, (lbf-s2/foot-lbm)

As a good expression of pressure drop by gravity, the following correlation developed for steam flow in vertical tubing (7) was used:

$$\triangle P_{gravedad_{100p}} = \frac{-1.91 \times 10^{-3} P_1^{0.9588}}{X_1} \quad \ldots\ldots\ldots \quad (5)$$

This expression predicts quite good values when used under the following conditions: 100-foot long tubing sections, steam pressures below 1000 psi, and qualities greater than or equal to 80%.

The saturated steam properties required to make the calculations related to the former expressions were computed through Farouq Ali, Bingham, and Kestin-Richardson correlations (7).

Assuming an average quality value in the block and a pressure drop, a trial and error procedure is started with equations (1-5), until a pressure difference value adjusted to block conditions is obtained. The quality value is checked by calculating heat losses as explained hereinbelow. If there is no adjustment between the assumed quality value and the calculated one, a new quality value is selected and the foregoing procedure is repeated until a good adjustment is reached.

3.2.2 Determining heat losses

The steam caloric energy, evaluated at a temperature T above the reference temperature (0 F) in generic block i is expressed by:

$$Q_{V_i} = W_i \times \left(h_{f_i} + X \times h_{fg_i} \right) \qquad \ldots\ldots\ldots\ldots \quad (6)$$

where:

Q_{Vi} = steam caloric energy, (Btu/s)

W_i = steam mass flow, (lbm/s)

h_{fi} = sensitive heat, (Btu/lbm)

h_{fgi} = latent vaporization heat, (Btu/lbm)

X = steam quality, (dimensionless)

By definition, heat transfer is just the amount of energy that is transferred from a body to another body due to a temperature difference between them, and it is represented by radiation, conduction and convection mechanisms.

Heat transfer problems basically involve the three mechanisms at the same time. Therefore, it is advisable to define a global heat transfer resistance combining the three resistances by means of the following equation (8):

$$Q_l = \frac{\Delta T_{a-b}}{RHT_{a-b}} \quad \text{.....} \quad (7)$$

where:

Q_l = heat transferred to the formation (Btu/h-foot)

T_{a-b} = temperature difference between the formation and steam, (F)

RHT_{a-b} = global resistance opposed by the system to temperature changes (foot-h-F/Btu)

In the well, heat is transferred to the adjacent formations by means of the following mechanisms (see Fig. 7):

1. Convection through the steam film in the internal tubing wall (1st expression).
2. Convection through the layers in the external and internal surfaces due to scales and dirt deposited (2nd and 4th expressions).
3. Conduction through injection tubing and casing walls (3rd and 7th expressions).
4. Conduction through the insulator, the cement and the altered earth zone surrounding the well (5th, 8th, and 9th expressions).
5. Convection-radiation through the fluid injected in the annulus (6th expression).
6. Resistance formation is a function of time (10th expression).

These mechanisms are represented by the following equation:

$$RHT = \frac{1}{2\pi}\left\{ \frac{1}{h_f R_i} + \frac{1}{h_{pi} R_i} + \frac{ln\left(\frac{R_O}{R_i}\right)}{K_T} + \ldots\ldots \right.$$
$$\ldots \frac{1}{h_{po} R_O} + \frac{ln\left(\frac{R_{ins}}{R_O}\right)}{K_{ins}} + \frac{1}{h_{RC} R_{ins}} + \frac{ln\left(\frac{R_{CO}}{R_{Ci}}\right)}{K_P} + \ldots$$
$$\left. \ldots\ldots\ldots \frac{ln\left(\frac{R_W}{R_{CO}}\right)}{K_{cem}} + \frac{ln\left(\frac{R_{EA}}{R_W}\right)}{K_{EA}} + \frac{f_{(TD)}}{\lambda_E} \right\} \ldots\ldots (8)$$

where:

h_f = coefficient of heat transfer by convection of the water film in the internal tubing surface, (Btu/foot2- F-h).

h_{pi} and h_{po} = coefficient of heat transfer by convection of the layer (scales, rust, dirt, etc.) in the internal tubing and casing surface, respectively, (Btu/foot2- F-h).

h_{RC} = coefficient of heat transfer by fluid convection and radiation in the annulus, (Btu/foot2- F-h).

K_T, K_{ins}, K_{cem} and K_{EA} = coefficients of heat transfer by insulator, cement, earth, and tubing conduction, respectively, (Btu/foot- F-h).

Ro, Ri, Rins, Rci, Rco, Rw and K_{EA} = represent in order of appearance, the tubing inside and outside radius, the insulator radius, the casing inside and outside radius, the well radius, and the altered earth zone radius.

The average fluid temperature in the annulus depends upon the insulator and the internal casing surface temperatures (Tins and Tci), which in turn depend upon the well

global resistance. Tins and Tci are determined by the following equations:

$$T_{ci} = T_A + \frac{(T_B - T_A)}{2\pi RHT} \times \left(\frac{ln\left(\frac{R_{CO}}{R_{Ci}}\right)}{K_P} + \frac{ln\left(\frac{R_W}{R_{CO}}\right)}{K_{cem}} + \frac{ln\left(\frac{R_{EA}}{R_{CO}}\right)}{K_{EA}} + \frac{f_{(TD)}}{\lambda_E} \right) \quad \ldots\ldots \quad (9)$$

$$T_{ins} = T_B - \frac{(T_B - T_A)}{2\pi RHT} \times \left(\frac{1}{h_f R_i} + \frac{1}{h_{pi} R_i} + \frac{ln\left(\frac{R_O}{R_i}\right)}{K_T} + \frac{1}{h_{PO} R_O} + \frac{ln\left(\frac{R_{ins}}{R_{CO}}\right)}{K_{ins}} \right) \ldots\ldots \quad (10)$$

Similarly, the dimensionless time factor f(TD) depends on both the block's global resistance and the time and formation resistance.

To evaluate the previously described equations, one must obtain the radiation-convection resistance values and the factor f(TD) through trial and error procedures. The value of the global heat transfer resistance is then assumed, annular temperatures are determined, and hRC and f(TD) are calculated and compared with the assumed value. The procedure is repeated until a good agreement is found between assumed and calculated values.

In this study, it is important to highlight the heat transfer mechanisms being involved in the annulus, in order to understand the performance of those fluids introduced in the annulus and establish the conditions at which the highest resistance to heat transfer will be obtained in this zone. Therefore, it is of utmost importance to consider the term representing the resistance to heat transfer by convection and radiation in the annulus:

$$R_{anular} = \frac{1}{h_{RC} R_{ins}} \qquad \text{..... (11)}$$

The coefficient of heat transfer by convection- radiation $h_{RC} = h_C + h_R$ depends upon the mean temperature of the fluid injected into the annulus and upon the properties thereof at the same temperature.

This term reflects the changes in heat transfer caused by a variation in the fluid type (nitrogen or natural gas) or a change in the confinement pressure thereof.

As a result, in order to establish the conditions and the type of gas to be introduced in the annulus, it is necessary to identify the values corresponding to this term in terms of resistance to heat transfer towards the formation.

The radiation coefficient hR is a function of the emissivity factor of the material and of temperatures Tins and Tci, whereas the convection coefficient hC depends upon the Pr and Gr numbers, which in turn are a function of the annular fluid properties evaluated at an average temperature.

Radiation is defined as the energy leaving a surface in the form of radiant heat, and it depends on the surface nature and the absolute temperature. In the pressure and temperature intervals evaluated in this study, nitrogen and natural gas are virtually transparent to thermal radiation because they are gases having symmetrical molecules (neutral charges). In other words, they neither emit nor absorb considerable amounts of radiant energy.

In the case of the coefficient of heat transfer by convection, the annular gases and the pressure and temperature conditions thereof contribute in a significant manner to the convective heat transfer process.

To calculate the convective coefficient, hc, it is necessary to predict the properties of the annular fluid. This is the reason why PERCAL includes routines that allow to calculate density through the Peng-Robinson equation (9), viscosity through the Reichenberg-Chung correlations (10), and thermal conductivity through the Eucken, Stiel, Thodos and Yorizane expressions (10), for methane, ethane, propane, carbon dioxide, and nitrogen, as well as mixtures thereof.

PERCAL model evaluates nitrogen properties between 14.7 and 1500 psi and 160 and 600 F, the properties of natural gas being assessed between 600 and 1500 psi for the above mentioned temperature interval.

To evaluate nitrogen and natural gas performance as insulators, a series of runs were carried out taking as fixed parameters those considered for WELMOD and presented in Table 1. In these runs, pure nitrogen at LP(14.7 psi) and HP(600 and 1500 psi), and pure natural gas, methane, and CO2, at 600 and 1500 psi, were used in the annulus with no tubing insulation. Besides, the calcium silicate-insulated tubing and the natural gas (SiCa/NG) or nitrogen (SiCa/N2) filled annulus were considered (see Table 2).

TABLE 2 TEST CONDITIONS

I. PRESURE (psi):

- H.P. = 1500 – 600
- L.P. = 14.7

II. ANNULUS FLUID COMPOSITION (%):

- N_2 = 100
- Natural Gas

  C_1= 81.5

  C_2= 9.0

  C_3= 4.5

  N_2= 2.0

  CO_2= 3.0

- C_1= 100
- CO_2= 100
- SiCa/N_2 (100%, Thick=1 inch)
- SiCa/N.G. (100%, Thick=1 inch)

3.2.3 Discussion of Results

Fig. 8 shows the results from total heat losses for the above-mentioned conditions, the following aspects being illustrated:

* Heat losses decreased in the order of 4.3 times when the calcium silicate-preinsulated string is used, irrespective of the gas and pressure used in the annulus.

* When natural gas as an annular fluid is compared to other fluids, the following percentages are found:

	600 (psi)	1500 (psi)
	(%)	(%)
N2-NG	-4.5	-3.0
SiCa/N2-SiCa/NG	-3.5	-2.6
C1-NG	-0.6	-0.5
CO2-NG	+6.7	+6.3

As shown in the previous Table, natural gas at both pressures is a slightly better insulator than nitrogen, but it is worse than carbon dioxide and it is exactly the same as pure methane.

Fig. 8 illustrates that heat losses differences between 14.7 and 1500 psi are important . They favor working conditions at low pressure by 28.4%. However, between 600 and 1500 psi, even though the trend is maintained, the difference is hardly 3%.

If heat losses due to a pressure increase from 600 to 1500 psi in the annular fluids are compared, it is observed that changes in the global thermal resistance (equation (8)) are not significant because of the high value of the formation resistance and the cement, which will become the most important contributions in the expression, being kept constant

Fig. 8 RESULTS HEAT LOSSES FOR DIFFERENT INSULATORS AT HIGH AND LOW PRESSURE.

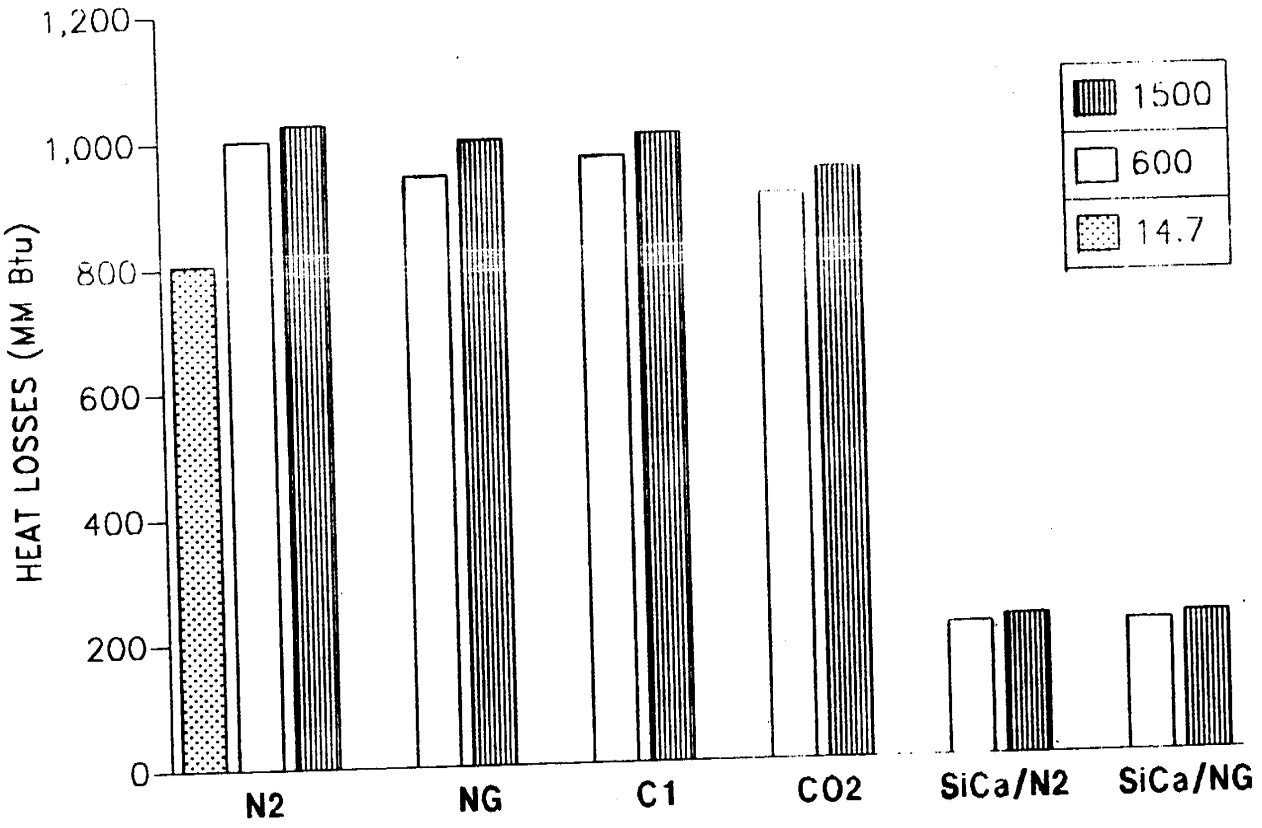

irrespective of the changes in the annular conditions. For the case of 14.7, there is indeed a major difference, but the orders of magnitude of caloric losses are still considerable.

Table 3 presents the quotients for annular resistance values at high and low pressures, which shows the effect of the pressure change and the formation on the annulus for 14.7, 600 and 1500 psi. This Table allows to observe that even if annular resistance is 1.4 and 4.9 times greater at 600 and 14.7 psi, respectively, the formation resistance + cement is higher than that of the annulus 3.0 to 14.9 times.

Comparing the results obtained from both simulators, one may notice that when N2 is present in the annulus, heat losses obtained with WELMOD and PERCAL show a 1.8% difference at 14.7 psi and a 12.2% difference at 1500 psi. Regarding natural gas, results show a 3.3% difference at H.P., which means a good agreement between the results obtained from both simulators.

TABLA 3 ANNULUS AND FORMATION + CEMENT RESISTENCE RATIOS

Injection Time (15 days)

		Low Pressure	High Pressure
INSULATOR	Rann(LP)/Rann (HP)	R(form+cem)/Rann	R(form+cem)/Rann
N2 (LP=600)	1.4	10.5	14.9
NG (LP=600)	1.4	6.6	9.1
C1 (LP=600)	1.4	6.8	9.4
CO2 (LP=600)	1.3	4.5	5.8
N2 (LP=14.7)	4.9	3.0	–

LP=600, 14.7 psi.

HP=1500 psi.

Rann= Annulus Resistance

Rform= Formation Resistance

4 CONCLUSIONS

1. A numerical model (PERCAL) was developed to evaluate the performance of different insulators.
2. Calcium silicate is the best option to insulate steam tubing.
3. At the same conditions, natural gas is better than nitrogen.
4. Regardless of the type of insulator and of the physical properties conditions, heat losses will be approximately the same if annular resistance is smaller or in the order of the formation or cement resistance.

5 REFERENCES

1. VENEZUELA – MEM/USA – DOE FOSSIL ENERGY REPORT JV-1 Enchanced oil Recovery "EOR THERMAL PROCESSES", April 1983. (Thermal Protection systems-Review of Venezuela Experience – Intevep-Maraven), pag. 2-2.

2. Dominique Bernard – Vaca Pedro, "MODELO DE FLUJO DE AGUA Y VAPOR EN POZOS INYECTORES DE VAPOR", 1984, INTEVEP-Informe Técnico INT-01219,84.

3. Mc Clintock, R.B., Richardson, P.W. and Spencer. "ASME STEAM TABLE IN SI UNITS. A.S.M.E., 1977.

4. Juza J. y Mares R, "EQUATION OF STATE FOR SATURATED AND SUPER-HEATED STEAM OF ORDINARY WATER SUBSTANCE IN THE RANGE 0 TO 650°C AND PRESSURES TO 30 MPa", Pag. 91–97 in Straub-Scheffler, "WATER

AND STEAM. THEIR PROPERTIES AND CURRENT INDUSTRIAL APPLICATION. Pergamon Press N.Y., 1979.

5. Watson J.T.R., Basu R.S. and Sengars J. B., "AN IMPROVED EQUATION FOR THE VISCOSITY OF WATER AND STEAM", Pag. 336–343 in Straub-Scheffler.

6. R. Roca Vila, "INTRODUCCION A LA MECANICA DE FLUIDOS", Coleccionnoc Ciencias del Ingeniero, Edic. LIMUSA, 1987.

7. Recuperacion Termica, Manual de Maraven.

8. Prats M. "PROCESOS TERMICOS DE EXTRACCION DE PETROLEO", Soc. Pet. Eng., Edic. Tec. INTEVEP S.A., 1987

9. Peng D. and D. B. Robinson, "A NEW TWO-CONSTANT EQUATION OF STATE", Ind. Eng. Chem Fundam 15.59, 1976.

10. Robert Reid. J. Prausnitz B. Pouling, "THE PROPERTIES OF GASES & LIQUIDS", Fourth Edition, 1986.

Task 48 - DOE shall provide INTEVEP with information from computer modeling, system design, and field tests conducted by the Lawrence Livermore National Laboratory on the use of cross-borehole electromagnetic induction tomography for imaging the two-dimensional conductivity distribution between wells in heavy oil strata and thermal injection zones.

ELECTROMAGNETIC THERMAL FRONT IMAGING DURING ENHANCED OIL RECOVERY

by

Michael Wilt

Lawrence Livermore National Laboratory

Livermore, California

Electromagnetic Thermal Front Imaging during Enhanced Oil Recovery

Michael Wilt
Lawrence Livermore National Laboratory

Introduction:

During the past two years at LLNL we have applied the EM induction method to the problem of thermal front tracking during EOR operations. In this paper we will describe the progress made during this past year and discuss the problems remaining to be solved.

Much of the progress during this past year has been achieved through a joint effort combining the work of researchers at LLNL, Lawrence Berkeley Lab (LBL) and University of California at Berkeley (UCB). These groups are applying the EM induction method to subsurface imaging although the focus of each research project is separate. The decision to work together on research problems common to these programs has speeded the progress of the efforts.

The LLNL research program consists of three parts a) to make laboratory measurements of the resistivity of steam saturated rock b) to develop a field system to accurately collect cross-borehole data in hostile environments and c) to develop algorithms to interpret these data in terms of the electrical resistivity distribution between boreholes.

Measurement of the resistivity of steam-saturated sands

At present there are no adequate models describing the electrical resistivity changes due to steam injection during EOR operations. Electrical conductivity (reciprocal of resistivity) data collected thus far come from some early laboratory simulations and some coarsely sampled field data (Mansure, 1990). This lack of information means that accurate simulations of steam front imaging are not possible.

To help remedy this situation we have begun making laboratory measurements of electrical conductivity in water and petroleum bearing sands during steam injection. This project is being done in cooperation with Dr. Kent Udell of U.C. Berkeley using his laboratory facilities. Mr Peter Vaughn, a graduate student, is making the measurements and will be using the data as part of his Masters thesis.

The initial stage of this project involved one-dimensional studies where pure steam is injected into one end of a sand pack and the temperature, steam saturation and electrical conductivity of the pack is monitored while the steam displaces the water (Figure 1).

Figure 2 displays the temperature and electrical conductivity for a point in the center of the one-dimensional column during a steam displacement experiment. Initially, the temperature and conductivity are unchanging but the plot shows a slight increase in electrical conductivity at about 2000 seconds that corresponds to an increase in temperature.This is evidence that the thermal front advances ahead of the steam front. As the steam front passes the measurement point the conductivity is drastically reduced while the temperature sharply increases to 100 degrees C and gradually thereafter up to 112 degrees C.

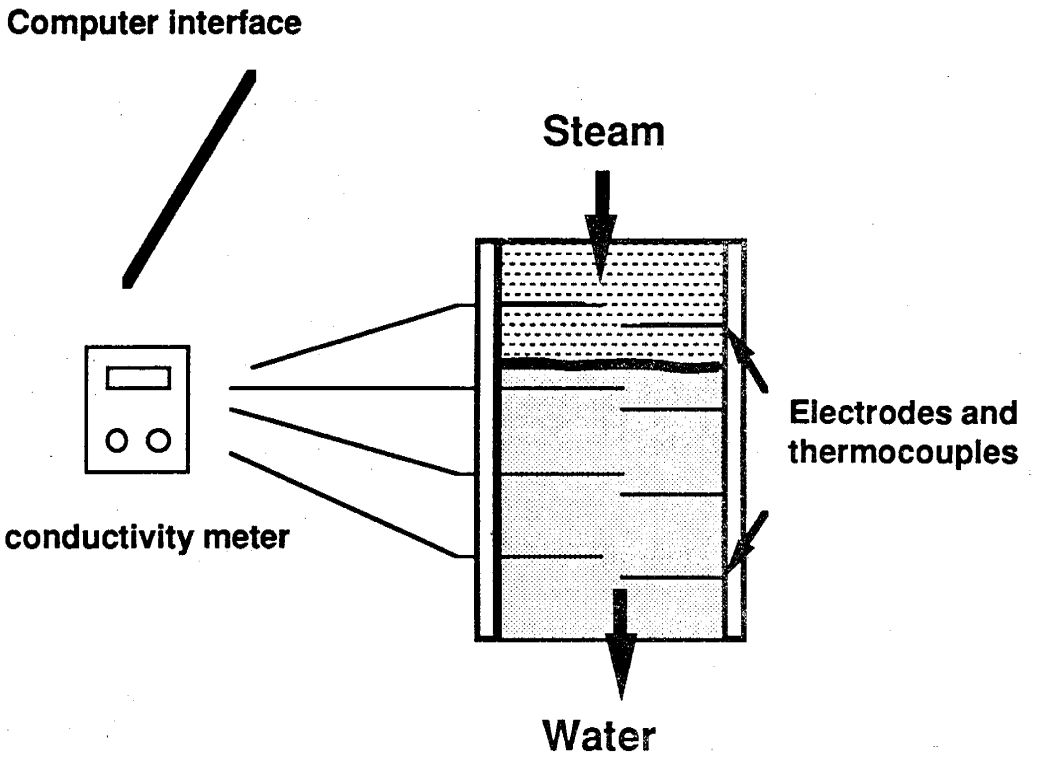

Figure 1 Schematic Diagram of the one-dimensional laboratory steam displacement cell.

The plot shows that the steam front is not an abrupt feature; it requires about 200 seconds to fully sweep past the measurement point at the center of the column. Towards the end of the column this transition zone is much broader. During steam injection the column may be subdivided into three regions: a steam saturated zone, a steam condensate zone (where the pure steam condenses and mixes with in-situ water), and a water saturated zone. The transitional steam condensate zone is also a zone of transitional electrical conductivity.

The conductivity of a sedimentary formation depends primarily on the pore fluid, its saturation, and the temperature. In general, the resistivity of the rock decreases significantly with temperature and increases with steam saturation. In an ideal steam flood the existing oil and water are displaced by dry steam or steam condensate; the resistivity of the affected region should therefore increase (at least slightly). In the field, however, it is observed that the resistivity of these swept zones typically decreases by a factor of two or three. These observations may be explained in part by the fact that in practice the steam quality is typically 50-70 percent (by volume) and the residual water is often higher in conductivity than the in-situ oil sand.

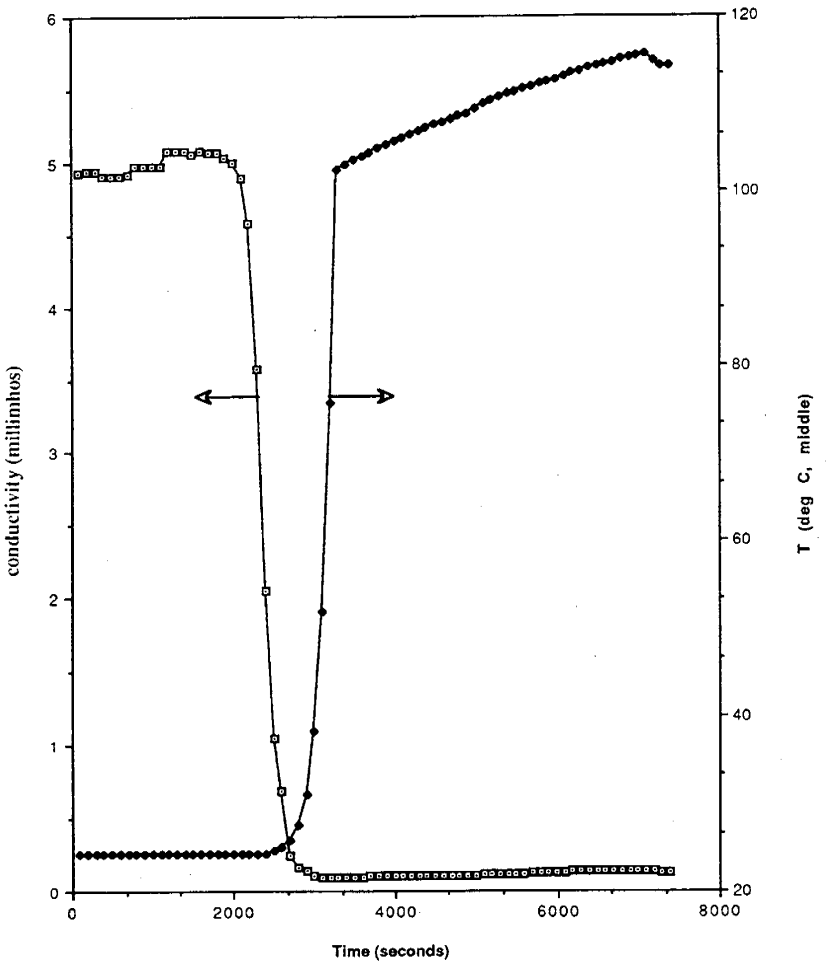

Figure 2 Plot of the temperature and electrical conductivity at the center of a one-dimensional sand-pack column during steam injection.

In succeeding phases of the experiment the water in the sands will be replaced by hydrocarbons and the quality of the steam (ie percentage of pure steam) will adjusted to correspond to actual EOR experiments. The final studies will be made in a two dimensional cell where it is possible to study the steam override phenomena and the effects of inhomogeneous structure.

Description of the Cross-Borehole Field System

The LLNL/LBL cross-borehole EM prototype system was developed in 1989 and 1990. It is a vertical component induction EM system designed for cross-hole imaging from boreholes spaced up to 300m apart.

The transmitter section consists of a custom-designed vertical coil driven by a commercially available EM transmitter. The coil is 8cm in diameter and 4m long weighing approximately 100 kg. At an operating current of 6 amps and frequencies from 100-100,000 hz, it supplies sufficient signal for propagation through conductive rocks for up to 500m. Signals are detected in a second borehole with a vertical-axis custom-designed coil. This is an ultrasensitive device, operable in the frequency range from 100-100,000 hz, and designed for depths up to 2 km. Detected signals are amplified within the coil then transmitted to the surface up the logging cable. At the surface they are further amplified and filtered before input to a lock-in detector at the receiver van. In the van all instruments are controlled from an HP 332 desktop computer via the GPIB interface. The computer can adjust instrument gains and sensitivities as well as select sample and averaging rates for the logging system.

A particular borehole segment is logged by moving the transmitter coil at a fixed rate while the receiver remains stationary. The source coil is typically moved at a rate of 3-5 m /minute. This allows sufficient time for signal averaging but is still a reasonable rate for data collection.

Sample cross-borehole magnetic field plots are given in Figure 3. These plots show the amplitude and phase of vertical magnetic fields at 512 hz as the transmitter moves between 550m and 670m in a borehole with the receiver fixed at 598m in a second borehole located 100m away. The amplitude plot shows a smoothly varying magnetic field that forms a peak where the source and receiver are in closest proximity and an approximately symmetrical decrease in field strength away from the peak. The phase data are also smooth but they display more character than the amplitude results. Near 600m the phase forms a peak and it "rolls off" sharply above this depth which correlates to a change in subsurface resistivity.

The above profile was measured twice on successive days to establish the precision level of the system; the difference between the data sets is displayed in Figure 4. This Figure shows that the amplitude difference over the 24 hour period was less than 1.0 percent for all points with an average of 0.3 percent. The difference in phase averaged less than 0.3 degree. Both of these are well within the guidelines of 1.0 percent for amplitude variations and 0.5 degrees for phase established for imaging requirements (Zhou,1989).

Field Test: BP/SOHIO Test Site Devine, Texas

The Devine test site, established and operated by BP/SOHIO, is located some 30 miles southwest of San Antonio, Texas. The site was established to test geophysical methods and instrumentation. It is located in an isolated area, away from sources of cultural noise, but still within reasonable access to population centers. Three wells are available for experimental use; two of the wells are steel-cased to 160m and plastic lined below this to a depth of 900m. The geology at the site consists of a sequence of sandstones, shales and limestones. Individual beds are continuous and flatlying across the entire site as is evident from an examination of the well logs. The borehole resistivity logs show variations from 1 to 300 ohm-meters with the higher resistivity layers (limestones) concentrated towards the base of the section and the sandstone and shale layers ranging in resistivity from 1 to 10 ohm-m.

The Devine field experiment, conducted between September 10-22, 1990, consisted of three stages: system checkout, cross-borehole measurement and surface-to-borehole measurements.

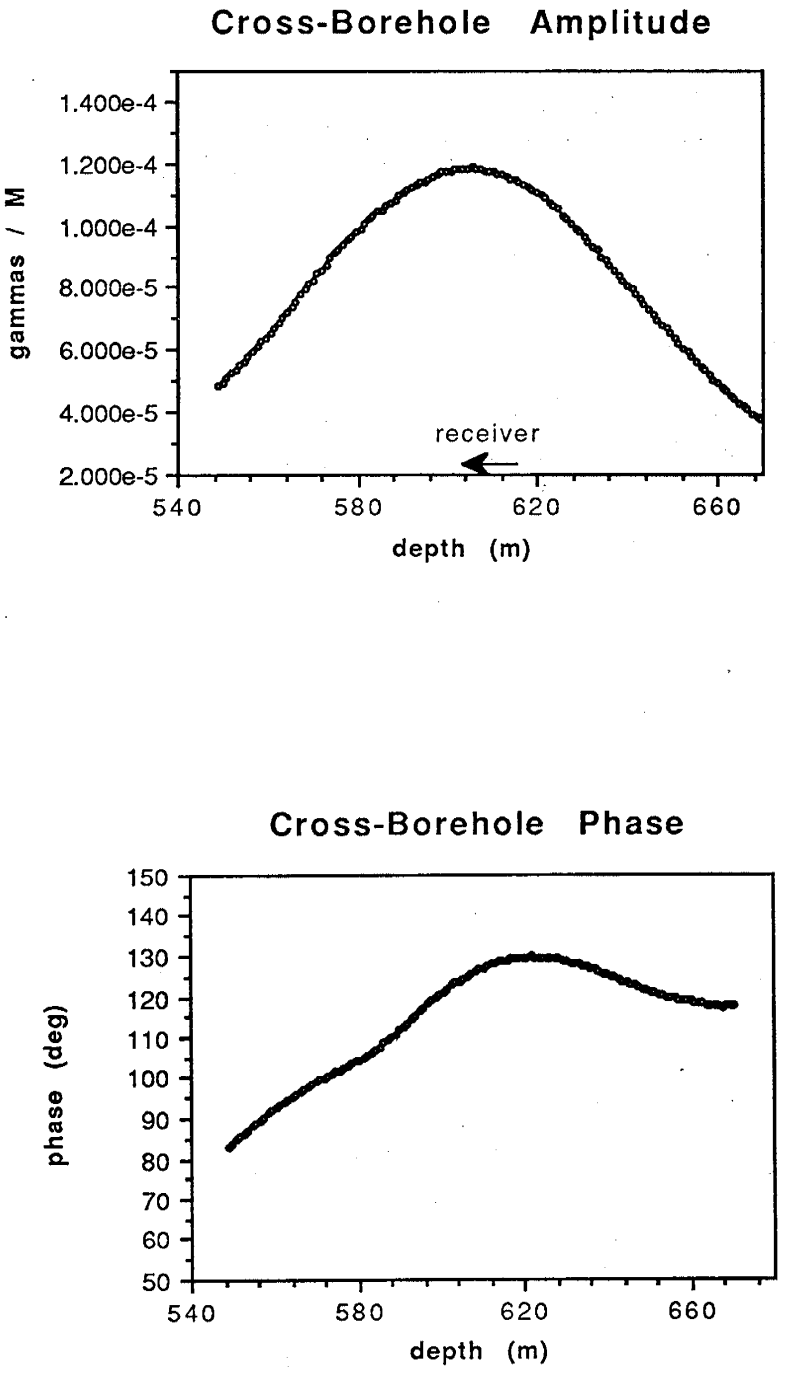

Figure 3 Sample cross-borehole amplitude and phase profiles.

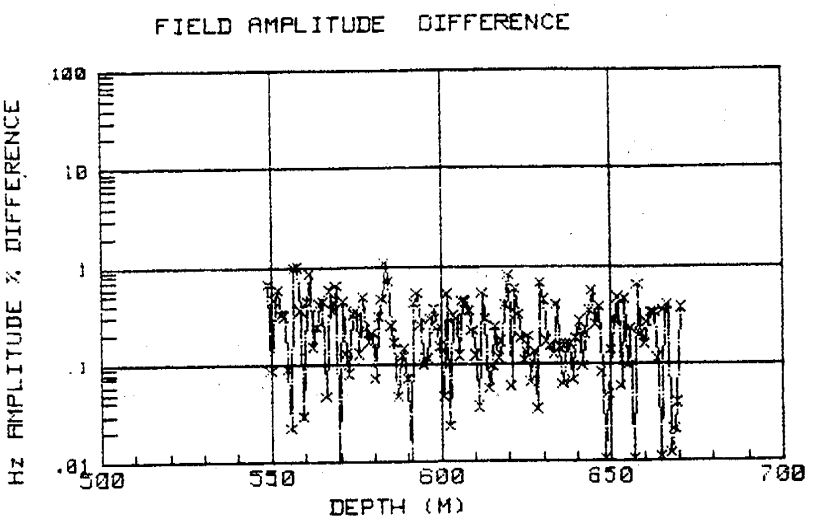

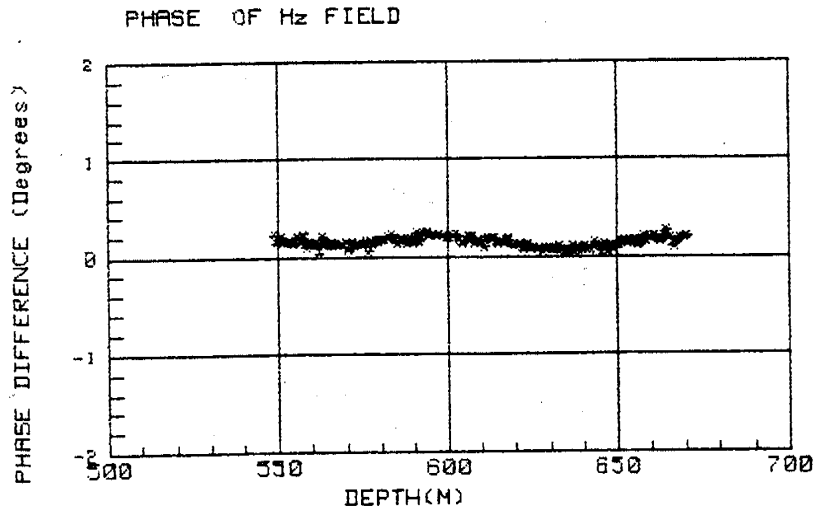

Figure 4 Percent difference of amplitude and phase measurements for a 24 hour repeat test.

During the checkout stage data is collected to a) determine repeatability of measurements over time and b) do "ground truth" checks by fitting observed data to layered models electrically equivalent to the borehole induction logs. These tests are necessary for attaching confidence limits to subsequent profiles and soundings.

Cross-borehole data were typically collected in 120m long profiles. For each profile the source moves between fixed depths 120m apart and the receiver remains fixed in the other borehole at a depth within these limits. Subsequent profiles are then made between the same source positions using different receiver locations. Each set of profiles corresponds to 13-16 receiver position covering a similar depth span as the source coil. .

Data Interpretation : Layered Model Inversion

A further test of our system is to match the field data to simple layered models. In areas where the rocks are flatlying a layered resistivity model should be electrically equivalent to the resistivity well log. Fortunately at the Devine site the resistivity logs indicate that the strata are continuous and flatlying and therefore this site should be well suited for a layered model interpretation.

For this test we selected a field profile and fit the observed data using computer program **NLSEM1D** developed by Ms. M. Descz-Pan of the University of California and Dr. K. Lee of Lawrence Berkeley Laboratory. The program does a layered model inversion, of up to 20 distinct layers, using arbitrary cross-borehole or surface-to-borehole magnetic field data. Only every fifth point in the cross-borehole profile is used in an effort to save computer time. (Fitting all 128 points with a 20 parameter model would require 11.5 hours on a VAX 8650 computer). First-guess layer boundaries and resistivities were assigned to match within about 20 percent with the induction resistivity log. The program was then free to adjust resistivities and layer boundaries until a fit was achieved.

The results of the inversion are given in Figure 7 along with the misfit of the observed and calculated data. The plot shows that the observed and calculated data match almost perfectly and that the layered section is a good approximation to the well log resistivity.

Next, we examine the sensitivity of the measurement to variations in the layered models. Beginning with a seven layer model that fits the observed data on profile DVD1950 we added a thin layer within the uppermost horizon that is slightly less conductive than the host. The resulting magnetic field differences from this new model serve to indicate the sensitivity to the change in model parameters. For a 3m thick layer of 25 percent reduced conductivity with a variable thickness the results show a substantial data misfit over large portions of the profile with a maximum error of more than six percent. Since the precision of the measurement is approximately 0.5 percent, this layer is an easily detectable feature. Note that this level of sensitivity is far greater than the surface or surface-to-borehole EM surveys can achieve.

Cross-Borehole Profiles

Sample cross-borehole profile sets are shown as a staggered set of amplitude and phase plots in Figure 6. The plots from the DV2K profile set are useful in verifying data quality and also in qualitative evaluation of results.

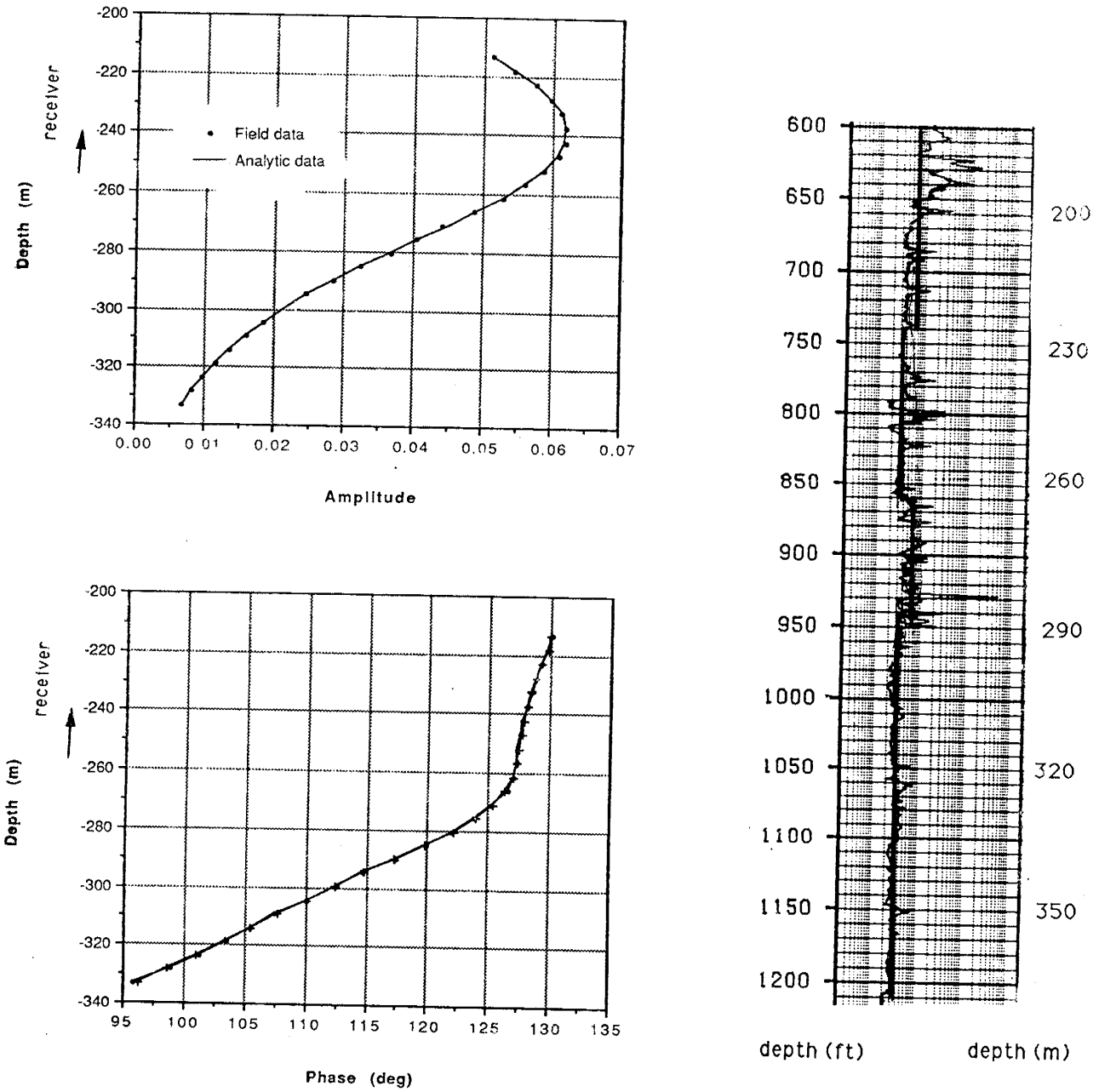

Figure 5 Layered model inversion results for a cross-borehole profile in Devine, Texas.

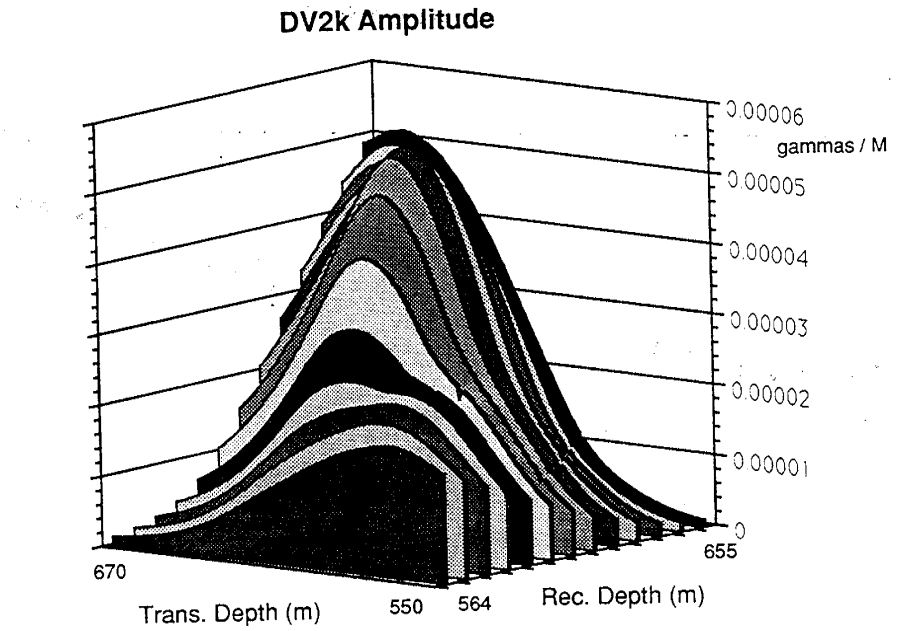

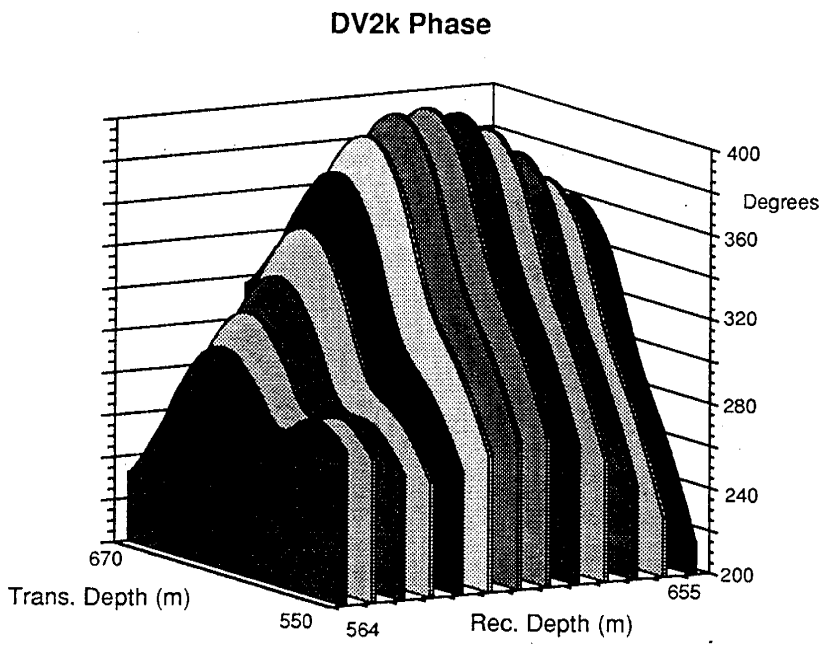

Figure 6 Staggered plots of cross-borehole amplitude and phase profiles for Devine data set.

rature near t

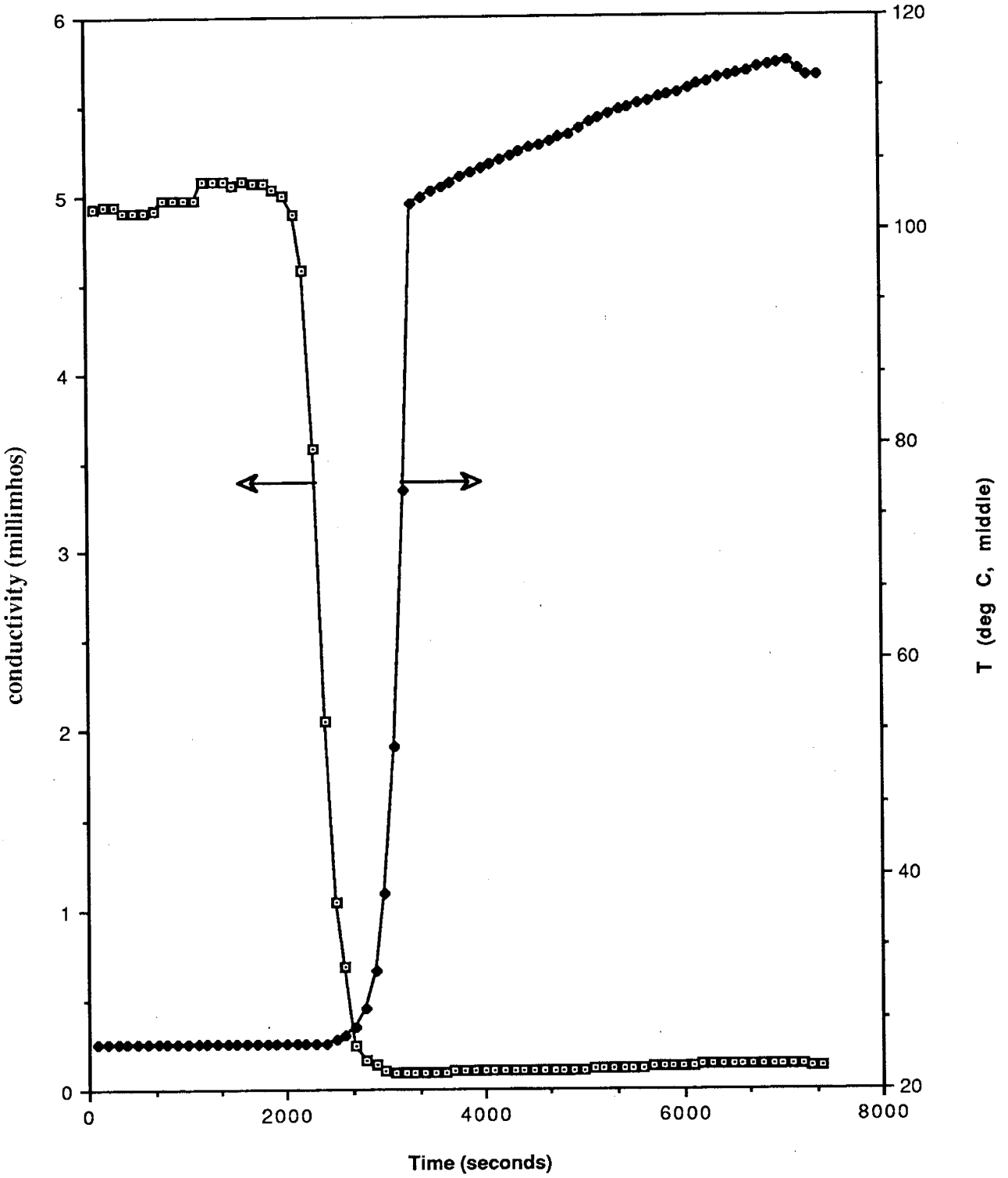

Figure 7

Note that the section spans a change in resistivity from 2-3 ohm-meter sands and shales at a depth of approximately 600m to 5-15 ohm-meter limestone beds below this. In the deeper, more resistive, section the staggered amplitude plots form peaks corresponding to the closest transmitter-receiver separation (Figure 6). For the shallower part of the section the peaks are much smaller in amplitude (reflecting the greater attenuation by the medium) and some peaks are centered near the layer boundary at 600 m instead of at the closest transmitter-receiver separation. The phase plots show an almost static peak near a depth of 620m and a phase roll-off above this point that is common to all of the profiles. This large phase shift is also due to the increased conductivity above 600m.

The staggered cross-borehole profiles shown above are rich in character and show significant sensitivity to a known conductivity change. This implies that this data can be effectively utilized for imaging.

Future Research Objectives

The results from the research in 1990 showed that an injected steam front does produce a sizeable change in resistivity and that the field system developed is more than adequate to detect this change and provide the data to accurately model the zone of changing resistivity. Three principal program objectives remain a) further develop modeling capability so that collected data can be properly interpreted b) harden the field system to survive in the hostile borehole conditions in EOR boreholes and c) undertake a field experiment to monitor the resistivity changes in an operating oil field undergoing EOR .

The first objective is being addressed through cooperative efforts between LLNL and LBL/UCB. Several modeling approaches are being pursued including 3 dimensional integral equation forward and inverse modeling and two dimensional approximate imaging algorithms.

Field system hardening is presently underway at LLNL. The problem is that the electronic components of the downhole sensors that require the temperature protection also generate heat. These components must therefore be mounted in high quality insulating dewars with an internal heat sink. The engineering of these system is currently underway at LLNL.

The final component is do a monitoring experiment at an industrial field site where an EOR process can be monitored. At such a site fiberglass monitoring boreholes must be available for measurements before, during and after steam flood operations. Acquiring the access to such a site is a priority in the coming year.

References

Mansure, A.J., and Meldua, R.F., 1989. Steam-Zone Electrical Characteristics for Geodiagnostic Evaluation of Steamflood Performance. Society of Petroleum Engineers regional meeting Bakersfield, California. Paper no. SPE 18797

Zhou Q., 1989, Audio Frequency Numerical Modeling and Tomographic Inversion for Reservoir Evaluation. Phd Thesis department of Engineering Geosciences University of California, Berkeley.

Task 49 - INTEVEP shall provide DOE with information from research conducted on the mechanistic studies associated with heavy oil production. The effect of steam distillation on the performance on steam injection processes will be studies as well as the kinetics of gas liberation in heavy oils.

MECHANISTIC STUDIES ASSOCIATED TO HEAVY OIL PRODUCTION: GAS DESORPTION

by

Sonia Embid, Antonio Cavero* and Claudio Olivera*

INTEVEP, S.A., Gerencia General de Exploración y Producción
Apdo. Postal 76343, Caracas 1070-A, Venezuela
* Simón Bolívar University, Venezuela

MECHANISTIC STUDIES ASSOCIATED TO HEAVY OIL PRODUCTION: GAS DESORPTION

Sonia Embid, Antonio Cavero*, Claudio Olivera*
INTEVEP, S.A., Gerencia General de Exploración y Producción
Apdo. Postal 76343, Caracas 1070-A, Venezuela
* Simón Bolívar University, Venezuela

ABSTRACT

This report is a summary of the results obtained in a series of experimental and theoretical studies on gas desorption in viscous liquids, which is one of the mechanisms associated with heavy crude production.

The theoretical study focuses on the development of a model for desorption kinetics, which will mainly consist of a nucleation model and a gas desorption model. The first model represents homogeneous nucleation in binary liquid dissolution, where thermodynamic properties are predicted by means of the equation of state developed by Peng and Robinson, and nucleation pressure and rate by the classic kinetic theory. The desorption model considers both desorption due to diffusion through the liquid/gas interface and desorption by bubble formation, growth and escape towards the gas phase. Finally, the experimental set-up for desorption tests is presented in order to provide a better understanding of the phenomenon, the results of which will be used in the adjustment of the model developed.

INTRODUCTION

At reservoir conditions, the crude may contain a considerable amount of dissolved gas. During the production period, near the wells and inside the pipes, the crude undergoes a strong decompression. As a result, gas solubility decreases, gas desorption occurs, and a biphase current is formed.

When a desorption phenomenon takes place, the dissolved gas becomes a part of a gas phase going through different stages. Initially, some nucleation centers are formed, in which the bubbles already generated grow and go up due to the density difference, until they reach the liquid surface. The dissolved gas molecules are transported from the liquid bulk to the liquid/bubble interface through molecular diffusion, the driving force being the existing concentration gradient (oversaturated in the liquid bulk and saturated in the interface). The growth rate of each bubble will be proportional to the surrounding gas concentration gradient, the gas diffusion coefficient, and the bubble surface area.

The process in which the dissolved gas is released takes place rapidly in light crudes when reservoir pressure decreases. Nevertheless, this process is slow in heavy crudes, where high viscosities are observed. The slow kinetics taking place during desorption affects both equilibrium conditions and present phase composition, thus altering fluid properties such as viscosity, density, and compressibility. This phenomenon is held responsible for the inexistence of a good historical comparison of heavy crude reservoir production rates, the problem becoming more serious when steam injection is used. As a result, it is impossible to predict the reservoir behavior and design an adequate operating plan. This has been observed particularly in heavy crude reservoirs undergoing steam-soak at Costa Bolívar, where high production levels cannot be justified with the subsidence observed in the surface.

This work consists of a series of experimental and theoretical studies that will provide a better understanding of the mechanisms leading to the phenomenon of dissolved gas desorption in viscous liquids.

The theoretical study aims at developing a model for desorption kinetics, which will basically include a nucleation model and a desorption model. These models will allow to obtain pressure profiles in time and integrate them into a computer package that will facilitate the study and interpretation of the phenomenon. To make some of the calculations, the models use a cubic-type equation of state. Therefore, a previous fluid characterization is needed to obtain the parameters required by said equation of state. A study of the desorption phenomenon inside the porous medium will then be undertaken, a model representing said phenomenon will be developed and, finally, an attempt will be made to incorporate said model into the thermal simulators used in reservoir studies.

The experimental part of this work will be conducted outside the porous medium in order to determine the effect of desorption on fluid properties. Experiments will be initially carried out on transparent silicones that will allow to observe bubble formation

and movement, representative heavy crudes being subsequently used. The test procedure is as follows: silicone is introduced in the cell, methane pressurization through a pump takes place, some time has to elapse to reach equilibrium conditions, and a gradual decompression starts until the first bubbles are formed. By recording the pressure at which this occurs and knowing the equilibrium data of the system selected, it is possible to determine the nucleation driving force. The experimental determination of different parameters during gas desorption in viscous liquids is intended to contribute to a better understanding of nucleation mechanisms and provide some basic information for adjusting the model developed.

NUCLEATION MODEL

A homogeneous nucleation phenomenon can be defined as the spontaneous emergence of steam bubbles in a liquid phase bulk when exposed to a pressure lower than the saturation pressure. This may be easily represented if one considers an isothermal decompression process of a component like the one schematically shown in Fig. 1. At a sufficiently high initial pressure (point A), the least free energy aggregation state is found in the liquid phase. It is not possible for a steam phase to exist in a stable manner if one takes into account the thermodynamic criterion:

$$\triangle G = \mu_v(T,P) - \mu_L(T,P) > 0 \quad for\ P > P_{sat}$$

This situation continues until the saturation or boiling pressure (point B) is reached. Since the steam and liquid free energies become equal at that pressure, they can both coexist in equilibrium:

$$\triangle G = \mu_v(T,P_{sat}) - \mu_L(T,P_{sat}) = 0$$

This condition is traditionally known as "bubble point". However, this term is not correct because bubble formation in the liquid bulk implies the creation of a curve liquid-steam interface, for instance a spherical interface of radius R, having an internal steam pressure exceeding that of the liquid due to the action of interfacial tension,

$$P_b = P_{sat} + 2\sigma/R$$

and the steam free energy would be greater than that of the liquid,

$$\triangle G = \mu_v(T,P_{sat} + 2\sigma/R) - \mu_L(T,P_{sat}) > 0$$

Therefore, it is necessary to decompress the liquid beyond the saturation pressure so that homogeneous nucleation will take place. At each pressure P lower than P_{sat} (point C),

bubble formation is thermodynamically feasible, since there is a finite equilibrium radius, Rc, for which free energies of both phases are identical.

$$\Delta G = \mu_v(T, P + 2\sigma/R) - \mu_L(T, P) = 0 \quad for\ P<P_{sat}$$

Unlike the heterogeneous nucleation process (in which bubbles generate around promoting sites alien to the liquid phase, for instance in the zone being in contact with the recipient walls, or on impurities present in suspension), homogeneous nucleation must be reached by spontaneous clustering of molecules in low density aggregates, due to the molecular agitation typical of the fluid. The nucleation pressure corresponds to the so-called kinetic decompression (or overheating) limit, and it is defined as a pressure low enough to permit statistical nucleation frequency to result in a macroscopically observable bubble generation. This pressure cannot be calculated by merely thermodynamic or macroscopic methods because it requires kinetic and molecular considerations.

Nevertheless, thermodynamics provides an absolute lower limit for nucleation pressure (the saturation pressure Psat being the corresponding upper limit). At a pressure sufficienly low (point D), the liquid phase would be intrinsically unstable, even when facing the smallest fluctuations, and its transformation into steam would take place in an instantaneous and even explosive way, no previous nucleus formation being required. This condition corresponds to the so-called spinodal point, which is equivalent to a thermodynamic decompression (or overheating) limit, and for the simple case in Fig. 1, it is the pressure at which the mechanical stability frontier is reached,

$$\left(\frac{\partial P}{\partial v}\right)_T = 0$$

Saturation, nucleation, and spinodal pressures for a same fluid depend upon temperature. At supercritical temperatures (curve A'D'), the discontinuous transformation of the liquid into steam does not occur since aggregation states are not distinguishable one from the other. At relatively low temperatures (curve A"D"), kinetic and thermodynamic decomposition limits may correspond to negative pressures. Physically, this behavior means that the pressure acting on the liquid may not only be reduced to zero with no bubble formation, but it may also become a hydrostatic tension reaching the limit of resistance to intermolecular force rupture. In this case, the "bubbles" created are indeed cavities or vacuums in the liquid bulk, and bubble formation and growth phenomena are known as cavitation.

Our mathematical model for simulating the nucleation process of gases dissolved in viscous liquids aims at predicting for the system studied, whose composition and temperature are known, the limits for nucleation (saturation, composition, and spinodal pressures), and the bubble emergence rate, as well as the size and composition thereof.

In order to predict the thermodynamic properties necessary for nucleation calculations, the cubic equation of state model was adopted for both phases, liquid and steam (bubbles). This approach advantageously requires a limited number of parameters, which mainly consist of a series of pure component properties. The equation of state developed by Peng and Robinson [1976] was the one selected among the numerous equations of state available, because it offers favorable simplicity and accuracy predictions [Peng and Robinson, 1977; Valderrama and Molina, 1986; Mohamed and Holder, 1987; Nghiem el al., 1985; Firoozabadi et al., 1978]

Interfacial Tension

Experimental data on dissolution interfacial tension are rare. The expression developed by Deam and Maddoz [1970] was used for this model:

$$\sigma^{1/4} = \sum P_i(x_i/V_L - y_i/V_V)$$

where x,y are the liquid and steam phase compositions, V_L and V_V are the corresponding molar volumes in $[cm^3/mol]$, and P_i is the "parachor", a parameter typical of each pure compound calculated in this case by contributions of the molecule structural groups and whose results are summarized in Table 2.

Predicting the saturation pressure

For a given composition and temperature of the liquid phase, the traditional saturation pressure or "bubble point" is calculated by solving for $P_{sat}, y_i, ..., y_n$ the system of isofugacity equations

$$\phi_{iV}(T, P_{sat}, \underline{y})y_i = \phi_{iL}(T, P_{sat}, \underline{x})x_i \qquad i = 1, ..., n$$

with the restriction over the sum of the steam molar fractions:

$$\sum y_i = 1$$

The saturation pressure is calculated in this model through a Rachford-Rice-type algorithm. The previous equations are combined in the expression:

$$F = \sum y_i - 1 = (\sum \phi_{iL}x_i/\phi_{iV}) - 1$$

where the unknown steam compositions have been formally eliminated. If the effect of the components on steam fugacity coefficients is neglected in the first place, the quantity F may be considered as an exclusive function of pressure, the derivative being

$$\frac{dF}{dP_{sat}} \approx \frac{1}{RT}(\sum y_i \overline{V}_{iL} - V_v)$$

where the following thermodynamic relations have been used:

$$\frac{\partial ln\phi_i}{\partial P} = \frac{\overline{V}_i}{RT}$$

$$\sum y_i \overline{V}_i = V$$

If one combines these equations, it is possible to iterate on the saturation pressure by a Newton-Raphson-type method and generate new values for steam compositions by using successive substitutions with standardization to satisfy the restriction. The iterative scheme may be summarized by the following equations:

$$y_i^n = \frac{\phi_{iL}^n x_i}{\phi_{iV}^n}$$

$$P_{sat}^{n+1} = P_{sat}^n - \frac{RTF^n}{\sum y_i^n \overline{V}_{iL}^n - V_V^n}$$

$$y_i^{n+1} = \frac{y_i^n}{F^n + 1}$$

The first estimates for P_{sat} and $\underline{y}$ are derived from Raoult's Law with equilibrium coefficients approximated by a generalized three-parameter correlation [Fussell, 1979]. Fugacity coefficients are calculated through the equation of state.

Predicting the mechanical spinodal pressure

The stability limit to determine spinodal pressures is obtained by minimizing Gibbs energy. For a pure fluid, it will be represented by the minimum value in a P-v diagram:

$$F_{22} = -(\frac{\partial P}{\partial V})_{T\underline{N}} = 0$$

and it is solved for V by using the Newton-Raphson-type iteration:

$$V^{n+1} = V^n - \frac{F_{22}^n}{F_{222}^n}$$

with $F_{222} = -(\frac{\partial^2 P}{\partial V^2})_{TN}$ analytically obtained from the equation of state. With the initial estimate $V = V_{sat}$, convergence occurs in a maximum of four iterations for a final accuracy of $10^{-5}[cm^3/mol]$ in V.

Even though the mechanical spinodal pressure does not represent the true thermodynamic stability limit in a binary system, its evaluation is desirable because diffusive spinodal pressure must be located between the mechanical pressure and the saturation pressure.

Predicting the diffusive spinodal pressure

By minimizing Gibbs energy in a binary system, one obtains the stability limit with the expression:

$$\left(\frac{\partial \mu_1}{\partial N_1}\right)_{TPN_2} = \left(\frac{\partial \mu_1}{\partial N_1}\right)_{TVN_2} - \frac{[(\partial P/\partial N_1)_{TYN_2}]^2}{(\partial P/\partial V_1)_{TN_1N_2}} = 0$$

which can be rewritten as:

$$G_{33} = F_{33} - (F_{23})^2/F_{22}$$

this equation may be solved by using a simple algorithm to directly search the volume by interval bisection:

$$\begin{aligned} &a) \quad V_{min} = V_{sat}, \qquad V_{max} = V_{mec} \\ &b) \quad V^n = (V^n_{min} + V^n_{max})/2 \\ &c) \quad if\ G^n_{33}{>}0, \qquad V^{n+1}_{min} = V^n, \quad V^{n+1}_{max} = V^n_{max} \\ &\qquad\quad if\ G^n_{33}{<}0, \qquad V^{n+1}_{min} = V^n_{min}, \quad V^{n+1}_{max} = V^n \end{aligned}$$

The corresponding pressure is directly obtained from the equation of state.

Predicting the liquid-bubble equilibrium

Given the liquid phase temperature and composition, and once a pressure lower than that of saturation has been assigned, the composition, pressure, size of bubbles in (unstable) equilibrium with the liquid are calculated through a procedure similar to the one used for saturation pressure:

$$\phi_{ib}(P_b, T, \underline{y}) y_i P_b = \phi_{iL}(P_L, T, \underline{x}) x_i P_L \qquad i = 1, ..., n$$

$$P_b = P_L + \frac{2\sigma}{R_c}$$

with the restriction

$$\sum y_i = 1$$

being the liquid phase fugacity constant in this case and defining the Rachford-Rice F function as:

$$\frac{dF}{dP_b} \approx \frac{V_b}{RT} = \frac{z_b}{P_b}$$

One starts the calculations with the previously computed composition and pressure values for the saturation point, and the method converges in a maximum of five iterations at an accuracy level of 10^{-8} in the sum of compositions, even in the immediate neighborhood of the critical point. Equation $P_b = P_L + \frac{2\sigma}{R_c}$ is reserved for determining the bubble critical radius, once surface tension has been assessed.

Predicting the nucleation pressure

The model developed uses the frequency factor and the nucleation rate suggested by Reid [1978]:

$$J = \frac{N_0}{V_L} f \quad exp[\frac{16\pi N_o \sigma^3}{3RT(P_b - P_L)^2}] \geq 10^{12}[cm^{-3}s^{-1}]$$

$$f = 10^{11}[s^{-1}]$$

which, through the Peng-Robinson equation, reproduce the nucleation limits experimentally obtained by Porteous and Blander [1975] for the butane-ethane system.

Results of the nucleation model

For a first model test, isotherms, saturation pressures, and mechanical spinodal pressures were calculated for n-hexane, in order to check the thermodynamic routines and have an idea of its representativeness in reality. Fig. 2 shows the calculation results and enlarges and extends the graphs presented by Reid [1978] and Modell and Reid [1983]. The isotherms shown correspond to reduced temperatures of 0.90, 0.93, 0.96, and 0.98. It can be clearly seen that at a lower temperature the stability limit is obtained at a negative

pressure, which is the equivalent of decompressing the liquid to a null pressure with no bubble formation.

The same results are shown in the pressure-temperature diagram in Fig. 3, where a comparison is made with nucleation pressure and saturation pressure experimental values [Salerno et al., 1986]. Notice first of all that the equation of state selected provides an excellent representation of the liquid-steam equilibrium for this compound. Likewise, spinodal pressures are lower than experimental nucleation pressures, according to the general discussion presented in the first section of this chapter.

Fig. 4 repeats the same comparison, incorporating now experimental nucleation values and calculated spinodal values, for pure n-pentane. Notice that the spinodal curves of two fluids maintain the same qualitative relation as the measured nucleation points, thus announcing a wider metastability range for the heaviest hydrocarbon.

The effect of the presence of a second component, generally a dissolved gas, is shown in Fig. 5, where Fig. 2 calculations are repeated, this time for a 10% carbon dioxide and 90% n-hexane (in moles) dissolution, incorporating besides the nucleation pressures predicted by the model. The first obsevation that is needed in this regard is that a binary dissolution has in general an intermediate behavior ranging from the behavior of pure compounds to the behavior of the most concentrated component. In this manner, a 10% CO_2 addition produces a higher volatility and increases spinodal and nucleation pressures in the system, but the general behavior is still "hexane-like" rather than "CO_2-like". At a temperature of 400°K, both the diffusive spinodal pressure and the nucleation pressure are negative, and bubble formation is only possible through a heterogeneous nucleation mechanism.

The need for high temperatures to favor nucleation is clearly observed in the exponential term of the equation used to determine the value, which increases rapidly with temperature due to a three-effect combination: explicit dependence is inversely proportional to temperature, the bubble pressure increases (essentially equal to saturation pressure), and surface tension is reduced as the two phases become similar in the critical region. Under these circumstances, Fig. 5 shows that the nucleation pressure approaches the saturation pressure much more rapidly than the thermodynamic stability curve.

Tables 3 and 4 present results for the methane-decane system at two levels of composition: 10% methane and 5% methane in moles. In both cases, nucleation pressures are negative below 500°K , but they increase very rapidly approaching the saturation values in the critical region. This situation is illustrated in Fig. 6 for both compositions, and in Fig. 7, where for the 10% molar dissolution in methane nucleation rates J calculated for several temperatures have been plotted as functions of the pressure acting on the liquid. The curves obtained confirm the assertion that the nucleation rate increases abruptly in several orders of magnitude in the surroundings of the nucleation point. On the one hand, this fact guarantees that the calculated nucleation pressure will be relatively insensitive to the critical value selected for J, and explains the unequal values chosen by authors

such as Blander and Katz [1975], Reid [1978] and Lienhard et al. [1986]. However, it can be concluded that an accurate measurement of the nucleation pressure poses an extremely complicated experimental problem, and that the determination of a critical rate from laboratory values will be subject to considerable uncertainty.

MODEL OF GAS DESORPTION IN VISCOUS LIQUIDS

The desorption of a gas A dissolved in a liquid B due to a sudden depressurization in the system may be caused by two different mechanisms: by gas desorption from the liquid bulk to the gas phase through the liquid's free surface due to molecular diffusion, and/or by formation, growth and escape of gas bubbles.

Desorption without bubble formation

When the thermodynamic conditions in the system are not the necessary ones for nucleation to occur, gas desorption takes place only by diffusion from the liquid's free surface. The general equation of unidimensional mass transfer, neglecting convective flows, is reduced to:

$$\partial C_A/\partial t = D_{AB}\partial^2 C_A/\partial y^2$$

with the boundary and initial conditions:

$$C_A(0,y) = C_A^0$$

$$C_A(t,H) = C_A^*$$

$$\partial C_A(t,0)/\partial y = 0$$

The first boundary condition states that equilibrium is instantaneously reached in the liquid's free surface (y = H), and the second condition indicates that the recipient bottom (y = 0) is not permeable. This differential equation obtained through the method of variable separation is solved as follows:

$$C_A = C_A^* + 2(C_A^0 - C_A^*)\sum_{n=0}^{\infty}\frac{1}{\lambda n}\ exp(-\lambda n^2 D_{AB}t/H^2)sen(\lambda n)cos(\lambda n\ \ y/H) \qquad (1)$$

with

$$\lambda n = (n + 1/2)\pi$$

By integrating this expression, it is possible to obtain the amount of gas dissolved in the liquid for a given time. The rate of gas desorbed through the free surface is directly calculated by differentiating the equation and applying Ficks' law:

$$N_q = 2(D_{AB}/H)(C_A^0 - C_A^*) \sum_{n=0}^{\infty} exp(-\lambda n^2 D_{AB} t/H^2) sen^2(\lambda n)$$

Desorption with bubble formation

When the system conditions allow bubble formation, the first step to describe the phenomenon is to make a population analysis that leads to the spatial distribution of bubbles according to size and time. Consider a volume V of liquid containing dissolved gas. in which the liquid does not evaporate, capilarity effects are negligible, and the system is isothermal, where nucleation occurrence leads to the presence of spherical bubble formation, with no breakage or coalescence thereof. A general balance of the bubble population would be represented as follows:

$$\frac{d}{dt} \int \Psi dV = \int (B - D) dV$$

where the left hand term represents bubble accumulation and the right hand term is the net bubble generation, the entity distribution being defined as:

$$\Psi(x, y, z, \zeta_1, \zeta_2, ...\zeta_m, t)$$

where (x, y, z) are the spatial coordinates, $(\zeta_1, \zeta_2 ....\zeta_m)$ are the properties inherent in each particle and quantitatively describing their individual state, and t is time. B is the birth function expressed in entity births per time, volume, and property variation unit. D is the death function expressed in entity deaths per time, volume, and property variation unit.

Applying Reynolds transport theorem to the first term:

$$\frac{d}{dt} \int \Psi dV = \int [\frac{\partial \Psi}{\partial t} + \nabla(\overline{v}\Psi)] dV$$

where the velocity vector can be split into two components, $\overline{v} = \overline{v}_s + \overline{v}_i$, where $\overline{v}_s$ is the velocity vector described in spatial coordinates, and $\overline{v}_i$ the velocity vector described in each bubble's internal coordinates.

Since the region is arbitrary, the equation will be fulfilled only if the constituent is equal to zero, thus giving rise to the differential equation:

$$\frac{\partial \Psi}{\partial x} + \frac{\partial}{\partial x}(v_x \Psi) + \frac{\partial}{\partial y}(v_y \Psi) + \frac{\partial}{\partial z}(v_z \Psi) + \sum_{i=1}^{m} \frac{\partial}{\partial \zeta_i}(\vartheta_i \Psi) + D - B = 0 \qquad (2)$$

Predictive Model for Desorption in Viscous Liquids

Fig. 8 is a representation of the phenomenon to be modelled, a viscous liquid with a dissolved gas exposed to sudden depressurization until conditions allowing nucleation are reached. The following conditions are then assumed:

- Bubbles are formed with an initial radius equal to zero (B = 0).
- Bubbles do not die. They escape through the liquid's free surface (D = 0).
- Bubbles move only vertically (y direction) and escape through the liquid's free surface ($v_x = v_z = 0$)
- Each bubble behaves as if it were alone in an infinite medium whose velocity at any point is equal to zero. This means that bubbles do not induce any movement in the liquid with their upward movement

The internal property of interest is bubble diameter (L), therefore:

$$\vartheta_i = dL/dt = G$$

According to these considerations, equation (2) is reduced to:

$$\frac{\partial \Psi(y, L, t)}{\partial t} + \frac{\partial}{\partial y}[v_y(L)\Psi(y, L, t)] + \frac{\partial}{\partial L}[G(L, t)\Psi(y, L, t)] = 0$$

Dividing the liquid volume into slices of thickness Δy, and assuming that each slice has a uniform bubble distribution (which does not depend upon spatial coordinates) and that no liquid flow exists between slices, one has for each slice i:

$$\int_{y_{i-1}}^{y_i} \frac{\partial \Psi(y, L, t)}{\partial t} dy + \int_{y_{i-1}}^{y_i} \frac{\partial}{\partial y}[v_y(L)\Psi(y, L, t)] dy + \int_{y_{i-1}}^{y_i} \frac{\partial}{\partial L}[G(L, t)\Psi(y, L, t)] dy = 0$$

for i = 1,...n

integrating and dividing by Δy:

$$\frac{\partial \Psi_i}{\partial t} + \frac{\partial}{\partial L}(G\Psi_i) = (v_y \Psi_{i-1} - v_y \Psi_i)/\Delta y \tag{3}$$

said equation must be solved with the initial and boundary condition

$$\Psi_i(L, 0) = 0$$

$$\Psi_i(0, t) = J(t)/G(0, t)$$

whose solution allows to describe bubble distribution in slice i as a function of diameter and time.

The next step is to make a mass balance of the solute for each volume element of perfectly agitated liquid, thus obtaining:

$$dC_{Ai}/dt = -W_{Ai}/V_i = f_i(t, C_{Ai}) \tag{4}$$

with the initial condition $C_{Ai}(0) = C_A^0$. Molar flow W_{Ai} will be given by:

$$W_{A(i)} = W_{Ab(i)} + W_{As(i)} - W_{As(i-1)}$$

being the rate of gas desorbed into bubbles in slice i, $W_{As(i)}$ the rate of gas desorbed through the upper area in slice i, and $W_{As(i-1)}$ the rate of gas desorbed through the upper surface in slice i-1, which is then the gas absorbed through the lower surface in slice i. For the first slice (i=1), which corresponds to the tank bottom, no molar flow will be obtained from the lower face, and for the last slice (i=n), the term $W_{As(i)}$ will correspond to the rate of gas desorbed through the liquid's free surface.

The rate of gas desorbed to bubbles for any slice i may be expressed as a function of bubble size distribution:

$$W_{Ab(i)} = V_i \int_{Lmin}^{Lmax} N_{b(i)} \pi L^2 \Psi_i dL$$

The rate of gas desorbed by diffusion through each slice's surface is expressed as follows:

$$W_{As(i)} = V_{(i)} N_{s(i)} a_f$$

where a_f, the free surface area per volume unit of liquid, is expressed in $[\frac{1}{m}]$.

The flows N_s generated by molecular diffusion result from a concentration gradient and are defined by Fick's law. The diffusive flow between slices may be calculated by a first-order approximation:

$$N_{si} = \frac{D_{AB}(C_{Ai} - C_{A(i+1)})}{\Delta y}$$

No selection has yet been made of the adequate expressions to determine mass flow to bubbles, N_b, growth rate, G, and rise velocity, v_y.

The bubble distribution function is calculated by solving equation (3) by finite differences, discretizing by means of an explicit scheme. Dividing the particle size distribution in m diameter numbers, the following system of equations is obtained for each slice i:

$$\Psi^j_{il}(1 + \frac{k}{L^*_i}G^j_{il} + \frac{k}{\Delta y}U_{tl}, + k\frac{dG^j_{il}}{dL}) - \frac{k}{L^*_i}G^j_{il}\Psi^j_{i,,l-1} = \Psi^{j-1}_{il} + \frac{k}{\Delta y}(U_{tl,}\Psi^j_{i-1,l}) \qquad (5)$$

for

$$l = 1, ..., m$$

$$j = 1, 2, ...$$

$$L^*_i = (L_{i,max} - L_{i,min})/m$$

$k = t/j$ (time step)

The diameter number m in which distribution Ψ_i has been discretized is the same for all slices. However, $L_{i,max}$ depends upon the slice under study and it is calculated from the time a bubble in slice i takes to go to slice $i + 1$, and the maximum growth rate, that is, considering a constant initial concentration medium. The maximum possible bubble diameter for slice i, based on the bubble's growth rate (G_{ij}) and the rise or terminal velocity (U_t), will be given by:

$$L_{max} = (\frac{36\alpha H \mu_L}{\rho_L i \Delta y})^{1/3}$$

where

$$\alpha = \frac{C^0_A}{\rho_g}(\frac{D_{AB}\ g\ L_{min}\ \rho_L}{3\pi\mu_L})^{1/2}$$

From equation (4) it is possible to explicitly solve for Ψ_{il}, thus obtaining for each time the distribution variation with diameter. In the same equation, U_{tl} represents the terminal velocity corresponding to each bubble diameter, which is calculated through simplificated Hadamard and Rybzynsky equation for rise velocity in systems which do not contain tensoactives

$$U_t = \frac{2(\rho_L - \rho_b)gR^2(1+\mu^*)}{3\mu_L(2+\mu^*)}$$

where μ^* was the relation between μ_G and μ_L. When gas viscosity and density (inside the bubble) are small compared to the liquid's properties, the equation is reduced to:

$$U_t = gR^2\rho_L/3\mu_L$$

The remaining parameters are defined as:

$$G_{il}^j = \frac{dR}{dt} = \frac{1}{\rho_G}\frac{\partial C}{\partial r}|_{r=R}$$

$$G_{il}^j = \frac{1}{\rho_G}N_{bl} = \frac{C_A^0}{\rho_G}(\frac{D_{AB}\ g\ L_l\ \rho_L}{3\pi\mu_L})^{1/2}$$

$$\frac{dG_{il}^j}{dL} = \frac{1}{\rho_G}\frac{dN_{bi}}{dL} = \frac{C_{AO}}{\rho_G}(\frac{D_{AB}\ g\ \rho_L}{12\pi\mu_L L_l})^{1/2}$$

The function $f_i(t, C_{Ai})$ may be transformed into

$$\int_{Lmin}^{Lmax} N_{bi}\pi L^2\Psi_i dL = \int_{Li,min}^{Li,max} C_{Ai}^j\Psi_{il}^j(\frac{D_{AB}\ g\ \pi\ \rho_L}{3\mu_L})L^{5/2}dL$$

which is integrated by the Simpson method.

The molar fraction is previously determined by means of a FLASH subroutine fixing the initial temperature and pressure, based on an equation of state. To calculate the liquid's density, Goyal equation as reported by Perry and Chilton [1973] is used, as a function of the compund's critical properties:

$$\rho_L = \frac{P_c M}{T_c}(\frac{0,0653}{\omega_c^{0,773}} - 0,09Tr)$$

where units for ρ_L, P_c and T_c are respectively [g/ml], [atm abs] and [K].

The liquid's viscosity is estimated through Thomas equation,

$$\mu_L = 0,1167\rho_L^{1/2}10^{\gamma}$$

with

$$\gamma = B(1 - Tr)/Tr$$

where μ_L is expressed in [cp], ρ in $[g/cm^3]$ and B is a constant calculated with the sum of atomic contributions (Table 3-321, [Perry and Chilton, 1973]).

Gas density is determined with the equation of state. Once the properties of the mixture's components are known, the binary diffusion coefficient is determined through the correlation developed by Sovová [1976]:

$$D_{AB} = 14,8x10^{-5}/\mu_L^{B_m}V_G^{0,6}f_m$$

where the coefficients' value depends upon the system:

- $f_m = 1,00$ *and* $B_m = -1,15$ for water.
- $f_m = 1,80$ *and* $B_m = -1,15$ for aromatic hydrocarbons and by-products thereof (benzene, toluene, chlorobenzene, nitrobenzene, tetrachloromethane, methanol, etc).
- $f_m = 2,28$ *and* $B_m = 0,50$ for aliphatic hydrocarbons and alcohols (n-paraffins, n-paraffin alcohols, cyclohexane, cyclohexene, etc).

The problem is thus reduced to solving n first-order integro-differential equations (4) representing the mass balance for component A in each slice, which is here solved by using the Runge-Kutta method of order 4th.

Input data required when applying the algorithm described are pressure, temperâture, initial molar fractions, and final temperature and pressure. Besides, the program needs the tank height value, the nucleation rate function J, and the critical properties of both components in the mixture, the latter being used to determine the thermodynamic properties.

Results of the Desorption Model

The methane-decane system was selected to evaluate the model under the following conditions: $P_{inicial} = 30[bar]$, $T_{inicial} = 423,15[K]$, $H = 0,4[m]$, $C_A^0 = 0,1884[mol/m^3]$, $P_{final} = 15[bar]$, $T_{final} = 423,15[K]$, and $C_A^* = 0,00016[mol/m^3]$

First of all, the results obtained were compared with the numerical method used and the analytical solution. Fig. 9 shows the concentration's spatial distribution values,

numerically obtained for the case in which not only desorption occurs through the liquid's free surface, and the analytical solution calculated by means of equation (1). Three curves corresponding to different times elapsed since decompression were plotted. The program was evaluated by dividing the liquid volume into 6, 10, and 15 slices. An analysis of these results allows to conclude that the numerical method used in the program approximates very well to the analytical solution. Besides, a significant improvement is not observed as the number of slices increases, and results are acceptable with only six slices.

To verify whether this last conclusion is valid for a nucleation rate different from zero, a calculation was made for two different times of the concentration variation with the position for different numbers of slices. Results shown in Fig. 10 indicate the same effect as in the previous case.

The nucleation rate J is one of the parameters having a stronger influence on desorption rate. It is feasible to adjust said parameter on the basis of experimental data. Fig. 11 shows how concentration along the tank varies for the cases in which J is equal to zero compared to J equal to $10^6[m^{-3}s^{-1}]$. A sudden increase is observed in the speed at which concentration decreases in the slices as bubbles emerge in the system. The same trend is still observed as the nucleation rate J increases.

Figures 12 and 13 show concentration distribution in the liquid at different times for $J = 10^6$ *and* $10^8[m^{-3}s^{-1}]$ respectively. Fig. 12 indicates that the upper slice reaches equilibrium at a time of 10,000 s., whereas in Fig. 13 equilibrium in the upper part of the tank is reached after 100 seconds have elapsed. A change in one order of magnitude in the nucleation rate produces a two-order of magnitude change in the time necessary to reach equilibrium.

Since the main interesting feature here is applying the model to viscous liquids, a study was conducted to determine the influence of viscosity variation on desorption rate, all other properties and parameters in the system being kept constant. Fig. 14 shows concentration distribution in time for four different viscosities (corresponding to different diffusion coefficients). As expected, it is obvious that as the liquid's viscosity increases, the time to reach equilibrium becomes longer, due to a decrease both in desorption to bubbles and diffusion towards the free surface.

The results previously shown allow to conclude that the mathematical model developed in this project successfully predicts, in qualitative terms, the phenomenon of gas desorption in a viscous liquid. The only thing that remains to do is to corroborate its applicability by comparing said model with experimental results.

EXPERIMENTAL DEVELOPMENT

The experimental study may be summarized in three activities. The first one was a

conventional PVT study about the fluids used in the tests, with the aim of obtaining basic data for a characterization thereof. The second activity is designing and assembling an equipment for desorption tests and phenomenon observation. Finally, the third activity is carrying out the tests themselves.

The system studied in our experiences consists of silicone and methane. Silicone was chosen for availability reasons. Besides, it has a wide range of viscosities and it is transparent, which will allow to visualize nucleation and desorption phenomena. On the other hand, methane was selected because it is the major component found in dissolved gas in heavy and extra-heavy crudes.

FLUID CHARACTERIZATION

Conventional PVT was carried out for the three silicones studied (100, 1000, and 10000 cSt), at a temperature of 102, 150 and 200^oF. It is an expansion at constant composition (where the system saturation pressure is determined), a differential (to obtain the solution gas as a function of pressure), and a flash release (to determine the amount of gas dissolved). Moreover, density and viscosity variation was studied as a function of pressure.

The graphs for relative volume and dissolved gas show that the three silicones behave in a very similar manner. The reason for this is that they were all saturated at the same pressure (800 psia), thus presenting a solubility degrees very similar to that of methane. Viscosity curves versus pressure, for the bubble point, illustrate how the presence of methane reduces silicone viscosity by 50 to 75the reduction being more significant for the least viscous silicone. An opposite behavior is observed in crude-gas systems. Silicone density as a function of pressure was measured for four temperatures, covering a 100 - 250 F range. These measurements were mainly made to improve fluid characterization.

The model developed to predict gas desorption uses the equation of state developed by Peng and Robinson. In order to use that equation of state it is necessary to characterize the fluids in the system under study. In other words, the properties thereof must be known. Critical properties (pressure and temperature), acentric factor, and molecular weight should be defined for each component.

Silicone characterization: An attempt was made to characterize silicone by using the group contribution techniques, especially the methods developed by Lydersen and Ambrose [Reidetal, 1977]. As expected, results were not satisfactory because these techniques were designed for substances having lower molecular weights.

As a result, fluids were characterized by adjusting some parameters of the equation of state until the liquid phase densities in the system were reproduced. Peng Robinson equation is cubic-like and, as already seen, it may be represented as:

$$P = \frac{RT}{v-b} - \frac{a(T)}{v^2 + 2bv - b^2}$$

where a(T) is a function of temperature representing the cohesion parameter, and constant b is the covolume parameter. These parameters characterize each fluid and are generally obtained from critical properties.

Since the critical properties for silicone are not known, values a and b are obtained by regression of the experimental volumetric data.

The restrictions used in regression take into account that parameters a and b must be positive by definition and that the molar volume cannot be lower than b (in the limit v $\rightarrow$ b an infinite repulsion pressure is generated), o greater than the fluid's residual volume.

To satisfy the restrictions for all experimental isotherms, it is required to assign a dependence of b with temperature, and use the data with pressures lower than 1000 psia to make sure that parameters will have positive values.

Figure 15 show the adjustment results for the 100cSt silicone, where a higher deviation is observed at low pressures and it becomes even higher as viscosity increases. Parameters obtained for three silicones are summarized in Table 5, where a dependence of b with temperature is observed. The isotherm curvature calculated with these parameters is much stronger than the one obtained experimentally, the result being error presence in pressure prediction. An attempt is being made to improve this characterization.

To represent "methane", the steam pressure equation and the critical properties taken from the project API 44 [1980] were employed. It was observed that the dependence of the attraction parameter a with temperature was not adequate at temperatures close to the critical one. A correlation suggested by Mollerup [1986] was proposed, which improves the saturation pressure prediction in the whole range of reduced temperatures used ($0.4 \leq Tr \leq 1.0$), and allows a reliable extrapolation of **a** for supercritical temperatures.

Van der Waals-type mixture rules were used. To reproduce the experimental differential release PVT data, a binary interaction parameter was introduced in the mixture rule for ñañ. Optimum values for the interaction parameter proved to be dependent on the composition and they were correlated through Redlich-Kister-type equations, suggested by Adachi and Sugie [1986]:

$$k_{ij} = l_{ij} + m_{ij}(x_i - X_j) + n_{ij}(x_i - x_j)^2 + ...$$

a quadratic adjustment being enough for our system. The results obtained in the characterization allow to predict saturation pressures in the equilibrium with a average error of 0.6%.

Description of the experimental equipment

The experimental equipment designed and outlined in Fig. 16 allows to obtain the pressure history during desorption tests and record bubble formation through photographs.

Said equipment consists of a displacement pump which allows to inject the fluids stored in vessels in the testing cell. The cell is submerged in a thermal bath. Desorption occurs in the testing cell, which is made out of glass (inside diameter = 2 cm and volume = 40 cc) to make it possible to visualize the phenomenon. Two additional vessels are used, one as a reference cell and the other one as an expansion tank (stainless steel/volume = 500 cc).

The equipment includes three pressure sensors. Gauge (SP1) measures the differential pressure in a -50 - 50 psi range, and it is located between the testing cell and the reference cell. Gauge (SP2) measures the absolute pressure in the experimental cell with a 0 - 1000 psi range, and gauge (SP3) measures the barometric pressure in the expansion cylinder in a 0 - 1250 psi range. The expansion cylinder is filled with methane until a pressure previously determined according to the pressure desired in the experimental cell after expanding is reached. The differential gauge was added to the equipment to improve measurement accuracy, since the absolute pressure gauge resolution - 1 psi - is insufficient for the pressure increases expected in the experiment.

The experiment basically includes the following steps: the experimental cell is filled with a silicone-methane mixture saturated at high pressure (800 - 1000 psi), Then the mixture is rapidly expanded and methane is allowed to escape from the cell until a desired pressure is reached and the valve is quickly closed to isolate the cell again.

As an example, Fig. 17 shows a record of pressure as a function of time for an expansion for the 10000 cSt silicone at $102°F$. The curve indicate a rise in pressure due to gas desorption. A summary of the tests carried out and the comparison thereof with the model developed will be presented in a future report.

Data Acquisition System

The desorption process evolves rapidly in time. Therefore, it is virtually impossible to record all the variables of interest and take pictures simultaneously in order to obtain an appropriate sequence for the experience. The problem is even worse if the pressure gradient in the cell increases. As a result, it is of utmost importance to automate the data acquisition system. This will allow to obtain a more reliable and complete information to be used for parameter comparison purposes within a model.

The data acquisition system includes a hardware and a software. The hardware consists of a personal computer, model 70, with a 3-mega RAM memory and a 40-mega hard disk with a data acquisition card (MC-MI 0-16 by National Instruments). The logical part consists of a data acquisition package (MEASURE by National Instruments) and a

data processing package (LOTUS 123 by Lotus Development).

Spreadsheets are used for data acquisition. They are preprogrammed with some macros facilitating the data handling and acquisition process. As a result, the process is even more automatized.

CONCLUSIONS

A predictive model has been developed for homogeneous nucleation in binary dissolutions. The model uses critical constants, the acentric factor and the pure component parachor as input parameters. Thermodynamic properties, including stability limits, are predicted with the Peng- Robinson equation of state. Nucleation rate and pressure are predicted by means of the kinetic theory in the Reid version [1978].

Calculations effected with the nucleation model coincide with results presented by Reid [1978] and Modell and Reid [1983]. Besides, they agree with some fundamental characteristics of the homogeneous nucleation process, described in various references in the literature. Positive nucleation pressures are closely related to high temperatures or significant concentrations of the most volatile component. Bubble formation rate speeds up in a narrow range of pressures. As a result, pressure prediction (and therefore bubble size) is relatively insensitive to the critical value assumed for said rate.

Nucleation predictions are presented for the methane-decane system at 5% and 10% molar methane concentrations. In both cases, nucleation pressure is negative at temperatures lower than 500 K. As a conclusion, at lower temperatures gas desorption results from a purely diffusive mechanism or a heterogeneous nucleation process.

A desorption model including two mechanisms for gas release was developed: gas desorption from the liquid to the gas phase through the surface due to molecular diffusion, and gas desorption due to bubble formation, growth and escape. The methane-decane system was used to conduct a sentitivity study on the most important variables involved in the desorption phenomenon. Said study gave the qualitative results expected. Experimental data are required to quantitatively evaluate the model.

Experimental results will be required to obtain the information for validating the model. The silicone-methane system was selected and characterized by using experimental PVT information. Some equipment to observe the phenomenon and record the pressure history during the desorption process was designed and assembled. It was necessary to automate the data acquisition system because of the information volume generated during the tests in a relatively short time.

A series of activities have been planned to improve the model: repeating the tests by using escualene (a hydrocarbon whose critical properties are known), and replacing the

glass cell by a steel cell (to be able to use more severe temperature and pressure conditions, similar to those in the reservoir). Results obtained will allow to see whether it is feasible to extend the study to a heterogeneous desorption model where the porous medium will be considered, this being the ultimate objective of the project.

REFERENCES

1. BLANDER M. *Bubble Nucleation in Liquids.* Adv. Colloid Interf. Sci., 10 p. 1979.

2. BLANDER M. + HENGSTENBERG D. + KATZ S.L. *Bubble Nucleation in n-Pentane n-Hexane, n-Pentane + Hexadecane Mixtures, and Water.* J. Phys Chem, 75(23) p. 1971.

3. BLANDER M.+ KATZ, S.L. *Bubble Nucleation in Liquids.* AICHE, 21 p. 1975.

4. CAVERO A. + Olivera C + RODRIGUEZ O. + EMBID S. *Bases Teórica para el Modelo de Desorción de gases enLíquidos Viscosos.* INTEVEP S.A. Internal Report , 1990.

5. FIROZABADI A. + HEKIM Y. + KATZ D.L. *Reservoir Depletion Calculations for Gas Condensates using Extended Analysis in the Peng-Robinson Equation of State.* Can. J. Chem. Eng., 56 p. 1978.

6. FUSSELL L.T. *A Technique for Calculating Multiphase Equilibria.* SPE, 1979.

7. LIENHARD J.H. + SHAMSUNDAR + BINEY P.O. *Spinodal Linea and Equations of States: a Review.* Nucl. Eng. Desing, 95,297-314 p. 1986.

8. MARQUEZ L. + GOMEZ W. + BORGES. A. *Estudio Experimental del Proceso de Desorción de gases enfluidos viscosos.* INTEVEP S.A. Internal Report , 1991.

9. MAZZA G. + GARATE J. *Adquisición de Datos en las Pruebas de Desorción de gases enLíquidos Viscosos.* INTEVEP S.A. Internal Report , 1991.

10. MODELL M. + REID R. C.. *Thermodynamics and its Applications.* Nueva Jersey 2da Ed. ; Prentice-Hall , 1983.

11. MOHAMED R.SS. + HOLDER G.D. *High Pressure Phase Behaviour in Systems Containing Carbon Dioxide and Heavier Compounds with Similar Vapor Pressure.* Fluid Phase Equil, 32 p. 1987.

12. MOLLERUP J.. *Thermodynamics Properties from a Cubic Equation of State.* Institutte for kemiteknid, Helsingor , 1986.

13. NGHIEM L. X. + LI Y. K. + HEIDEMANN R. A.. *Application of the Tangent Plane Criterion to Saturation Pressure and Temperature Computations.* Fluid Phase Equil , 39-60 p. 1985.

14. PERRY R. + CHILTON C.. *Chemical Engineers Handbook.*. Mc Graw Hill , 1973.

15. PENG D. Y. + ROBINSON D. B. *A New Two-Constant Equation of State.* Ind. Eng. Chem. Fundam, 15 p. 1976.

16. PENG D. Y. + ROBINSON D. B.. *Two and Three Phase Equilibrium Calculations for Systems Containing Water,.* Can. J. Chem Eng 54. , 595-9 p. 1976.

17. PENG D. Y. + ROBINSON D. B.. *Calculation of Three-Phase Solid-Liquid-Vapor Equilibrium using an Equation os State Cap. 10 en K. C. Chao y R. L. Robinson (eds) Equations of state in engineering and research.*. Washington D. C. ; Adv. Chem. Ser. 182 , 1979.

18. REID R.C. *Superheated Liquids. A Laboratoy Curiosity and, Possibly, an Industrial Course.* Chem Eng Educ, 12(2), 60-63, 83-87, (3), 108-11, 127-9(4), 194-6,203-6 p. 1978.

19. REID R. C. + PRAUNSNITZ J. M.+ SHERWOOD T. K.. *The Properties of Gases and Liquids*.. Nueva York; 3a Ed., 1977.

20. SOVOVA H.. *A Correlation of Diffusivities of Gases Liquids,.* Collection Czechoslow Chem. Commun 41 , 3715-3723 p. 1976.

21. ZELDOVICH Y. *On the Theory of New Phase Formation Cavitation, Acta Physicochimica URSS, XVII (1).* 1-22 p. 1943.

TABLE 1. Interaction Parameters k_{12} for the Methane-Decane System. Peng-Robinson EOS

TEMPERATURE [°K]	k_{12}
423,15	0,036
510,95	0,077
542,75	0,141
563,25	0,182
583,05	0,280

Correlation: $K_{12} = -0,01159 + \frac{0,016595}{1-T/T_{c2}}$

TABLE 2. Group Contributions for the Parachor Calculation

Group	Contribution
C	9,0
H	15,5
CH_3^-	55,5
CH_2^-	40,0
0	20,0

Example: Methane, $CH_3^- + H$, $[P] = 15,5 + 55,5 = 71,0$

TABLE 3. Nucleation, Spinodals and Saturation Pressures for a 10% Molar Methane Dissolution in Decane

	Temperature [°K]									
Pressures [bar]	300	360	400	450	500	515	525	550	575	585
Saturation	19,79	26,12	28,62	30,21	31,01	31,27	31,48	32,21	32,26	32,29
Nucleation	<0	<0	<0	<0	10,09	15,62	18,95	25,99	30,21	31,15
Spinodal diffusive	-380,45	-240,48	-166,84	-93,10	-36,96	-23,23	-14,84	-3,54	17,79	22,30
Spinodal	-381,43	-241,52	-167,91	-94,24	-38,20	-24,52	-16,17	-2,05	16,06	20,35
Crit. Radius $[m]x10^9$	-	-	-	-	4,45	5,00	5,47	7,27	11,40	15,13

TABLE 4. Nucleation, Spinodals and Saturation Pressures for a 5% Molar Methane Dissolution in Decane

	Temperature [°K]									
Pressures [bar]	300	360	400	450	500	515	525	550	575	585
Saturation	9,58	12,72	14,07	15,32	16,89	17,58	18,14	19,92	21,90	22,82
Nucleation	<0	<0	<0	<0	<0	0,46	4,40	13,07	19,58	21,62
Spinodal diffusive	-398,68	-257,31	-182,58	-107,24	-49,26	-34,92	-26,10	-6,62	9,07	14,26
Spinodal	-398,81	-257,55	-182,83	-107,51	-49,54	-35,22	-26,41	-6,96	8,68	13,84
Crit. Radius $[m]x10^9$	-	-	-	-	-	4,71	5,13	6,72	10,22	13,23

TABLE 5. Calculated EOS Parameter

μ[cP]	T[^oK]	a[$\frac{barm^6}{kmol^2}$]	b[$\frac{m^3}{kmol}$]
100	313,43	13515	13,211
100	340,59	14233	13,507
100	369,09	15892	13,820
100	395,21	15328	14,106
1000	310,87	153880	55,599
1000	338,93	117900	56,827
1000	368,04	126020	58,107
1000	395,37	87478	59,216
10000	311,87	955990	112,67
10000	340,37	599850	115,40
10000	368,71	774400	118,11
10000	396,04	1439600	120,76

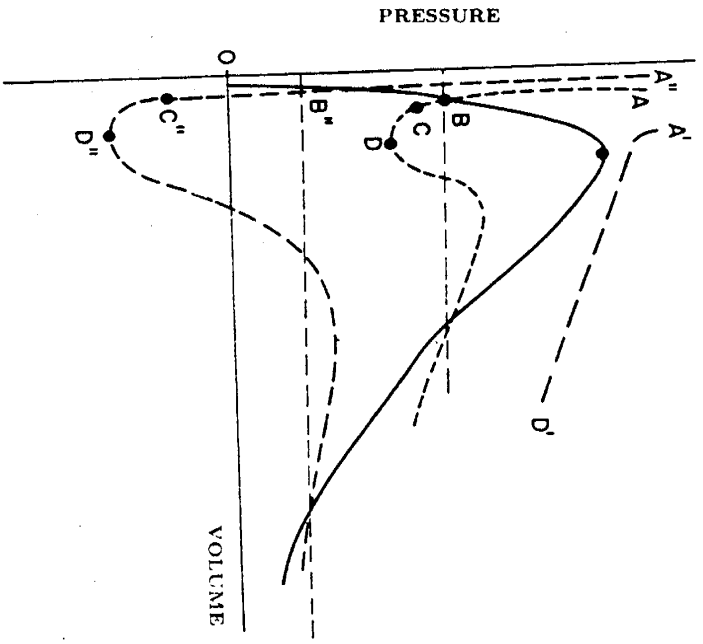

Fig. 1. **Constant Temperature Curves for Pure Substances**

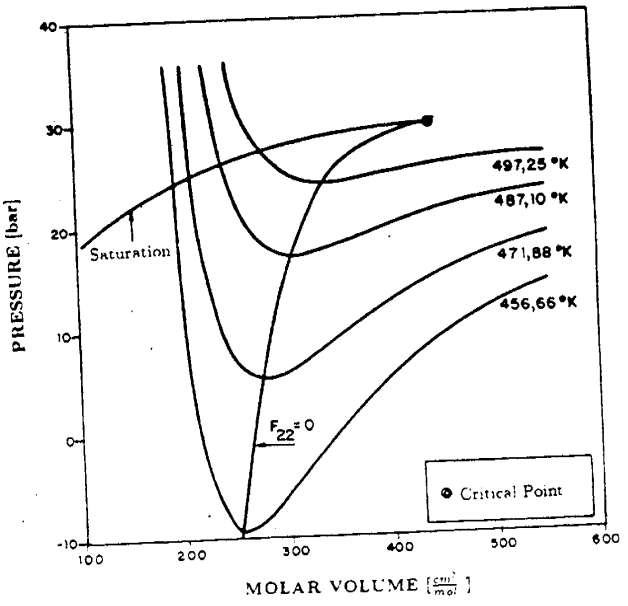

Fig. 2. **Calculated Isotherms, Saturation Pressures and Spinodal Curve for n-Hexane**

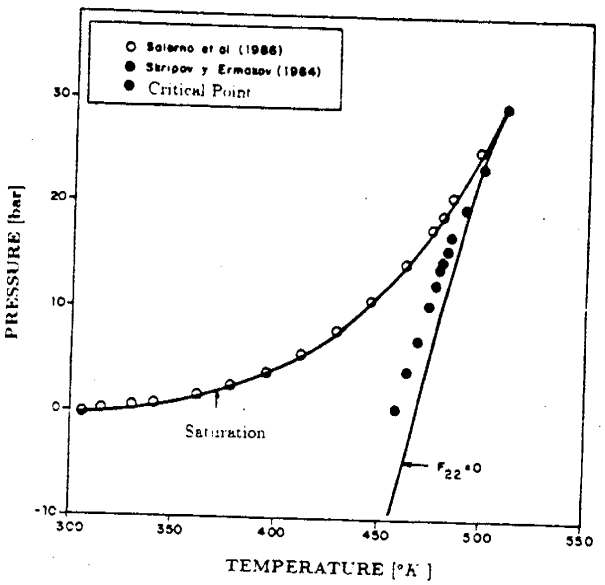

Fig. 3. Saturation Pressures and Spinodal Curve for Liquid n-Hexane: Experimental and Calculated Results

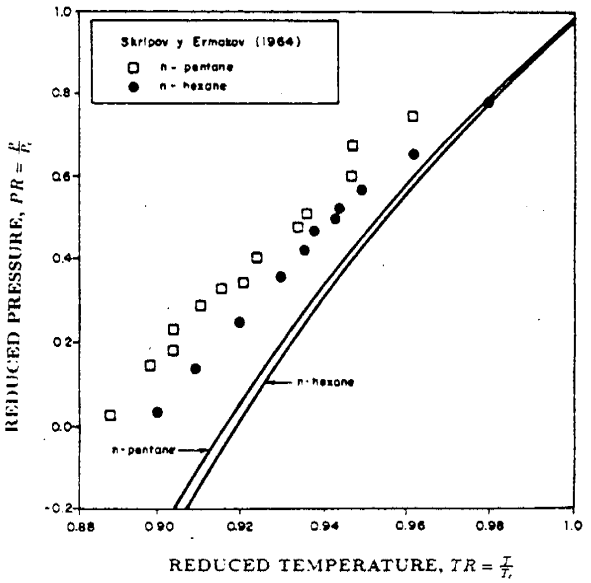

Fig. 4. Spinodal Pressures for Liquid n-Hexane and n-pentane, predicted by the Peng-Robinson Equation, and Comparison with Experimental Nucleation Data.

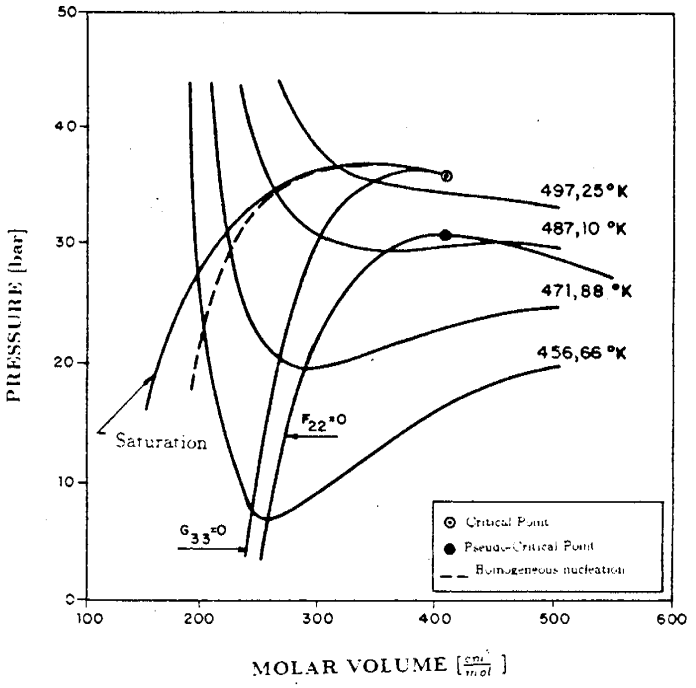

Fig. 5. **Calculated Isotherms, Saturation Pressures and Diffusive and Mechanical Spinodal Curves for a Mixture of 10% CO_2 in n-Hexane.**

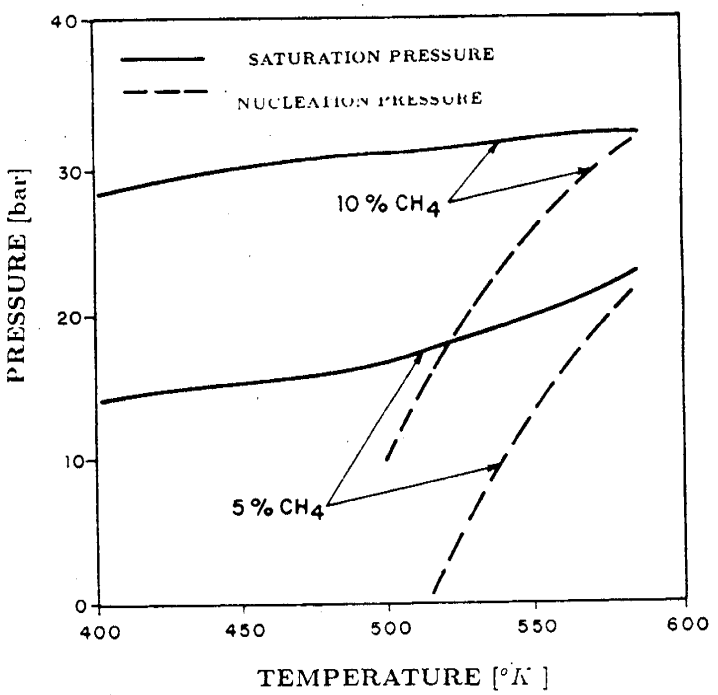

Fig. 6. **Saturation and Nucleation Pressures for 5% and 10% Methane Dissolutions in Decane, calculated with the Model.**

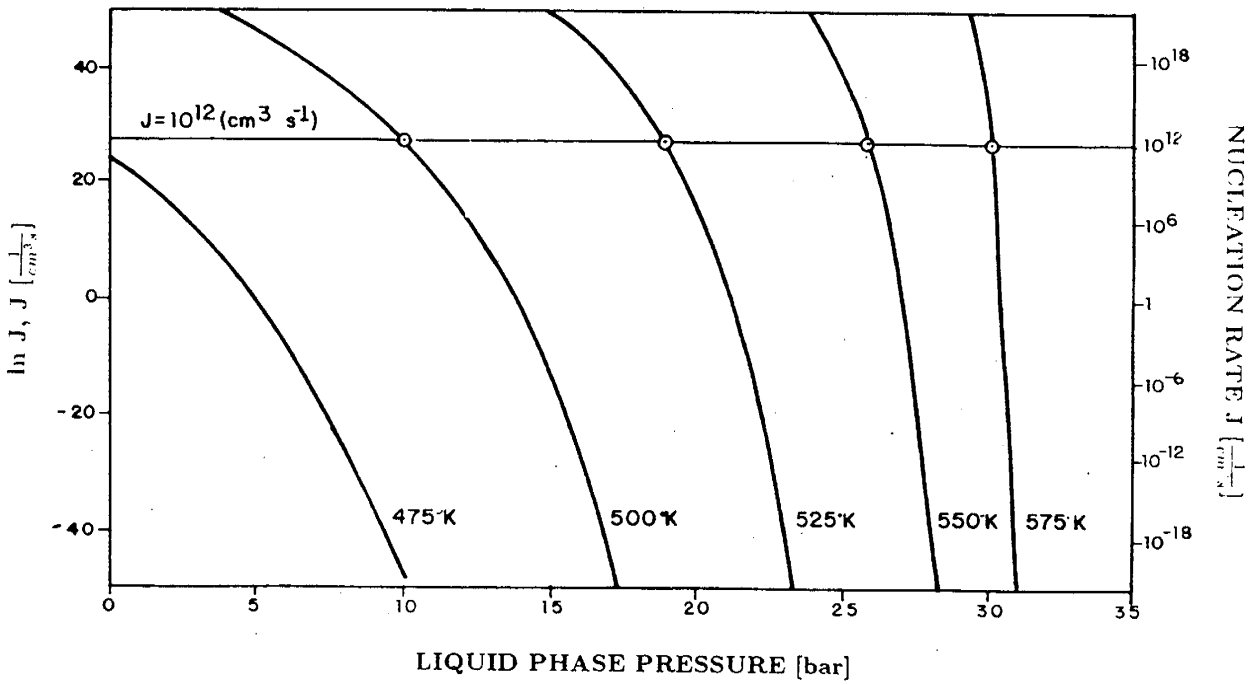

Fig. 7. **Nucleation Rate and Nucleation Pressure for a Mixture of 10% Methane in n-Decane**

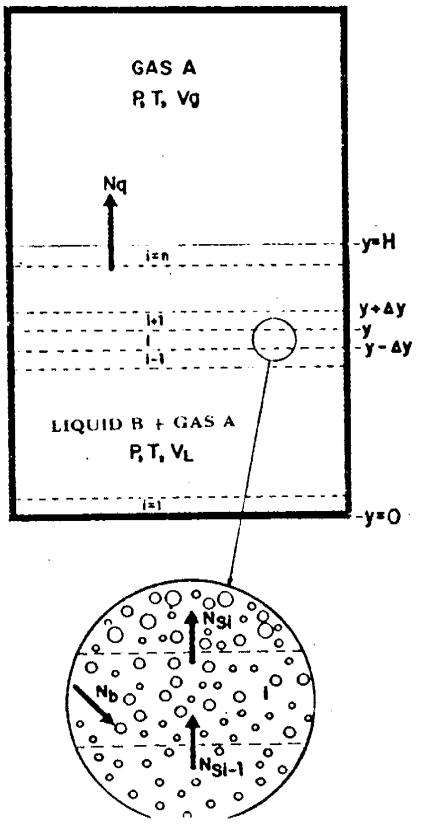

Fig. 8. **System Diagram**

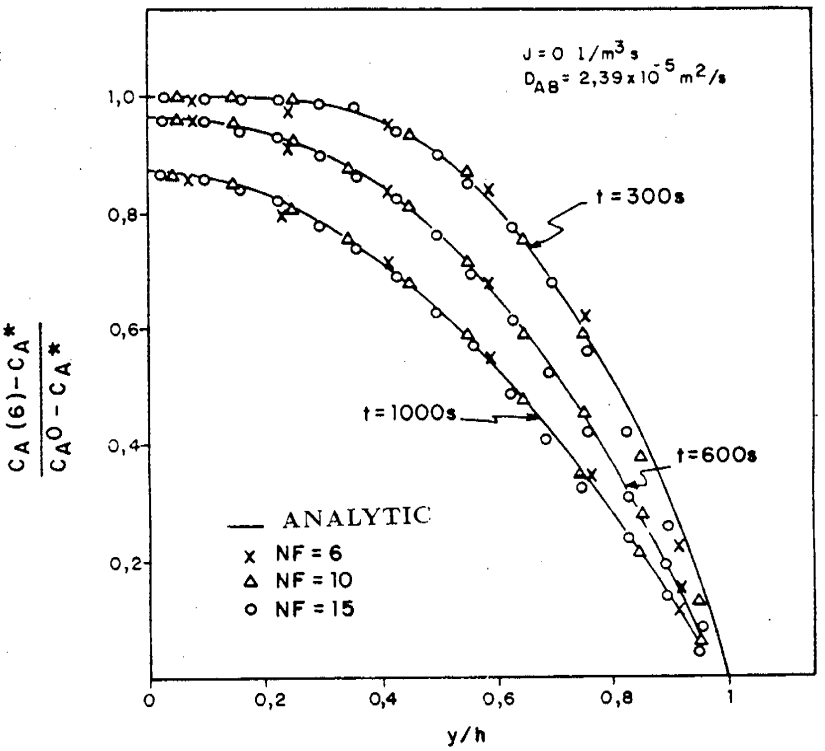

Fig. 9. Comparison of the Model with the Analytical Solution for Different Slice Numbers.

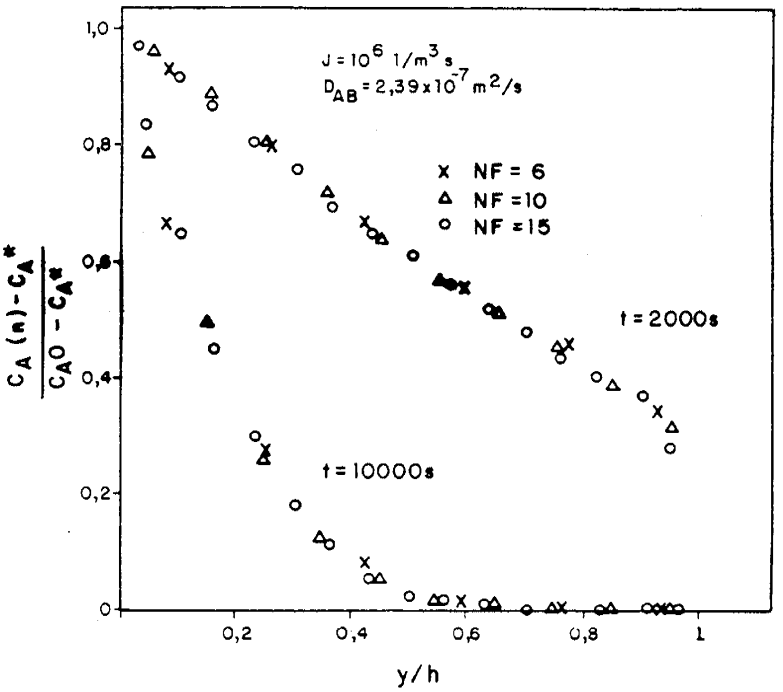

Fig. 10. Concentration Distribution as a Function of the Number of Volume Elements

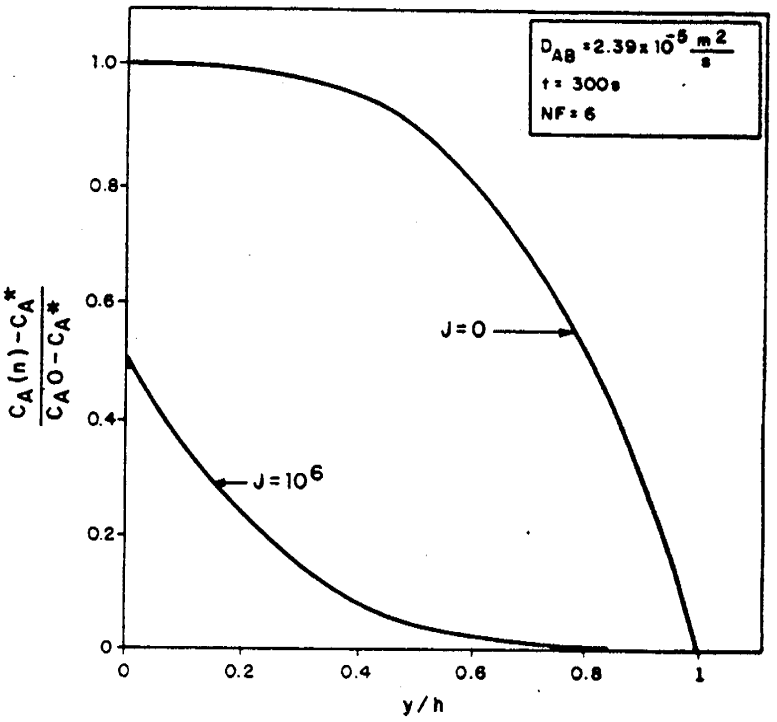

Fig. 11. Comparison of the Concentration Distribution for Desorption with Nucleation and without Nucleation.

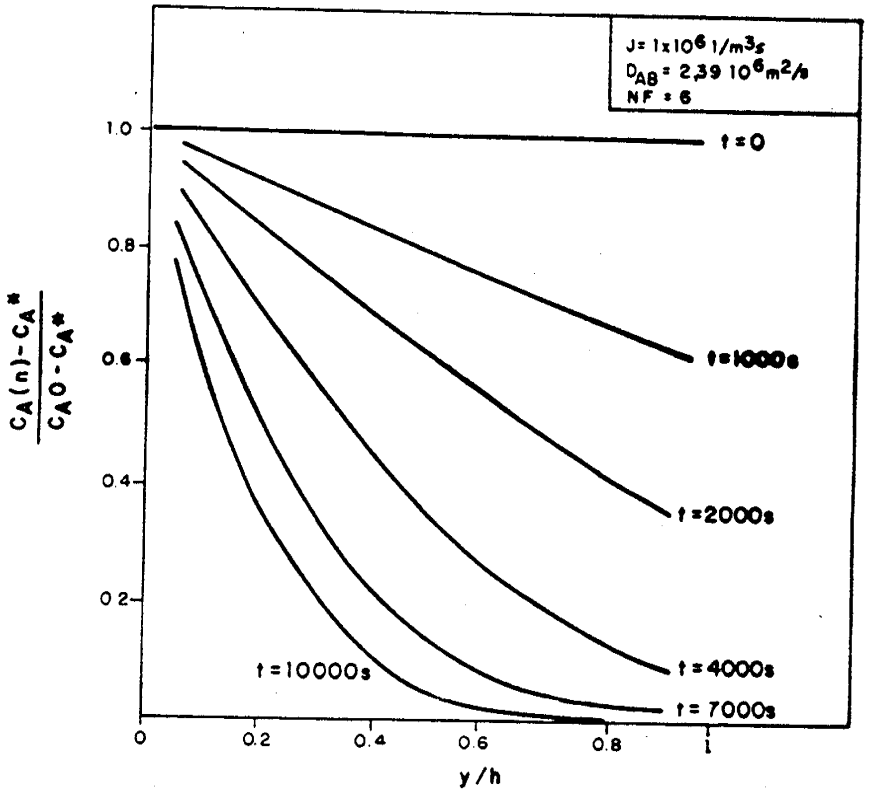

Fig. 12. Concentration Distribution as a Function of Time for $J = 12^6[1/m^2 s]$

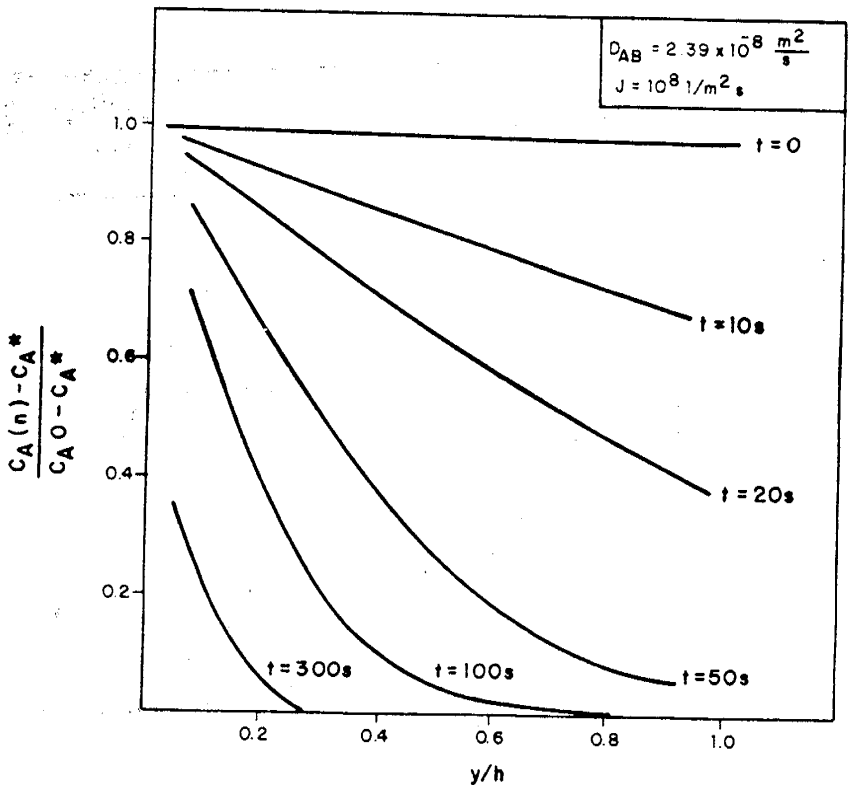

Fig. 13. **Concentration Distribution as a Function of Time for** $J = 12^8[1/m^2 s]$

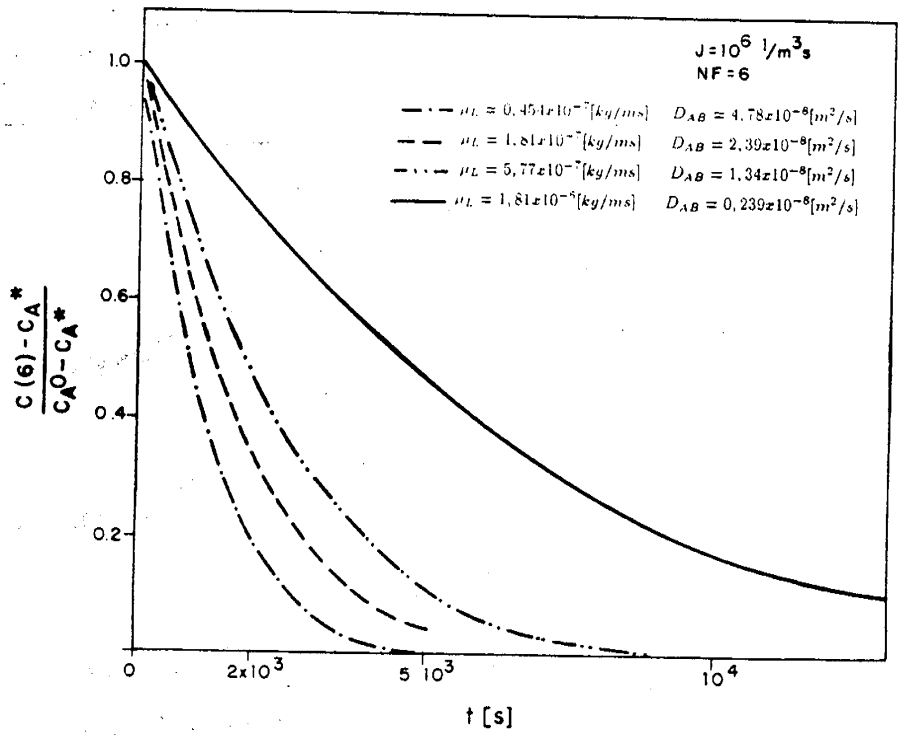

Fig. 14. **Influence of the Liquid's Viscosity on Desorption Rate**

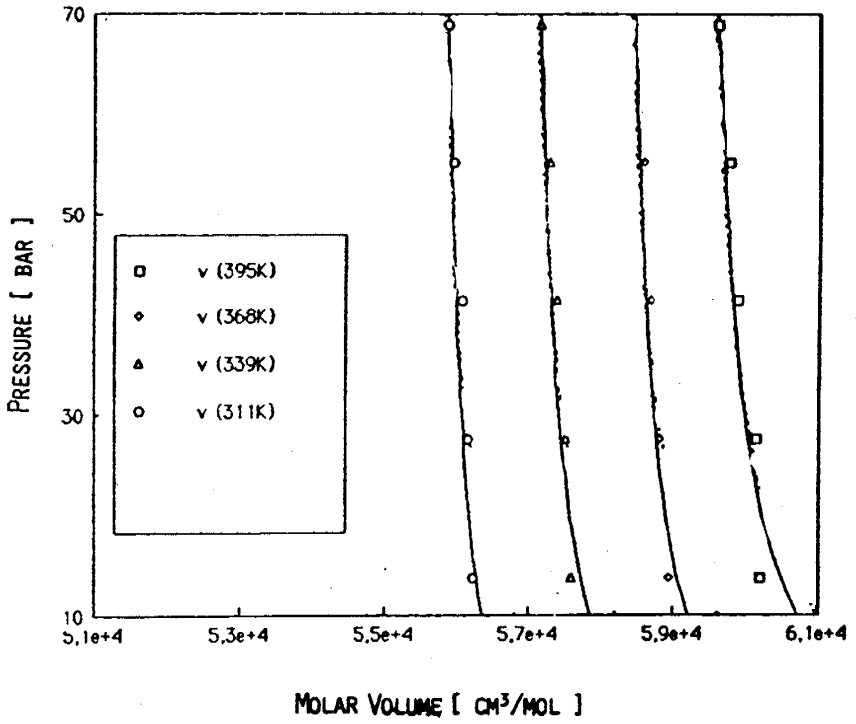

Fig. 15. **Results for the Density Matching, Silicone with 1000 cSt**

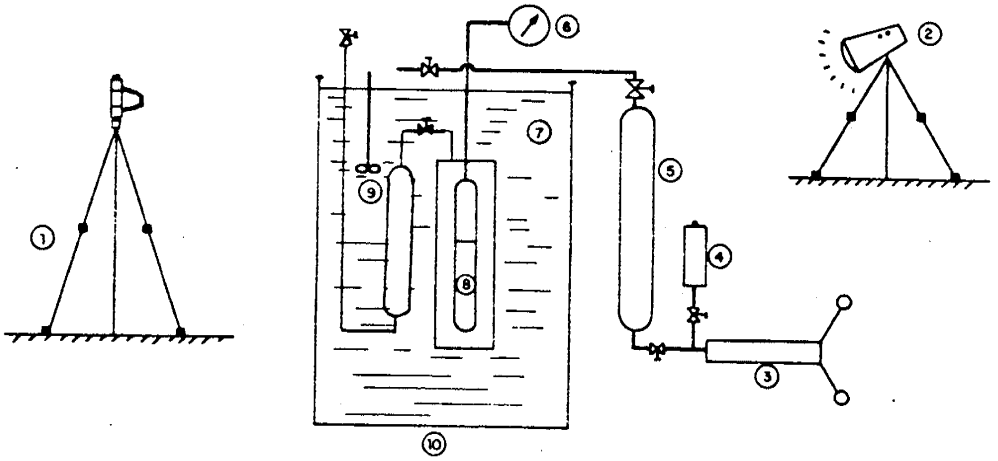

1) camera
2) reflector
3) mercury pump
4) mercury deposit
5) cilinder with silicone+methane
6) manometer
7) thermal bath (soltrol-170)
8) sample
9) stirrer
10) plexi-glass tank

Fig. 16. **Experimental Equipment**

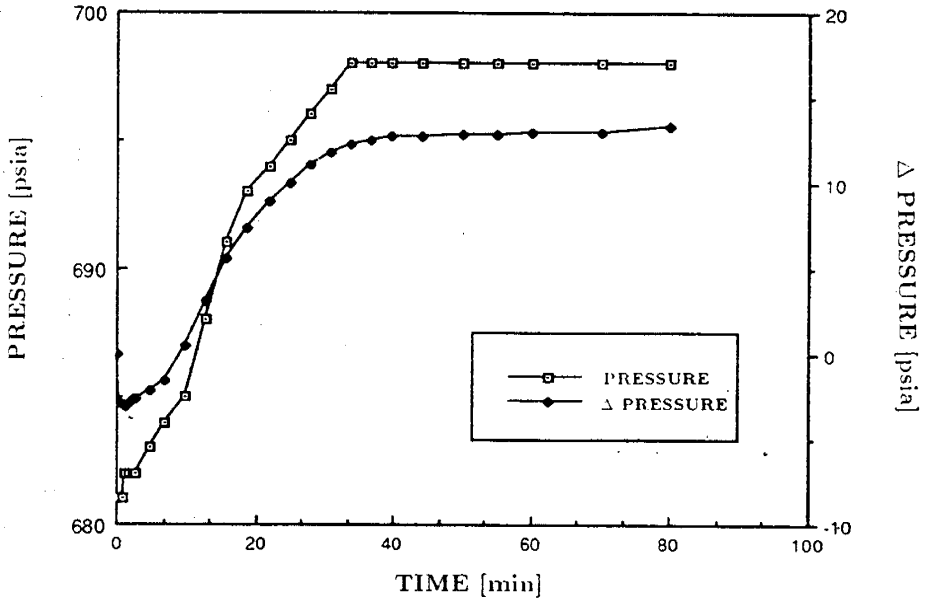

Fig. 17. **Pressure vs Time @ 839 psia, 102 ^{o}F for a 10000 cSt Silicone**

APPENDIX A

Full text of the "Sixth Amendment and Extension of Implementing Agreement IV Between the Department of Energy of the United States of America and the Ministry of Energy and Mines of the Republic of Venezuela in the Area of Enhanced Oil Recovery Thermal Processes."

SIXTH AMENDMENT TO ANNEX IV OF THE

IMPLEMENTING AGREEMENT BETWEEN

THE DEPARTMENT OF ENERGY OF THE UNITED STATES OF AMERICA

AND

THE MINISTRY OF ENERGY AND MINES OF THE REPUBLIC OF VENEZUELA

IN THE AREA OF

ENHANCED OIL RECOVERY THERMAL PROCESSES

WHEREAS, the United States Department of Energy (DOE) and the Ministry of Energy and Mines of Venezuela (MEMV) did on the 29th day of September 1980, enter into an Implementing Agreement for cooperation in the area of Enhanced Oil Recovery Thermal Processes (hereinafter referred to as the Implementing Agreement);

WHEREAS, DOE and MEMV have previously agreed to the First, Second, Third, Fourth and Fifth Amendments and Extension to the Implementing Agreement;

WHEREAS, DOE and MEMV have discharged their principal obligations and duties under the Implementing Agreement and the First, Second, Third, Fourth and Fifth Amendments and Extension to their mutual satisfaction and benefit;

WHEREAS, DOE and MEMV now desire to further extend ongoing cooperative efforts and further desire to initiate and pursue new and additional cooperative activities;

WHEREAS, the need exists to increase the recovery efficiency of steam injection methods for the recovery of heavy oil, and the use of additives continues to be an attractive method of potentially increasing recovery efficiency;

WHEREAS, DOE and MEMV desire to cooperative in the application of in-situ combustion for the recovery of heavy oil;

WHEREAS, DOE and MEMV desire to further cooperative efforts on the understanding of the thermal processes and the reservoir and its fluids where these processes are conducted;

IT IS AGREED AS FOLLOWS;

ARTICLE 1

In accordance with Article 7 of the Implementing Agreement, and in accordance with Article V of the Energy Research and Development Agreement of March 6, 1980, DOE

and MEMV hereby further amend and extend the Implementing Agreement as hereinafter provided.

ARTICLE 2

Article 1 of the Implementing Agreement and all other articles and provisions not herein amended are extended as written. The identification of Parties in Article 1 of the Implementing Agreement shall be used throughout this Amendment and Extension Agreement.

ARTICLE 3

Article 2 of the Implementing Agreement is amended by adding the following Tasks 44 through 49.

A. Steam Additives

Task 44 – DOE shall provide INTEVEP with information from the work performed by SUPRI on the transient flow behavior of steam and steam/foam flow and low pressure foam flow including data and analysis from CAT-SCAN measurements of these processes. In addition DOE/SUPRI will provide information on in-situ combustion and combustion kinetics experiments with various crudes with and without catalysts used to affect the nature and amount of fuel formed.

Task 45 – INTEVEP shall provide DOE with information from two-dimensional laboratory displacements and numerical simulation studies on the influence of surfactants on steam injection profiles and oil production performance under conditions typical of steam drive and cyclic steam processes.

B. Steam Injection

Task 46 – DOE shall provide INTEVEP with information from laboratories studies on light oil steamflooding conducted by NIPER. The research is to describe the influence of reservoir rock and its wettability, oil and its composition, brine and steam temperature on the oil recovery from light oil reservoirs.

Task 47 – INTEVEP shall provide DOE with information from laboratory work and field experience on methods to minimize heat losses in steam injection wells. Information will include well completion and injection strategies as well as types of insulating materials used.

C. Reservoir Fluid and Rock Characterization

Task 48 – DOE shall provide INTEVEP with information from computer modeling, system design, and field tests conducted by the Lawrence Livermore National Laboratory on the use of cross-borehole

electromagnetic induction tomography for imaging the two-dimensional conductivity distribution between wells in heavy oil strata and thermal injection zones.

Task 49 – INTEVEP shall provide DOE with information on research conducted on the mechanistic studies associated with heavy oil production. The effect of steam distillation on the performance on steam injection processes will be studies as well as the kinetics of gas liberation in heavy oils.

ARTICLE 4

The Implementing Agreement between DOE and INTEVEP shall hereafter consist of the Implementing Agreement as amended by the First, Second, Third, Fourth, Fifth and Sixth Amendments and Extensions.

ARTICLE 5

This Sixth Amendment and Extension shall become effective when signed by the members of the Joint Steering Committee or their designed representatives. The Implementing Agreement, as amended, shall remain in effect until March 31, 1991, or until terminated by written notice as provided in Article 8 of the Implementing Agreement.

Done in Washington, D.C. and Caracas, Venezuela.

THE JOIN STEERING COMMITTEE

On behalf of DOE

Member - Marvin Singer

Member - George Stosur

Member - Tom Wesson

9-24-89
Date

On behalf of MEMV

Member - Gunter Spasic

Member - Richard Corrie

Member - Hans Krause

Aug 24 1989
Date